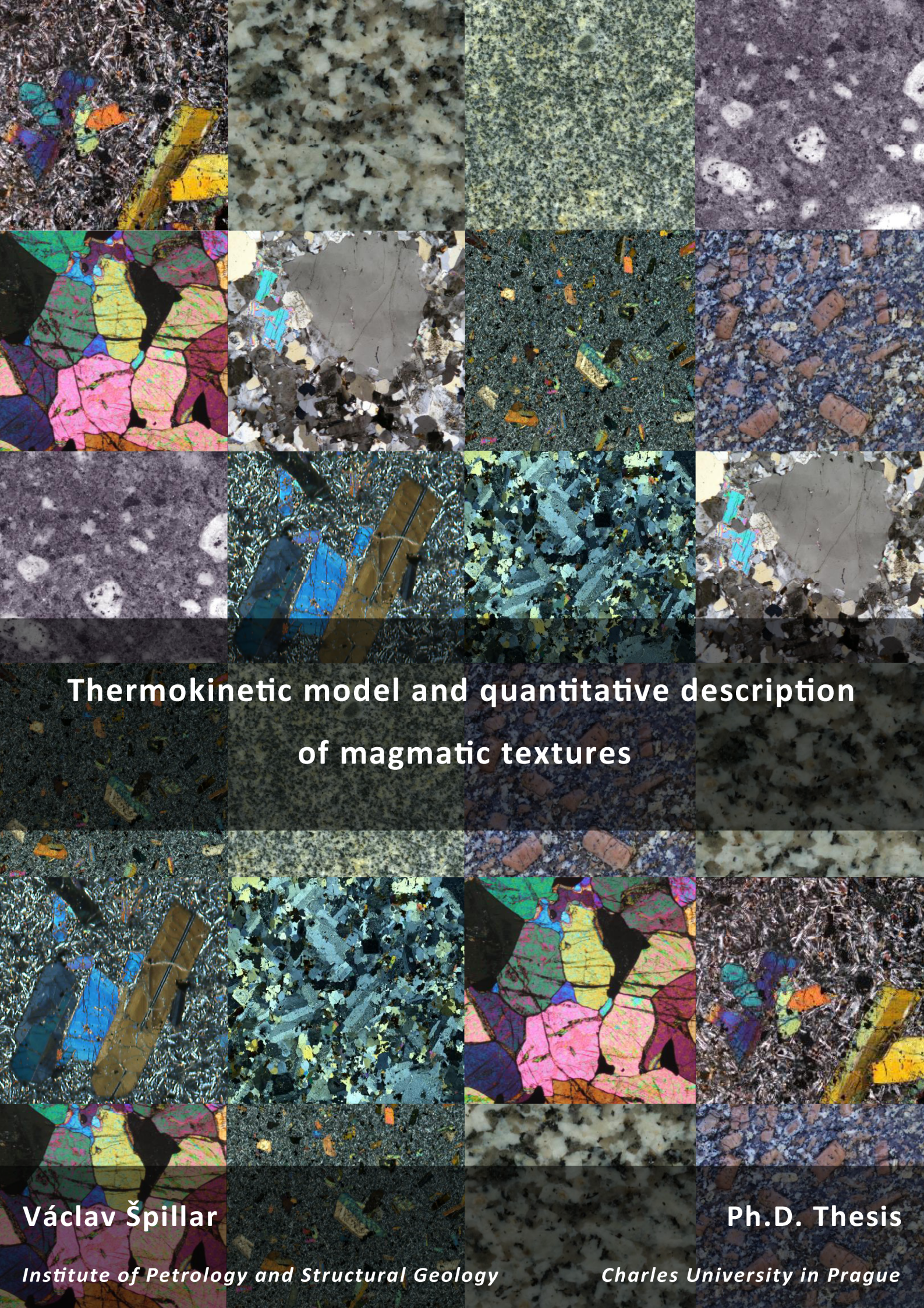

Thermokinetic model and quantitative description of magmatic textures

Václav Špillar

Institute of Petrology and Structural Geology

Ph.D. Thesis

Charles University in Prague

CHARLES UNIVERSITY IN PRAGUE
FACULTY OF SCIENCE

INSTITUTE OF PETROLOGY
AND STRUCTURAL GEOLOGY

Study program / *Studijní program*: **Geology / *Geologie***

Václav Špillar

Thermokinetic model and quantitative description of magmatic textures

Termokinetické modelování a kvantitativní popis magmatických textur

Ph.D. Thesis / *Disertační práce*

Supervisor / *Školitel*: David Dolejš

Praha, 2016

Statement of authorship

I declare that this thesis, presented for the Ph.D. degree at Charles University in Prague, is a result of my own original research and that I have cited all resources used in its preparation. Neither this thesis nor its substantial part has been submitted to fulfill requirements for other master or any other academic degree.

Prohlášení

Prohlašuji, že jsem závěrečnou práci vypracoval samostatně a že jsem uvedl všechny použité informační zdroje a literaturu. Tato práce ani její podstatná část nebyla předložena k získání jiného nebo stejného akademického titulu.

.....

Václav Špillar

V Praze, 29.6.2016

Abstract

Variability of magmatic textures records a wide array of physicochemical and mechanical processes that have operated in a magma chamber during its crystallization. Here I investigate how the final textural record can quantitatively be used to decipher the magma crystallization history and internal dynamics of magma chambers. The thesis is based on a formulation of numerical models of texture formation under the activity of various crystallization processes. Numerical results are then compared to the new quantitative textural datasets derived from four distinct magmatic systems in the Bohemian Massif: (*i*) Fichtelgebirge-Smrčiny granite batholith; (*ii*) Krkonoše-Jizera plutonic complex; (*iii*) Kdyně mafic intrusion; (*iv*) České středohoří volcanic complex. Combination of the field textural studies with their interpretation *via* numerical crystallization models provides new implications regarding magmatic crystallization and internal dynamics of magma chamber. The most important results of this Ph.D. thesis are as follows:

(*i*) a new method has been developed that allows the rates of nucleation and growth of crystals to be derived from quantitative textural data. The method requires using the crystallinity evolution in time as an independent constraint in order to provide unique solution. In case of the Hawaiian lava lakes, where direct observation of magmatic crystallization was possible, the calculated rates are in the order of 10^{-11} cm s^{-1} and agree well measured values;

(*ii*) forward numerical modeling of texture formation provided a quantitative connection between the rates of nucleation and growth and final textural record. Simulated textures suggest that the effects of crystallization processes other than is homogeneous nucleation and growth of crystals on final textural record can be separated using conventional and non-traditional textural descriptors. Quantitative relationships are calibrated between the

textural parameters and the extent of heterogeneous nucleation and mechanical interstitial melt extraction efficacy;

(*iii*) application of numerical results to natural magmatic textures ranging from granites and mafic cumulates to porphyritic volcanic rocks suggests that heterogeneous nucleation is generally a dominating mechanism of formation of nuclei in silicate magmas. Extraction of interstitial melt thus the crystal/liquid separation and accumulation of crystals is ubiquitous process in porphyritic rocks where large crystals are supposedly present in magmatic suspension;

(*iv*) in porphyritic granites the textural record indicates that large intrusive unites of plutonic complexes can be emplaced rapidly as single magmatic batches that undergo subsequent internal differentiation by mechanical processes as crystallization proceeds;

(*v*) in the Jizera granite (Krkonoše-Jizera plutonic complex) the melt extraction was most effective close to the floor and roof of more than 550 m thick intrusive unit while the crystal-melt separation was negligible in the unit interior. These observations support a new differentiation model in which the crystals suspended in a convecting magma are captured from the suspension as the melt percolated through the rigid crystal frameworks of the upper and lower solidification fronts.

In general, these results illustrate that integration of numerical modeling and field textural studies provides a powerful tool for interpreting the solidification dynamics and internal lifestyle of magma chambers.

Abstrakt / *Czech abstract*

Variabilita magmatických textur zaznamenává širokou škálu termokinetických a mechanických procesů fungujících v magmatických krbech v průběhu jejich krystalizace. Tato disertační práce se zaměřuje na kvantitativní využití texturního záznamu k pochopení krystalizační historie a vnitřní dynamiky magmatických krbů. Základem předkládané práce je formulace numerických modelů pro vznik magmatických textur za účasti různých krystalizačních procesů v průběhu tuhnutí magmatu. Výsledky numerických simulací jsou porovnávány s novými sadami texturních dat získanými ze čtyř odlišných magmatických systémů v Českém masivu, a to ze: (*i*) smrčinského granitového batolitu; (*ii*) krkonošsko-jizerského plutonického komplexu; (*iii*) kdyňské mafické intruze; (*iv*) vulkanitů Českého středohoří. Kombinace terénních texturních studií s interpretací texturních dat pomocí nových numerických modelů krystalizace poskytuje nové implikace ohledně magmatické krystalizace a vnitřních procesů v magmatických krbech. Nejdůležitější výsledky této disertační práce jsou:

(*i*) rychlosti nukleace a růstu krystalů v magmatu mohou být odvozeny z texturních dat. Další nezávislý parametr v podobě průběhu krystalinity v čase je však nezbytný k získání jednoznačného řešení. Tam, kde je možné přímé pozorování krystalizace (lávová jezera na Havaji), jsou vypočtené rychlosti v dobré shodě s rychlostmi pozorovanými v přírodních magmatických systémech;

(*ii*) numerické krystalizační modely ukazují, že s použitím obvyklých i nových kvantitativních texturních parametrů je možné oddělit texturní záznam dílčích procesů aktivních během krystalizace magmatu. Jsou kalibrovány kvantitativní vztahy mezi texturními parametry a intenzitou heterogenní nukleace a efektivitou mechanické extrakce intersticiální taveniny;

(*iii*) použití numerických modelů k interpretaci přírodních magmatických textur z různých horninových typů a prostředí vzniku ukazuje, že heterogenní nukleace je obecně dominantním mechanizmem vzniku krystalů. Extrakce intersticiální taveniny, a tím i oddělování taveniny a krystalů a akumulace krystalů se ukazuje jako zásadní proces, který je všudypřítomný v porfyrických horninách, kde se krystaly během krystalizace vyskytovaly v magmatické suspenzi;

(*iv*) texturní záznam porfyrických granitů ukazuje, že velké intrusivní jednotky plutonických komplexů mohou být vmístěny rychle v podobě jednoho magmatického pulsu, který prochází následnou vnitřní diferenciací mechanickými procesy během krystalizace v prostoru vmístění;

(*v*) v jizerském granitu (krkonošsko-jizerský plutonický komplex) textury dokumentují nejvíce efektivní extrakci taveniny v blízkosti dna a stropu a zanedbatelnou extrakci taveniny v centru více než 550 m mocného magmatického tělesa. K vysvětlení pozorovaného průběhu míry extrakce taveniny je navržen nový diferenciační model, který předpokládá zachycování krystalů z konvektující magmatické suspenze v horní a dolní solidifikační frontě;

Tato disertační práce ukazuje, že spojení terénních texturních studií a kvantitativního modelování vzniku textur poskytuje silný nástroj k pochopení magmatické krystalizace, vnitřní dynamiky a vývoje magmatických krbů.

Table of Contents

Chapter 2.

Calculation of Time-dependent Nucleation and Growth Rates from Quantitative Textural Data: Inversion of Crystal Size Distribution

Contribution of authors and Structure of the thesis

This thesis consists of the introductory chapter (Chapter 1), four published manuscripts (Chapters 2 to 5), one manuscript being prepared for submission (Chapter 6), and summary (Chapter 7).

All manuscripts are co-authored by the candidate (Václav Špillar) and his supervisor (David Dolejš). The candidate was responsible for the development of numerical models, programming, data processing, quantitative textural analyses, field work in the Krkonoše-Jizera pluton, and participated in the formulation of hypotheses and prepared manuscript drafts. Both authors were involved in the sample acquisition in the Fichtelgebirge-Smrčiny granite batholith, Kdyně mafic intrusion, and České středohoří Mts. David Dolejš participated in the formulation of scientific objectives and working hypotheses and manuscript preparations, provided technical revision and consultations of the manuscripts. This contribution is estimated to be 10 %.

List of published manuscripts (Chapters 2–5):

ŠPILLAR V. & DOLEJŠ D. (2013): Calculation of time-dependent nucleation and growth rates from quantitative textural data: Inversion of crystal size distribution. – ***Journal of Petrology*** 54, 913–931.

ŠPILLAR V. & DOLEJŠ D. (2014): Kinetic model of nucleation and growth in silicate melts: Implications for igneous textures and their quantitative description. – ***Geochimica et Cosmochimica Acta*** 131, 164–183.

ŠPILLAR, V. & DOLEJŠ, D. (2015): Heterogeneous nucleation as the predominant mode of crystallization in natural magmas: numerical model and implication for crystal-melt interaction. – ***Contributions to Mineralogy and Petrology*** 169, 1–16.

ŠPILLAR, V. & DOLEJŠ, D. (2015): Melt extraction from crystal mushes: Numerical model for texture evolution and calibration of crystallinity-ordering relationships. – ***Lithos*** 239, 19–32.

Manuscript being prepared for submition to *Journal of Petrology* (Chapter 6):

ŠPILLAR, V. & DOLEJŠ, D.: Internal dynamics of granitic magma chambers revealed by quantitative analysis of K-feldspar size and spatial distribution pattern: A case study from the Krkonoše-Jizera pluton, Bohemian Massif.

Acknowledgements

This thesis would never became a reality without continuous support, stimulating discussions, and opportunity to work on a fantastic subject with huge degree of freedom which were all provided to me by my supervisor, David Dolejš. So, thank You, David. All the staff members at the Institute of Petrology and Structural Geology are thanked for providing me a friendly place to stay and work. In addition, individual manuscripts making up the chapters of this thesis greatly benefited from constructive comments of reviewers and editors listed separately at the end of each chapter. I am also indebted to Honza for his helpful grammar suggestions.

This thesis would also never be possible without continuous support from my family and my girlfriend Bára; thank you for all your patience and support! For friendly companionship and lot of fun during the last couple of years I am indebted to all the mates; Filip, Honza, Jarda, Kuba, Ráďa, Vítek (alphabetically), and many others.

Last but not least, I received a financial support from the University Grant Agency Nr. 8210 and the Czech Science Foundation Nr. 210/12/0986 (to David Dolejš). During the last year I appreciate a funding by the Czech Science Foundation Nr. 13-06958S (to Shah Wali Faryad). Finally, I am grateful for the long-term support from the Faculty of Science's STARS program for Ph.D. students.

Chapter 1.

Introduction

1.1. Crystallization and magma chamber dynamics

Internal dynamics and evolution of magma chambers is a combined result of magma cooling and crystallization and mechanical interaction between melt and crystals (e.g., Bea, 2010). As the cargo of crystals suspended in magma increases so does the effective viscosity of magmatic suspension (e.g., Barnea & Mizrahi, 1973; Petford, 2009; Picard et al., 2013), and motion of crystals relative to the magma and flow of the bulk suspension becomes progressively hindered. Once the crystal fraction reaches the critical value when the solid phases interconnect, the crystal mush becomes essentially rigid and it develops a yield strength (Marsh, 1981; Vigneresse et al., 1996; Vigneresse & Tikoff, 1999; Saar et al., 2001; Petford, 2003). The crystallization progress thus predetermines rheological and mechanical behavior of magmatic suspension (crystal mush).

In natural magma chambers cooling as well as crystallization is non-uniform and it varies spatially. Cooling starts from intrusion contact and progresses into the magma chamber interior. As a result, solidification fronts form through which crystallinity increases and magma evolves from a liquid or sparse suspension to nearly solid slurry while magma chamber interior remains in a liquid state (e.g., Marsh, 1989, 1995, 2002). Initially, the solidification fronts are sharp and thin and located close to the intrusion contacts. As cooling progresses, the fronts become thicker and they propagate into the magma chamber at the expanse of the liquid or suspension zone. The suspension zone is able to flow and it may be convecting (e.g., Marsh, 1989, 1995; Verhoeven & Schmalzl, 2009; Bea 2010; Huber et al.,

2012), and suspended crystals are able to move by gravitational settling due to density difference relative to melt (e.g., Schwindinger, 1999; Verhoeven & Schmalzl, 2009). Efficacy of both the crystal settling and magma convection depends, among other factors, on the thickness and viscosity of the suspension zone. If conditions are favorable, the settling velocity exceeds the propagation rate of the upper solidification front. In turn, the upper solidification front is effectively being disaggregated as it grows and all new crystals are gravitationally dragged away and deposited onto the lower solidification front (Fig. 1.1).

Two general end-member cases of magma chamber solidification are thus theoretically possible: (*i*) solidification front-dominated, where crystallization mainly proceeds *in-situ* and it takes place symmetrically within the upper and lower solidification fronts; (*ii*) accumulation-dominated, where the rate of crystal settling exceeds the front propagation and the lower solidification front grows as a cumulate pile. Needless to say, the transition between the two end-member cases is driven by the magma crystallization kinetics. Crystallization kinetics dictates the appearance rate and crystal size at the solidification front edge, thus the crystal settling efficacy. This problem will be discussed later and it will be illustrated how kinetics comes into play in determining the mode of magma chamber solidification (Section 1.3).

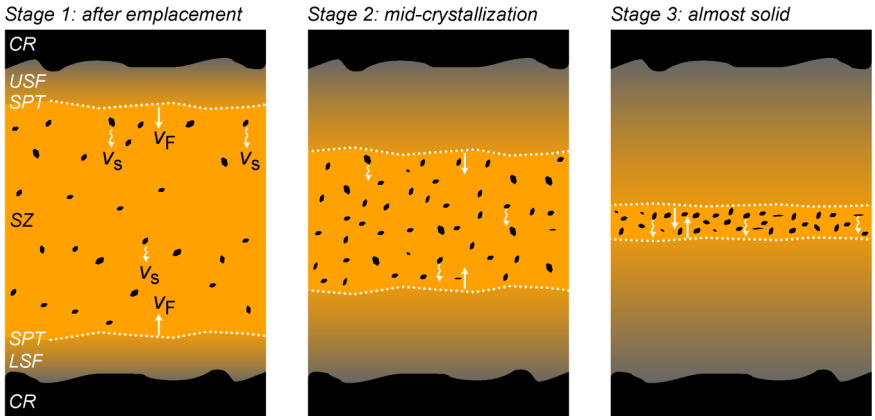

Fig. 1.1. *Evolution of a sill-shaped magma chamber by propagation of solidification fronts and suspension crystallization. Abbreviations: CR – country rock; USF – upper solidification front; SPT – solid percolation threshold; SZ – suspension zone; LSF – lower solidification front. Symbols: v_S – crystal settling velocity; v_F – solidification front propagation velocity.*

Excepting outstanding cases of the Hawaiian lava lakes (e.g., Cashman & Marsh, 1988; Cashman, 1993), magma chambers are inaccessible to direct observations. Understanding their internal processes thus remains restricted to the indirect evidence and to laboratory and numerical modeling studies. In this thesis, I will show that magmatic textures provide a valuable record of the kinetics and mechanics of magma crystallization process and may serve as an important tool in our understanding of a magma chamber evolution.

1.2. Physicochemical principles of magmatic crystallization

When a melt cools below the equilibrium liquidus temperature it becomes oversaturated in one or multiple solid phases and begins to crystallize. The crystallization proceeds by two mechanisms – nucleation and growth of crystals. After crystallization the system may experience a period of textural coarsening in which small crystals are destroyed in order to reduce the excessive surface energy. These processes operate in a closed system and represent *in-situ* crystallization. Apart from that, mechanical movement of crystals can occur and distant parts of the crystallizing magma chamber can exchange their crystals.

1.2.1. *In-situ* kinetic crystallization

Below the liquidus, bulk solid phase is energetically favorable with respect to liquid state as Gibbs energy per unit volume, mass, or number of moles of solid is lower than that of the melt. Crystals, however, have finite surface area and associated surface energy (surface tension) contributes to the energy budget. While generally small, the surface energy becomes important in small crystals, whose surface to volume ratio is high and the surface energy tends to destabilize them. As a result, crystals are unstable below certain critical size and atomic, molecular or ionic clusters smaller than the critical size would dissolve. To form a thermodynamically stable crystal, the critical size must be overcome. This happens as a result

of random collisions of building units (atoms, molecules, ions) in the melt. The formation of clusters with structure analogous to crystal lattice is called homogeneous crystal nucleation (e.g., Becker & Doring, 1935; Lasaga, 1998; Hammer 2004).

Critical cluster size is a strong function of the crystal surface energy. However, the surface energy is considerably lowered if the cluster shares part of its surface with another solid phase. In turn, presence of solid surfaces on which clusters may be formed decreases the critical cluster size and facilitates crystal nucleation. In this case, the nucleation is termed heterogeneous as it takes place on heterogeneities in a heterogeneous system composed of multiple phases (e.g., Lasaga, 1998). Due to the smaller critical cluster size and lower associated energy barrier of nucleation, heterogeneous nucleation is easier and a majority of crystals are supposed to be formed by this process (e.g., Lofgren, 1983; Hammer et al., 2010).

Once a thermodynamically stable crystal (larger than the critical size) is formed, it continues to grow by addition of building units on its surface (e.g., Kirkpatrick, 1975; Lasaga, 1998). Building units remain most stable in locations where the largest number of bonds can be formed to the existing crystal surface. However, the specificity with which the positions are chosen depends on the degree of undercooling. At low undercooling, only the most favored locations are always chosen and the crystal surface remains, on the atomic level, ideally flat. As undercooling increases the specificity of attachment decreases and the surface evolves to rough with large elevation differences (e.g., Lasaga, 1998). Depending on the degree of undercooling, concentration of impurities or defects in crystal lattice or other environmental variables, the crystal growth thus occurs by several growth mechanisms which differ on the atomistic scale (e.g., Kirkpatrick, 1975).

1.2.2. *In-situ* static recrystallization and size-dependent growth

The crystal growth mechanisms considered in the previous section (1.2.1) are jointly termed surface-controlled growth, as the reaction on the crystal surface is the rate limiting step that determines the overall crystal growth rate (e.g., Kirkpatrick, 1975; Lasaga, 1998). In

surface controlled growth, the crystal size increases steadily and the growth rate remains constant when all the intensive variables remain fixed.

In contrast to the surface control of growth, the transport of the reactants to the crystal surface may be the rate-determining factor. In such a case, the crystal growth becomes diffusion-controlled. During the diffusion-controlled growth a depleted zone impoverished in nutrients concentrated in the crystal forms around its surface and the nutrients must be transported through the depleted zone by diffusion. Larger crystals are surrounded by larger depleted zones and the reactant transport is thus slower. As a result, the growth rate of crystal decreases with increasing crystal size (e.g., Lasaga, 1998).

Transport of nutrients is not the only process leading to the crystal size-dependent growth rate. As already stated (Section 1.2.1) the surface energy contribution adds to the energy budget of crystallization and it reduces the effective driving force for crystallization experienced by a crystal. The size-dependent surface energy effect propagates into the growth rate which also becomes size-dependent. For macroscopic crystals, the surface energy contribution is usually unimportant compared to the bulk Gibbs energy of crystallization. However, close to the equilibrium, at low undercooling, the bulk Gibbs energy of crystallization is small and the surface effects become important. Small crystals are thus energetically unfavorable compared to the large ones and in a system held close to the equilibrium the material tends to be transferred from small to larger grains. This effect is variably referred to as textural coarsening, Ostwald ripening or textural equilibration and it decreases the total surface area thus the surface energy of the system (e.g., Higgins, 2011).

The differences in the driving force due to surface effects are generally small leading to miniscule rates of textural coarsening. The coarsening is thus ineffective in rapidly crystallizing systems, where bulk Gibbs energy of crystallization dominates, but it becomes important where the crystallization is slow and the system is held at high temperatures for a prolonged period of time. In turn, while volcanic rocks are expected to be rarely affected by coarsening, the coarsening effects are ubiquitous in metamorphic rocks and their importance in plutonic rocks is being increasingly recognized (Fig. 1.2; e.g., Higgins, 2011).

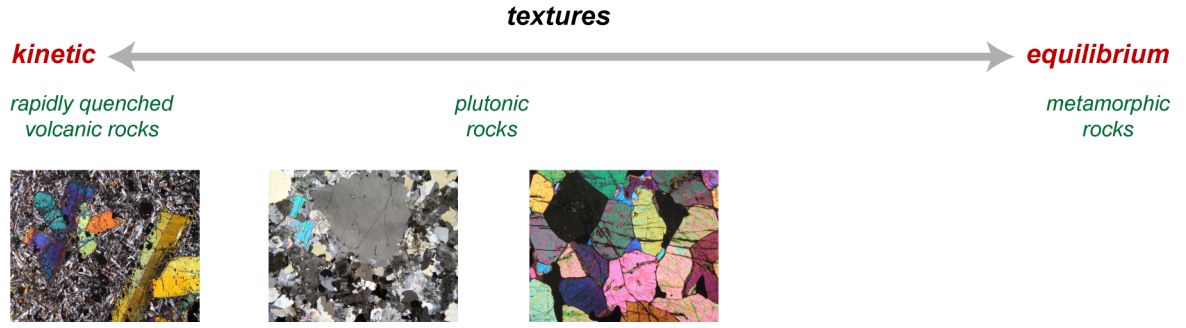

Fig. 1.2. *Concept of kinetic and equilibrium textures. In rapidly quenched (volcanic) rocks, the textural equilibration is unlikely, whereas in metamorphic rocks it is expected to be widespread. Examples of textures (from left to right): porphyritic trachybasalt, České středohoří Mts.; porphtyritic granite, Fichtelgebirge granite batholith; dunite cumulate, Kdyně basic intrusion. All geological units are located within Bohemian Massif, central Europe.*

1.2.3. Open system processes

So far, we have considered the crystallization processes involving local transport of material on a grain-scale only. *In-situ* crystallization almost certainly represents a suitable model for crystallization in some settings such as in chilled margins of larger magma bodies or in small sills and dikes. However, it is being increasingly recognized that in many cases the crystals with very different growth histories are assembled together in the final solidified rock (e.g., Davidson et al., 2007). This assertion is supported by numerical simulations of magma chamber dynamics which suggest that originally unrelated domains of magma with their phenocrysts can be brought together by chaotic convection (Bea, 2010). Detailed study of major and trace elements, isotopic or cathode luminescence zoning can be used to track the variations of melt composition from which a crystal grew as well as to constrain the time-scale of crystal residence or magma mixing (e.g., Davidson et al., 2007; Morgan et al., 2004; Słaby & Götze, 2004). In addition, density differences between crystals and melt are expected to promote gravitational separation by Stokes' settling (e.g., Schwindinger, 1999). While (partial) cumulate origin of resulting rocks can be identified geochemically, textural distinction between cumulates and *in-situ* crystallized rocks is still controversial (e.g., Vernon, 1986; Vernon & Collins, 2011).

1.2.4. Rates of crystal nucleation and growth in magmatic systems

The rates of crystal nucleation and growth are functions of environmental variables of which the most important is undercooling below the temperature of liquidus. Both rates equal to zero in the equilibrium and as undercooling increases, the rates also increase. After reaching maxima, the rates turn to decrease (Fig. 1.3). The decreasing trends are due to the temperature decrease and associated Arrhenian deceleration of kinetics (e.g., Lasaga, 1998).

A number of experimental studies measured the growth rate as a function of undercooling in melts of geologically relevant composition while comparable studies of the nucleation rate are much more limited (e.g., Kirkpatrick, 1975, 1976, 1977, 1979; Fenn, 1977; Swanson, 1977; Lofgren, 1983; Swanson & Fenn, 1986; Muncill & Lasaga, 1987, 1988; see Hammer 2008 for review). The undercooling itself, however, remains poorly known in magmatic systems. Alternatively, empirical studies of solidification of lava lakes and dikes suggest that both kinetic quantities are related to the cooling rate of magma (e.g., Cashman, 1993). In these studies, the time-integrated rates of nucleation and growth come from the total

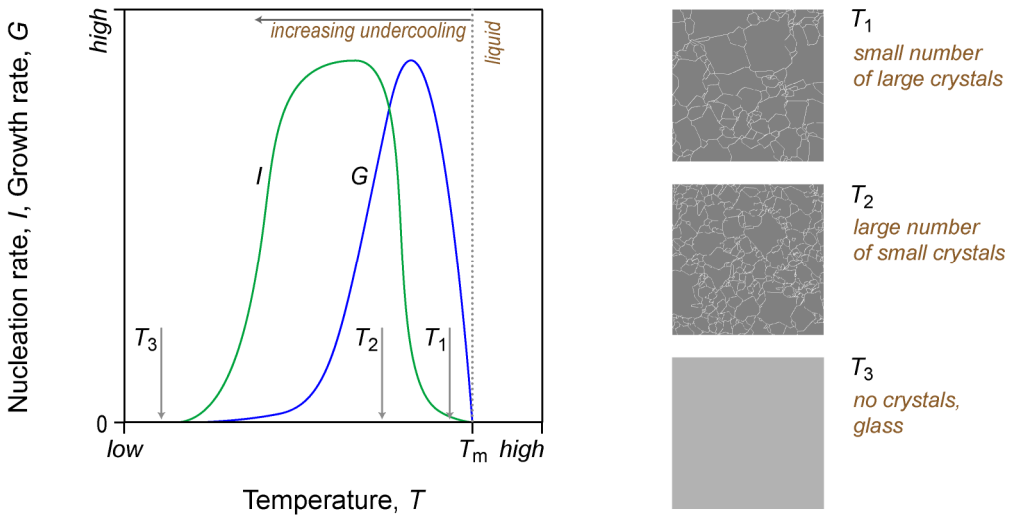

Fig. 1.3. *The rates of nucleation, I, and growth, G, as a function of undercooling below the temperature of liquidus, T_m. See Section 1.4.2 for the discussion of textural evolution during crystallization at temperatures T_1, T_2, and T_3.*

numbers and sizes of crystals in a given rock volume. Combined with the cooling rate from thermal models, this approach provides characteristic, time-averaged rates of nucleation and growth as a function of the cooling rate.

Experimental studies conducted mostly on analogue materials indicate the size-dependent nature of the crystal growth laws and suggest that inherent variability may exist between the growth rates of otherwise comparable crystals (i.e., dispersion of growth rate) (e.g, Eberl et al., 2002). The physical origin of these effects as well as its potential significance in magmatic crystallization is, however, not yet known.

1.3. Crystallization and magma chamber dynamics revisited: Illustrative exercise on the upper solidification front stability

In this section I will use an example of upper solidification front propagation *vs*. destruction due to crystal settling to illustrate the interplay of mechanical and kinetic effects during magma crystallization. As cooling progresses the isotherms and the crystallinity isolines propagate into the magma chamber and a zone in which crystal mush locks into the interconnected crystal framework expands through the suspension zone (e.g., Marsh, 1995, 2002). A rheologically rigid zone of interconnected crystal framework is bounded by the solidus isotherm on its outer side and by the isotherm at which critical crystallinity of interlocking occurs on the inner side. At the isotherm of critical crystallinity, the rigid crystal mush evolves to mobile suspension. The crystals at the boundary are subjected to gravity and can escape from being captured in the upper solidification front by Stokes' settling. A ratio of the crystal settling to the solidification front propagation velocity thus determines whether the magma chamber solidifies by crystal accumulation or whether an *in-situ* solidification front is stable and propagates.

1.3.1. Crystallization of sills: Cooling, crystallization, and characteristic crystal size

Let us assume tabular magma chamber (sill) of half-thickness D emplaced horizontally deep into host rocks and cooling conductively. To keep this exercise simple, I will ignore the effects of internal magma convection, cooling due to volatile release and transport within the host rock, or latent heat release during the crystallization. The temperature within the magma can be calculated analytically and is given by (e.g., Marsh, 2002):

$$\frac{T\left(x',t'\right)-T_w}{T_0-T_w}=\frac{1}{2}\left(\operatorname{erf}\frac{1+x'}{2\sqrt{t'}}+\operatorname{erf}\frac{1-x'}{2\sqrt{t'}}\right), \tag{1.1}$$

where $T(x',t')$ is temperature at dimensionless position x' at dimensionless time t', T_w is initial wall-rock temperature, and T_0 is initial temperature of magma. Dimensionless time and position are defined as

$$x'=\frac{x}{D}, \qquad t'=\frac{K}{D^2}t, \tag{1.2}$$

where x and t are absolute position and time, respectively, D is the magma chamber half-thickness, and K is thermal diffusivity. The dimensionless time, t', is thus the absolute time normalized by the characteristic cooling time, $t_{char} = D^2/K$, leading to $t' = t/t_{char}$. The position x is a vertical coordinate with origin in the center of the magma chamber.

Let us further assume that the magma was emplaced into the upper crust (T_w = 200 °C) at its liquidus temperature (T_0 = 1200 °C), and that its solidus temperature is 200 °C lower than the liquidus. These values broadly approximate the liquidus and solidus temperatures of basaltic magmas, as measured for example in Hawaiian lava lakes (e.g., Cashman & Marsh, 1988; Cashman 1993). The cooling model (Eqn. 1.1) enables us to calculate the temperature evolution (Fig. 1.4a) and the time of arrival of solidus isotherm thus the duration of the crystallization interval at any point within the magma body. As expected, the crystallization is short close to the wall-rock, but longest in the center of the sill (Fig. 1.4b), where the solidus

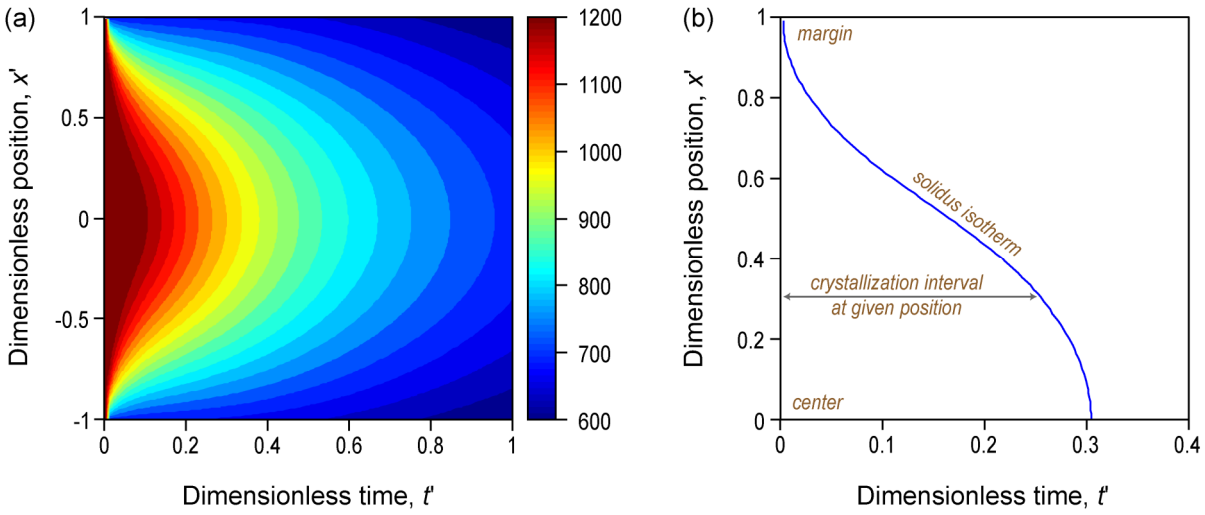

Fig. 1.4. *Thermal model of sill-shaped conductively cooling magma chamber.* **(a)** *thermal evolution (°C) of solidifying sill-shaped magma chamber. Model parameters: magma liquidus temperature, T_L = 1200 °C; magma emplaced at its liquidus temperature; magma solidus temperature, T_S = 1000 °C; wall-rock temperature, T_W = 200 °C; thermal diffusivity, K = 10^{-6} m^2 s^{-1}.* **(b)** *time of arrival of solidus isotherm as a function of relative position within a magma chamber.*

isotherm arrives at t' ≈ 0.3, that is, at 30 % of the characteristic cooling time. During this crystallization interval the temperature drops by the liquidus minus solidus temperature difference, i.e., by 200 °C. Using the time and temperature difference, the cooling rate (in °C s^{-1}) at any point within the magma chamber of arbitrary half-thickness can be evaluated.

A number of crystallization studies recognized that the rate of growth and nucleation relates to the cooling rate. For basaltic magmas, the relationships for the growth rate, G, and nucleation rate, I, were quantitatively calibrated (Cashman, 1993):

$$\log G = -7.81 + 0.88 \log \frac{\mathrm{d}T}{\mathrm{d}t}, \qquad \log I = 0.72 + 1.35 \log \frac{\mathrm{d}T}{\mathrm{d}t}, \tag{1.3}$$

with original units of °C $hour^{-1}$ for the cooling rate, $\mathrm{d}T/\mathrm{d}t$, cm s^{-1} for the growth rate, cm^{-3} s^{-1} for the nucleation rate. Using the rates of growth and nucleation, the characteristic crystal size, L_0, can be estimated (e.g., Marsh, 1998):

$$L_0 = C\left(\frac{G}{I}\right)^{\frac{1}{4}}, \tag{1.4}$$

where the constant C is a geometrical factor of the order of one and we further use $C = 1$. The characteristic crystal size is smallest near the intrusive contact and it increases into the magma chamber interior, where crystallization period is longer and cooling rate slower (Fig. 1.5). In addition and as expected, greater sill thickness leads to overall greater crystal size.

1.3.2. Crystallization of sills: Formation of upper solidification front

The simple cooling-crystallization model (Section 1.3.1) allows a typical grain size in a solidified rock to be estimated as a function of the position within the magma chamber and magma chamber thickness (Fig. 1.5). Interlocking and mutual capture of crystals to form the rigid part of the solidification front, however, occurs earlier during the crystallization and the crystals at the capture front are thus smaller than the expected characteristic crystal size, L_0. The interlocking occurs at rheologically critical crystallinity, Φ_{crit}, whose estimates vary

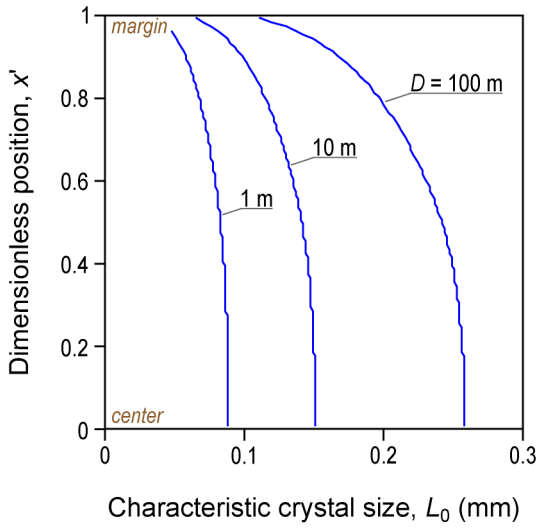

Fig. 1.5. *Characteristic crystal size, L_0, as a function of relative position within the magma chamber for three representative values of magma chamber half-thickness, D.*

greatly according to crystal shape or size sorting (e.g., Marsh, 1981; Vigneresse et al., 1996; Vigneresse & Tikoff, 1999; Saar et al., 2001; Petford, 2003). In further calculations we will use a conservative estimate of $\Phi_{crit} = 0.3$. I will further assume that crystallinity increases linearly with time and temperature during the crystallization interval. The critical crystallinity, $\Phi_{crit} = 0.3$, is thus reached during the 30 % of the crystallization interval and the characteristic crystal size at which the critical crystallinity and rheological transition occurs reaches 30 % of the final size L_0. In general and under above-mentioned assumptions, the characteristic crystal size at the critical isotherm, L_{crit}, can be estimated as

$$L_{crit} = L_0 \Phi_{crit}. \tag{1.5}$$

The crystals at the critical isotherm are located on a boundary between the mobile suspension and the rigid zone of the solidification front. These crystals are thus the largest and the most mobile ones which are still able to escape from being captured in the advancing upper solidification front by settling. The settling velocity, v_s, is given by the Stokes' law:

$$v_s = \frac{2}{9} \frac{g \Delta\rho}{\eta} \left(\frac{L_{crit}}{2} \right)^2 \tag{1.6}$$

where g is acceleration due to gravity, $\Delta\rho$ is density difference between the crystals and the melt, and η is effective viscosity of suspension. As solidification front advances towards the center of the magma chamber, the characteristic crystal size at the isotherm of critical crystallinity increases and so does the settling velocity. In other words, the settling velocity of crystals at the solidification front edge increases as the front thickens (Fig. 1.6).

The balance between the settling velocity, v_s, and the front propagation velocity, v_f, determines whether the upper front is stable and propagates by crystal formation or the front disaggregates by crystal release and settling into the chamber interior. In case of stable and propagating front the front propagation velocity equals to the propagation velocity of the isotherm of critical crystallinity. In this simple model, the propagation velocity is quantified

as a numerical derivative of the front position in discrete time steps. The front propagation velocity is high in the initial period of cooling, then it decreases and finally increases before the upper and lower solidification fronts merge (Fig. 1.6). This behavior corresponds to the shape of isotherms in the time *vs*. position in the magma chamber diagram (Fig. 1.4a).

Three kinds of a relationship between the settling and propagation velocity are possible: (*i*) the settling velocity is always lower that the propagation velocity (Fig. 1.6a). The upper solidification front forms and expands until it meets with the lower front near the center of the sill; (*ii*) the settling velocity is always greater than the propagation velocity (Fig. 1.6c) and the upper solidification front never forms as all newly formed crystals are removed by settling; (*iii*) transitional case, in which the propagation velocity is initially higher, thus the upper front starts growing, but the settling velocity overwhelms before the fronts merge and propagation of the upper front is thus terminated (Fig. 1.6b). The two end-members, (*i*) and (*ii*), correspond to the solidification regime dominated by solidification fronts (case (*i*)) and by crystal accumulation (case (*ii*)).

Importantly, the solidification regime depends on the magma viscosity and sill thickness (Figs. 1.6, 1.7). At any relevant magma viscosity, relatively thin sills develop the

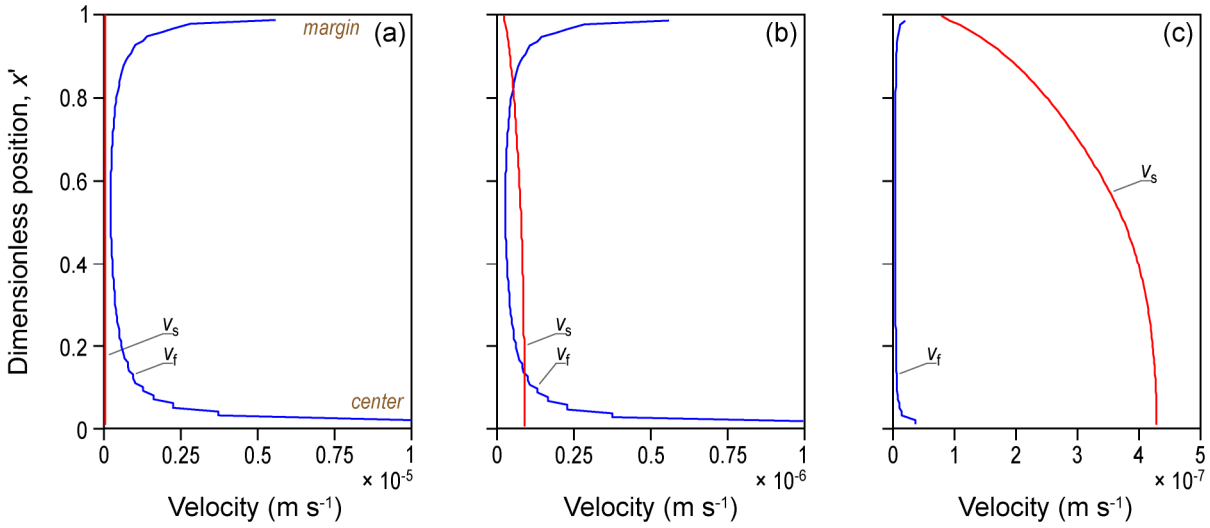

Fig. 1.6. *Crystal settling and solidification front propagation velocities, v_s and v_f, respectively. Calculated for magma viscosity, $\eta = 10^2$ Pa s (basaltic melt) and three magma chamber half-thicknesses:* **(a)** *D = 3 m;* **(b)** *D = 30 m;* **(c)** *D = 1000 m. Further computational details are given in Fig. 1.4.*

upper solidification front (model (*i*)), while solidification of thicker sills is dominated by accumulation (model (*ii*)). Surprisingly, the crystal accumulation is thus more effective in larger magma bodies. This is due to the fact that cooling time scales vary with square of magma chamber size but the dependence of a crystal settling time on the chamber size is only linear. The regime diagram (Fig. 1.7) shows the transition between the two modes of solidification as a function of the sill thickness and melt viscosity.

A number of simplifications were made in the above outlined approach. For example, the effect of convection on cooling and front propagation was neglected. Additionally, the kinetic relationships (Eqn. 1.3), originally calibrated for basaltic composition, were extrapolated over a wide range of viscosities. While almost surely oversimplified to be correct in detail, the qualitative inferences are generally valid and this simple model illustrates how the interplay of kinetic and mechanical effects can be used to decipher the solidification processes and internal evolution of magma chambers.

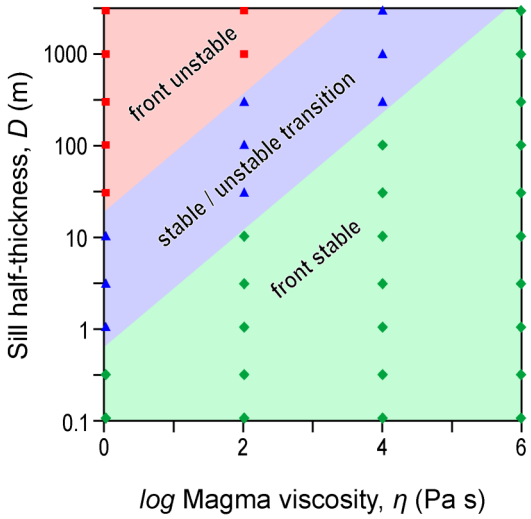

Fig. 1.7. *Regime-diagram of a magma chamber solidification style as a function of melt viscosity, η, and magma chamber half-thickness, D. In the "front stable" field, the upper solidification front progresses into the magma chamber center, where it meets the lower solidification front. In contrast, in the "front unstable" field, the upper solidification front never forms, since all crystals are gravitationally dragged to the chamber interior before they are incorporated into the rigid crystal framework. In the "stable/unstable transition" the upper front starts propagating but the crystal settling overwhelms before the upper front meets the lower front. The magma chamber behavior was determined at discrete set of points (indicated by point symbols). Further computational details are given in Fig. 1.4.*

1.4. Textures as a record of crystallization processes and their rates

1.4.1. Quantitative description of magmatic textures

Quantitative description of size, shape, spatial, and contact parameters of magmatic textures is essential for various comparative and interpretation purposes (*cf*., Higgins, 2006). The crystal size distribution, CSD, is a conventional measure of the grain size and its variability in rocks (e.g., Cashman & Marsh, 1988; Marsh, 1998; Higgins, 2000, 2002a). The CSD illustrates variations of crystal population density, that is, the relative number of crystals per unit volume, as a function of the crystal size. In magmatic rocks, the natural logarithm of population density show straight relationship with crystal size. As a consequence, possible deviations from linearity can provide information about the crystallization process, such as mixing of crystal populations, textural coarsening, or heterogeneous nucleation (e.g., Armienti et al., 1994; Marsh, 1998; Higgins, 2002, 2006; Špillar & Dolejš, 2015). While frequently used in textural quantification of volcanic and mafic plutonic rocks (Armienti et al., 1994; Higgins, 1996; 2002; Boorman et al., 2004; Higgins & Chandrasekharam, 2007), comparable CSD studies of felsic plutonic rocks and felsic rock in general are much more sparse (e.g., Mock et al., 2003; Yang, 2012).

Spatial distribution of crystals bears additional information on the kinetics and dynamics of the crystallization process. The simplest method of spatial distribution analysis is evaluation of the clustering index (e.g., Clark & Evans, 1954; Kretz, 1966, 1969; Jerram et al., 1996, 2003). Individual crystals of a texture of interest are substituted by points placed at the crystal centers and for each point the distance to the nearest neighbor is evaluated. The clustering index is then defined as a ratio of the average nearest neighbor distance to its expected value in a perfectly random assembly of points. The clustering index is thus smaller than unity when the crystal population is clustered and it is greater than unity when the assembly is ordered (anti-clustered). The method provides a simple tool to characterize the clustering, ordering or randomness of crystal suspensions and to identify effect of various

other mechanical or kinetic processes during the magma solidification (e.g., Mock et al., 2003).

The clustering index works with the nearest neighbors only and it ignores the pattern of spatial distribution of crystals on longer scales. More detailed characterization of the spatial distribution pattern is possible using the spatial distribution functions such as Ripley's K function or pair correlation function (e.g., Baddeley, 2008; Rudge et al., 2008). These statistical tools characterize the area density of crystals as a function of distance which can again be benchmarked against theoretical values for random, ordered or clustered distributions on various length scales.

1.4.2. Origin of magmatic textures and interpretation of textural measurements

Magmatic textures are a combined result of kinetically driven nucleation and growth of crystals, textural equilibration and mechanical processes such as crystal accumulation, flow sorting or mixing of magmas (e.g., Lasaga, 1998; Marsh, 1998; Higgins, 2006). Here I examine how these processes affect the resulting magmatic texture and its CSD in particular. Across various rock types, geotectonic settings of their origin and shape and cooling regime of their parental magma bodies, the CSDs of large fraction of magmatic rocks are characterized by a straight line in a crystal size *vs*. logarithm of the population density projection (Cashman & Marsh, 1988; Wilhelm & Wörner, 1996; Higgins, 2002; Zieg & Marsh, 2002; Boorman et al., 2004). It is generally accepted that straight CSDs result from kinetic crystallization by nucleation and growth (e.g., Lasaga, 1998; Marsh, 1998). During kinetic crystallization, both nucleation and the growth rate contribute to the characteristic grain size and CSD slope of the resulting texture. Both rates are non-monotonous functions of undercooling, but maximum of the nucleation rate is shifted towards higher undercooling (lower temperature) compared to the growth rate maximum (Fig. 1.3; e.g., Swanson, 1977). At low undercooling (T_1), the nucleation rate is low compared to the growth rate. Few nuclei control the growth of crystals to larger dimensions over longer timescales. The resulting

texture is thus coarse-grained with flat CSD slope. At moderate undercooling (T_2), both rates are high and leading to a fine-grained texture with a steep CSD slope. Finally, at extremely high undercooling (T_3) on the order of hundreds degrees, both nucleation and growth rates are close to zero, no crystals are formed and melt cools below glass transition without significant crystallization and vitrifies.

Two end-member models characterize the crystallization leading to the textures with straight CSDs: (*i*) open-system crystallization; (*ii*) closed-system crystallization (e.g., Lasaga, 1998; Marsh, 1998; Higgins, 2006). In the open-system model, the crystals migrate through the reference volume and are characterised by a mean residence time, τ. During which half of the crystals is removed from the system by outflow of magma or by crystal settling (Randolph & Larson, 1971). While in the system, the crystals grow by a constant growth rate, G_0. The largest crystals are those present in the system for the longest period of time, thus in the smallest quantities. The CSD slope is thus inversely proportional to the G_0 and τ (e.g., Wilhelm & Wörner, 1996).

In the closed-system crystallization, variations in the crystal number as a function of size are only due to the temporal variations of rates of nucleation and growth. A large number of combinations of the nucleation and the gorwth rate functions can produce a texture with straight CSD. One simple and particularly usefull combination consistent with straight CSDs is constant a growth rate coupled to the nucleation rate increasing exponentially in time (e.g., Marsh, 1998).

In detail, CSDs of many magmatic textures deviate from the straight course and various kinks and curvatures have been reported (Armienti et al., 1994; Waters & Boudreau, 1996; Higgins & Roberge, 2003; Higgins, 2006; Simakin & Bindeman, 2008; Yang, 2012). Kinked CSDs are composed of two or more straight segments, each of them characterized by a distinct slope. Conventionally, kinked CSDs are interpreted to be a result of multiple crystal populations mixing due to mixing of magmas with contrasting crystallization histories. Alternatively, the CSD trend may be modified in response to abrupt change of crystallization conditions. For example, eruption of magma to the surface or its transfer from deeper to shallower magma chamber increases the cooling rate and the two CSD segments then represent the groundmass and phenocryst populations of crystals (e.g., Marsh, 1998).

The CSDs with distinct kink can be regarded as a special case of concave-up curved distributions. The concave-up curvature has been interpreted as due to magma mixing, increased cooling rate, crystal aggregation or size-dependent growth (Burkhart et al. 1980; Eberl et al., 2002; Pupiere et al. 2008). On the other hand, the concave-down CSD curvature is typical for textures coarsened to some degree, where the population of small crystals was partially eliminated (e.g., Higgins, 2011).

Comparably less is known about the effect of various crystallization processes on other textural descriptors than the CSDs. Variations of the clustering index record variable degree of mechanical flow sorting of crystals during the emplacement of porphyritic rhyolite (Mock et al., 2003) or reflect the crystallization mechanism or porphyroblasts in metamorphic rocks (e.g., Hirsch et al., 2000).

1.4.3. Experimental studies and numerical simulations of textural evolution

Crystallization of magma is essentially inaccessible to direct observation and the exceptional observations are limited to shallow-level systems such as in Hawaiian lava lakes (e.g., Cashman & Marsh, 1988; Cashman, 1993). Laboratory experiments on natural and synthetic samples as well as numerical modeling provide an alternative opportunity to study the crystallization process and the formation of igneous textures. The crystallization mechanism dictates three-dimensional structure of the crystal framework and its rheological properties or permeability for interstitial liquid and thus has direct consequence for magma transport, emplacement, differentiation and eruption (e.g., Hoover et al., 2001; Hersum et al., 2005; Annen, 2009; Verhoeven & Schmalzl, 2009; Bea, 2010).

Majority of experimental studies of magmatic crystallization focused on extracting the rates of nucleation and growth as a function of undercooling (e.g., Kirkpatrick, 1975, 1976, 1977, 1979; Fenn, 1977; Swanson, 1977; Lofgren, 1983; Swanson & Fenn, 1986; Muncill & Lasaga, 1987, 1988). These studies inherently use rapid quenching of experimental charges which allows only the final state of the sample to be observed. Rare attempts were made to

characterize the textural evolution using a set of samples and multiple quenches at various stages of crystallization (e.g., Zieg & Lofgren, 2006; Pupier et al., 2008) or by direct *in-situ* observation in a moissanite cell (Schiavi et al., 2009). The in-situ crystallization observations demonstrate the size-independent growth and important role of coalescence of crystals. On the other hand, experiments on analogue materials suggest that size-dependent growth, growth rate dispersion or textural coarsening might be more important than previously assumed (e.g., Means & Park, 1994; Eberl et al., 2002; Mills et al., 2011).

Various crystallization processes can be described by phenomenological or physical laws and numerical modeling can be used to study the formation and evolution of the geometry of crystal framework as well as the resulting texture. Simulated textures can be compared to the rock textures in order to decipher the crystallization processes active in natural magmas. Existing three-dimensional numerical models of crystallization (e.g., Hersum & Marsh, 2006; Amenta et al., 2007) provide rough approximation to continuous crystallization by nucleation and growth. The computational requirements, however, increase with increasing resolution of the simulated domain and become large or prohibitive for spatial resolution necessary to provide statistically representative sample of the texture.

1.5. Structure of the thesis

This thesis develops forward and inverse models of textural analysis that are used to illustrate and interpret physicochemical and mechanical processes and internal evolution of magma chambers. The thesis consists of the introductory chapter (Chpt. 1), five manuscripts (Chpts. 2–6), and a summary (Chpt. 7).

In the introduction (Chpt. 1), I provide elementary theoretical foundations of the crystallization process and its implications for the origin of magmatic textures. To illustrate the interaction of kinetic and mechanical processes during magma crystallization I further formulate a simple model of sill solidification.

In Chpt. 2, a method of the CSD inversion is developed to extract the rates of nucleation and growth from textural data. The effect of the crystallization process on other textural parameters than the CSD is explored in Chpt. 3 *via* forward modeling. A high-resolution three-dimensional numerical model of texture evolution under arbitrary rates of nucleation and growth is developed. Simulated textures allowed us to derive quantitative properties of kinetic textures which are useful indicators of activity of other crystallization processes than homogenous nucleation and growth of crystals is.

In the subsequent chapters, I expand the forward crystallization model to simulate the textural effect of heterogeneous nucleation and crystal accumulation. In Chpt. 4, the effect of heterogeneous nucleation on textural parameters is explored and quantitative relationships are calibrated to extract the ratio of heterogeneous *vs*. homogeneous nuclei number based on the measurements of several independent textural parameters. A widespread occurrence of heterogeneous nucleation is shown to provide consistent explanation of observed textural features, such as concave-up curved CSDs, in a variety of rock types. The effect of mechanical crystal accumulation or melt extraction on textural parameters is studied in Chpt. 5. It is shown that the spatial distribution pattern of crystal centers becomes progressively ordered (i.e., anti-clustered) as accumulation of crystals or extraction of interstitial melt progresses.

Finally, the Chpt. 6 is a quantitative study of phenocryst distribution patterns in the porphyritic Jizera granite, northern Bohemian Massif. Continuous textural variations across more than 550 m of vertical section suggest that the granitic melt was emplaced as a single batch that subsequently underwent mechanical *in-situ* differentiation. The new melt extraction model is applied to estimate the amount of melt extracted from the system and it provides inferences about connection to shallower magma chambers or to surface volcanic activity.

1.6. References

AMENTA R., EWING A., JENSEN A., ROBERTS S., STEVENS K., SUMMA M., WEAVER S. & WERTZ P. (2007): A modeling approach to understanding the role of microstructure development on crystal-size distributions and on recovering crystal-size distributions from thin slices. – *American Mineralogist* 92, 1936–1945.

ANNEN C. (2009): From plutons to magma chambers: Thermal constraints on the accumulation of eruptible silicic magma in the upper crust. – *Earth and Planetary Science Letters* 284, 409–416.

ARMIENTI P., PARESCHI M. T., INNOCENTI F. & POMPILIO M. (1994): Effect of magma storage and ascent on the kinetics of crystal growth. – *Contributions to Mineralogy and Petrology* 115, 402–414.

BADDELEY A. (2008): *Analyzing spatial point patterns in R. Workshop notes*. – CSIRO online technical publication, http://www.csiro.au/resources/pf16h.html.

BARNEA E. & MIZRAHI J. (1973): A generalized approach to the fluid dynamics of particulate systems. Part I. General correlation for fluidization and sedimentation in solid multiparticulate systems. – *Chemical Engineering Journal* 5, 171–189.

BEA F. (2010): Crystallization dynamics of granite magma chambers in the absence of regional stress: Multiphysics modeling with natural examples. – *Journal of Petrology* 51, 1541–1569.

BECKER R. & DORING W. (1935): Kinetische Behandlung der Keim bildung in übersättingten Dämpfen. – *Annalen der Physik* 5, 719–752.

BOORMAN S., BOUDREAU A. & KRUGER F. J. (2004): The Lower Zone-Critical Zone transition of the Bushveld Complex: A quantitative textural study. – *Journal of Petrology* 45, 1209–1235.

BURKHART L. E., HOYT R. C. & OOLMAN T. (1980): Control of particle size distribution and agglomeration in continuous precipitations. *In*: KUCZYNSKI G. C. (ed.) *Sintering Processes*. – Plenum, New York, pp 23–38.

CASHMAN K. V. (1993): Relationship between plagioclase crystallization and cooling rate in basaltic melts. – *Contributions to Mineralogy and Petrology* 113, 126–142.

CASHMAN K. V. & MARSH B. D. (1988): Crystal size distribution (CSD) in rocks and the kinetics and dynamics of crystallization II: Makaopuhi lava lake. – *Contributions to Mineralogy and Petrology* 99, 292–305.

CLARK P. J. & EVANS F. C. (1954): Distance to nearest neighbour as a measure of spatial relationships in populations. – *Ecology* 35, 445–453.

DAVIDSON J. P., MORGAN D. J., CHARLIER B. L. A., HARLOU R., & HORA J. M. (2007): Microsampling and isotopic analysis of igneous rocks: Implications for the study of magmatic systems. – *Annual Review of Earth and Planetary Sciences* 35, 273–311.

EBERL D. D., KILE D. E. & DRITS V. A. (2002): On geological interpretation of crystal size distributions: Constant *vs*. proportionate growth. – *American Mineralogist* 87, 1235–1241.

HAMMER J. E. (2004): Crystal nucleation in hydrous rhyolite: Experimental data applied to classical theory. – *American Mineralogist* 89, 1673–1679.

HAMMER J. E. (2008): Experimental studies of the kinetics and energetics of magma crystallization. – *Reviews in Mineralogy and Geochemistry* 69, 9–59.

HAMMER J. E., SHARP T. G. & WESSEL P. (2010): Heterogeneous nucleation and epitaxial crystal growth of magmatic minerals. – *Geology* 38, 367–370.

HERSUM T., HILPERT M. & MARSH B. (2005): Permeability and melt flow in simulated and natural partially molten basaltic magmas. – *Earth and Planetary Science Letters* 237, 798–814.

HERSUM T. G. & MARSH B. D. (2006): Igneous microstructures from kinetic models of crystallization. – *Journal of Volcanology and Geothermal Research* 154, 34–47.

HIGGINS M. D. (1996): Magma dynamics beneath Kameni volcano, Thera, Greece, as revealed by crystal size and shape measurements. – *Journal of Volcanology and Geothermal Research* 70, 37–48.

HIGGINS M. D. (2000): Measurement of crystal size distributions. – *American Mineralogis* 85, 1105–1116.

HIGGINS M. D. (2002): A crystal size-distribution study of the Kiglapait layered mafic intrusion, Labrador, Canada: Evidence for textural coarsening. – *Contributions to Mineralogy and Petrology* 144, 314–330.

HIGGINS M. D. (2006): *Quantitative textural measurements in igneous and metamorphic petrology*. – Cambridge University Press, Cambridge, 265 pp.

HIGGINS M. D. (2011): Textural coarsening in igneous rocks. – *International Geology Review* 53, 354–376.

HIGGINS M. D. & ROBERGE J. (2003): Crystal size distribution of plagioclase and amphibole from Soufrière Hills Volcano, Montserrat: Evidence for dynamic crystallization-textural coarsening cycles. – *Journal of Petrology* 44, 1401–1411.

HIGGINS M. D. & CHANDRASEKHARAM D. (2007): Nature of sub-volcanic magma chambers, Deccan Province, India: Evidence from quantitative textural analysis of plagioclase megacrysts in the giant plagioclase basalts. – *Journal of Petrology* 48, 885–900.

HIRSCH D. M., KETCHAM R. A. & CARLSON W. D. (2000): An evaluation of spatial correlation functions in textural analysis of metamorphic rocks. – *Geological Materials Research* 2, 21 pp.

HOOVER S. R., CASHMAN K. V. & MANGA M. (2001): The yield strength of subliquidus basalt – experimental results. – *Journal of Volcanology and Geothermal Research* 107, 1–18.

HUBER C., BACHMANN O. & DUFEK J. (2012): Crystal-poor versus crystal-rich ignimbrites: A competition between stirring and reactivation. – *Geology* 40, 115–118.

JERRAM D. A., CHEADLE M. J., HUNTER R. H. & ELLIOTT M.T. (1996): The spatial distribution of grains and crystals in rocks. – *Contributions to Mineralogy and Petrology* 125, 60–74.

JERRAM D. A., CHEADLE M. J. & PHILPOTTS A. R. (2003): Quantifying the building blocks of igneous rocks: Are clustered crystal frameworks the foundation? – *Journal of Petrology* 44, 2033–2051.

KIRKPATRICK R. J. (1975): Crystal growth from the melt: A review. – *American Mineralogist* 60, 798–814.

KIRKPATRICK R. J., ROBINSON G. R. & HAYS J. F. (1976): Kinetics of crystal growth from silicate melts: Anorthite and diopside. – *Journal of Geophysical Research* 81, 5715–5720.

KIRKPATRICK J. R. (1977): Measurement and calculation of crystal growth rates in silicate systems. – *Canadian Mineralogist* 14, 195–195.

KIRKPATRICK R. J., KLEIN L., UHLMANN D. R. & HAYS J. F. (1979): Rates and processes of crystal growth in the system anorthite-albite. – *Journal of Geophysical Research* 84, 3671–3676.

KRETZ R. (1966): Grain-size distribution for certain metamorphic minerals in relation to nucleation and growth. – *Journal of Geology* 74, 147–173.

KRETZ R. (1969): On the spatial distribution of crystals in rocks. – *Lithos* 2, 39–66.

LASAGA A. C. (1998): *Kinetic theory in the Earth sciences*. – Princeton University Press, Princeton, 811 pp.

LOFGREN G. E. (1983): Effect of heterogeneous nucleation on basaltic textures: A dynamic crystallization study. – *Journal of Petrology* 24, 229–255.

MARSH B. D. (1981): On the crystallinity, probability of occurrence, and rheology of lava and magma. – *Contributions to Mineralogy and Petrology* 78, 85–98.

MARSH B. D. (1989): Magma chambers. – *Annual Review of Earth and Planetary Sciences* 17, 439–474.

MARSH B. D. (1995): Solidification fronts and magmatic evolution. – *Mineralogical Magazine* 60, 5–40.

MARSH B. D. (1998): On the interpretation of crystal size distributions in magmatic systems. – *Journal of Petrology* 39, 553–599.

MARSH B. D. (2002): On bimodal differentiation by solidification front instability in basaltic magmas. Part 1: Basic mechanics. – *Geochimica et Cosmochimica Acta* 66, 2211–2229.

MEANS W. D. & PARK Y. (1994): New experimental approach to understanding igneous texture. – *Geology* 22, 323–326.

MILLS R. D., RATNER J. J. & GLAZNER A. F. (2011): Experimental evidence for crystal coarsening and fabric development during temperature cycling. – *Geology* 39, 1139–1142.

MOCK A., JERRAM D. A. & BREITKREUZ C. (2003): Using quantitative textural analysis to understand the emplacement of a shallow-level rhyolitic laccoliths – a case study from the Halle volcanic complex, Germany. – *Journal of Petrology* 44, 833–849.

MORGAN D. J., BLAKE S., ROGERS N. W., DEVIVO B., ROLANDI G., MACDONALD R. & HAWKESWORTH C. J. (2004): Time scales of crystal residence and magma chamber volume from modelling of diffusion profiles in phenocrysts: Vesuvius 1944. – *Earth and Planetary Letters* 222, 933–946.

MUNCILL G. E. & LASAGA A. C. (1987): Crystal-growth kinetics of plagioclase in igneous systems: One-atmosphere experiments and applications of a simplified growth model. – *American Mineralogist* 72, 299–311.

MUNCILL G. E. & LASAGA A. C. (1988): Crystal-growth kinetics of plagioclase in igneous system: Isothermal H_2O-saturated experiments and extension of a growth model to complex silicate melts. *American Mineralogist* 73, 982–992.

PETFORD N. (2003): Rheology of granitic magmas during ascent and emplacement. – *Annual Review of Earth and Planetary Sciences* 31, 399–427.

PETFORD N. (2009): Which effective viscosity? – *Mineralogical Magazine* 73, 167-191.

PICARD D., ARBARET L., PICHAVANT M., CHAMPALLIER R. & LAUEAU P. (2013): The rheological transition in plagioclase-bearing magmas. – *Journal of Geophysical Research* 118, 1363–1377.

PUPIER E., DUCHENE S. & TOPLIS M. J. (2008): Experimental quantification of plagioclase crystal size distribution during cooling of a basaltic liquid. – *Contributions to Mineralogy and Petrology* 155, 555–570.

RANDOLPH A. D. & LARSON M. A. (1971): *Theory of particulate processes*. – Academic Press, New York, 251 pp.

RUDGE J. F., HOLNESS M. B. & SMITH G. C. (2008): Quantitative textural analysis of packing of elongate crystals. – *Contributions to Mineralogy and Petrology* 156, 413–429.

SAAR M. O., MANGA M., CASHMAN K. V. & FREMOUW S. (2001): Numerical models of the onset of yield strength in crystal-melt suspensions. – *Earth and Planetary Letters* 187, 367–379.

SCHIAVI F., WALTE N. & KEPPLER H. (2009): First in situ observation of crystallization processes in a basaltic-andesitic melt with the moissanite cell. – *Geology* 37, 963–966.

SCHWINDINGER K. (1999): Particle dynamics and aggregation of crystals in a magma chamber with application to Kilauea Iki olivines. – *Journal of Volcanology and Geothermal Research* 88, 209–238.

SIMAKIN A. G. & BINDEMAN I. N. (2008): Evolution of crystal sizes in the series of dissolution and precipitation events in open magma systems. – *Journal of Volcanology and Geothermal Research* 17, 997–1010.

SŁABY E. & GÖTZE J. (2004): Feldspar crystallization under magma-mixing conditions shown by cathodoluminescence and geochemical modelling – a case study from the Karkonosze pluton (SW Poland). – *Mineralogical Magazine* 68, 561–577.

ŠPILLAR V. & DOLEJŠ D. (2015): Heterogeneous nucleation as the predominant mode of crystallization in natural magmas: Numerical model and implication for crystal-melt interaction. – *Contributions to Mineralogy and Petrology* 169, 1–16.

SWANSON S. E. (1977): Relation of nucleation and crystal-growth rate to the development of granitic textures. – *American Mineralogist* 62, 966–978.

SWANSON S. E. & FENN P. M. (1986): Quartz crystallization in igneous rocks. – *American Mineralogist* 71, 331–342.

VERHOEVEN J. & SCHMALZL J. (2009): A numerical method for investigating crystal settling in convecting magma chambers. – *Geochemistry, Geophysics, Geosystems* 10, 1–21.

VERNON R. H. (1986): K-feldspar megacrysts in granites: Phenocrysts, not porphyroblasts. – *Earth-Science Reviews* 23, 1–63.

VERNON R. H. & COLLINS W. J. (2011): Structural criteria for identifying granitic cumulates. – *Journal of Geology* 119, 127–142.

VIGNERESSE J. L., BARBEY P. & CUNEY M. (1996): Rheological transitions during partial melting and crystallization with application to felsic magma segregation and transfer. – *Journal of Petrology* 37, 1579–1600.

VIGNERESSE J. L. & TIKOFF B. (1999): Strain partitioning during partial melting and crystallizing felsic magmas. – *Tectonophysics* 312, 117–132.

WATERS C. & BOUDREAU A. E. (1996): A reevaluation of crystal size distribution in chromite cumulates. – *American Mineralogist* 81, 1452–1459.

WILHELM S. & WÖRNER G. (1996): Crystal size distribution in Jurassic Ferrar flows and sills (Victoria Land, Antarctica): Evidence for processes of cooling, nucleation, and crystallisation. – *Contributions to Mineralogy and Petrology* 125, 1–15.

YANG Z.-F. (2012): Combining quantitative textural and geochemical studies to understand the solidification process of a granite porphyry: Shanggusi, East Qinling, China. – *Journal of Petrology* 53, 1807–1835.

ZIEG M. J. & LOFGREN G. E. (2006): An experimental investigation of texture evolution during continuous cooling. – *Journal of Volcanology and Geothermal Research* 154, 74–88.

ZIEG M. J. & MARSH B. D. (2002): Crystal size distributions and scaling laws in the quantification of igneous textures. – *Journal of Petrology* 43, 85–101.

Preface to Chapter 2

Rates of nucleation and growth of crystals in undercooled magmas are principal factors which determine the evolution and final appearance of igneous textures. Mechanical behavior of a crystal framework/suspension and its potential for crystal-liquid separation thus for the magma differentiation is driven by crystal size and interconnectivity and is therefore directly related to the rates of nucleation and growth. With a few exceptions, the crystallizing magmas are inaccessible to direct observations thus the rates of crystal nucleation and growth in natural systems remain poorly constrained. In this chapter, we formulate a new inverse numerical model to extract the nucleation and the growth rate from measurable textural data. We employ the crystal size distribution as principal textural information and use temporal evolution of crystallinity as another input parameter in order to constrain a unique solution.

This chapter was published as **ŠPILLAR, V**. & DOLEJŠ, D. (2013): *Calculation of time-dependent nucleation and growth rates from quantitative textural data: Inversion of crystal size distribution*. – ***Journal of Petrology*** *54, 913–931*. The manuscript was formatted to conform to general layout of this thesis.

Chapter 2.

Calculation of Time-dependent Nucleation and Growth Rates from Quantitative Textural Data: Inversion of Crystal Size Distribution

2.0. Abstract

Magmatic textures provide an insufficiently explored tool to interpret physical processes and environmental variables that drive differentiation and crystallization in magma chambers. We derive a new method, which utilizes the crystal size distribution (CSD), to retrieve the rates of nucleation and growth from natural igneous rocks. However, a single CSD results from arbitrary number of combinations of nucleation and growth rates, if additional parameters such as crystallinity evolution are employed, the solution for rates becomes unique. Interpretation of representative log-linear CSD trends shows that the nucleation rates are sensitive to even minor features of the CSD, whereas the growth rate functions are mainly related to the crystallinity evolution. The reconstructed growth rates become minimal at intermediate crystallinities but diverge to very high values at the beginning and the end of crystallization. This general result is related to the small effective area of the solid-liquid interface close to liquidus (few small grains) and near solidus (largely solidified with diminishing melt pools). Assuming that growth rate is related to environmental variables such as magma undercooling, these results suggest that solid fraction in many magmas increased in a sigmoidal manner over their crystallization time and indicate the system's tendency for largest undercooling at the beginning and at the end of crystallization. For crystallization times constrained by conductive cooling models, the growth rates

calculated for representative CSDs are on the order of 10^{-11} cm s^{-1}, which is in a good agreement with *in situ* observations of Hawaiian lava lakes. Calculated growth rates are inversely proportional to the magma body size and increase from the chamber interior to the margins.

Key words:

Crystal size distribution; crystallinity; nucleation rate; growth rate; magmatic texture.

2.1. Introduction

Mechanisms of igneous crystallization exert major control on chemical differentiation in magma chambers, approach to solid-melt (-fluid) equilibrium, efficiency of melt extraction from crystal phases and time scales of these processes (Boudreau & Philpotts, 2002; Hersum et al., 2005; Aarnes et al., 2008). Since magmatic processes are commonly inaccessible to direct observation, various indirect approaches, in particular the determination of crystal size distributions, were devised to unravel the magma crystallization history (Marsh, 1988; Cashman & Marsh, 1988; Cashman, 1993; Wilhelm & Wörner, 1996; Marsh, 1998; Higgins, 2002a; Mock et al., 2003; Bindeman, 2003; Simakin & Bindeman, 2008). The theory of crystal size distribution (CSD), originally developed for industrial systems (Randolph & Larson, 1971), uses the nucleation and growth rates to predict observable number densities of crystals of different sizes. Rates of nucleation and growth thus determine final rock texture and its temporal evolution. Furthermore, knowledge of development of solid phase framework is crucial for determining dependant rheological and transport properties of the magma (Petford, 2003; Hersum et al., 2005; Hersum & Marsh, 2006; Champallier et al., 2008), thus for testing the physical models of magma chambers (e.g., Tait & Jaupart, 1992; Jaupart & Tait, 1995; Marsh, 2002).

The CSDs in many natural magmatic systems approach linear relationship between crystal size and logarithm of population density (e.g., Higgins, 2002a; Zieg & Marsh, 2002;

Boorman et al., 2004; Mock & Jerram, 2005). The rates of nucleation and growth and their variations can only exceptionally be determined from natural samples and their CSDs when constraining parameters on magma solidification are known, as in the case of solidification of Hawaiian lava lakes (Cashman & Marsh, 1988; Cashman, 1993). For fossil magmatic systems, theories were proposed that place constraints on nucleation and growth rates in order to reproduce observed log-linear CSDs (e.g., Marsh, 1998). If crystallization is assumed to occur in a simple open system a product of characteristic growth rate and growth time can be determined from a slope of the CSD (e.g., Cashman & Marsh, 1988; Mangan, 1990; Wilhelm & Wörner, 1996). On the other hand, batch crystallization in a closed system is usually supposed to occur under exponentially increasing rate of nucleation while the growth rate remains roughly constant (e.g., Marsh, 1998).

Both rates are functions of intensive parameters such as Gibbs energy of crystallization or undercooling that are expected to vary as crystallization proceeds (Kirkpatrick et al., 1976, 1979; Swanson, 1977; Muncill & Lasaga, 1987, 1988; Couch, 2003; see Hammer, 2008 for review). In general, log-linear CSDs can result from an arbitrary number of combinations of crystal growth and nucleation rates, therefore interpretation of these time-dependent kinetic parameters is an ambiguous problem. Determination of complex variability of both rates, required for conceptual understanding of magma chamber dynamics, thus remains elusive.

In this study, we formulate a new method of inversion of the crystal size distribution curve, which allows retrieval of time-dependent growth and nucleation rates. The solution becomes unique, when we use temporal variation of crystal volume fraction as additional parameter. We first formulate our model for a single-phase system but its extension to multiple crystallizing phases is straightforward. Our model solutions are directly applicable to magmas where one solid phase dominates or to multicomponent systems where crystallization kinetics of all solids is approximately similar. We emphasize that this approach only applies to igneous textures directly resulting from crystal nucleation and growth but were not affected by subsequent annealing or coarsening processes (*cf*. Higgins, 2011).

2.2. Kinetics of crystal nucleation and growth

Crystal size distribution at time t, $n(L, t)$, provides a quantitative measure of the number of crystals of size L in a unit magma volume. It is a population density function, hence the number of crystals of size between L and $L + \mathrm{d}L$ in a unit sample volume is $n(L, t)\mathrm{d}L$ (e.g., Marsh 1998, 2007). During crystallization, the crystal size distribution reflects temporal variations of the nucleation rate, i.e., number of nuclei formed in a unit melt volume per unit time, $I(t)$, and of the growth rate, i.e., advance of crystal-melt interface per unit time, $G(t)$. In an inversion problem, we look for time-dependent rates, $I(t)$ and $G(t)$, that satisfy the observed crystal size distribution, $n(L, T)$, at time T.

2.2.1. Evolution of crystallinity

During progressive crystallization, the total volume of solid phases increases at the expense of melt. To quantify fraction of solid and liquid phases, respectively, as a function of time, we sum up the contributions of all crystals in a control volume while assuming their spherical shape. For volume $V(t)$ of the crystal nucleating at time τ we obtain at any later time t

$$V(t) = \frac{4}{3}\pi \left[\int_{\tau}^{t} G(\tau')\,\mathrm{d}\tau' \right]^3, \tag{2.1}$$

where G is the growth rate and τ' is the integration variable. Since crystals nucleate with the rate that may vary with time, it must be accounted for by second integration over the time interval of crystallization. Crystallinity $\Phi(t)$, i.e., volumetric fraction of crystals in the system, at any time $t > 0$ is then given by:

$$\Phi(t) = \frac{4}{3}\pi \int_0^t I(\tau) \left[\int_\tau^t G(\tau') \mathrm{d}\tau' \right]^3 \mathrm{d}\tau, \tag{2.2}$$

where $I(t)$ is the nucleation rate, i.e., the number of nuclei formed per unit melt volume per unit time.

Eqn. (2.2) is valid at low crystallinities only; at moderate to high crystallinities, it does not account for shrinkage of volume available for crystal nucleation and for variations in growth due to crystal impingement (e.g., Lasaga, 1998). These drawbacks are solved by mean field approach *via* the Avrami theory (Avrami 1939, 1940; see Lasaga, 1998 and Marsh, 1998). The Avrami relationship provides quantitative link between the rates of crystal growth and nucleation, $G(t)$ and $I(t)$, respectively, and the volume fraction of the solid phase as a function of time. As follows from Avrami's mean field approximation, the correct expression for the volume fraction of crystals as a function of time resembles the exponential of our Eqn. (2.2). In the environment where crystals nucleate at random positions this expression reads (see Lasaga (1998) for derivation):

$$\Phi(t) = 1 - \exp\left\{ -\sigma_A \int_0^t I(\tau) \cdot \left[\int_\tau^t G(\tau') \mathrm{d}\tau' \right]^3 \mathrm{d}\tau \right\}, \tag{2.3}$$

where factor σ_A accounts for various crystal shapes. It relates the crystal volume V to the half of its linear dimension R as $V = \sigma_A R^3$. For spheres, the shape factor thus becomes $\sigma_A = 4\pi/3$ as it has already appeared in Eqn. (2.2).

2.2.2. Crystal population balance

Development of CSD, described by population density, $n(L, t)$, as a function of time t and grain size L has been conventionally evaluated from crystal population balance (Randolph & Larson, 1971; Lasaga, 1998; Marsh, 1998; Resmini, 2007):

$$\frac{\partial n}{\partial t} + \frac{\partial G^{\text{eff}} n}{\partial L} = R \tag{2.4}$$

where G^{eff} is an effective growth rate, and R is a source term describing changes in a population balance due to effects other than crystal nucleation and growth, thus incorporating processes such as crystal settling, grain coarsening, etc. Eqn. (2.4) represents an analogue of the advection equation describing the transfer of crystals from one size class to another by process of crystal growth (Lasaga, 1998). For a closed system with $R = 0$ and growth rate independent of grain size, the population balance equation becomes

$$\frac{\partial n}{\partial t} + G^{\text{eff}} \frac{\partial n}{\partial L} = 0 \,. \tag{2.5}$$

The assumption of independency of growth rate and crystal size (McCabe 1929, *cf.* Kile & Eberl 2003) was repeatedly confirmed by experimental studies (e.g., Kirkpatrick et al., 1979; Muncill & Lasaga, 1987; Schiavi et al., 2009) and applied in many CSD studies (e.g., Marsh, 2007). Size-dependent growth, however, was also observed (e.g., Eberl et al., 2002) and attributed to various physical processes like depletion of a boundary layer (Muncill & Lasaga, 1987) or grain coalescence (Schiavi et al., 2009). For simplicity, we use size-independent growth as a first-order approximation. Size-dependent rates can easily be incorporated into our method, if desired.

With increasing crystallinity, probability of crystal impingement increases and the total area of solid-melt interface decreases, thus leading to a decrease in effective growth rate, G^{eff}. The G^{eff} becomes progressively smaller when compared to an ideal, or nominal, growth rate, G, describing the rate by which any surface element of crystal-melt interface advances in its normal direction. Note that the ideal growth rate, G, is the rate determined purely by the crystallization kinetics. Differences between the ideal and effective growth rates stem from geometrical causes only.

In order to use the population balance equation with ideal rates, functional dependence between G and G^{eff} must be defined. At very low crystallinities, when crystals do not touch

each other, G and G^{eff} are equal. At very high crystallinities, G^{eff} approaches zero as surface area of crystals available for growth diminishes. These two conditions may be stated as

$$\begin{aligned} G^{\text{eff}}(t) &= G(t), \quad \text{for} \quad \Phi(t) \to 0, \\ G^{\text{eff}}(t) &= 0, \quad \text{for} \quad \Phi(t) \to 1, \end{aligned} \tag{2.6}$$

where $\Phi(t)$ stands for crystallinity (solid fraction) at time t. Lasaga (1998) proposed a simple scaling, which conforms with Eqns. (2.6)

$$G^{\text{eff}}(t) = G(t)\left[1-\Phi(t)\right]^{1/3}, \tag{2.7}$$

where the exponent of 1/3 results from cubic relationship between linear growth rate and volume fraction. In our approach, we note that the effective growth rate is a time derivative of the (observable) grain size as follows:

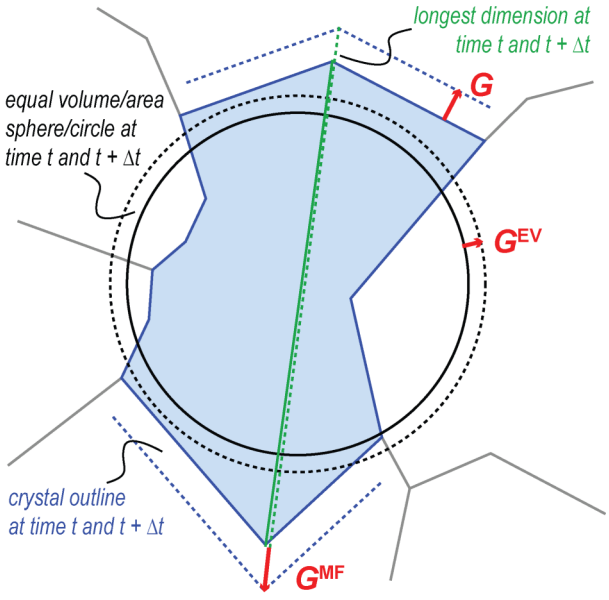

Fig. 2.1. *Two-dimensional illustration of various definitions of the grain size and of the effective growth rate. The time derivative of length of the longest line connecting two points on a grain boundary defines the growth rate, G^{MF}. Growth rate G^{EV} is based on a diameter of the circle which has an equal area as the crystal outline. The G^{MF} and G^{EV} are related to measurable size of crystal and hence provide alternative definitions of effective growth rate. The same approach can be extended to three-dimensions.*

$$G^{\text{eff}} = \frac{1}{2}\frac{\mathrm{d}L}{\mathrm{d}t}, \tag{2.8}$$

where one half accounts for growth in two opposite directions away from the crystal center. That is, an effective growth rate is directly related to the definition of the grain size (see Higgins, 2000, 2006 for various definitions of the grain size) and the $G - G^{\text{eff}}$ relationship must be consistent with the adopted definition. Fig. 2.1 illustrates how the change in the grain topology over some finite time span can be described by different effective growth rates while using different definitions of the grain size. Throughout this paper, we use rate G^{EV} as an effective growth rate, G^{eff}, whereas G is an ideal growth rate directly related to the thermodynamic driving force for crystallization.

In order to derive a more rigorous expression for the effective growth rate than the approximation afforded by Eqn. (2.7), we have employed an approach based on a CSD second moment (Marsh, 1988; Resmini, 2007). Consider relationship between a grain volume V and its size L,

$$V = \sigma_{\text{CSD}} L^3, \tag{2.9}$$

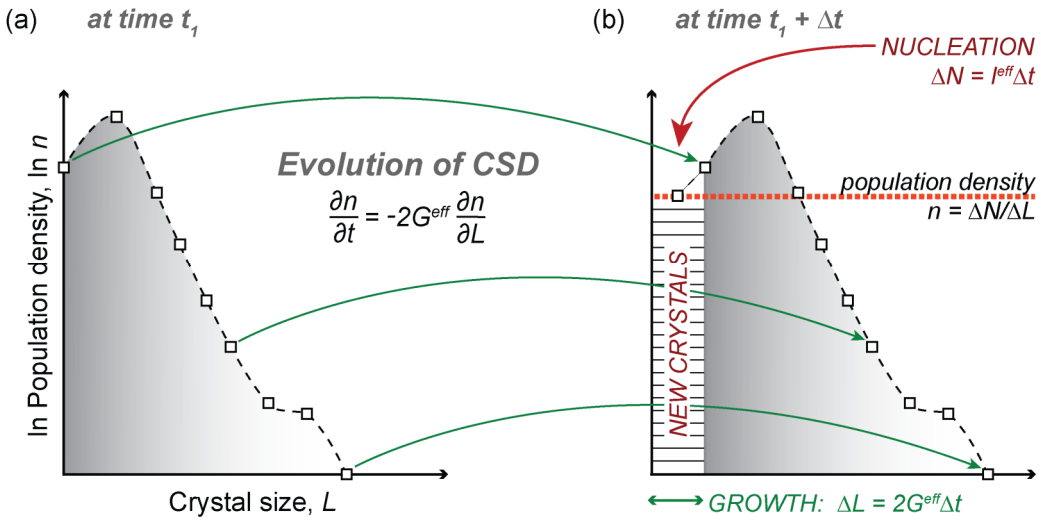

Fig. 2.2. *The CSD at time t_1 and $t_1 + \Delta t$. During the time instant Δt, all grains grow by the size increment $\Delta L = 2G^{eff}\Delta t$ and move to higher size classes, as given by the crystal population balance Eqn. (2.5).*

where σ_{CSD} is a shape factor relating volume to linear dimension of a model geometrical object (for instance, $\sigma_{CSD} = \pi/6$ for a sphere when the sphere diameter is used as a linear size). Shape factor σ_{CSD} differs from the σ_A used previously in the Avrami equation (Eqn. (2.3)) in two respects: (*i*) σ_{CSD} is related to the shape of a geometrical object from whose size CSD is calculated, rather than to the real growth shape of a crystal as σ_A is; (*ii*) σ_{CSD} is related to a full linear dimension, whereas σ_A works with a "radius", defined as a distance to which crystal faces moved from the nucleation center during the growth. Eqn. (2.9) provides a definition of the crystal size based on its volume. With this grain size definition, equation for G^{eff} will have the following form (see Appendix 1 for derivation):

$$G^{\text{eff}}(t) = \left[6\sigma_{\text{CSD}} \cdot \int_0^{\infty} n(L,t) L^2 \mathrm{d}L \right]^{-1} \cdot \frac{\mathrm{d}\Phi}{\mathrm{d}t}(t). \tag{2.10}$$

While based on different physical assumptions, Eqns. (2.7) and (2.10) provide two alternative conversion methods between ideal (kinetic) and effective growth rate as a function of time and previous crystallization history. Note that ideal rates are contained in a crystallinity function, $\Phi(t)$ (see Eqn. (2.3)) that enters both equations. We have tested both methods (see Section 2.3) and used the later one as superior through our calculation.

2.2.3. Relationship between growth and nucleation rates

Consider crystal size distribution $n(L, t)$ at some time t as shown in Fig. 2.2a. After time step Δt, the entire grain population moves by increment ΔL toward greater size (Fig. 2.2b), in agreement with the population balance, Eqn. (2.5). The size increment ΔL is related to the growth rate as follows:

$$\Delta L = 2 \cdot \int_t^{t+\Delta t} G^{\text{eff}}(\tau)\,\mathrm{d}\tau, \tag{2.11}$$

where the factor of two ensures consistency with convention in Eqn. (2.8) due to crystal growth on opposite crystal faces. In addition, ΔN new crystals nucleate during the time interval Δt, as follows:

$$\Delta N = \int_{t}^{t+\Delta t} I^{\text{eff}}(\tau)\,\mathrm{d}\tau\,, \tag{2.12}$$

where $I^{\text{eff}}(t)$ is the effective nucleation rate. As with the effective growth rate, the effective rate of nucleation is lower than ideal nucleation rate owing to decreasing melt volume available for nucleation as crystallization proceeds. The ideal and effective nucleation rates are related by volume fraction of melt as follows (Lasaga, 1998; Marsh, 1998):

$$I^{\text{eff}}(t) = I(t)\left[1-\Phi(t)\right]. \tag{2.13}$$

Conventional definition of the population density (e.g., Lasaga, 1998; Marsh, 1998) relates increments of the crystal number and size to the observable crystal size distribution at any time t:

$$n\left(L=0, t+\Delta t\right) = \frac{\Delta N}{\Delta L}. \tag{2.14}$$

Substituting from Eqns. (2.11) and (2.12) for ΔN and ΔL, respectively, into Eqn. (2.14) we obtain at the limit of $\Delta t \rightarrow 0$:

$$n\left(L=0, t\right) = \frac{I^{\text{eff}}(t)}{2G^{\text{eff}}(t)}. \tag{2.15}$$

This provides a relationship between the effective nucleation and growth rates, and the crystal size distribution at any time t during solidification. Since all natural CSDs record

solidification at some final time T, described by population density $n(L, T)$, Eqn. (2.15) will now be reformulated to time T, at which the crystal size distribution is observed. Recalling that the crystal balance Eqn. (2.5) represents an advective transfer, its solutions at different times t_1 and t_2, where $t_2 \geq t_1$, are shifted by the rate of advection integrated over the interval of t_2 - t_1. Since the effective growth rate has a meaning of rate of advection, we obtain a simple relationship relating the crystal size distributions at different times

$$n\left(L,t_1\right)=n\left(L+2\cdot\int_{t_1}^{t_2}G^{\mathrm{eff}}\mathrm{d}\tau,\ t_2\right), \tag{2.16}$$

where the G^{eff} integral is an increase in the grain size over the interval of t_2 - t_1. Substituting T for t_2 and $t \leq T$ for t_1 and inserting Eqn. (2.16) into Eqn. (2.15) yields a relationship between crystal size distribution at the end of solidification, at time T, and both the nucleation and the growth rate as a function of time

$$n\left(2\cdot\int_{t}^{T}G^{\mathrm{eff}}\mathrm{d}\tau,\ T\right)=\frac{I^{\mathrm{eff}}\left(t\right)}{2G^{\mathrm{eff}}\left(t\right)}. \tag{2.17}$$

When CSD of the sample is known, Eqn. (2.17) together with relations between effective and ideal rates, Eqns. (2.7), (2.10) and (2.13), provide a fundamental relationship between the rate of nucleation and that of growth. If one rate is known or assumed, the other becomes dependent and can be uniquely calculated. This reasoning is similar to that of Zieg & Marsh (2002), however, our equations account for the time-dependent rates of nucleation and growth instead of employing their characteristic values. Eqn. (2.17) also highlights the inherent ambiguity in inversion of CSD into growth and nucleation rates. For every growth rate function, that is suitable to generate some observed CSD, a corresponding nucleation rate function can be expressed. Note that a suitable growth rate function must satisfy:

$$L_{\mathrm{MAX}} = 2 \cdot \int_0^T G^{\mathrm{eff}} \mathrm{d}\tau \,, \tag{2.18}$$

where L_{MAX} is size of the largest crystal. The integral constraint, Eqn. (2.18), is satisfied by unlimited number of various non-negative functions, therefore an arbitrary number of corresponding pairs of nucleation and growth rate functions can be constructed from a single CSD curve. One such pair is exponential nucleation rate and constant growth rate (e.g., Marsh, 1998; Hersum & Marsh, 2006; Amenta et al., 2007) but this is not a restrictive requirement for the origin of log-linear CSDs in natural magmatic systems.

2.3. Numerical implementation

If neither the nucleation nor the growth rate function is known or can be assumed as is the general case in magmatic systems, the unique solution to the CSD inversion can still be formulated if one additional independent parameter (function) is provided. Here we use crystallinity, $\Phi(t)$, as the only necessary constraint for simultaneous determination of $I(t)$ and $G(t)$ from final CSD. Progress of crystallinity can be obtained from kinetic experiments (e.g., Zieg & Lofgren, 2006), from unique natural observations (e.g., Marsh, 1981; Kirkpatrick, 1976), approximated by phase equilibrium calculations (e.g., Ghiorso & Sack, 1995; Holland & Powell, 2001) coupled with relevant cooling models, or varied in exploratory manner. Eqns. (2.3) and (2.17) with (2.7) or (2.10) and (2.13) provide a complete set of relationships needed to calculate both the nucleation rate $I(t)$ and the growth rate $G(t)$ as functions of time from the CSD and the evolution of crystallinity, $\Phi(t)$.

Our numerical technique employs finite discretization of length and time domain to solve the set of equations involved in the inversion of a crystal size distribution $n(L)$, which is from some time of interest T. Let us discretize the length scale of CSD into a regularly spaced sequence $\{L_i\}$, where $i \in \{0...N\}$ such that $L_0 = 0$, $L_{i+1} = L_i + \Delta L$, and $L_N = L_{\mathrm{MAX}}$, where L_{MAX} is the size of the largest crystal. Let us further denote n_i the population density corresponding to size L_i, hence $n_i = n(L_i)$. In this formulation, ΔL represents a size step at which the CSD is

sampled in its discretized representation. Furthermore, we define sequence $\{t_i\}$, $i \in \{0...N\}$, where each t_i represents the time of nucleation of crystals that reached the size L_i at the time of interest T. Note that t_0 and t_N represent boundary conditions of the simulation. Crystals of size L_0 (i.e., the population of smallest grains) must have nucleated last, hence $t_0 = T$. On the other hand, crystals of size $L_N = L_{\mathrm{MAX}}$ must have nucleated first, hence $t_N = 0$.

We will approximate the unknown functions, $I^{\mathrm{eff}}(t)$ and $G^{\mathrm{eff}}(t)$, by a set of discrete values in a piecewise constant fashion as follows:

$$\begin{gathered} I^{\mathrm{eff}}\left(t\right) = I_i^{\mathrm{eff}}, \quad G^{\mathrm{eff}}\left(t\right) = G_i^{\mathrm{eff}}, \\ \text{for all } t \in \left(t_i, t_{i-1}\right\rangle, \quad \text{where } i \in \left\{1...N\right\}. \end{gathered} \tag{2.19}$$

Unsymmetrical parentheses in Eqn. (2.19) indicate, in conventional mathematical notation, that the interval of t excludes or includes the start and end point, respectively. Substituting t_i and $t_{i\text{-}1}$ for the lower and upper bound of integration in Eqn. (2.11) and using above defined discretization we obtain

$$\Delta L = 2G_i^{\mathrm{eff}}\left(t_{i-1} - t_i\right), \tag{2.20}$$

for a grain size increment ΔL over a time interval $\left(t_i, t_{i-1}\right\rangle$. Similarly, the number of nuclei formed during the same time interval in a unit volume of system follows from Eqn. (2.12):

$$\Delta N = I_i^{\mathrm{eff}}\left(t_{i-1} - t_i\right). \tag{2.21}$$

By definition $t_{i\text{-}1}$ and t_i are times of nucleation of grains with size $L_{i\text{-}1}$ and L_i, respectively, at the time of interest T, hence the analogous quantity ΔN is obtained by integration from a crystal size distribution

$$\Delta N = \int_{L_{i-1}}^{L_i} n\left(L, T\right) \mathrm{d}L. \tag{2.22}$$

When using trapezoidal approximation for numerical integration

$$\Delta N = \frac{\left(n_i + n_{i-1}\right)}{2} \Delta L \,, \tag{2.23}$$

and combining Eqns. (2.20), (2.21) and (2.23) we arrive at a relationship that couples nucleation and growth rates:

$$n_i + n_{i-1} = \frac{I_i^{\text{eff}}}{G_i^{\text{eff}}} \,. \tag{2.24}$$

Eqn. (2.24) represents a discrete analogue of Eqn. (2.17), and it allows us to relate the effective rates of growth and nucleation to one another at time t_i using the population density. At this point, however, the value of time t_i is also unknown variable to be solved for.

We will illustrate the numerical method for two types of calculations: (*i*) calculation of nucleation rate from the CSD and an assumed growth rate and (*ii*) calculation of the nucleation and the growth rate from the CSD and crystallinity.

2.3.1. Calculation of nucleation rate

The growth rate $G(t)$ is often expected to be less variable than the rate of nucleation $I(t)$ that may increase exponentially (e.g., Cashman, 1993; Hammer & Rutherford, 2002; Marsh, 2007). If we assume that the growth rate is a simple, prescribed function, the nucleation rate necessary to produce an observed CSD, is uniquely defined and can be calculated. In this calculation, the crystallinity constraint is eliminated by the explicit assumption of the growth rate function. Furthermore, we demonstrate how distinct pairs of nucleation and growth rates generate identical final CSD. We employ Eqn. (2.24) to couple the nucleation and the growth rate at every time step *i*. Duration of each step is then calculated

from Eqn. (2.20) to provide a time reference at which the i-th discrete value of nucleation and growth rate is considered.

The solution procedure (Fig. 2.3) starts at time step N, where $t_N = 0$ is the initial condition, and the oldest crystals nucleated in the system. The prescribed ideal growth rate, G_N, is first converted into the effective growth rate, G_N^{eff}, before Eqn. (2.24) is employed to couple the nucleation and the growth rate; the conversion is performed using Eqn. (2.7) or (2.10). Both methods were compared and the discrete form of Eqn. (2.10), that is, Eqn. (2.A.4) was used in final calculations. The corresponding effective nucleation rate, I_N^{eff}, is then obtained from Eqn. (2.24). Since the CSD is discretized into regular ΔL steps and the growth rate is time-dependent, duration of each time step is generally different. The time of next step, t_{N-1}, is thus obtained from Eqn. (2.20). Finally, the effective nucleation rate is transformed to the ideal rate using Eqn. (2.13) and the crystallinity at the current time step is calculated *via* the discretized Avrami equation (Eqn. (2.27)). This procedure is repeated at time steps t_{N-1}, t_{N-2}, etc. until the time t_0, when the youngest crystals nucleated in the system, is reached.

Since relationships between effective and ideal rates (Eqns. (2.7) and (2.10)) make use of actual crystallinity Φ_i or its derivative $d\Phi/dt(t_i)$, these quantities must be calculated at each

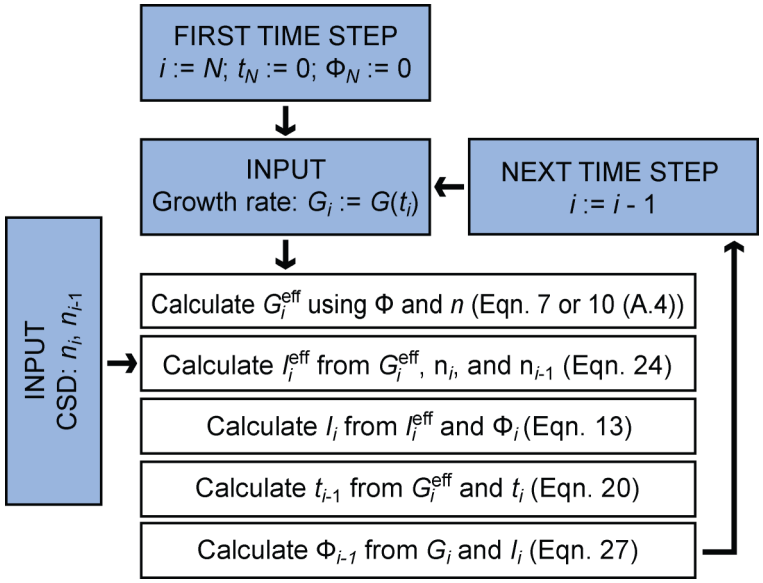

Fig. 2.3. *Flow chart for calculation of the nucleation rate from the CSD and the prescribed growth rate function.*

time step t_i. In our computations, we use the Avrami equation (Eqn. (2.3)) or its discrete analogue (Eqn. (2.27)) to calculate crystallinity at any time step. The time derivative of crystallinity is obtained from crystallinities at current and previous time steps using backward difference scheme (see Appendix 2).

It is noteworthy that the growth rate function must remain positive throughout the crystallization, otherwise Eqn. (2.24) would predict negative a nucleation rate and Eqn. (2.20) would lead to negative time step. As expected, the method cannot be applied to stagnant or dissolving grains.

2.3.2. Calculation of nucleation and growth rate from CSD and crystallinity

For calculation of rates of nucleation, $I(t)$, and growth, $G(t)$, we use Eqns. (2.20) and (2.24) coupling CSD, I_i^{eff}, G_i^{eff}, and $t_{\text{i-1}}$. The solution procedure starts at time step N, where crystallinity $\Phi_N = 0$ and time $t_N = 0$ are the initial conditions. To calculate the rates of nucleation and growth that satisfy the CSD and the crystallinity requirements simultaneously, an iterative approach based on the method of bisection is utilized at each time step i (Fig. 2.4).

The lower limit, $G_i^{(\text{L})}$, and upper limit, $G_i^{(\text{U})}$, for ideal growth rate are taken as zero and very large positive value, respectively, and are averaged to provide the mean rate, $G_i^{(\text{M})}$. The ideal growth rate, $G_i^{(\text{M})}$, is converted to the effective growth rate, $G_i^{\text{eff}\,(\text{M})}$, using Eqn. (2.7) or (2.10). In the present calculations we used the discrete form of Eqn. (2.10), that is, Eqn. (2.A.4). The effective nucleation rate, $I_i^{\text{eff}\,(\text{M})}$, is calculated for the effective growth rate using the CSD information (Eqn. (2.24)). Due to the regular discretization of the CSD with a ΔL step, duration of the time steps is irregular and it is determined from Eqn. (2.20). The ideal rate of nucleation, $I_{\text{i}}^{(\text{M})}$, is then calculated from the corresponding effective rate using Eqn. (2.13). Based on the ideal rates, the crystallinity, Φ_{i-1}^{calc}, is obtained (see below). The new estimate for $G_i^{(\text{M})}$ is sought until the predicted crystallinity $\Phi_{i-1}^{\text{calc}} = \Phi_{i-1}$ and prescribed crystallinity $\Phi_{i-1}^{\text{pres}} = \Phi\left(t_{i-1}^{(\text{M})}\right)$ are equal (Fig. 2.4). If $\Phi_{i-1}^{(\text{M})} < \Phi\left(t_{i-1}^{(\text{M})}\right)$ then $G_i^{(\text{L})}$ is replaced by $G_i^{(\text{M})}$ in next iteration; in an opposite case $G_i^{(\text{U})}$ accepts the value of $G_i^{(\text{M})}$. Such an approach

forces the true value of the growth rate to be progressively more constrained by $G_i^{(L)}$ and $G_i^{(U)}$ as iterations proceed. When the iterations have converged to a desired precision, the solution proceeds to the next (i-1)th time step until the step N = 0, when the youngest crystals nucleated, is reached.

In order to calculate Φ_{i-1}^{calc} we use the Avrami equation (Eqn. (2.3)). The equation will now be recast into a discrete form, compatible with our definition of time steps. Eqn. (2.3) taken at time t_{i-1} yields:

$$\Phi_{i-1} = 1 - \exp\left\{-\sigma_A \int_0^{t_{i-1}} I(\tau) \cdot \left[\int_\tau^{t_{i-1}} G(\tau')\,\mathrm{d}\tau'\right]^3 \mathrm{d}\tau\right\}. \tag{2.25}$$

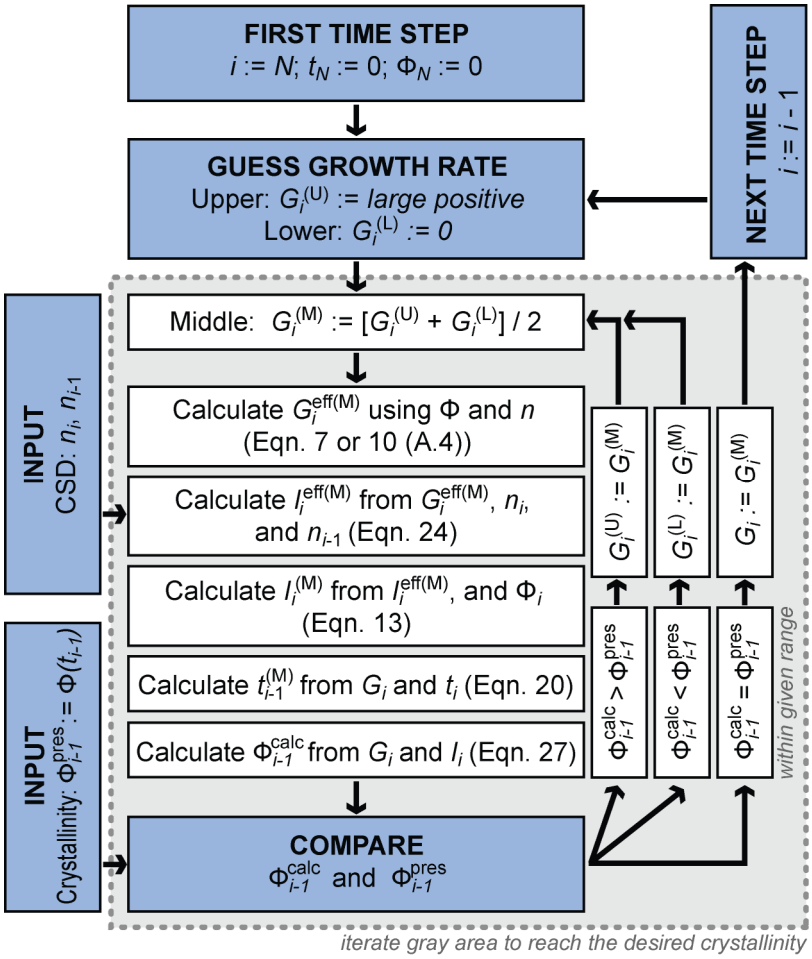

Fig. 2.4. *Flow chart with solution algorithm for calculating the rates of nucleation and growth from the CSD and crystallinity trends. Superscripts (L), (U), and (M) correspond to the lower, upper, and middle guess of the growth rate, respectively, in the actual time step.*

and this form allows us to calculate the crystallinity at time t_{i-1} using discrete values representing functions $I(t)$ and $G(t)$ at given time step. Integrals involved in Eqn. (2.25) can therefore be rewritten as sums of integrals over subintervals, which are defined by a set of time steps $\{t_i\}$:

$$\Phi_{i-1} = 1 - \exp\left\{ -\sigma_A \sum_{j=i}^{N} \int_{t_j}^{t_{j-1}} I(\tau) \cdot \left[\int_{\tau}^{t_{j-1}} G(\tau')\,\mathrm{d}\tau' + \sum_{k=i}^{j-1} \int_{t_k}^{t_{k-1}} G(\tau')\,\mathrm{d}\tau' \right]^3 \mathrm{d}\tau \right\}. \qquad (2.26)$$

Using constant values of $G(t)$ and $I(t)$ in each subinterval, as defined in Eqn. (2.19), we obtain:

$$\Phi_{i-1} = 1 - \exp\left\{ \frac{\sigma_A}{4} \cdot \sum_{j=i}^{N} \frac{I_j}{G_j} \left[\left(\sum_{k=i}^{j-1} G_k \left(t_{k-1} - t_k \right) \right)^4 - \left(\sum_{k=i}^{j-1} G_k \left(t_{k-1} - t_k \right) + G_j \left(t_{j-1} - t_j \right) \right)^4 \right] \right\}, \qquad (2.27)$$

where current values of $I_i^{(M)}$ and $G_i^{(M)}$ are used to calculate the current estimate of crystallinity.

2.3.3. Verification of the method

Our method of the CSD inversion was tested using synthetic CSD and crystallinity functions, which were obtained from predefined nucleation rate $I(t)$ and growth rate $G(t)$ functions. The correspondence of the resulting $I(t)$ and $G(t)$ with the predefined functions verifies the algorithm and its accuracy.

We have chosen an exponentially increasing rate of nucleation and constant rate of growth in order to produce a log-linear CSD that is observed in natural samples (e.g., Marsh, 1998; Hersum & Marsh, 2006; Amenta et al., 2007), with the shape factors $\sigma_A = 4\pi/3$ and $\sigma_{CSD} = \pi/6$ representing spherical shape of isolated unimpinged grains (Fig. 2.5). At extremely

low crystallinities ($\Phi < 0.0001$), the calculated growth rate $G_{calc}(t)$ is numerically scattered around the exact value $G(t)$, however, above this crystallinity threshold, the scatter is reduced to approximately 1 % of the exact value. Nucleation rate is reproduced accurately, with an exception of a few data points at the highest crystallinities ($\Phi > 0.9$) where longer calculation time steps were used that lead to larger accumulated integration errors. As shown in Figs. 2.5c and 2.5d, these errors do not propagate substantially to the calculated CSD or to the crystallinity function.

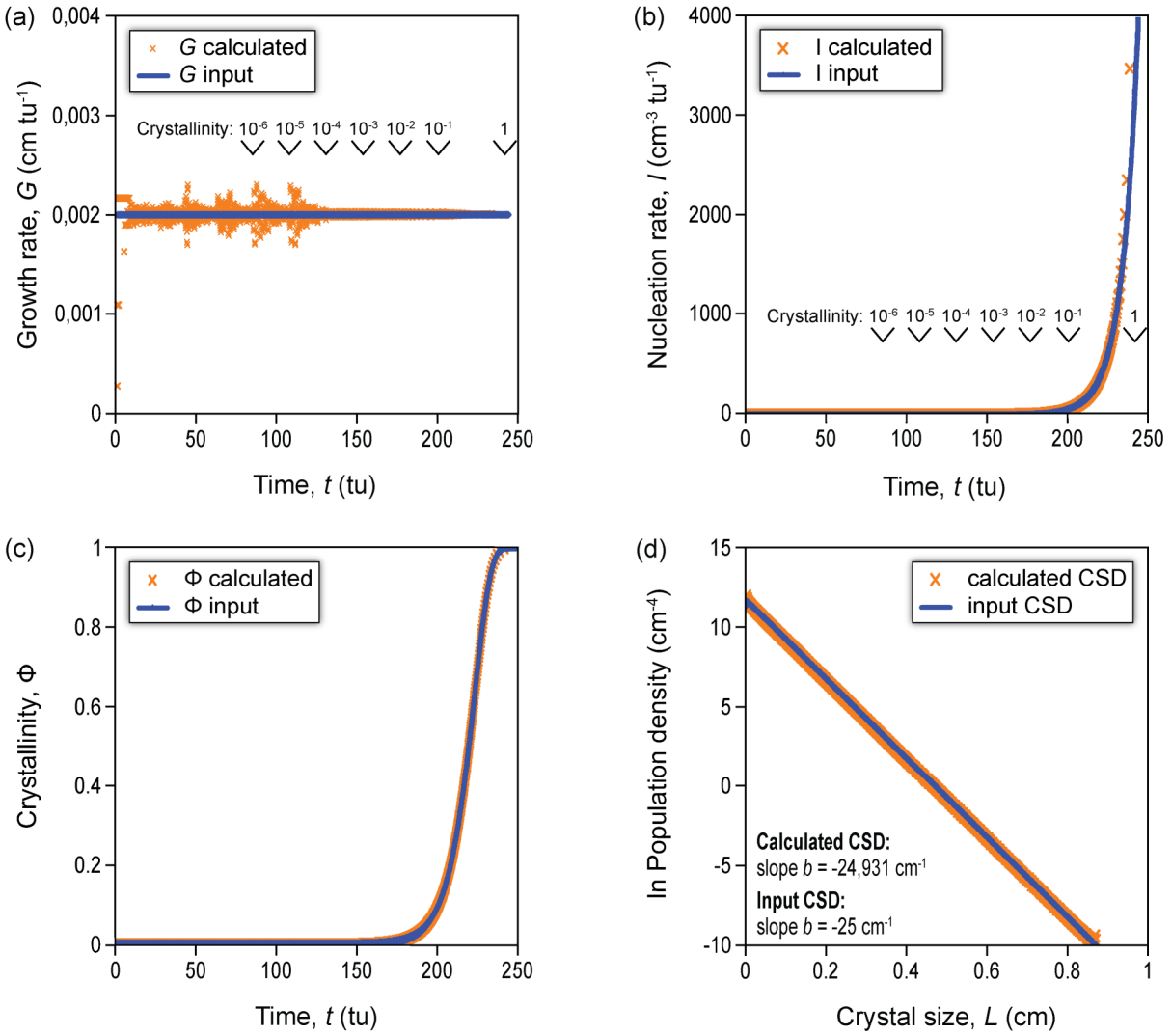

Fig. 2.5. *Numerical verification of the CSD inversion method. First, we use predefined rates of nucleation and growth to predict the evolution of crystallinity and the resulting CSD. Second, the crystallinity function and CSD are used as input for the inversion algorithm and the retrieved rates of nucleation and growth are compared with the original ones:* **(a)** *growth rate;* **(b)** *nucleation rate;* **(c)** *crystallinity;* **(d)** *crystal size distribution. The predefined functions are shown as solid curves; calculated values are indicated by point symbols. Symbol tu refers to arbitrary time units.*

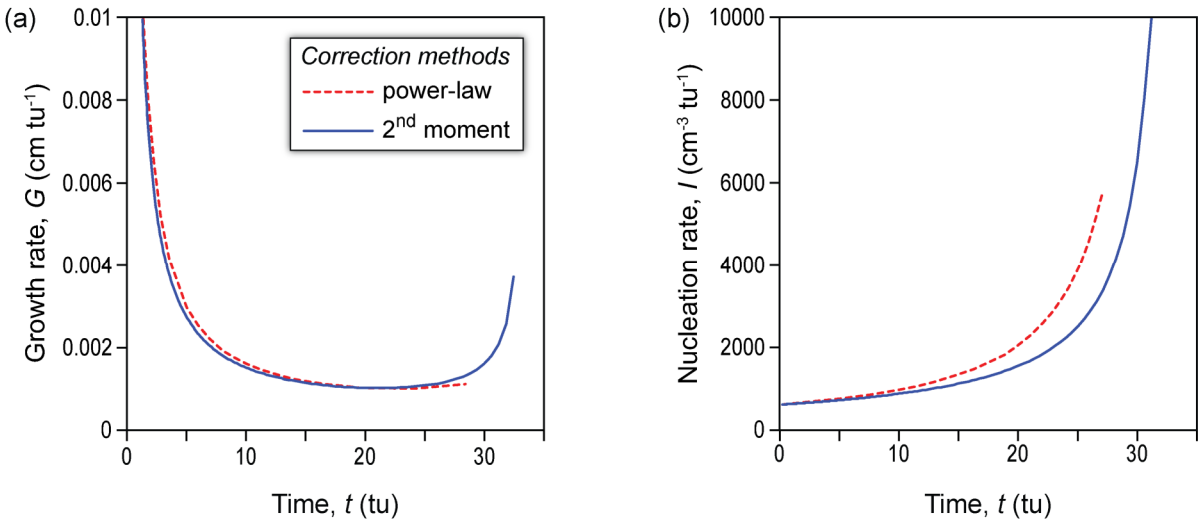

Fig. 2.6. *Comparison of correction methods for the effective growth rate. The straight log-linear CSD with a slope of b = -40 cm^{-1} (population density considered as a natural logarithm) and linear crystallinity function Φ(t) = 0.03t were transformed to obtain the nucleation and growth rates using power-law correction (Eqn. (2.7)) and a correction based on the 2nd CSD moment (Eqn. (2.10)). The CSD's value of ln n at zero grain size was chosen to represent a sample with crystallinity of 100 % (see Appendix 3). Symbol tu refers to arbitrary time units. Note the crystallization terminates at different times when distinct correction methods are used (see text for further discussion).*

2.3.4. Comparison of correction methods for effective growth rate

Our algorithm for inversion of CSD and crystallinity function to $I(t)$ and $G(t)$ (see Section 2.3.2) can now be used to compare the appropriateness and applicability of two distinct relationships between G^{eff} and G (Eqns. (2.7) *vs*. (2.10)). An arbitrary CSD and crystallinity function was inverted to nucleation and growth rates using Eqn. (2.7) or Eqn. (2.10) as leading relationship between G^{eff} and G (Fig. 2.6).

The power-law relationship (Lasaga, 1998; Eqn. (2.7)) predicts marginally higher ideal growth rates (Fig. 2.6a), when compared to the correction based on CSD's 2nd moment (Eqn. (2.10)). This difference propagates into the nucleation rate (Fig. 2.6b), which increases more steeply with time (that is, with advancing crystallization). Also, the effective growth and nucleation rate predicted by a power-law relationship is higher. As a consequence of higher effective rates, the prescribed CSD, from the largest crystal sizes down to the smallest ones, is generated and crystallization terminated in a shorter crystallization time. This comparison highlights the discrepancy caused by the two different corrections for the effective rates. The

power-law relationship will lead to a complete CSD in the shorter time but the crystallinity has not reached 100 % yet. In detail, for our set of parameters, crystallization terminates at $\Phi = 82$ % when the power-law correction is employed, while it reaches $\Phi = 98$ % with a correction based on the 2nd moment of CSD. 2nd moment correction hence provides very close match of both CSD and crystallinity function.

Our model example thus reveals inconsistency between CSD and crystallinity, when a power-law correction (Eqn. (2.7)) is used for calculating the effective growth rate, as crystallization is terminated long before the prescribed final crystallinity is reached. On the other hand, Eqn. (2.10), which utilizes the CSD's 2nd moment, is internally consistent with the initial CSD and it allows a much closer approach to the prescribed final crystallinity. Therefore, the method based on CSD's 2nd moment should be used preferentially and we employ Eqn. (2.10) in all calculations presented in this study.

2.4. Results

We derived an algorithm, which utilizes the crystal size distribution of igneous rocks, to obtain the rates of nucleation and growth that are consistent with the observed texture. In order to make the solution unique, we must use additional constraints in the CSD inversion model: (*i*) one can assume a functional form for one of the rates, which leads to a unique solution for the other one, or (*ii*) we constrain the evolution of crystallinity in time, as discussed below, and the both rate functions can be solved for uniquely. We illustrate several applications of the CSD inversion method to calculations of nucleation rates and crystallinity functions from prescribed CSDs and growth rates, and to calculations of nucleation and growth rates from several model CSDs and crystallinity functions. All simulations were run up to complete crystallization and assume uniform properties of all grains, that is, a one-component (single-phase) system. They are also applicable to multiphase crystallization, when differences in crystallization behavior of individual phases are insignificant. For all simulations, we use shape factors $\sigma_A = 4\pi/3$ and $\sigma_{CSD} = \pi/6$, representing spherical shape of

isolated unimpinged grains because grain shapes are not explicitly evaluated in our calculations.

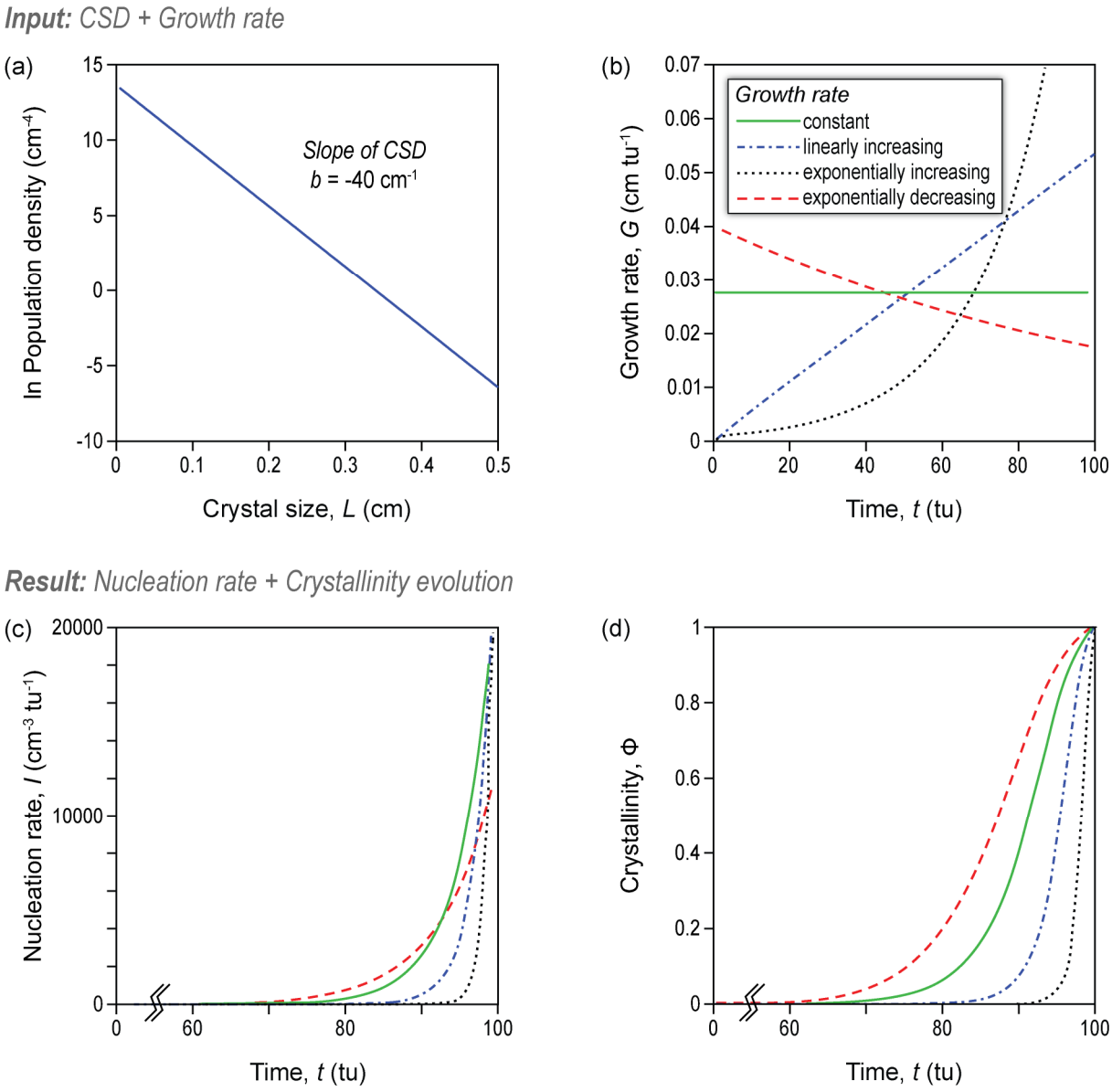

Fig. 2.7. *Representative reconstruction of the nucleation rate I(t) from CSD and growth rate G(t). All pairs of I(t) and G(t) produce identical CSDs at the end of the crystallization. The CSD is straight with a slope of b = -40 cm^{-1} (population density is considered as a natural logarithm). The value of ln n at zero grain size was chosen such that the CSD represents a sample with crystallinity of 100 % (see Appendix 3).* **(a)** *input CSD;* **(b)** *input growth rate functions: constant G(t) = 0.00276, linear G(t) = 0.000053t, exponentially increasing G(t) = 0.0001 exp(t/20.5), and exponentially decreasing G(t) = 0.004 exp(-t/120). Constants involved in the expressions for the growth rates are adjusted such that crystallinity of 100 % is reached at approximately same time of 100 tu for all growth rate functions considered;* **(c)** *calculated nucleation rates;* **(d)** *calculated crystallinities for each pair of nucleation and growth rate. Symbol tu refers to arbitrary time units.*

2.4.1. Calculations using CSD and growth rate

We performed four inversions of log-linear CSD with a slope b = -40 cm^{-1}. This value is based on CSDs of norites from the Sudbury Igneous Complex, Canada (Zieg & Marsh, 2002) and it is representative of a texture formed in a plutonic environment. The corresponding intercept value ln $n(0)$ = 13.611 (cm^{-4}) is defined by a mass-balance constraint to represent a sample with 100% modal content of crystals (see Appendix 3). We explored the effects of four different growth rate functions (Fig. 2.7): constant, linear, exponentially increasing, and exponentially decreasing. Arbitrary time units (tu) are normalized so that the complete crystallinity is reached after 100 tu in each run.

In all runs both the nucleation rate and crystallinity function increases quasi-exponentially (Figs. 2.7c, d). Remarkably, the nucleation rates remain negligibly low for up to 60-90 % of the crystallization time. In simulation where growth rate remains constant throughout the crystallization, exactly exponential nucleation rate is predicted, in agreement with the theory (e.g., Marsh, 1998). Decreasing growth rate leads to the sub-exponential but initially greater nucleation rate. This in turn causes an early increase of crystallinity and a higher crystallinity is observed at any arbitrary time than in a system with a constant growth rate. When the growth rate increases with time, the reverse behavior is observed, that is, the nucleation rate increases super-exponentially but crystallization is delayed, then more rapid. Steeper increase in the growth rate causes larger delays in the increase of the nucleation rate and crystallinity.

2.4.2. Calculations using CSD and crystallinity

We carried out six simulations with log-linear CSDs and different crystallinity functions, $\Phi(t)$. Both functions are usually available for natural samples, the CSD is a measurable quantity and the crystallinity function can be approximated from experimental studies or thermodynamic calculations, hence the nucleation and growth rates can be

recovered without additional constraints or kinetic models. We have chosen two CSDs with slopes b = -40 or -10 cm^{-1}, respectively, that are similar to the range of slopes reported by Zieg and Marsh (2002) from norites of the Sudbury melt sheet (Sudbury Igneous Complex, Canada) and hence resemble natural samples from a plutonic environment. The intercept values were set to ln $n(0)$ = 13.611 and 8.066 (cm^{-4}), respectively, as required by the mass-balance constraint for the 100% crystallinity of the sample (see Appendix 3). We have explored three various crystallinity functions, namely sigmoidal, linear, and sinusoidal. From a sine function, only the first quarter-period is considered, since we are interested in a crystallinity increasing with time. The linear function was chosen to be tangent to the sine at the origin (onset of crystallization). Choice of these functions is motivated by relationships between crystallinity (or melt fraction) and temperature observed in phase equilibrium studies (e.g., Wyllie, 1977; Marsh, 1981; Douce & Johnson, 1991; Dufek & Bergantz, 2005). As demonstrated by the conductive cooling models (e.g., Kirkpatrick, 1976), the dependence of temperature on time, even in more realistic models of cooling of sheet-like magma body, is still well characterized by a linear relationship, if considered far enough from the contact. The monotonous functions can thus serve as simple first-order models of crystallinity-time relationships which are, however, variable enough to cover possible geological variations.

Fig. 2.8 shows the input CSD and crystallinity functions and the calculated rates of crystal nucleation and growth. Rates calculated from both the linear and the sinusoidal crystallinity functions share common characteristics at the beginning of crystallization, i.e., at the time, when both crystallinity functions have similar slope. In both cases, the nucleation rates at time t = 0 have some finite nonzero value and always increase with time. When the sinusoidal crystallinity function starts to depart from the linear trend towards lower crystallinities, the lower nucleation rates are observed.

► **Fig. 2.8.** *Inversion of straight log-linear CSDs.* **(a)** *input crystallinity functions are as follows: linear $\Phi(t) = 0.030208t$, sinusoidal $\Phi(t) = \sin(t\pi / 104)$, sigmoidal $\Phi(t) = 1 - \exp(-3\times10^{-6}\pi t^4)$. The linear function was chosen to be tangent to the sinusoidal function at t = 0. All functions were chosen to span similar time interval between zero and full crystallinity;* **(b)** *input CSDs: b = -40 or -10 cm^{-1} with intercepts of 13.611 or 8.066 (cm^{-4}), respectively. The population density is considered as a natural logarithm. Intercept values were chosen to represent samples with 100% crystal content (see Appendix 3);* **(c)** *calculated nucleation rates for CSD with b = -40 cm^{-1};* **(d)** *calculated growth rates for CSD with b = -40 cm^{-1};* **(e)** *calculated nucleation rates for CSD with b = -10 cm^{-1};* **(f)** *calculated growth rates for CSD with b = -10 cm^{-1}. Symbol tu refers to arbitrary time units.*

Input: *Evolution of crystallinity + CSD*

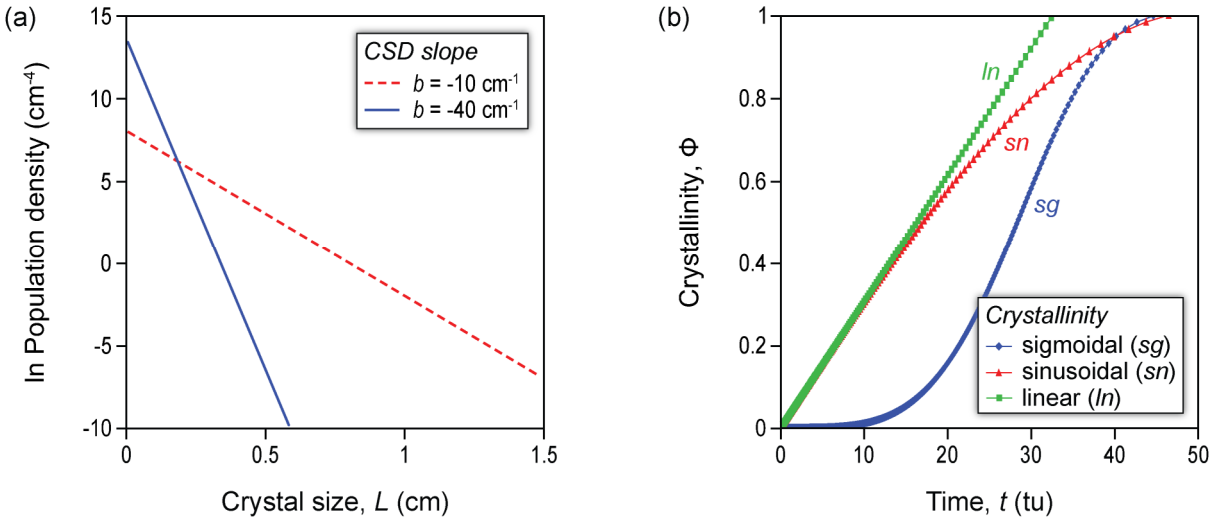

Result: *Nucleation and growth rates. For different crystallinities and CSD with b = -40 cm-1*

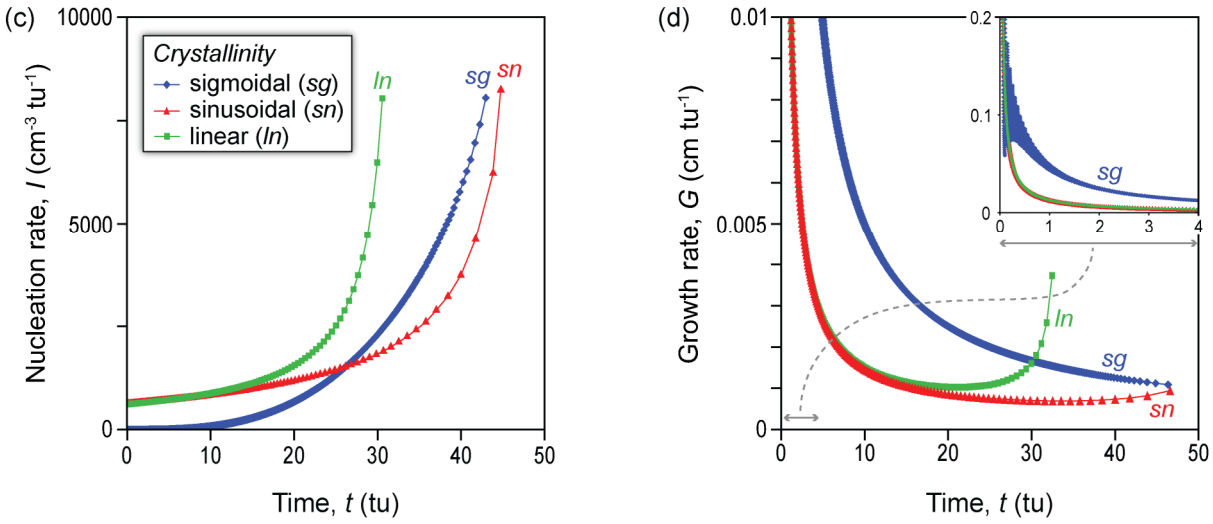

Result: *Nucleation and growth rates. For different crystallinities and CSD with b = -10 cm-1*

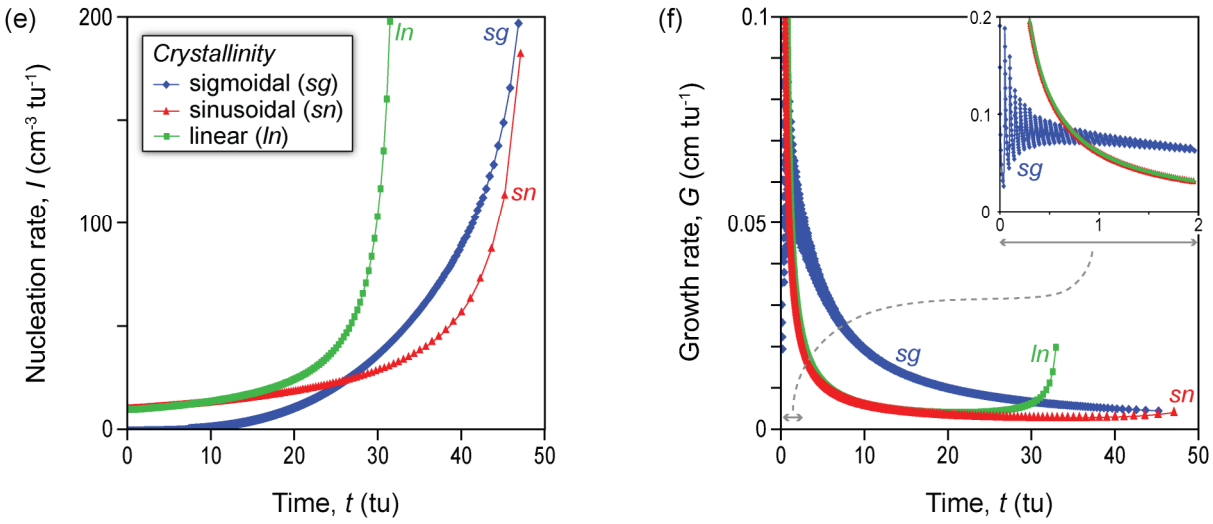

In contrast, growth rates initially exhibit very high values because crystal nuclei are not abundant and the surface area is small, and they decrease as crystallization progresses during the most of the crystallization time in both the linear and sinusoidal case. At the end of the crystallization interval the growth rates increase again. Similarly to the nucleation rate, when the slope of the $\Phi(t)$ curve becomes smaller, as in the sinusoidal case, lower growth rates are obtained. In addition, the final increase in the growth rate is less pronounced in the case of sinusoidal crystallinity function when compared to the linear case.

Behavior of both the nucleation and growth rates is different when the sigmoidal increase in crystallinity is assumed. In this scenario, the nucleation rate increases with time, but starting from zero value. The growth rate is decreasing during the entire crystallization interval. Despite substantial numerical oscillations during the first few percent of crystallization time, the growth rate starts at some finite value at time $t = 0$, which is in contrast with the two other cases of crystallinity functions.

The resulting rates of nucleation and growth are qualitatively similar for both CSD slopes tested. The most notable difference is a scale of both rates; greater CSD slope propagates to larger values of the nucleation rate (about two orders of magnitude) and to smaller growth rates (about a factor of five for b from -10 to -40 cm^{-1}). This effect can easily be understood by realizing that the lower CSD slope implies larger crystal sizes, hence higher growth rates are needed to produce such crystals during any given crystallization time. On the other hand, the higher CSD slope indicates higher crystal number, and it thus requires higher rate of nucleation.

The simulations indicate that the main factors controlling the course of nucleation and growth rates are the initial and final slope of the crystallinity function, $\Phi(t)$, that is, the initial and final crystallization rate. The zero initial slope forces the nucleation rate to start from a zero value and the growth rate from some finite positive value. In case of any nonzero initial slope of $\Phi(t = 0)$ the initial nucleation rate is positive and the growth rate diverges positively, that is, it starts at positive infinity at the liquidus and it decreases as time increases. Analogous behavior appears at the end of the crystallization: nonzero slope of $\Phi(t)$ curve at the solidus forces rate of growth to diverge positively. On the other hand, zero slope of the crystallinity

curve at the end of crystallization prevents the growth rate from its final divergence. These findings are general and do not depend on a particular CSD slope. The CSD slope only affects scales of both rates in order to achieve appropriate numbers and sizes of crystals within a given crystallization time.

2.4.3. Calculations with natural CSDs

To illustrate the effects of irregular CSD patterns measured on natural magmatic rocks, we transformed three representative CSDs using model crystallinity functions to nucleation and growth rates. This approach mainly addresses consequences of various curved shapes, kinked segments and sensitivity to scatter due to the measurement errors on both rates, provided that the crystallization occurred in a closed system. The input CSD functions are (*i*) compound CSD of plagioclase from Sudbury norite, Canada (Marsh, 2007), with predominantly large grains and limited amount of fine crystal fraction; (*ii*) kinked CSD of plagioclase from Atka high alumina basalt, Alaska (Resmini, 1993; Marsh, 1998), with two approximately straight segments that differ in their slopes; and (*iii*) a cumulate CSD of chromite Stillwater, Montana (Waters & Boudreau, 1996), with a pronounced deficiency of small grains (see Fig. 2.9). The last sample, despite not being the product of closed system crystallization, was included for comparison to unravel the consequences of significant peaking in the CSD for rates of nucleation and growth, if formed as a batch system. Because the representative CSDs were originally acquired for single phases in distinct modal amounts, the distributions must be rescaled to 100 %. We applied linear scaling of both size and population density by such factor that a volume fraction of analyzed phase, as determined from the 3rd moment of the scaled CSD, equals to unity (see Appendix 3).

Fig. 2.10 shows the rates of crystal growth and nucleation, as retrieved from natural CSDs (Fig. 2.9) and crystallinity functions (Fig. 2.8a). The growth rate functions are very similar in all three cases but differ in their absolute magnitude. The growth rate behavior strongly depends on the crystallinity function $\Phi(t)$ whereas the CSD shape has a subordinate

effect only. This demonstrates that variations in growth rate during magmatic crystallization predominantly control the evolution of mode (crystallinity) but do not significantly affect the resulting CSD. In contrast, the nucleation rate is particularly sensitive to both the CSD and the crystallinity function. Kinks and fluctuations on CSD remarkably propagate into the nucleation rate, however, the exact expression depends on a crystallinity function. Similarities in some crystalinity functions in the initial or final stages of crystallization propagate into analogous behavior of the nucleation rates. For the linear and sinusoidal crystallinity functions, which have the same initial slope, the nucleation rate behaves similarly near $t = 0$.

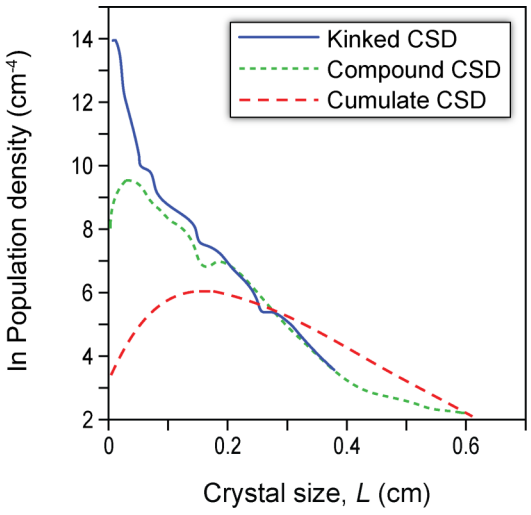

Fig. 2.9. *Natural CSDs used for reconstruction of the nucleation and growth rates: (i) compound CSD: plagioclase from the Sudbury norite, Canada (Marsh, 2007); (ii) kinked CSD, plagioclase from Atka, Alaska, high-alumina basalt (Resmini, 1993; Marsh, 1998); (iii) cumulate CSD: chromite from the Stillwater layered mafic intrusion, Montana (Waters & Boudreau, 1996). Original data were linearly scaled in both size and population density to represent sample with 100% crystal content. No smoothing was applied to raw measurements, therefore, this approach also illustrates the effects of small-scale features of the CSD on the resulting rates and their fluctuations.*

► **Fig. 2.10.** *Nucleation and growth rates reconstructed from natural CSDs. Input CSDs are shown in Fig. 2.9, and input crystallinity functions Φ(t) are in Fig. 2.8a.* **(a)**, **(c)**, **(e)** *illustrate the resulting nucleation rates whereas* **(b)**, **(d)**, **(f)** *show the resulting growth rates referring to:* **(a)**, **(b)** *compound CSD with deficient small grains;* **(c)**, **(d)** *kinked CSD with two straight segments;* **(e)**, **(f)** *cumulate CSD with significant peak. See Fig. 2.9 caption for references. Symbol tu refers to arbitrary time units.*

Compound CSD: *plagioclase from Sudbury norite*

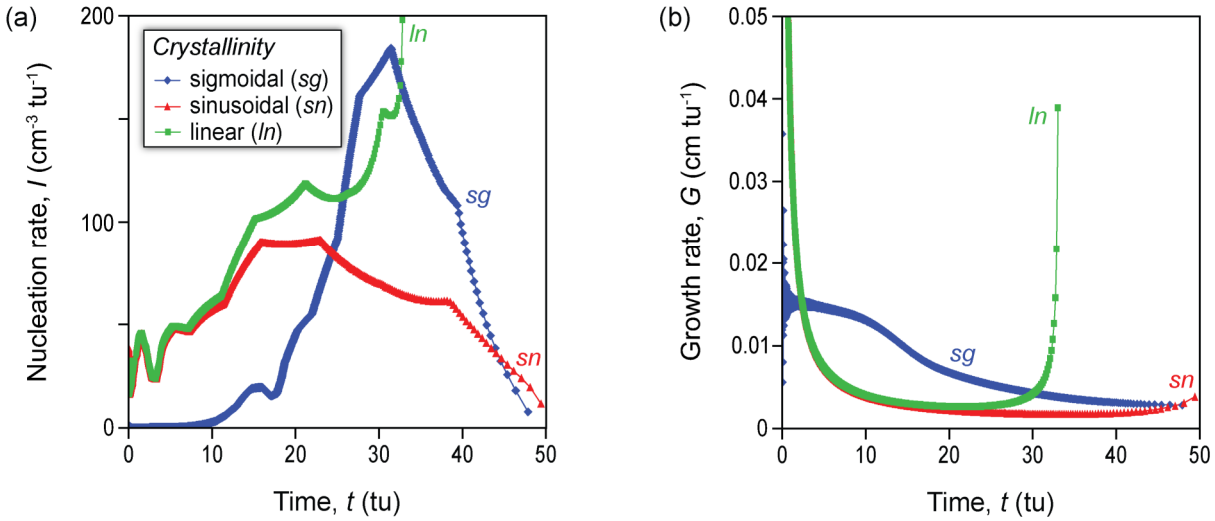

Kinked CSD: *plagioclase from Atka basalt*

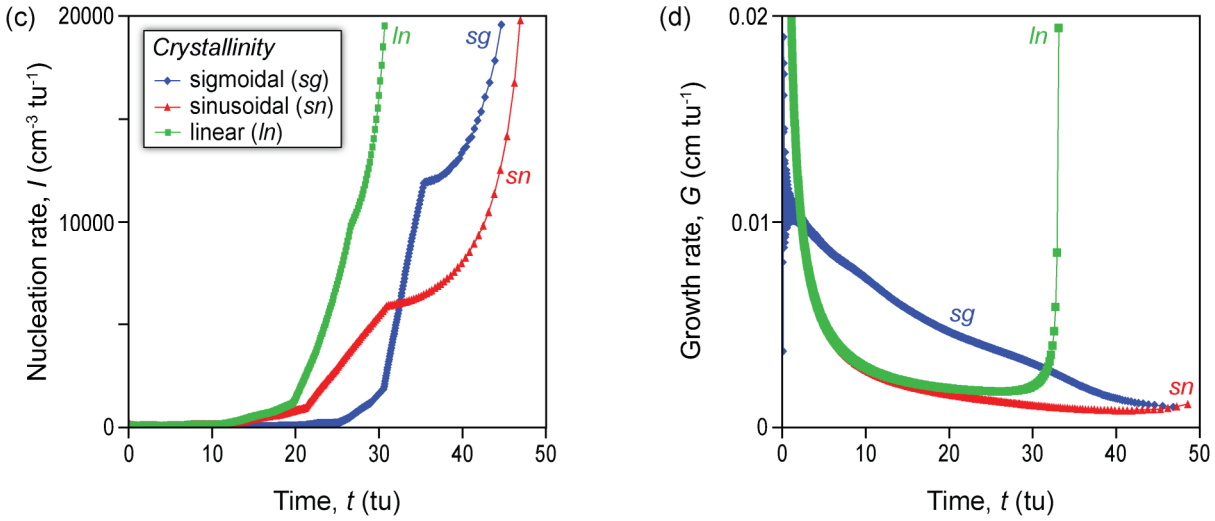

Cumulate CSD: *Chromite from Stillwater intrusion*

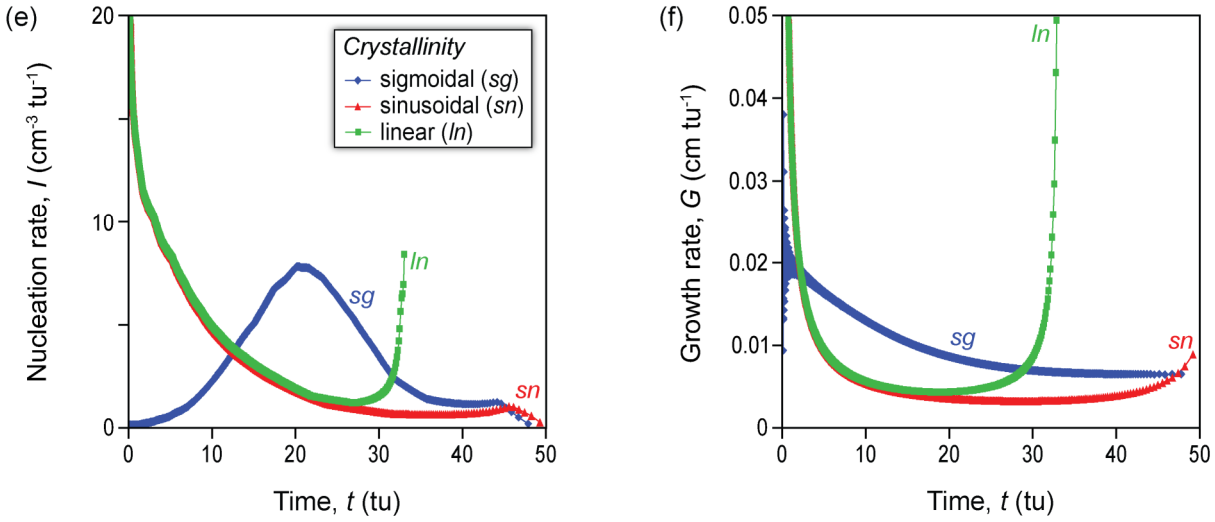

On the other hand, slopes of both sinusoidal and sigmoidal crystallinity functions approach zero at the end of crystallization and, accordingly, nucleation rates converge to each other.

Linear crystallinity function always leads to the nucleation rate increasing towards the end of crystallization, regardless of the actual CSD. Bent CSDs with a population density decreasing at smallest grain sizes require the nucleation rate to decrease after some peak value (with sinusoidal and sigmoidal crystallinity function). Conversely, the nucleation rate for the kinked CSD with a steep straight segment at the smallest grain sizes behaves similarly to the simple straight CSD, that is, the nucleation rate always increases with time. It is interesting to note that smooth $\Phi(t)$ functions translate into the smooth growth rates, whereas the smooth variations in nucleation rate require smooth CSDs.

2.5. Discussion

2.5.1. Interpretation of the calculated rates of nucleation and growth

We have shown that the nucleation rate function reflects minor features of the CSD, whereas shape of the growth rate function is largely insensitive to the same factors. If the length scale of CSD is changed, only the relative scale of the growth rate changes. The growth rate for both CSDs reaching $L \approx 0.6$ cm is about twice as large as for a CSD ending at $L \approx 0.4$ cm (in the case of sigmoidal crystallinity function), when crystallization rate functions, $\Phi(t)$, are equal. This does not imply that a coarser-grained rock requires the growth rate to be higher compared to a finer grained one, with steeper CSD, because the time scale of crystallization may differ.

The predicted growth rates largely depend on the shape of the crystallinity functions. Any positive slope of the crystallinity function, $\Phi(t)$, at the beginning or near the end of the crystallization forces the growth rate to increase to large values. In contrast, zero initial (or final) slope of the crystallinity function allows the growth rate to remain at some finite value at the beginning (or at the end) of crystallization. The divergence of growth rates to very large

values at the beginning and the end of crystallization is simply a consequence of the small surface area on which growth may occur. At the beginning of crystallization, when (nearly) no crystals are present, very large or infinite growth rates are required to produce a finite increment in crystal fraction (crystallinity). Similarly, at the end of crystallization, the surface area of the grains exposed to the melt approaches zero hence the growth rate must again increase *ad infinitum* to produce any observable increment of crystallinity. Since an infinite growth rate is unphysical, this observation implies that only a sigmoidal crystallinity function (with $d\Phi/dt = 0$ at liquidus and solidus) is realistic in natural or synthetic systems.

During the intermediate part of crystallization, the reactive surface is large enough to enable growing crystals to most closely approach equilibrium crystallinity *vs*. time relationship. This is expected to occur under moderate crystallinities. The lows on the calculated growth rate *vs*. time curves can thus be interpreted as minimal growth rates, which are to occur under conditions of nearest approach to equilibrium (see Figs. 2.8 and 2.10).

2.5.2. Transformation of rates to real time units

The predicted nucleation and growth rates are in arbitraty units that reflect scaling of the crystallization interval to given number of units. If the time span between liquidus and solidus is known or chosen, the rates can be converted into real time units. We explore the duration of crystallization by using the time span between liquidus and solidus temperature of magma in a conductively cooling magma chamber. The linear crystallinity-time relationship that we employ in our calculations prescribes, by definition, the full crystallinity to be reached at the time of 33 tu, which also corresponds to the liquidus-solidus time span, $t_{\text{sol-liq}}$. Thus from the identity

$$33 \text{ tu} \equiv t_{\text{sol-liq}}, \tag{2.28}$$

conversion between tu and specific (physical) time units is obtained. Choice of the actual shape of the crystallinity-time curve is largely arbitrary as long as we are interested in the intermediate part of crystallization, when essentially any crystallinity function can be reproduced (see above).

Liquidus-solidus time span remains to be specified now. We illustrate this approach by using a model of a melt sheet cooling conductively from both sides due to the temperature difference between magma and a country rock (see Fig. 2.11 caption for the model parameters). We assume infinite lateral extent of the melt sheet hence the model applies to horizontal dykes or to tabular plutons whose lateral extent is much grater than their thickness.

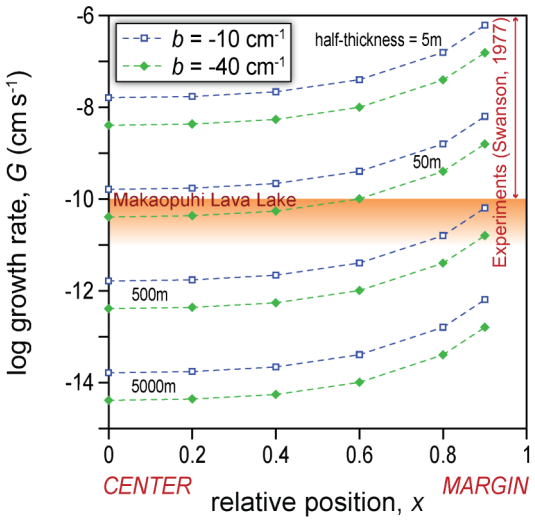

Fig. 2.11. *Calculated minimal growth rates as a function of relative position in a tabular magma body for fixed CSD slope. Calculations were performed for various magma body thicknesses and for two CSDs with slopes* $b = -40\ cm^{-1}$ *and* $b = -10\ cm^{-1}$ *(population density is considered in a natural log units). Chosen CSDs represent textures formed in a plutonic environment and are based on a range of values reported by Zieg & Marsh (2002) from the Sudbury Igneous Complex, Canada. The intercepts of CSDs are 13.611* (cm^{-4}) *and 8.066* (cm^{-4})*. Intercepts were chosen to represent sample with 100% crystal content (see Appendix 3). Relative position x is x = 0 in the center of the magma body and x = 1 at the magma chamber wall. Parameters used in calculations are as follows: thermal diffusivity of magma and of country rocks* $\kappa = 1\times10^{-6}\ m^2\ s^{-1}$*, (see Whittington et al., 2009) magma temperature at the emplacement 1100 °C; country rock initial temperature 200 °C; magma liquidus temperature 1100 °C; magma solidus temperature 900 °C. Difference of magma liquidus and solidus temperature is chosen to be 200 ºC, which corresponds to usual span of crystallization (e.g., Marsh, 1981, 1989). No latent heat generation is considered.*

Analytical solution of the heat conduction problem (e.g., Carslaw & Jaeger, 1959) leads to a time period, $t_{sol\text{-}liq}$, over which the temperature decreases by 200 ºC from the liquidus (conventional temperature difference between a magma liquidus and solidus; e.g., Marsh, 1981, 1989) in any arbitrary location across the melt sheet. We have scaled both calculations performed for log-linear CSDs with slopes b = -10 and -40 cm^{-1} (see Section 2.4.2).

For fixed CSD slope, the minimal growth rate is predicted to increase non-linearly by about 1.5 orders of magnitude from the center of the pluton to the 90% distance to the magma chamber wall, and the relative magnitude of its increase is independent of the pluton thickness and the CSD slope. An order of magnitude increase in the pluton thickness leads to two orders of magnitude decrease in the minimal growth rate. For a fixed pluton thickness, a fourfold increase of the CSD slope (b = -10 to -40 cm^{-1}) results in a fourfold decrease of the minimal growth rate. From these scaling laws, a formula relating the minimal growth rate G^{MIN} between plutons of a half-thicknesses D and D_0 (in meters) and CSDs with slopes b and b_0 (in cm^{-1}, where population density is considered in a natural log units) can be written

$$G^{MIN}\left(D,\ b,\ x\right) = G^{MIN}\left(D_0,\ b_0,\ x\right)\cdot\frac{b_0}{b}\left(\frac{D_0}{D}\right)^2, \quad \text{in cm s}^{-1}, \tag{2.29}$$

where x is the relative position between the pluton center and the boundary (x = 0 for the center and x = 1 for the pluton roof). Since the choice of D_0 and b_0 is arbitrary, Eqn. (2.29) can be transformed to

$$G^{MIN}\left(D,\ b,\ x\right) = \frac{C\left(x\right)}{bD^2}, \quad \text{in cm s}^{-1}, \tag{2.30}$$

where the coefficient $C(x)$ incorporates values of b_0, D_0, and of $G^{MIN}(D_0, b_0, x)$. Using data shown in Fig. 2.11, $C(x)$ can be calculated for any location x across the magma chamber and its variations reflect differences in thermal evolution in different locations in the magma chamber. Apart from $C(x)$, only the actual value of the CSD slope b at given location x, and

the pluton thickness D are needed to estimate the growth rate G^{MIN} using Eqn. (2.30). We use Eqn. (2.30) to evaluate the absolute growth rates in a magma sheet with half-thickness $D = 0$ m and for the CSD slope $b = -500\ cm^{-1}$. Value of the slope is similar to the value reported by Cashman & Marsh (1988) as corrected by Higgins (2006) for plagioclase in their sample 65-1-17 from the crust of the Makaopuhi lava lake, Hawaii. We obtained minimal growth rate $G^{MIN} = 2.17 \times 10^{-11}$ cm s^{-1} in 65 % of the distance to the margin of the magma sheet. The position equals the depth in the Makaopuhi lava lake from where Cashman & Marsh (1988) obtained the growth rate of 3.5×10^{-11} cm s^{-1} (corrected by Higgins, 2006) for their sample. Our calculated value thus compares very well with previous results. This model approach demonstrates a self-consistent link between crystal size distribution parameters, nucleation and growth rates as well as time scale of crystallization predicted by thermal modeling.

2.6. Conclusions

The crystal size in natural igneous rocks is a final result of the nucleation and growth rates, and their variations during crystallization, combined with possible subsequent modification of the texture by surface-energy driven processes such as grain annealing or coarsening. We derive a new method for retrieval of these kinetic parameters from the crystal size distribution of interest provided the post-crystallization modifications were insignificant. We illustrate two techniques of the CSD interpretation that apply to a limiting case of closed-system crystallization when no mechanical processes such as crystal movement or separation are affecting the resulting texture. A single CSD can be produced by various combinations of the nucleation and the growth rate functions, which, however, lead to different evolutions of the crystallinity with time. In an inverse approach, the CSD of interest in combination with appropriate crystallinity function, constrained by experimental phase equilibria or thermodynamic models, can be used to unambiguously determine the self-consistent nucleation and growth rates as a function of time. We applied the transformation procedure to

several straight log-linear and complex CSDs and explored several crystallinity-time relationships. Minor fluctuations in the CSDs propagate into significant variations in the nucleation rate, whereas the growth rate behavior is much less sensitive. In detail, the behavior of both rate functions is mostly determined by the initial and final rate of the crystallinity increase. This results from a small area of the crystal-melt interface at the initial and final stages of crystallization, when the number of crystals and their size are small or the area of crystal exposed to residual interstitial melt becomes very small, respectively. Nonzero initial or final increases in crystallinity thus imply large positive growth rates at both limits of crystallization. Consequently, the initial and final stages of crystallization are thus expected to record the highest departures from equilibrium, as any finite growth rate cannot, at this stage, offset a finite increment of crystallinity. In contrast, crystallinity is expected to approach equilibrium values during most of the intermediate crystallinity span, when a large surface area of crystals is available for their growth. Magnitudes of the rates of nucleation and growth are proportional to the CSD slope. Calculations with straight log-linear CSDs show that change in the CSD slope from -10 to -40 cm^{-1} results in two orders of magnitude increased rate of nucleation and four times decreased rate of growth.

When the crystallization time is known or independently estimated, for instance, from cooling models, the nucleation and growth rate functions can be scaled into real units. With the fixed CSD slope, our results predict the minimal growth rate (at intermediate crystallinities) to increase by ~1.5 orders of magnitude between the center of the magma body and the 90 % distance towards the contact. The growth rate is inversely proportional to the magma body size and the slope of the CSD. For conditions broadly similar to cooling lava lakes such as in Hawaii we obtain growth rates in order of 10^{-11} cm s^{-1} which is in agreement with natural observations (Cashman & Marsh, 1988).

2.7. Acknowledgements

This study was financially supported by the research projects of Ministry of Education of the Czech Republic Nr. MSM 0021620855, the Charles University Grant Agency Nr. 8210 (to Václav Špillar), and the Czech Science Foundation Nr. 210/12/0986 (to David Dolejš). We would like to thank Michael Higgins, Bruce Marsh, and Michael Zieg for their constructive reviews that helped to improve the manuscript, and Marjorie Wilson for editorial handling.

2.8. References

AARNES I., PODLADCHIKOV Y. Y. & NEUMANN E.-R. (2008): Post-emplacement melt flow induced by thermal stress: Implications for differentiation in sills. – *Earth and Planetary Science Letters* 276, 152–166.

AMENTA R., EWING A., JENSEN A., ROBERTS S., STEVENS K., SUMMA M., WEAVER S. & WERTZ P. (2007): A modeling approach to understanding the role of microstructure development on crystal-size distributions and on recovering crystal-size distributions from thin slices. – *American Mineralogist* 92, 1936–1945.

AVRAMI M. (1939): Kinetics of phase change I. General theory. – *Journal of Chemical Physics* 7, 1103–1112.

AVRAMI M. (1940): Kinetics of phase change II. Transformation-time relation for random distribution of nuclei. – *Journal of Chemical Physics* 8, 211–224.

BINDEMAN I. N. (2003): Crystal sizes in evolving silicic magma chambers. – *Geology* 31, 367–370.

BOORMAN S., BOUDREAU A. & KRUGER F. J. (2004): The Lower Zone-Critical Zone transition of the Bushveld Complex: A quantitative textural study. – *Journal of Petrology* 45, 1209–235.

BOUDREAU A. & PHILPOTTS A. R. (2002): Quantitative modeling of compaction in the Holyoke flood basalt flow, Hartford Basin, Connecticut. – *Contributions to Mineralogy and Petrology* 144, 176–184.

CARSLAW H. S. & JAEGER J. C. (1959): *Conductions of heat in solids* (2nd ed.). – Oxford University Press, New York, 510 pp.

CASHMAN K. V. (1993): Relationship between plagioclase crystallization and cooling rate in basaltic melts. – *Contributions to Mineralogy and Petrology* 113, 126–142.

CASHMAN K. V. & MARSH B. D. (1988): Crystal size distribution (CSD) in rocks and the kinetics and dynamics of crystallization II: Makaopuhi lava lake. – *Contributions to Mineralogy and Petrology* 99, 292–305.

CHAMPALLIER R., BYSTRICKY M. & ARBARET L. (2008): Experimental investigation of magma rheology at 300 MPa: From pure hydrous melt to 76 vol. % of crystals. – *Earth and Planetary Science Letters* 267, 571–583.

COUCH S. (2003): Experimental investigation of crystallization kinetics in a haplogranite system. – *American Mineralogist* 88, 1471–1485.

DOUCE A. E. P. & JOHNSON A. D. (1991): Phase equilibria and melt productivity in the pelitic system: implications for the origin of peraluminous granitoids and aluminous granulites. – *Contributions to Mineralogy and Petrology* 107, 202–218.

DUFEK J. & BERGANTZ G. W. (2005): Lower crustal magma genesis and preservation: a stochastic framework for the evaluation of basalt-crust interaction. – *Journal of Petrology* 46, 2167–2195.

EBERL D. D., KILE D. E. & DRITS V. A. (2002): On geological interpretation of crystal size distributions: Constant vs. proportionate growth. – *American Mineralogist* 87, 1235–1241.

GHIORSO M. S. & SACK R. O. (1995): Chemical mass transfer in magmatic processes IV, A revised and internally consistent thermodynamic model for the interpolation and extrapolation of liquid-solid equilibria in magmatic systems at elevated temperatures and pressures. – *Contributions to Mineralogy and Petrology* 119, 197–212.

HAMMER J. E. (2008): Experimental studies of the kinetics and energetics of magma crystallization. – *Reviews in Mineralogy and Geochemistry* 69, 9–59.

HAMMER J. E. & RUTHERFORD M. J. (2002): An experimental study of the kinetics of decompression-induced crystallization in silicic melt. – *Journal of Geophysical Research* 107, 1–24.

HERSUM T. G. & MARSH B. D. (2006): Igneous microstructures from kinetic models of crystallization. – *Journal of Volcanology and Geothermal Research* 154, 34–47.

HERSUM T., HILPERT M. & MARSH B. D. (2005): Permeability and melt flow in simulated and natural partially molten basaltic magmas. – *Earth and Planetary Science Letters* 237, 798–814.

HIGGINS M. D. (2000): Measurement of crystal size distributions. – *American Mineralogist* 85, 1105–1116.

HIGGINS M. D. (2002a): A crystal size-distribution study of the Kiglapait layered mafic intrusion, Labrador, Canada: Evidence for textural coarsening. – *Contributions to Mineralogy and Petrology* 144, 314–330.

HIGGINS M. D. (2002b): Closure in crystal size distributions (CSD), verification of CSD calculations, and the significance of CSD fans. – *American Mineralogist* 87, 171–175.

HIGGINS M. D. (2006): *Quantitative textural measurements in igneous and metamorphic petrology*. – Cambridge University Press, Cambridge, 265 pp.

HIGGINS M. D. (2011): Textural coarsening in igneous rocks. – *International Geology Review* 53, 354–376.

HOLLAND T. & POWELL R. (2001): Calculation of phase relations involving haplogranitic melts using an internally consistent thermodynamic dataset. – *Journal of Petrology* 42, 673–683.

HORT M. & SPOHN T. (1991): Crystallization calculations for a binary melt cooling at constant rates of heat removal: Implications for the crystallization of magma bodies. – *Earth and Planetary Science Letters* 107, 463–474.

JAUPART C. & TAIT S. (1995): Dynamics of differentiation in magma reservoirs. – *Journal of Geophysical Research* 100, 17615–17636.

KILE D. E. & EBERL D. D. (2003): On the origin of size-dependent and size-independent crystal growth: Influence of advection and diffusion. – *American Mineralogist* 88, 1514–1521.

KIRKPATRICK J. R. (1976): Towards a kinetic model for the crystallization of magma bodies. – *Journal of Geophysical Research* 81, 2565–2571.

KIRKPATRICK R. J., ROBINSON R. G. & HAYS J. F. (1976): Kinetics of crystal growth from silicate melts: Anorthite and diopside. – *Journal of Geophysical Research* 81, 5715–5720.

KIRKPATRICK R. J., KLEIN L., UHLMANN D. R. & HAYS J. F. (1979): Rates and processes of crystal growth in the system anorthite-albite. – *Journal of Geophysical Research* 84, 3671–3676.

LASAGA A. C. (1998): *Kinetic Theory in the Earth Sciences*. – Princeton University Press, Princeton, 811 pp.

MANGAN M. T. (1990): Crystal size distribution systematics and the determination of magma storage times: The 1959 eruption of Kilauea volcano, Hawaii. – *Journal of Volcanology and Geothermal Research* 44, 295–302.

MARSH B. D. (1981): On the crystallinity, probability of occurrence, and rheology of lava and magma. – *Contributions to Mineralogy and Petrology* 78, 85–98.

MARSH B. D. (1988): Crystal size distributions (CSD) in rocks and the kinetics and dynamics of crystallization I. Theory. – *Contributions to Mineralogy and Petrology* 99, 277–291.

MARSH B. D. (1989): Magma chambers. – *Annual Review of Earth and Planetary Sciences* 17, 439–474.

MARSH B. D. (1998): On the interpretation of crystal size distributions in magmatic systems. – *Journal of Petrology* 39, 553-599.

MARSH B. D. (2002): Dynamics of magmatic systems. – *Elements* 2, 287–292.

MARSH B. D. (2007): Crystallization of silicate magmas deciphered using crystal size distributions. – *Journal of American Ceramic Society* 90, 746–757.

MCCABE W. L. (1929): Crystal growth in aqueous solutions. – *Industrial and Engineering Chemistry* 21, 30–33.

MOCK A. & JERRAM D. A. (2005): Crystal size distribution (CSD) in three dimensions: Insight from the 3D reconstruction of a highly porphyritic rhyolite. – *Journal of Petrology* 46, 1525–1541.

MOCK A., JERRAM D. A. & BREITKREUZ C. (2003): Using quantitative textural analysis to understand the emplacement of shallow-level rhyolitic laccoliths – A case study from the Halle volcanic complex, Germany. – *Journal of Petrology* 44, 833–849.

MUNCILL G. E. & LASAGA A. C. (1987): Crystal-growth kinetics of plagioclase in igneous systems: One-atmosphere experiments and applications of a simplified growth model. – *American Mineralogist* 72, 299–311.

MUNCILL G. E. & LASAGA A. C. (1988): Crystal-growth kinetics of plagioclase in igneous system: Isothermal H_2O-saturated experiments and extension of a growth model to complex silicate melts. – *American Mineralogist* 73, 982–992.

PETFORD N. (2003): Rheology of granitic magmas during ascent and emplacement. – *Annual Review of Earth and Planetary Sciences* 31, 399–427.

RANDOLPH A. D. & LARSON M. A. (1971): *Theory of Particulate Processes*. – Academic Press, New York, 251 pp.

RESMINI R. G. (1993): *Dynamics of magma within the crust: A study using crystal size distribution*. – Ph.D. dissertation, Johns Hopkins University, 329 pp.

RESMINI R. G. (2007): Modeling of crystal size distributions (CSDs) in sills. – *Journal of Volcanology and Geothermal Research* 161, 118–130.

SCHIAVI F., WALTE N. & KEPPLER H. (2009): First in situ observation of crystallization processes in a basaltic-andesitic melt with the moissanite cell. – *Geology* 37, 963–966.

SIMAKIN A. G. & BINDEMAN I. N. (2008): Evolution of crystal sizes in the series of dissolution and precipitation events in open magma systems. – *Journal of Volcanology and Geothermal Research* 17, 997–1010.

SWANSON S. E. (1977): Relation of nucleation and crystal-growth role to the development of granitic textures. – *American Mineralogist* 62, 966–978.

TAIT S. & JAUPART C. (1992): Compositional convection in a reactive crystalline mush and melt differentiation. – *Journal of Geophysical Research* 97, 6735–6756.

WATERS C. & BOUDREAU A. E. (1996): A reevaluation of crystal size distribution in chromite cumulates. – *American Mineralogist* 81, 1452–1459.

ZIEG M. J. & LOFGREN G. E. (2006): An experimental investigation of texture evolution during continuous cooling. – *Journal of Volcanology and Geothermal Research* 154, 74–88.

WILHELM S. & WÖRNER G. (1996): Crystal size distribution in Jurassic Ferrar flows and sills (Victoria Land, Antarctica): Evidence for processes of cooling, nucleation, and crystallisation. – *Contributions to Mineralogy and Petrology* 125, 1–15.

WHITTINGTON A. G., HOFMEISTER A. M. & NABELEK P. I. (2009): Temperature-dependent thermal diffusivity of the Earth's crust and implications for magmatism. – *Nature* 458, 319–321.

WYLLIE P. J. (1977): Crustal anatexis: An experimental review. – *Tectonophysics* 43, 41–71.

ZIEG M. J. & MARSH B.D. (2002): Crystal size distributions and scaling laws in the quantification of igneous textures. – *Journal of Petrology* 43, 85–101.

2.9. Appendices

2.9.1. Appendix 1: Relationship for the effective growth rate based on the 2nd moment of CSD

The crystallinity variations with time allow us to define an effective growth rate as a time-derivative of a linear grain size. This variable would, when summed over all grains, provide the same volume change of a solid phase, as is required by known change in the crystallinity. As noted by Resmini (2007), the growth rate must be inversely proportional to the total surface of all grains, represented by 2^{nd} moment of CSD. Let us consider a CSD in a volume-equivalent grain size measure (i.e., crystal size is defined as a linear dimension of a geometrical object with fixed shape, whose volume equals that of the crystal). Over any finite time interval, equality must exist between the real volume change of any grain and of the

corresponding geometrical object, whose linear size is considered as a size measure of a CSD. In the other words:

$$\left(\frac{\mathrm{d}V}{\mathrm{d}t}\right)^{\mathrm{GRAIN}} = \left(\frac{\mathrm{d}V}{\mathrm{d}t}\right)^{\mathrm{MODEL\ OBJECT}}, \tag{2.A.1}$$

where t stands for time. Inserting relationship between volume and linear size of a geometrical object of interest (Eqn. (2.9)) into Eqn. (2.A.1) and integrating over all grains in a unit volume, we obtain

$$\sum_{i \text{ over all grains}} \frac{\mathrm{d}V_i}{\mathrm{d}t} = 3\sigma_{\mathrm{CSD}} \cdot \int_0^{\infty} n(L) L^2 \left(\frac{\mathrm{d}L}{\mathrm{d}t}\right) \mathrm{d}L, \tag{2.A.2}$$

where $n(L)$ represents the CSD at some time t. Using the definition of effective growth rate (Eqn. (2.8)) and noting that the volume change of all crystals in a unit volume of the system is the increment of crystallinity Φ, we obtain the expression for effective growth rate:

$$G^{\mathrm{eff}}(t) = \left[6\sigma_{\mathrm{CSD}} \cdot \int_0^{\infty} n(L,t) L^2 \mathrm{d}L \right]^{-1} \cdot \frac{\mathrm{d}\Phi}{\mathrm{d}t}(t), \tag{2.A.3}$$

which is based on our volume-equivalent definition of the crystal size. The growth rate calculated from Eqn. (2.A.3) is used through our numerical implementation of the CSD inversion.

2.9.2. Appendix 2: Numerical calculation of effective rates of growth and nucleation

Our numerical methods for inversion of CSD employ conversions between ideal (nominal) and effective rates of crystal nucleation and growth (see Eqns. (2.7), (2.10), and

(2.13)), which require knowledge of actual crystallinity, Φ, or its time-derivative, dΦ/dt. Crystallinity Φ(t) at any time instant t during crystallization is evaluated from discrete Avrami equation, Eqn. (2.27). The time-derivative of crystallinity, however, cannot be directly calculated since, at any instant t, Φ(t') is only known for $t' \leq t$. Thus dΦ/dt must be approximated using backward difference scheme (recall that time t_i increases with decreasing index i of a time step). Using backward differences, the trapezoidal rule for integration involved in Eqn. (2.10), and the discretization of CSD described in the Section 2.3, we obtain the following numerical formula for the effective growth rate:

$$G_i^{\text{eff}} = \left[6\sigma_{CSD} \cdot \sum_{j=0}^{N-1} \frac{n_j j^2 + n_{j+1}\left(j+1\right)^2}{2} \left(\Delta L\right)^3 \right]^{-1} \cdot \frac{\Phi_i - \Phi_{i+1}}{t_i - t_{i+1}}, \quad i \in \left\{0 \ldots N-1\right\}. \qquad (2.A.4)$$

At the beginning of calculation, that is, at $i = N$, quantities with $i + 1$ indices are undefined and the above formula cannot be evaluated, but the effective growth rate is constrained by initial conditions $G_N^{\text{eff}} = G_N$, because crystallinity is zero.

2.9.3. Appendix 3: Slope-intercept relationship for log-linear CSDs

As shown by Marsh (1998) or Higgins (2002b), slopes b and intercepts n_0 of straight log-linear CSDs are not independent but are related to crystallinity, Φ, by mass-balance constraints. For the volume-equivalent measure of the grain size, crystallinity is related to the 3rd moment of CSD as follows:

$$\Phi = \sigma_{\text{CSD}} \int_0^{\infty} L^3 n\left(L\right) \mathrm{d}L, \qquad (2.A.5)$$

where $n(L)$ is the population density at size L and σ_{CSD} is a shape factor (see Section 2.2). Note that different measures of the grain size such as maximum length would lead to different formulas that are generally less straightforward.

For straight log-linear CSDs, the integral in Eqn. (2.A.5) can be evaluated analytically to yield the following slope-intercept relationship,

$$4\ln(-b) = \ln\frac{6\sigma_{CSD}}{\Phi} + \ln n_0. \tag{2.A.6}$$

This equation is similar to Eqn. (73) of Marsh (1998) but here we adopt volume-equivalent measure of the grain size, which, in addition, allows us to obtain numerical values for all parameters involved in his Eqn. (73) and it yields analytical relationship between the slope and intercept of the CSD.

Preface to Chapter 3

Computational method for the inversion of crystal size distribution, CSD, (Chapter 2) has revealed that the extraction of nucleation and growth rates from the CSDs is non-unique unless additional constraints are considered. In order to explore other textural parameters than CSDs and their response to various nucleation and growth rates we developed a new three-dimensional forward crystallization model. We derive size, spatial, and contact parameters of textures resulting from crystallization by homogeneous nucleation and growth of crystals in a closed system. This approach has revealed that some textural descriptors are correlated while others are sensitive to crystallization processes other than homogeneous nucleation and growth (e.g., heterogeneous nucleation or mechanical accumulation of crystals).

This chapter was published as **ŠPILLAR, V**. & DOLEJŠ, D. (2014): *Kinetic model of nucleation and growth in silicate melts: implications for igneous textures and their quantitative description.* – ***Geochimica et Cosmochimica Acta*** *131, 164–183*. The manuscript was formatted to conform to general layout of this thesis.

Chapter 3.

Kinetic model of nucleation and growth in silicate melts: Implications for igneous textures and their quantitative description

3.0. Abstract

We present a new high-resolution numerical model for the simulation of crystallization and texture evolution using arbitrary rates of crystal nucleation and growth. The algorithm models single or multiphase solidification in a three-dimensional domain and 17 simulations using constant, linearly increasing, exponential, and Gaussian functions for the rates of nucleation and growth yield equigranular to seriate textures. Conventional crystal size distributions of all textures are nearly linear to concave-down (previously interpreted as formed by equilibration coarsening), and identical distribution patterns can result from multiple non-unique combinations of nucleation and growth rates. The clustering index is always a non-monotonous function, which initially increases then decreases with increasing crystal fraction. For texture from random homogeneous nucleation the index is substantially lower than previous predictions based on a random sphere distribution line, hence, natural samples interpreted as clustered now have greater degrees of randomness or ordering. The average number of contact neighbors and the average neighbor distance of a crystal depend linearly on crystal size, but one of the two remains insensitive to nucleation and growth kinetics and represents potential indicator of other crystallization processes than random nucleation and crystal growth. Simultaneous comparison of size, spatial and clustering patterns and of their departures from expected values are suggested to allow for separation of

effects of crystallization kinetics, melt-mineral mechanical interactions, suspension mixing, or postcrystallization re-equilibration and coarsening on natural igneous rocks.

Key words:

Crystal nucleation; growth; crystallization kinetics; texture description; crystal size distribution.

3.1. Introduction

Igneous textures provide an overall and time-integrated record of various processes that occurred during magma solidification. Crystallization dominantly involves nucleation of new crystals and growth of existing ones, with possible modifications arising from their mechanical motion or other interactions, as well as coarsening and annealing (Cashman & Marsh, 1988; Marsh, 1998; Higgins, 2011). These processes, acting in response to cooling, thermodynamic and other driving forces, control the evolution of crystallinity and crystallization rate, as well as sizes and mutual configurations of individual crystals (e.g., Cabane et al., 2005; Hammer, 2008). Crystallinity and geometry of the crystal framework, in turn, dictate the rheological behavior of magma or permeability of the framework for percolating melt or fluid (Hoover et al., 2001; Hersum et al., 2005; Walsh & Saar, 2008). These properties are crucial for models of magma differentiation, mechanical transport, and style of emplacement or eruption to the surface (e.g., Gerya & Burg, 2007; Bachmann and Bergantz, 2008; Annen, 2009; Verhoeven & Schmalzl, 2009; Bea, 2010).

Direct observations of crystallization processes in nature are inherently rare and limited to shallow-level systems, for example those in the Hawaiian lava lakes (Cashman & Marsh, 1988). Likewise, experimental studies allowing *in-situ* observation of crystallization are instrumentally difficult and sparse (Means & Park, 1994; Schiavi et al., 2009). Therefore, computational modeling of magma crystallization provides important insights into the transient evolution of texture and its properties during crystallization (Elliott et al., 1997;

Hersum & Marsh, 2006; Amenta et al., 2007). In addition, numerical models offer a tool to individually assess the effects of individual crystallization processes and their rates on the final rock texture.

The three-dimensional numerical model of crystallization of Hersum & Marsh (2006) used a cubic magma volume discretized into a large number of volume elements (voxels), where individual crystals grow by successive incorporation of adjacent voxels. These authors employed the rate of growth coupled with a predefined crystallinity function *via* the Avrami equation (Avrami, 1939, 1940; Lasaga, 1998; Marsh, 1998) in order to maintain self-consistency with the rate of nucleation. As noted by Amenta et al. (2007), such an approach results in artificial behavior if performed in discrete time steps. They used explicit rates of nucleation and growth to simulate crystallization by successive addition of virtual lattice units to individual crystals. Despite these efforts, discrete three-dimensional models of crystallization remain computationally expensive and provide only a rough approximation to continuous nucleation, growth, and impingement processes. Spatial resolution at affordable computational cost is limited, which introduces significant statistical noise into resulting textures. On the other hand, simple analytical models of crystallization based on the Avrami theory (e.g., Avrami, 1939, 1940; see Marsh, 1998) are useful in estimating the evolution of crystallinity and crystal size, but otherwise provide only limited characterization of resulting textures.

There are a number of quantitative parameters for the description of natural and synthetic textures, in particular, parameters characterizing the size, shape, spatial, and contact parameters of the crystal assembly in both 2D and 3D. Crystal size distribution (CSD; Randolph & Larson, 1971; Cashman & Marsh, 1988; Marsh, 1998; Higgins, 2006) is commonly used to assess sizes of crystals in the crystal population (e.g., Higgins, 2006; Morgan & Jerram 2006). The CSD itself cannot account for the spatial distribution, e.g., aggregation *vs*. spatial ordering of crystals, or for crystal shape variations resulting from space competition among adjacent grains, which require additional measurements (e.g., Jerram et al., 1996, 2003; Jerram & Cheadle 2000; Rudge et al., 2008). The use of synthetic/modeled textures involving single or multiple solid phases can be used to explore, define and evaluate

new distribution parameters, and to calibrate their dependencies and sensitivity to individual kinetic factors.

In this paper, we develop a new computational model for the simulation of crystal nucleation and growth in a three-dimensional melt volume. Our strategy uses the discrete voxel method (e.g., Hersum & Marsh, 2006) to characterize the grain-grain contacts, but the grain-melt interfaces are tracked continuously. The model, therefore, accurately characterizes the continuous nucleation, growth, and impingement of crystals, while it only requires moderate computational resources. High spatial resolution also affords accurate quantitative description of the resulting grain population aiming at identification of optimal and practical quantitative parameters that would augment current CSD methods applied to natural magmatic rocks.

We employ the model to explore the effects of various evolutionary trends of the nucleation and growth rates on the resulting texture, CSD, shape, contact, and spatial distribution patterns. Using our simulations we constrain the kinetic models that are consistent with natural igneous textures and point to ambiguities in current CSD interpretations. Subsequently, we calibrate variability or invariance of various properties of simulated textures in order to identify parameters sensitive to other processes active during magma solidification, e.g., mechanical crystal-melt interactions, heterogeneous nucleation, or coarsening of crystals.

3.2. Kinetic model

3.2.1. Computational implementation

The model is based on the voxel method (Hersum & Marsh, 2006) but it is modified to minimize the effects of discretization. We use a mixed discretized-continuous representation (Fig. 3.1a), with a simulation domain discretized into a large number of volume elements (voxels). Crystallization in the simulation domain is treated as progressive homogeneous and

heterogeneous nucleation of new grains and growth of preexisting grains, performed in short discrete time steps. Crystal faces propagating to the melt are tracked continuously, as is the position and orientation of all crystal nuclei and centers.

Initially, all voxels are occupied by melt phase. As crystallization proceeds, each voxel is progressively assigned a label of the solid crystal that first reaches the center of that voxel. Using this procedure, individual voxels are progressively transformed from melt to the respective solid phase. In our computational implementation, up to fifteen different solid phases can simultaneously crystallize in the simulation domain. At any stage, individual grains, when completely surrounded by melt (i.e., they do not impinge on each other), are arbitrary six-sided parallelepipeds, whose shape and orientation is described by three pairs of orthogonal vectors that represent growth rate vectors in three dimensions. The crystal face (grain-melt interface) is tracked as a plane that advances in the direction of its normal vector during each time step. Grain-grain interfaces are recorded when two adjacent voxels are assigned to different grains; the location of the voxel interface represents a grain boundary (Fig. 3.1a). This approach allows us to represent the final texture discretely, whereas distances of unimpinged crystal faces from the nucleation centers are continuous functions of time; hence, discretization artifacts are minimized. Similarly, locations and orientations of crystals are treated as real-value accurate values. Our simulation algorithm, named VoxelTex, performs high-resolution simulations with approximately 100 million voxels, 1200×1200

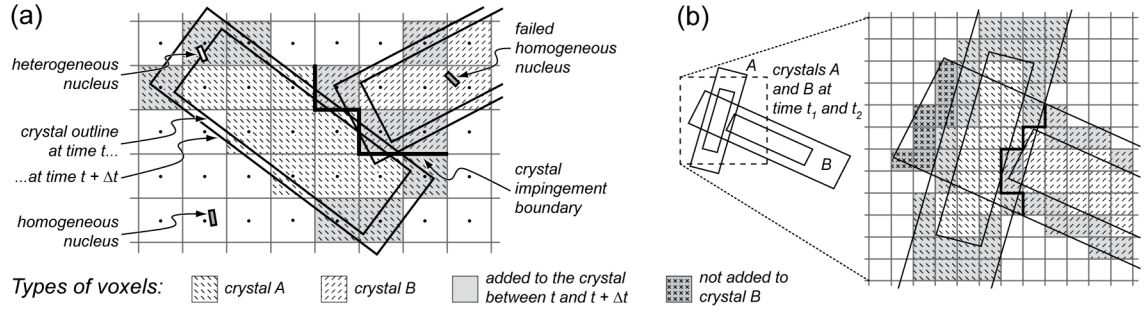

Fig. 3.1. *Two-dimensional analogy of the discrete-continuous texture representation used in the simulation algorithm. Voxels added to both crystals between time t and t + Δt are shown in gray color.* **(a)** *nucleation and growth over a short discrete time step; dots mark centers of the voxels;* **(b)** *illustration of the "continuity condition" applied to the addition of new voxels to the crystals. Voxels the positions of which fall within the boundary of crystal B but which are not added to the crystal B are indicated.*

pixel sections, and about 100 thousand grains. Runs on a 3.2 GHz PC as a single thread achieve full crystallinity in roughly 10 minutes with the requirement of 2 GB RAM memory.

3.2.1.1. Crystal nucleation

The algorithm employs homogeneous or heterogeneous nucleation of new crystals or a combination of both. The number of nuclei produced by homogeneous nucleation, N_{hm}^{0}, during each time step, results from the instantaneous nucleation rate, $I(t)$, and the length of the time step, Δt, as follows:

$$N_{\mathrm{hm}}^{0} = I\left(t\right) V \Delta t, \tag{3.1}$$

where V is the volume of the simulation domain. N_{hm}^{0} is generally a fractional number due to the rational nature of all variables in the product in Eqn. 3.1. In order to transform the rational number of nuclei predicted from the nucleation rate into an integer value we use the following rounding procedure: first, a number of nuclei corresponding to the integer part of N_{hm}^{0} is created, then the last nucleus is created with the probability equal to the fractional part of N_{hm}^{0}. This reflects the stochastic nature of nucleation and ensures that the correct number of nuclei is used.

Locations of the homogeneous nuclei are generated as random points inside the entire simulation domain. From all N_{hm}^{0} nuclei predicted, only those located in the melt region (N_{hm}) are considered as real nuclei. The decision for acceptance or rejection of a nucleus uses continuous (undiscretized) description of grain size, orientation and location of all crystals, and is, thus, precise and independent of discretization (Fig. 3.1a). This approach ensures that the nucleation rate per unit melt volume exactly follows the prescribed rate function. The actual number of nuclei formed in the entire simulation domain is, thus, implicitly scaled down as the available melt fraction decreases.

By contrast, heterogeneous nucleation takes places on pre-existing solid-melt interfaces. The rate of heterogeneous nucleation, $H(t)$, has the dimension of the number of

nuclei per unit area of the solid-melt interface and unit time. The number of heterogeneous nuclei formed at an arbitrary time step, N_{ht}^{0}, is obtained for each crystal face from the heterogeneous nucleation rate $H(t)$ for that crystal face:

$$N_{\mathrm{ht}}^{0} = H\left(t\right) S \Delta t, \tag{3.2}$$

where S is the total area of the crystal face, in which heterogeneous nucleation is considered, and Δt is the duration of the time step. The rational value of N_{ht}^{0} is rounded to an integer number using the same procedure as for the homogeneous nucleation, and locations of heterogeneous nuclei are determined as random points on the crystal face. Similar to homogeneous nucleation, only those heterogeneous nuclei, which are located outside of all other existing grains, are considered as real nuclei (Fig. 3.1a). The heterogeneous nucleation rate can be varied with time during crystallization, and it can be specific for each nucleation solid phase and for each solid phase on which nucleation occurs. To simulate different surface properties of faces with different crystallographic orientation, the heterogeneous nucleation rate can also differ for each face of the parent crystal. Additionally, the rate of heterogeneous nucleation can vary from crystal to crystal, thus reflecting possible spatial variations of intensive thermodynamic parameters due to formation of melt boundary layers.

When a homogeneous or heterogeneous nucleus is formed, we assign it an arbitrary random orientation in space. Grain orientation is described *via* three mutually perpendicular random unit vectors, $\boldsymbol{a}$, $\boldsymbol{b}$, and $\boldsymbol{c}$ that represent directions normal to the crystal faces. First, vector $\boldsymbol{a}$ with random distribution on a unit sphere is calculated using inverse transform sampling (e.g., Devroye, 1986). Vector $\boldsymbol{b}$ is then determined as a random unit vector perpendicular to $\boldsymbol{a}$. Lastly, vector $\boldsymbol{c}$ is calculated to be perpendicular to both $\boldsymbol{a}$ and $\boldsymbol{b}$. Two opposite candidates for vector $\boldsymbol{c}$ exist and an arbitrary one can be chosen, as grain orientation is invariant to swapping of $\boldsymbol{c}$ and $-\boldsymbol{c}$.

Wherever random numbers appear in our calculations, we always employ the Mersenne-Twister random number generator (Matsumoto & Nishimura, 1998) that provides high uniformity and randomness of the generated number distribution.

3.2.1.2. Crystal growth and boundary conditions of the simulation

During each time step, all crystal faces advance by a distance D according to current growth rate, $G(t)$, in direction of their normal vector:

$$D = G(t)\,\Delta t, \tag{3.3}$$

where Δt is the duration of the time step. Distinct rates of growth for each of the orthogonal crystal faces will produce tabular or prismatic grains. After positions of all crystal faces have been updated, the centers of all melt voxels are tested if they were not included in a solid phase. When the voxel is consumed by a growing grain, it is marked as part of it (Fig. 3.1a). When the center of the voxel that already belongs to crystal A is crossed by the advancing face of crystal B, its identity is not changed and it remains part of crystal A. That is, already solid crystals do not penetrate each other. The side of the parallelepiped, which represents the face of crystal B, however, continues to advance. After the virtual face leaves crystal A on its opposite side, it starts to consume melt voxels again (Fig. 3.1b); crystal B effectively grows through crystal A. To prevent crystals from growing through each other by this mechanism, a voxel becomes part of the grain only if at least one of its neighboring voxels already belongs to the same grain (Hersum & Marsh, 2006). As neighboring voxels we consider those sharing a face, edge, or corner (twenty-six neighbors are possible, in total). This condition is not applied to the voxel containing the nucleus itself and to its neighbors, because it would prevent initiation of growth after nucleation.

Duration of each time step, Δt, is set adaptively, to ensure that all crystal faces in the simulation advance by no more than a distance D_{max}, related to the voxel edge length. In our simulations, D_{max} was set to 1/10 of the voxel edge length. If desired, the growth rate can vary from crystal to crystal, thus simulating possible spatial variations of intensive thermodynamic parameters due to the formation of melt boundary layers or other transient processes.

Periodic boundary conditions are prescribed at all boundaries of the simulation domain. Crystals growing out of the domain through its sides appear as crystals growing into the domain on the opposite side. As a consequence, edge effects are minimized, that is, the

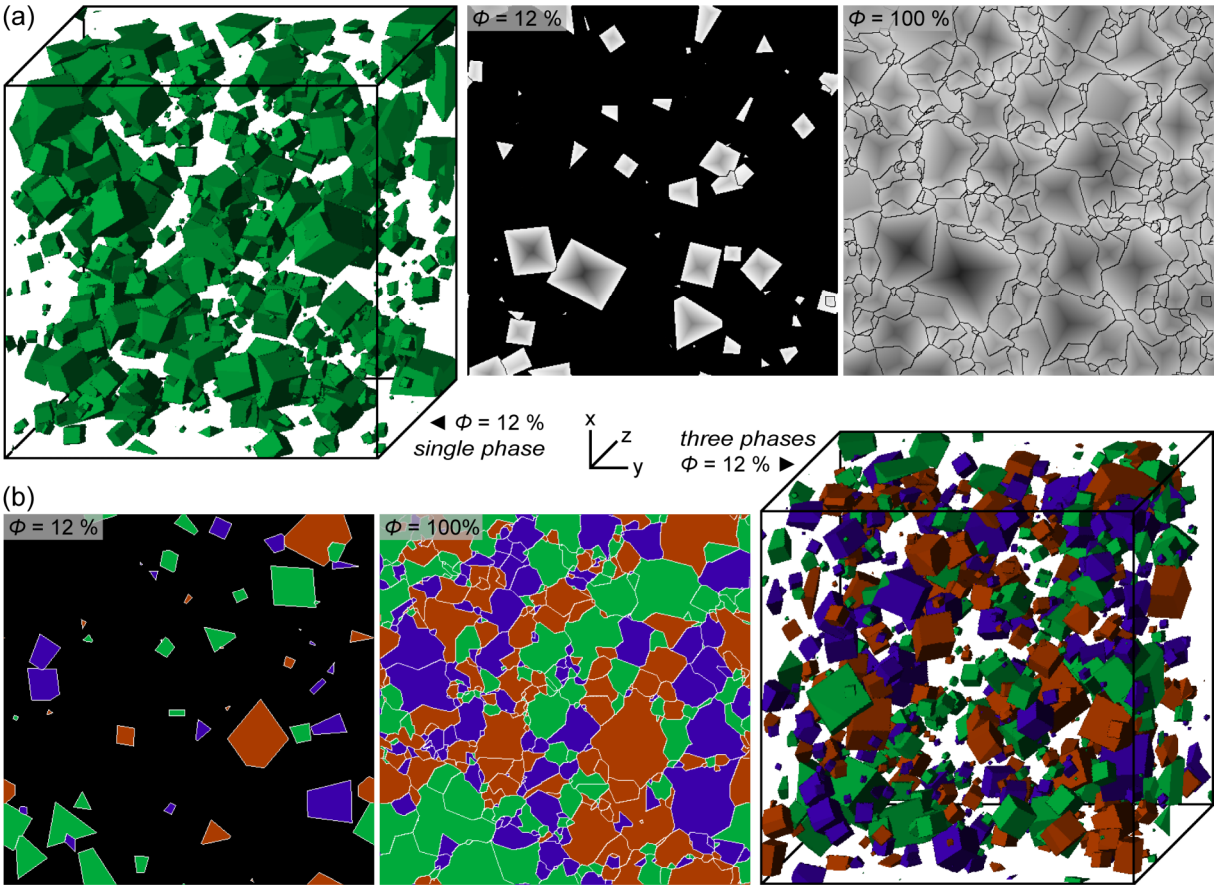

Fig. 3.2. *Simulation domain and its two-dimensional x-y sections. Example of texture evolution using exponentially increasing nucleation and constant growth rates.* **(a)** *single crystallizing phase.* **(b)** *three phases, distinguished by color, crystallizing simultaneously with same kinetics. Symbol Φ denotes crystallinity, i.e., volume per cent of all solid phases. In the plane sections, shades of gray indicate growth zoning.*

crystal number density is not lowered due to proximity to the domain boundary. Three-dimensional snapshots and two-dimensional sections of progressive crystallization are illustrated in Fig. 3.2.

3.2.1.3. Domain sectioning

All textures have been simulated in three dimensions; but in order to facilitate comparison with natural petrographic samples, we visualize and quantify them in two-dimensional sections as well. The distribution data from natural petrographic samples are almost exclusively two-dimensional (e.g., Higgins, 2000, 2002a, 2006; Mock et al., 2003; Boorman et al., 2004; Yang, 2012) and their transformation into three dimensions using

stereological methods is non-unique and approximate only (e.g., Higgins, 2000, 2006; Mock & Jerram, 2005; Morgan & Jerram, 2006; Jaret et al., 2008). To eliminate this ambiguity and the need for introducing conversion approximations, we use an additional set of apparent two-dimensional parameters that characterize the resulting texture in a two-dimensional section through the simulation box, which then allows direct comparison with conventional petrographic observations.

The simulation box is sectioned by an *x*-*y* plane, and the domain resolution in the *z*-direction is increased in its vicinity to increase accuracy. In our simulations, sections were sampled at half height of the simulation box in order to reduce any boundary effects. Ambiguous solutions arise when several grains are intergrown such that one grain appears as multiple isolated fragments in the section. Two general solutions are possible: (*i*) fragments are re-classified as independent grains, or (*ii*) fragments are labeled as belonging to one discontinuously intersected grain. The first approach tends to overestimate the number of grains, i.e., the nucleation rate, and underestimate the grain size, i.e., the growth rate, but it enables uniform comparison with natural samples. The second method does not affect interpretation of rates and has been used in this study. In routine petrographic work, chadocrysts of a single crystal can usually be identified from corresponding orientations of optical indicatrices and this guarantees complete correspondence between petrographic observations and our simulations.

3.2.2. Quantitative description of crystal populations

We employ scalar and functional parameters to quantitatively characterize the simulated texture. Scalar parameters are single values that characterize the entire crystal population (e.g., number of crystals per unit volume, average crystal size, etc.). Functional parameters, on the other hand, are a set of values that describe the functional dependence of two quantities. This can be either frequency distribution (e.g., crystal size distribution, CSD) or the dependence of two properties on each other (e.g., dependence of crystal axial ratio on

crystal size). In the calculations of functional parameters, we employ binning methods and use ten equally-sized bins of the independent variable.

3.2.2.1. Crystal sizes and volumes

A simple first-order measure of the overall grain size is provided by the number of grains in a unit area. In a two-dimensional section of area A through a simulation domain, a certain number of crystals is entirely present in the section (N_{tot}), whereas others are intersected by the boundary of the studied area (N_{part}). In the estimate of the crystal number, σ_{A}, we count crystals on the boundary as halves:

$$\sigma_{\mathrm{A}} = \frac{N_{\mathrm{tot}} + 0.5 N_{\mathrm{part}}}{A}. \tag{3.4}$$

By taking the 3/2 power of σ_{A}, the crystal number can be dimensionally converted to the approximate number of crystals per unit volume, whose reciprocal value provides a mean volume of the crystal. Mean crystal volume can be converted to the linear size if some uniform shape of all crystals is assumed. For simplicity we assume spherical shapes of all crystals here, but an arbitrary three-dimensional shape can be used and the resulting linear size would differ by the shape factor only. For an average three dimensional crystal size, $L_{\mathrm{3D}}^{\mathrm{mean}}$, it immediately follows from the volume of the sphere:

$$L_{\mathrm{3D}}^{\mathrm{mean}} = \left(\frac{6}{\pi}\right)^{\frac{1}{3}} \left(\sigma_{\mathrm{A}}\right)^{-\frac{1}{2}}. \tag{3.5}$$

In order to obtain the conventional crystal size distribution (*cf.* Cashman & Marsh, 1988; Cashman, 1993; Marsh, 1998; Higgins, 2002a; Mock et al., 2003; Bindeman, 2003; Boorman et al., 2004; Simakin & Bindeman, 2008), we use the three-dimensional simulation results directly. Volume of each crystal is measured as the number of voxels, N_{V}, that belong to the crystal. Linear three-dimensional size of the crystal, L_{3D}, is then calculated as a diameter of equal-volume sphere according to:

$$L_{3D} = 2L_V \cdot \sqrt[3]{\frac{3}{4}\frac{N_V}{\pi}}, \tag{3.6}$$

where L_V is the edge length of the voxel. The resulting population density, n, and its dependence on crystal size, L_{3D}, represents a true distribution of three-dimensional crystal sizes, which does not suffer from any two- to three-dimensional conversion effects (e.g., Higgins, 2000; Mock & Jerram, 2005). Other definitions of three-dimensional crystal size include the long axis of the crystal (the length of the longest inscribed line; e.g., Higgins, 2006; Jerram et al., 2009). However, the present procedure appears to be more robust, less sensitive to crystal shape variations, and less affected by statistical fluctuations. The estimate based on the size of the equivalent-volume sphere will be preferred here to maintain consistency with our previous study (Špillar & Dolejš, 2013).

The calculated CSDs are nearly linear to concave-down curves. Linear CSDs are conveniently characterized by the slope, b_{3D}, fitted to a relationship between logarithm of the population density, n, and crystal size, L_{3D}.

In two-dimensional sections, we introduce apparent grain size, L_{2D}, as the diameter of a circle with an area equal to that of the grain cross-section in the section of interest:

$$L_{2D} = 2L_V \cdot \sqrt{\frac{N_P}{\pi}}, \tag{3.7}$$

where L_V is the edge length of the voxel and N_P is a number of pixels that belong to the crystal in the section of interest. Note that sections are generally taken in one of the directions parallel to the sides of the voxels. That is, the edge length of the voxel and that of the pixel are equal. As most of the measurements on natural igneous textures come from two-dimensional data, we have also constructed CSDs from L_{2D} crystal sizes. Slopes of linear CSDs obtained from two-dimensional data are denoted as b_{2D}. Other ways of defining the crystal size in two-dimensional section are discussed by Higgins (2006) and are based on the longest dimension of a crystal, dimensions of the best fit ellipses, etc. We, however, prefer the equal area-based methods due to its simplicity and stability to variations in the crystal shape.

The overall appearance of the texture is related to the distribution of volume (or mass) of crystals per size class. To remain compatible with easily retrievable data from rock sections, we have calculated area distributions based on L_{2D} crystal sizes. Two-dimensional area distributions can still be compared to the true three-dimensional distributions of volumes based on the L_{3D} crystal size (e.g., Jerram et al., 2009). The range of crystal sizes is divided into regular bins, and the area of crystals is summed up in each bin. The ratio of the accumulated area to the total area of the section equals the modal fraction of crystals that pertain to the given size bin. The grain size with the highest modal fraction is denoted as the most voluminous grain size, L_{2D}^{vol}.

3.2.2.2. Crystal shape

Grain shape is a combined result of (*i*) habits of freely growing euhedral crystals as a function of any anisotropy in its growth rates, and (*ii*) truncations due to impingement on other grains. In addition, in two dimensions, orientation and location of the section influence the apparent crystal shape. Various methods for describing the shape of crystals are given in the metallographical and stereological literature to quantitatively describe and separate between elongation, irregularity, and other aspects of the grain shape (e.g., Kurzydłowski & Ralph, 1995, p. 257; Wojnar, 1999, p. 193). As grain shapes are not too complex in our simulated textures we only use a simple measure of the elongation of crystals. For each grain in a two-dimensional section, we define a rectangle of the smallest area and arbitrary orientation that can be circumscribed to the cross-section of the grain. The edge length ratio of this circumscribed rectangle, α, is used to represent the apparent axial ratio of the grain (e.g., Higgins, 2006; Wojnar, 1999, p. 193). An isotropic unimpinged crystal habit, that is, spherical cross-sections, have the axial ratio of unity. Random sections of a cube yield axial ratios greater than one, as some of the sections are elongated. Impingement, as a random process, does not occur symmetrically around a crystal and, therefore, progressively increases the axial ratio above unity. Distribution of apparent axial ratios and apparent axial ratio as a function of the crystal size are used here as additional quantitative measure of texture appearance.

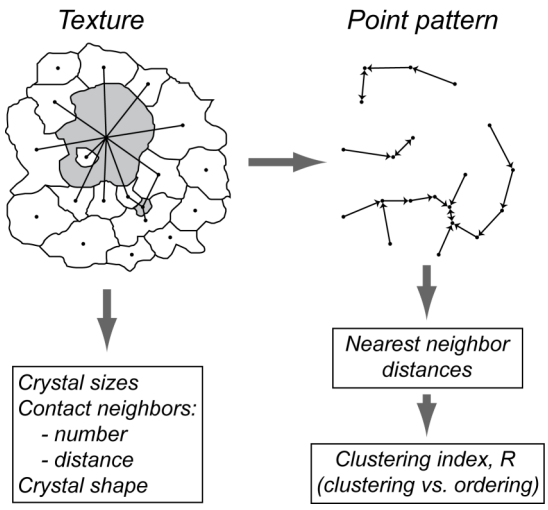

Fig. 3.3. *Reduction of the simulated texture to a point pattern. In a texture, two random grains with different sizes and their contact neighbors are highlighted. In a point pattern, the nearest neighbors are indicated by arrows.*

3.2.2.3. Contact relationships

Grains that share a common boundary in a two-dimensional section are considered as contact neighbors. The number of contact neighbors of the crystal, η, is a non-negative integer number (Fig. 3.3). Each grain can, thus, have none, one, or more neighbors; a grain completely surrounded by melt has no neighbor ($\eta = 0$). Such grains can exist only if the crystal fraction in the texture is less than 100 %. A chadocryst totally enclosed in an oikocryst has one neighbor ($\eta = 1$; inclusion). It is expected that η varies with grain size, L_{2D}, because larger crystals, on average, have more neighbors, as their perimeter in section is longer. The value of η also depends on the density of nuclei; therefore, nucleation and growth rate histories are recorded in the variations of neighbor number distribution and in the variations of η as a function of crystal size.

The crystal-to-crystal distance, defined as the distance between nucleation centers, cannot be measured directly because (*i*) locations of nucleation centers are unknown in natural samples, and (*ii*) nucleation centers are distributed in a three-dimensional space and do not generally lie in a section plane. Following the approach common in point pattern analysis (e.g., Rudge et al., 2008), we use centers of mass of the crystals (in two dimensions) and define the distance of crystals as the distance of their respective centers. Average neighbor

distance, ρ, is an arithmetic mean of neighbor distances evaluated over all neighbors of the crystal of interest (Fig. 3.3). Similar to η, the value of ρ is evaluated as a function of the grain size, L_{2D}. The nearest neighbor distance cannot be (when ignoring inclusions) less than the sum of the smallest dimensions of the two neighbors and it generally increases with the grain size; additional variations reflect the history of the nucleation and growth rates. In our simulations, all parameters are only evaluated for those grains that were entirely located in the two-dimensional sections; grains that are trimmed by edges of the simulation volume were not considered.

3.2.2.4. Spatial distribution of crystals

Spatial relationships of crystals provide additional information on the crystallization process, in particular on the mechanism of crystal nucleation, physical interactions of individual crystals, or on crystal framework formation (e.g., Jerram et al., 1996; Hirsch et al., 2000; Rudge et al., 2008). They can be measured within an individual phase or by looking at multiple phases (e.g., Jerram & Cheadle, 2000). Here, we adopt an approach common in spatial distribution analysis and describe crystals in two-dimensional section by their centers of mass (e.g., Rudge et al., 2008). The resulting point pattern (Fig. 3.3) is then analyzed to discriminate between a random distribution, clustering, or ordering of points/crystals. A simple method to discriminate between these types of spatial distribution, called the *R*-value technique, was introduced to geology by Kretz (1966, 1969) and Jerram et al. (1996). It compares the mean value of all distances of the nearest neighbors in a point pattern with its expected value for perfectly random distribution of points. The value of *R* is defined as a ratio:

$$R = \frac{R_A}{R_E}, \tag{3.8}$$

where R_A is the average distance to the nearest neighbor measured in the point pattern, and R_E is a value expected for randomly distributed points. The expected value of R_E depends on the

number of points in the point pattern, N, and on the area of the point pattern, A (e.g., Kretz, 1966):

$$R_E = \frac{1}{2 \cdot \sqrt{\frac{N}{A}}}. \tag{3.9}$$

From the definition (Eqn. 3.8), $R = 1$ indicates a random distribution of points, for $R < 1$ points are clustered, and $R > 1$ indicates ordering of points.

As noted by Jerram et al. (1996), $R = 1$ is an appropriate reference for a random distribution of points only. Crystals have finite sizes and cannot be as close to each other as infinitely small points could be. As a consequence, a random distribution of crystals must have $R > 1$ and an appropriate reference model for the random distribution of crystals as a function of their modal fraction must be constructed. Based on the packing of equally-sized spheres, Jerram et al. (1996) proposed a random sphere distribution line, RSDL, as a reference for the random distribution of crystals, to which we will compare our results from random nucleation and growth textures. These authors also modeled the texture variations away from the random reference line of equal-sized spheres due to crystal growth, compaction, and due to variations in size sorting.

Practical calculation of the R value is complicated by the edge effect. This arises from the fact that the point pattern is studied on a finite area. Crystals near the boundary, thus, may lack their nearest neighbors that are located outside of the observation window, which biases R towards higher values. To correct for the edge effect, we use an empirical correction after Donnelly (1978), which is implemented in the "Spatstat" library (Baddeley & Turner, 2005) of the R statistical programming language (R Development Core Team, 2011). Due to the large number of crystals present in our simulated textures, the magnitude of the correction is less than 0.02 of R-value in more than 90 % of the data points.

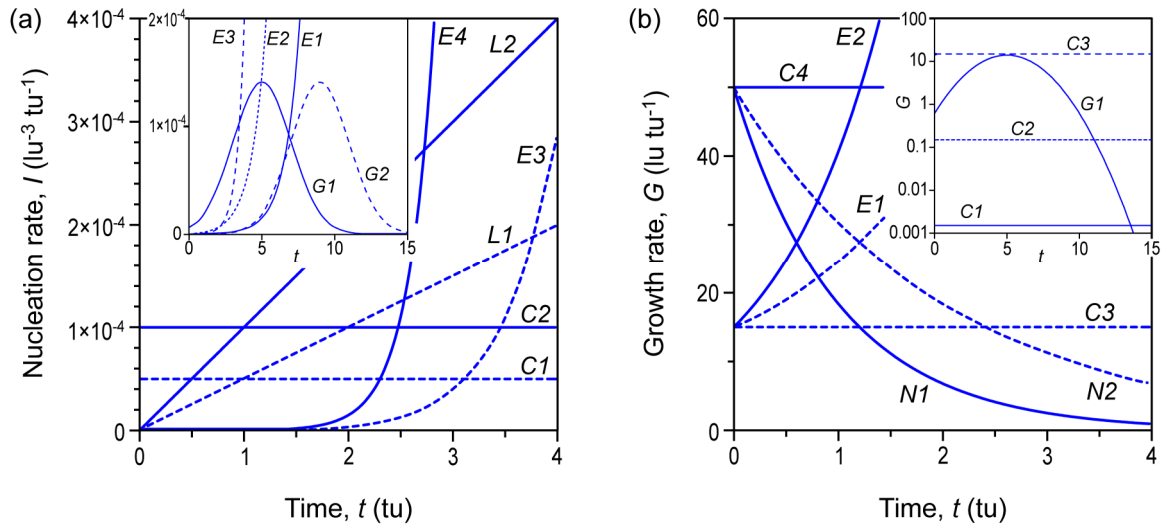

Fig. 3.4. *Nucleation* **(a)** *and growth* **(b)** *rate functions used in the simulations (see Tab 3.1 for equations and naming convention). Note the log scale of the vertical axis in the inset in part (a). Symbols lu and tu are arbitrary length and time units, respectively.*

Tab. 3.1. *Nucleation and growth rate functions used in simulations.*

Nucleation rate *I*(*t*)		**Growth rate *G*(*t*)**	
Labeling	**Equation**	**Labeling**	**Equation**
C1	5×10^{-5}	C1	0.0015
C2	10×10^{-5}	C2	0.15
L1	$5\times10^{-5}\cdot t$	C3	15
L2	$10\times10^{-5}\cdot t$	C4	50
E1	$1\times10^{-7}\cdot e^{t}-1\times10^{-7}$	E1	$15\cdot e^{t/2}$
E2	$1\times10^{-6}\cdot e^{t}-1\times10^{-6}$	E2	$15\cdot e^{t}$
E3	$1\times10^{-7}\cdot e^{2t}-1\times10^{-7}$	N1	$50\cdot e^{-t}$
E4	$5\times10^{-9}\cdot e^{4t}-5\times10^{-9}$	N2	$50\cdot e^{-t/2}$
G1	$\frac{5\times10^{-4}}{\sqrt{4\pi}}\cdot e^{\frac{-(t-5)^2}{8}}$	G1	$\frac{50}{2\sqrt{\pi}}\cdot e^{\frac{-(t-5)^2}{8}}$
G2	$\frac{5\times10^{-4}}{\sqrt{4\pi}}\cdot e^{\frac{-(t-9)^2}{8}}$		

Units for the nucleation rate are $lu^{-3}\ tu^{-1}$, units for the growth rate are $lu\ tu^{-1}$, where tu is an arbitrary time unit and lu is an arbitrary length unit, *t* stands for time. Symbols C, L, E, N, and G in the label of equations denote constant, linear, exponential, negative exponential, and Gaussian functions, respectively, and all rate functions are shown in Fig. 3.4. Simulations are labeled by the nucleation rate followed by the growth rate (e.g., simulation C1C3 uses the nucleation rate function C1 and the growth rate function C3).

3.3. Methodology

We have explored variability of textures and textural parameters by performing three-dimensional simulations with various nucleation and growth rate functions. Following experimental and theoretical studies (e.g., Lasaga, 1998; Marsh, 1998; Burkhard, 2002; Bindeman, 2003; Hersum & Marsh, 2006; Amenta et al., 2007), we use simple monotonous (constant, linear, positive and negative exponential) or Gaussian functional forms to characterize the temporal evolution of the nucleation and growth rates. Such functions approximate effects of constant or increasing undercooling, or depletion of interstitial melt, or provide an approximation to increasing undercooling followed by quenching (Lasaga, 1998).

Rate functions used in our simulations are defined in Tab. 3.1, shown in Fig. 3.4, and all simulations are listed in Tab. 3.2. Most rate functions were chosen to be within an order of magnitude in order to produce textures with comparable grain size. To explore scaling, on the other hand, three additional simulations with rates differing by several orders of magnitude were also performed (Tab. 3.2). All simulations were conducted in a three-dimensional simulation box with ~80 million voxels. Textural analysis was carried out on 1200 × 1200 pixel two-dimensional sections through the center of the simulation domain. Sections contain few hundreds to few thousands complete grains (i.e., grains not intersected by the domain boundary; Tab. 3.2), which ensures statistical reproducibility of our results. For simplicity, all simulations were performed with a single crystal phase (one-component system), although extension to multiphase population is straightforward. This treatment is strictly applicable to magmas crystallizing one phase only, or to multicomponent polyphase systems where nucleation and growth rates of different phases are similar. All crystals are assumed to have isotropic growth rates in three dimensions, that is, euhedral shape is a cube with six mutually perpendicular faces advancing at equal rate. The growth rate is considered to be independent of crystal size. Size-dependent growth or growth rate dispersion (e.g., Eberl et al., 2002), however, are easy to implement in future modifications.

Textural variations observed in our models result from the variation of the rates of nucleation and growth. Simulated textures must be considered as purely kinetic end members

with no involvement of texture coarsening or mechanical sorting (e.g., Higgins, 2011). While these effects can be incorporated into future models of texture evolution, simulations of simple kinetic textures provide an important reference for comparison with natural examples, where departures may point to mechanical effects, textural coarsening, or other processes.

Tab. 3.2. *List of textural simulations.*

Group	Nucleation rate	Growth rate	Section edge length [lu]	Number of grains in 2D section		σ_A [lu^{-2}]	L_{3D}^{mean} [lu]	L_{2D}^{vol} [lu]
				Complete	Incomplete			
Constant nucleation	C1	C3	1200	2916	263	0.00212	21.74	26.97
	C1	E1	1200	2529	241	0.00184	23.31	28.92
	C1	E2	1200	2339	227	0.00170	24.23	30.06
	C1	N1	1200	1867	206	0.00137	27.04	33.54
	C1	N2	1200	1694	217	0.00125	28.26	35.07
	C2	C3	1200	4170	311	0.00300	18.25	22.63
Linear nucleation	L1	C3	1200	2900	240	0.00210	21.84	27.09
	L2	C3	1200	3807	274	0.00274	19.11	23.71
Exponential nucleation	E1	C1	0.3	3003	205	34505	0.0054	0.0067
	E1	C2	30	2867	199	3.2961	0.5508	0.6834
	E2	C2	30	2966	239	3.4283	0.5401	0.6701
	E3	C3	1200	2095	221	0.00153	25.55	31.70
	E3	C4	1200	282	80	0.00022	66.87	82.97
	E4	C3	1200	7592	363	0.00540	13.61	16.89
	E4	C4	1200	686	102	0.00051	44.20	54.84
Gaussian rates	G1	G1	1200	5038	345	0.00362	16.62	20.63
	G2	G1	1200	1447	185	0.00107	30.58	37.95

The σ_A is area density of crystals as defined in Eqn. 3.4. Grains are considered to be incomplete if truncated by the boundary of the simulation domain. The L_{3D}^{mean} is a mean crystal size based on the crystal volume density, L_{2D}^{vol} is the most voluminous grain size. Units lu are arbitrary length units.

3.4. Results

3.4.1. Texture description

Simulated textures range from equigranular to seriate, and their representative examples are shown in Fig. 3.5 (for all textures, see Electronic Appendix 3.1). A simple combination of constant rates of nucleation and growth (simulation C1C3) leads to an equigranular texture (Fig. 3.5a). If the growth rate is allowed to decrease (C1N1) or the nucleation rate is increased (L1C3) in the course of crystallization, smaller interstitial grains begin to appear in the texture, which acquires a more seriate appearance (Fig. 3.5b, c). Finally, an exponential increase of the nucleation rate combined with constant growth rate (E4C3) leads to few large (old) crystals surrounded by many smaller (younger) interstitial grains and results in a seriate texture (Fig. 3.5d). Gaussian rate functions (simulations G1G1, G2G1) produce seriate textures similar to those formed by linearly increasing nucleation or exponentially decreasing growth rate (Fig. 3.5b, c). We have compared two cases of the Gaussian rate functions: (*i*) both rates reach their maxima at the same time (Fig. 3.5e), or (*ii*) the maximum in the nucleation rate is delayed and occurs after a decline of the growth rate (Fig. 3.5f), which simulates the nucleation lag known from the crystallization experiments (e.g., Fokin et al., 2006, 2008). The latter scenario produces a more coarse-grained texture because of the small number of nuclei.

Tab. 3.2 summarizes characteristic area densities of crystals and grain sizes. Area densities of crystals and mean crystal sizes in simulated textures depend more on the growth rate than on the nucleation rate. For instance, a twofold increase in the nucleation rate (from C1 to C2, or from L1 to L2), while keeping the growth rate constant, reduces grain size by about 15 % only. On the other hand, scaling of the growth rate scales the crystal size by a

► **Fig. 3.5.** *Two-dimensional sections through representative simulated textures. Width of each image corresponds to 600 length units and each snapshot covers ¼ of the area of simulated section. For all textures, see Electronic Appendix 3.1.*

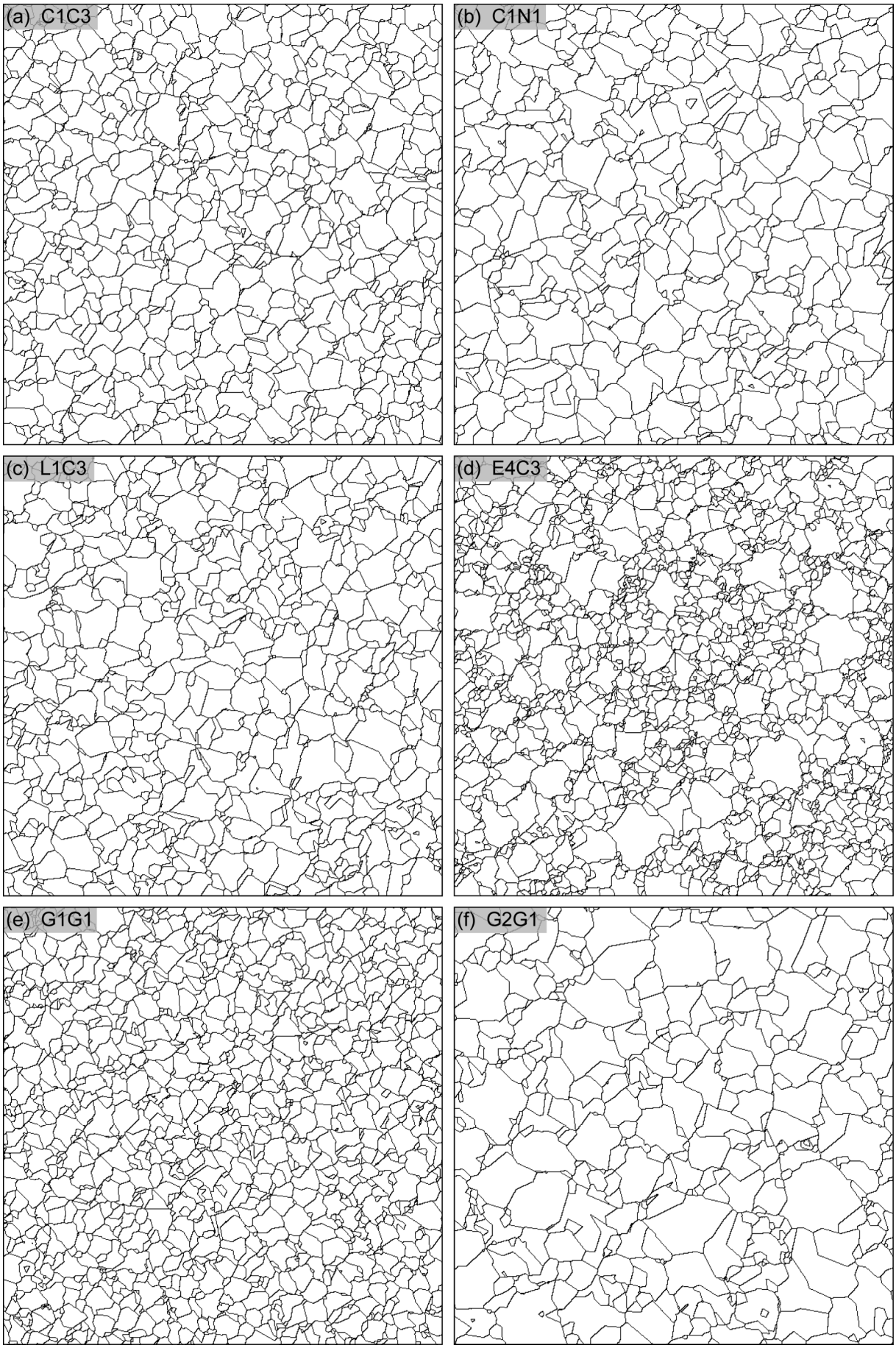
(a) C1C3
(b) C1N1
(c) L1C3
(d) E4C3
(e) G1G1
(f) G2G1

comparable factor (e.g., simulation E3C3 *vs*. E3C4). This effect results from the dimensional difference between the rates of nucleation and growth with respect to one-dimensional crystal size.

3.4.2. Crystal size and volume distribution

The crystal size distributions (CSDs) from our simulations are almost straight to concave down curves in the logarithm of the population density *vs*. crystal size diagram (Fig. 3.6). For all monotonous rate functions, the curvature of CSD reduces as the nucleation rate increases or the growth rate decreases more rapidly with time. We distinguish two classes of CSDs among our results: (*i*) straight CSDs with only minute decrease in the population density observed at smallest crystal sizes. Apart from this grain size segment, straight CSDs are well approximated by a linear relationship between the logarithm of the population density and crystal size; (*ii*) concave-down CSDs where curvature is distributed over all crystal sizes.

For simulations with exponential nucleation and constant growth rates, the resulting CSDs are straight. Depletion of the population density in smallest crystal sizes is in qualitative agreement with theoretical predictions using approximate solutions (*cf.* Marsh, 1998), but our model predicts a lesser extent of depletion. Straight parts of the CSDs result from rapid (exponential) increase of the number of new grains with time. In the final stages of crystallization, the decrease in the population density of small crystals occurs due to the shrinkage of melt volume available for nucleation. We neglect the concave-down lower end and parameterize the entire straight CSD by the respective values of the slope and the intercept. At any volume fraction of crystals in the system, the slope and the intercept of straight CSDs are related by the mass balance constraints (e.g., Marsh, 1998; Higgins, 2002b). Slopes of the straight CSDs depend on the rate functions (Tab. 3.3). Higher growth rate enables crystals to grow larger, thus reducing the slope, whereas steeply increasing nucleation rate leads to larger crystal numbers, that is it increases the CSD slope. A similar relationship

applies to both b_{2D} and b_{3D} slopes derived from apparent two-dimensional and true three-dimensional crystal sizes, respectively.

Combinations of monotonous rate functions other than those with the exponential nucleation rate and the constant growth rate yield concave-down CSDs. Textures resulting from the Gaussian rate functions also exhibit concave- down CSDs. Consistent with the

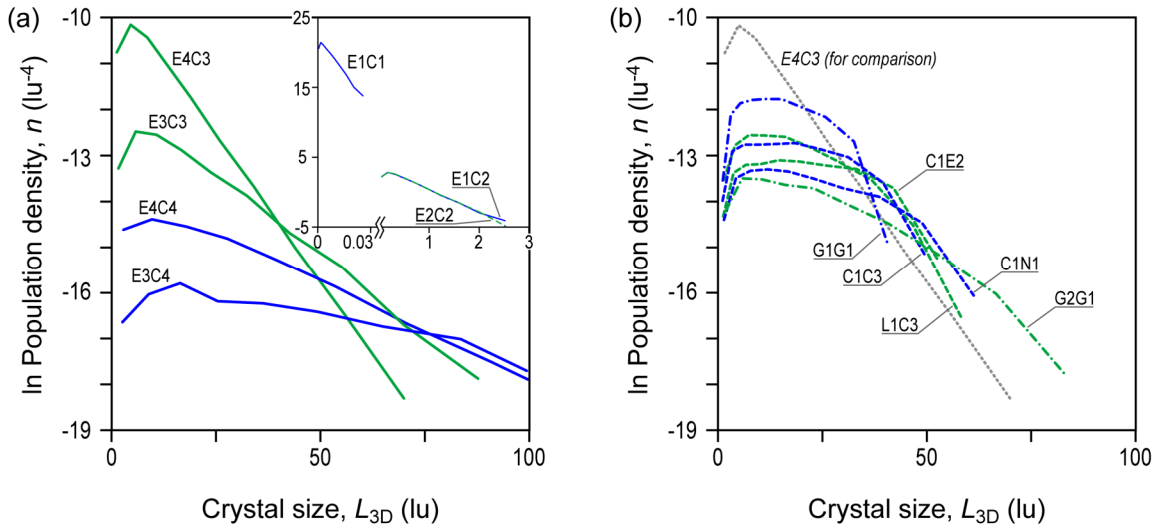

Fig. 3.6. *Representative crystal size distributions derived from the volume data. Symbol L_{3D} is a true crystal size calculated as a diameter of equal-volume sphere.*

Tab. 3.3. *Slopes of the straight CSDs.*

Nucleation rate	Growth rate	b_{2D}	b_{3D}
E1	C1	-332	-248
E1	C2	-3.09	-2.44
E2	C2	-3.28	-2.43
E3	C3	-0.067	-0.053
E3	C4	-0.024	-0.018
E4	C3	-0.126	-0.099
E4	C4	-0.043	-0.032

The b_{2D} is a slope of a CSD calculated based on the apparent crystal size in two-dimensional sections, L_{2D}; the b_{3D} is calculated from the volume data and uses L_{3D} as a true crystal size. Both slopes are calculated from the natural logarithm of the population density, n, in lu^{-4}, where lu is an arbitrary length unit. The smallest crystal sizes (smallest size class) are omitted from the regression. Note the close correlation between b_{2D} and b_{3D}.

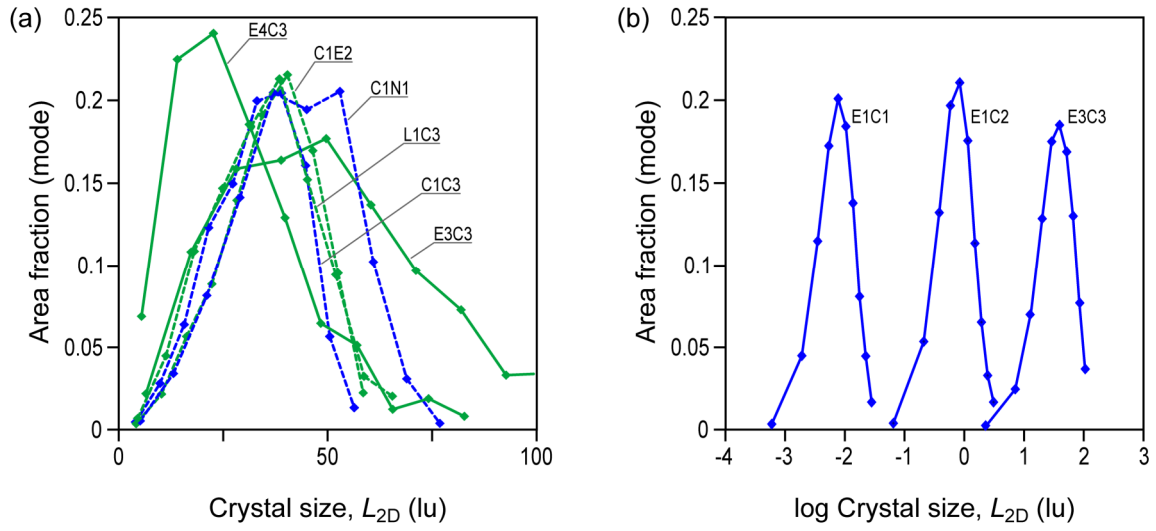

Fig. 3.7. *Representative apparent volume distributions in two-dimensional sections for* **(a)** *simulations with similar characteristic grain size, and* **(b)** *simulations with remarkably different characteristic grain size and straight CSDs only. Area fraction (mode) is for each size class.*

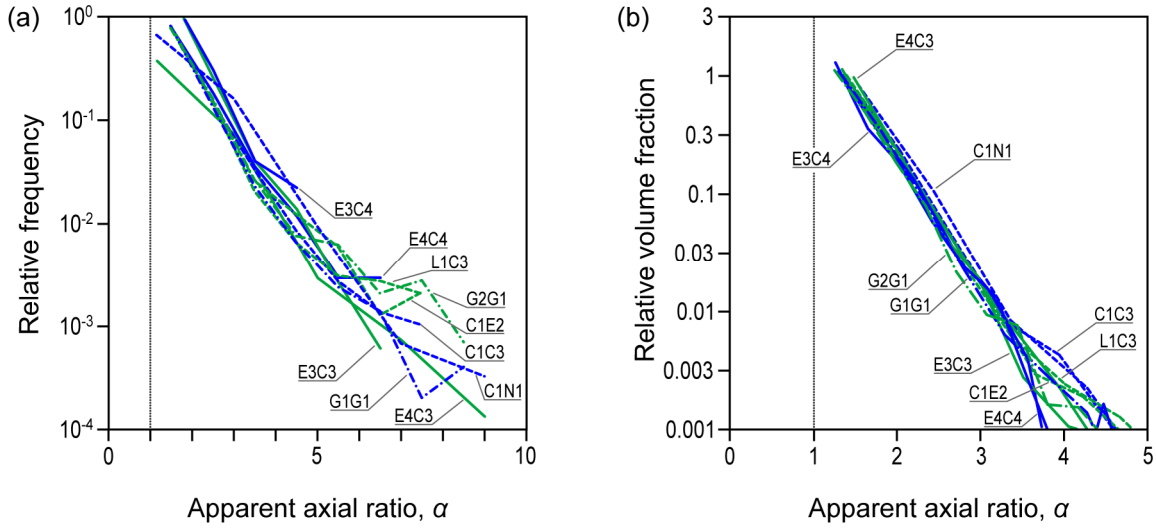

Fig. 3.8. *Apparent axial ratio, α, of crystals in two-dimensional sections. Frequency* **(a)** *and volumetric* **(b)** *distribution of α. All curves are density distribution functions.*

numerical results of Lasaga (1998), our simulations show that the curvature of CSDs is reduced when the time difference between peaks of the Gaussian nucleation rate and the Gaussian growth rate becomes greater (simulation G1G1 *vs.* G2G1). For all performed simulations, crystal size distributions by area fraction are bell-shaped curves with single,

variably broad maxima (Fig. 3.7a). That is, a certain crystal size is the most abundant one, by area (volume). Such a most abundant crystal size exists even in cases where the CSD is straight, without any maximum in the number density of crystals. In cases with constant or linear nucleation rate, volume distributions are almost perfectly symmetrical, which is consistent with the qualitative observation of more or less equigranular texture. Exponential nucleation, on the other hand, leads to the volume distribution being skewed to the left, where most of the volume is concentrated in smaller crystals. Larger phenocryst-like grains contribute to seriate appearance of these textures. When plotted on the *log* crystal size *vs.* modal fraction diagram (Fig. 3.7b), the left-skewed distributions become symmetrical and they only shift along the logarithmic size axis when the kinetic functions and corresponding CSDs are varied.

In our approach, we have considered the distributions by area as a proxy for the true volume distributions. A reversed approach, that is construction of a 3D distribution from 2D measurements, is often applied in interpretations of natural samples. This procedure includes estimate of the most representative three-dimensional crystal shape from the long and short axes of the crystals in the section (using the CSDslice algorithm; Morgan & Jerram, 2006), and the representative shape is then employed in the CSDcorrections software (Higgins, 2000) in order to derive an approximation of the true CSD. As our 3D simulations and 2D sections are directly corresponding and self-consistent, we can evaluate the applicability and accuracy of the above procedure. Our 2D *vs*. 3D distributions are well comparable, in agreement with the results of a previous study (Jerram et al., 2009). The reconstructed 3D distributions are significantly biased towards higher population densities for the smallest crystal sizes. Furthermore, because the true crystal sizes are always greater than or equal to the size of any of their two-dimensional sections, the 2D and 3D datasets differ slightly in the grain size leading to a consistent relative shift of approximately 10 length units; an analogous feature is expected to occur in reconstructed 3D distributions for natural samples.

3.4.3. Crystal shape

All simulations use growth rates that are constant for all crystal faces, and a euhedral unimpinged crystal would, therefore, acquire a cubic shape. Variation of the apparent axial ratio, α, thus results purely from impingement processes during crystal growth and from the cut-section effects.

The apparent axial ratio values range from unity to ~10 in our simulations (Fig. 3.8). High ratios, however, are scarce, as their frequency decreases exponentially (Fig. 3.8a). Distributions of axial ratio are rather similar for all studied textures and form a narrow band in the *log* frequency *vs.* axial ratio space. Similarly, the distribution of volume of crystals by its axial ratio decreases with the axial ratio, as most of the volume consists of isometric crystals, and this is in agreement with visual appearance of our simulated textures (Fig. 3.5).

The apparent axial ratios observed in two-dimensional sections can be used to reconstruct the representative crystal shape in three dimensions using the CSDslice algorithm (Morgan & Jerram, 2006). Since the growth shape of the crystals is known, this approach provides internal verification of the crystal shape reconstruction. Remarkably, the predicted crystal shapes are weakly prismatic with representative axial ratios of 1:1:1.8 (simulation E3C3) or 1:1:1.6 (simulation G1G1), respectively, which is in contrast to the cubic growth shape of all crystals. The crystal shapes, however, were estimated with a poor goodness-of-fit parameter, $R^2 \approx 0.65$, with the CSDslice procedure. This results from a large effect of crystal impingement, which obscures the primary growth shape. The indirect estimation procedures of the crystal shape are, thus, more meaningful for phenocryst populations as opposed to crystal aggregates.

Analysis of the axial ratios of crystal populations (Fig. 3.9a) allows us to define a general relationship between the crystal size and its axial ratio. On average, small crystals tend to be more elongate with $\alpha \approx 2$ and the average axial ratio decreases with increasing crystal size (Fig. 3.9). Small crystals are formed generally late; thus, their growth is more constrained by surrounding pre-existing crystals, which changes their axial ratios to higher values. The relationship between the axial ratio and the crystal size, however, depends on the

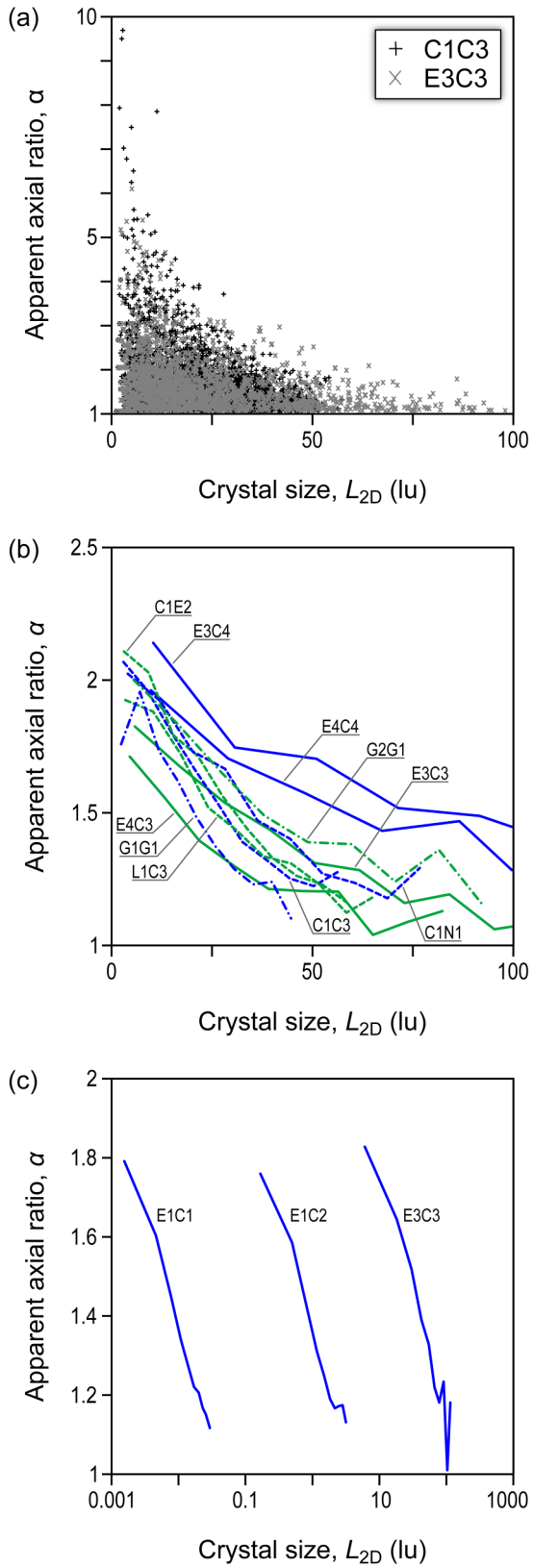

◄ **Fig. 3.9.** *Two-dimensional crystal size, L_{2D}, and apparent axial ratio, α.* **(a)** *entire crystal population from the simulations C1C3 and E3C3. Dependence of α on apparent crystal size, L_{2D}, for simulations with similar* **(b)** *and different* **(c)** *characteristic grain size.*

rates of nucleation and growth, and its slope generally reflects the overall crystal size of the texture (e.g., G1G1 *vs.* E3C3; Fig. 3.9b). Dependencies of the α-ratio on the crystal size for

simulations with different length scales but with straight CSDs are compared in Fig. 3.9c. The shapes of these curves remain invariant and they only shift along the size axis as the overall crystal size changes by several orders of magnitude for the slopes of the corresponding CSD from ~ -300 to ~ -0.1 lu^{-1}.

3.4.4. Contact relationships

The number of contact neighbors of a crystal, η, ranges from one to about 15-30 in two-dimensional sections through simulated textures (Fig. 3.10c). The frequency distributions of neighbor numbers are similar for all textures, with η between 3 and 5 being the most frequent number of neighbors. Individual neighbor numbers depend on the crystal size, L_{2D}, because larger crystals tend to be, on average, in contact with more neighbors as documented by a nearly linear increase of η with L_{2D} (Fig. 3.10a). The curves of η *vs*. L_{2D} are characterized by different slopes for different textures; however, when projected towards zero crystal size they share a common intercept. The slope is related to overall grain size, thus more fine-grained textures (with greater slope of their CSD) are characterized by greater slope of their η *vs*. L_{2D} relationship (*cf*. E3C4 *vs*. E4C3 in Fig. 3.10a). Higher nucleation rate or lower growth rate, therefore, produce textures with greater slopes in the η *vs*. L_{2D} relationship.

The average neighbor distance, ρ, for a crystal has a bell-shaped frequency distribution with a pronounced maximum (Fig. 3.10d). For more coarse-grained textures (with shallower CSD slopes), the position of the maximum shifts towards higher distances and its amplitude decreases (*cf*. E3E4 *vs*. E4C3). This results from the fact that crystals cannot be closer to each other than their respective sizes allow. Average neighbor distance, thus, depends on the parent crystal size, L_{2D}, and this dependence is almost linear (Fig. 3.10b). Among different textures, the intercepts of the ρ *vs*. L_{2D} curves vary, but the slopes remain the same.

Crystals with just one neighbor (η = 1) are considered to be inclusions in a host grain, but some of them are only incidental cross-sections appearing as inclusions in the two-dimensional section. In our simulated textures, inclusions are rare and the fraction of crystals

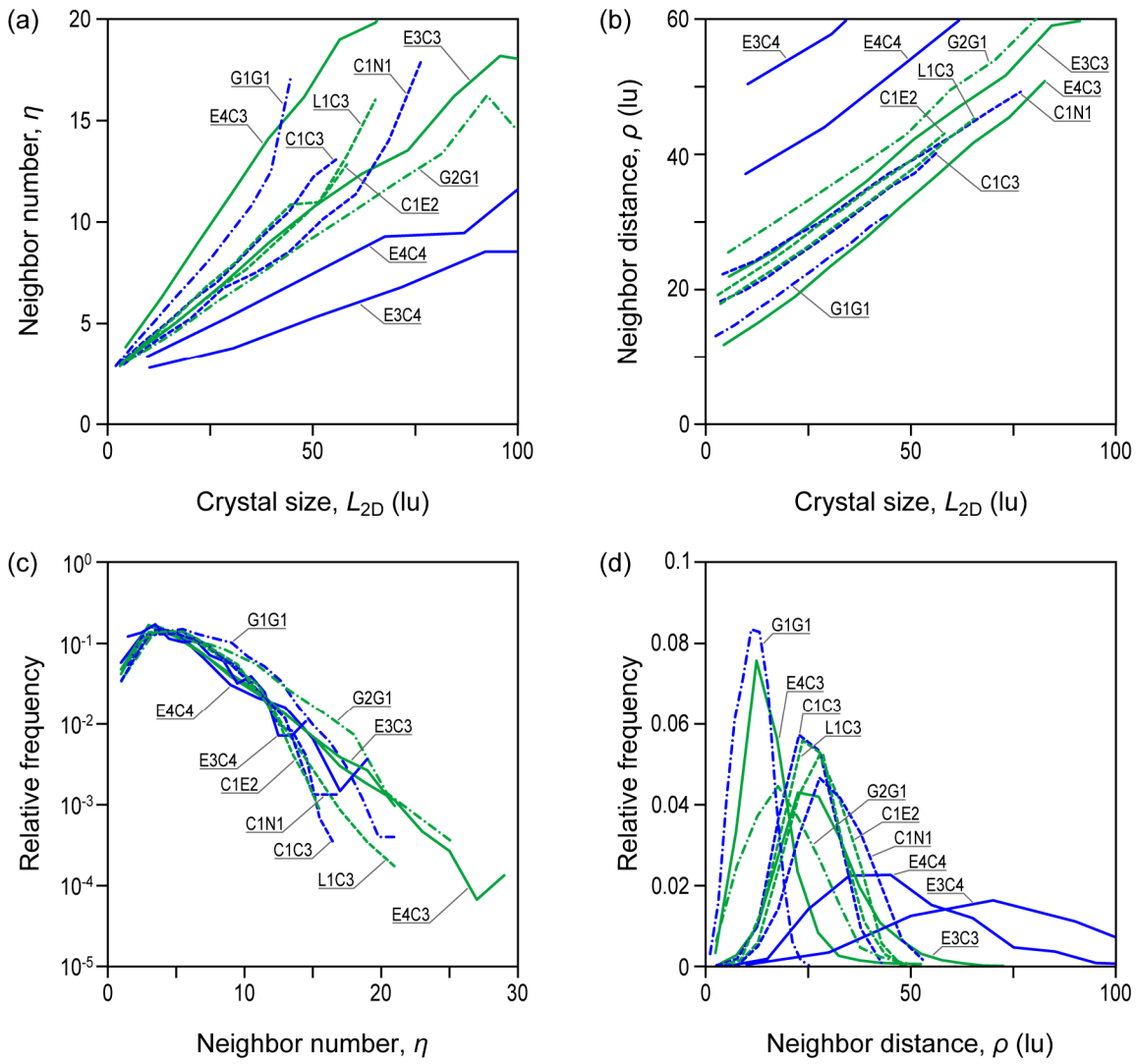

Fig. 3.10. *Contact relationships of crystals in a two-dimensional section. Relationship between the number* **(a)** *or distance* **(b)** *of contact neighbors and the crystal size, L_{2D}. Frequency distribution of neighbor number* **(c)** *and of neighbor distance* **(d)**.

having an inclusion is generally as low as 1/40 to 1/400. Both simulations with the Gaussian rates (G1G1 and G2G1) have the least number of inclusions (1/340 or 1/400 inclusion-bearing grains). On the other hand, mineral inclusions are most frequent in textures originating from exponential nucleation, where the fraction of crystals with inclusions is between 1/40 and 1/160, and it does not correlate with the slope of the CSD. Due to the general scarcity of inclusions, multiple inclusions in a single grain are so rare that their numbers cannot be evaluated with statistical confidence.

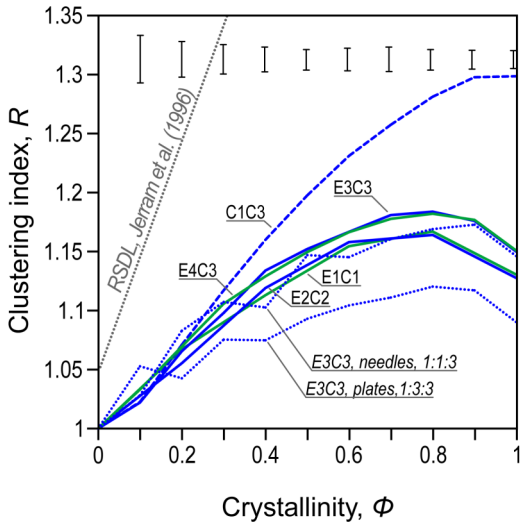

Fig. 3.11. *Clustering index, R, as a function of crystallinity for textures with straight CSDs and for a texture with constant rates of nucleation and growth (C1C3). Simulations of crystallization of needles and plates with aspect ratios of 1:1:3 and 1:3:3, respectively, are shown for comparison. Each simulation, except for those with needles and plates, was repeated 10 or 20 times, and the results were averaged to obtain more accurate trends. Error bars are 1σ values from averaging over multiple simulations and do not apply to needles and plates. The RSDL is the random sphere distribution line of Jerram et al. (1996).*

3.4.5. Spatial distribution pattern

We use the centers of mass of crystals to evaluate the degree of random distribution, clustering, or ordering of crystals *via* the clustering index, R (e.g., Kretz, 1966, 1969; Jerram et al., 1996). In Fig. 3.11, the value of R and its evolution during crystallization is shown for selected textures. At the limit of zero crystallinity, the clustering index converges to $R = 1$ in all simulated textures. In this case, crystals do not constrain positions of each other; thus, the value of R must be equal to that for a hypothetical random distribution of points. With increasing crystallinity, R generally increases because any new crystal cannot nucleate where a preexisting one is already present. Crystal centers, thus, become more distant from each other than expected for the random distribution of points, and this is also so where divergence between the individual textures appears. The texture originating from the constant rates of nucleation and growth (C1C3) evolves towards higher values of R when compared to the

textures from exponential nucleation and constant growth rate (e.g., E1C1). In contrast to C1C3, all cases with exponential nucleation lead to a reversal in R and, after reaching the maximum value of ~1.18 at about 80 % crystallinity (Φ) its value drops to 1.13-1.15 at complete solidification. The trend of increasing ordering is reversed due to the large number of small crystals being distributed randomly in the interstitial space.

Textures with straight CSDs, i.e., resulting from various exponential nucleation rates, are characterized by mutually similar trends in the R *vs*. Φ space where they define a narrow band no wider than ~0.02 of the R-value. The dispersion between the individual textures remains small in spite of the differences by nearly four orders of magnitude in the slope of their respective CSDs. For each kinetic model, the trend of the R-value with respect to Φ defines a random texture. Values of R above this trend indicate ordering of crystals, whereas lower values indicate clustering. Note that the trends of R for all simulated textures are located well below the random sphere distribution line of Jerram et al. (1996). Such deviation is expected as simulated textures contain a distribution of sizes and are not made of equally sized spheres as considered by Jerram et al. (1996). The trends of crystal growth at low to moderate crystallinities are also similar to those modeled by Jerram et al. (1996).

3.5. Discussion

3.5.1. Characteristic grain size

Grain size is one of the most important and traditionally employed parameters for the characterization of igneous textures (e.g., Cross et al., 1906; Teuscher, 1933; Niggli, 1954; Le Maitre, 2002). However, CSDs in many igneous rocks are almost straight in logarithm of the population density *vs*. crystal size projection (e.g., Cashman & Marsh, 1988; Wilhelm & Wörner, 1996; Marsh, 1998; Higgins, 2002b; Zieg & Marsh, 2002) implying that the number of grains increases exponentially with decreasing crystal size. Thus, an arithmetic average of grain size is not a statistically valid measure of the grain size. Instead, approaches based on

higher statistical moments of the CSD (e.g., Marsh, 1988) can provide such a measure. We suggest that a grain size appearing dominant to the observer as well as being constrained statistically is that with the most significant volume (or area) fraction in the sample. Our simulated textures show that the crystal volume distributions, in contrast to conventional CSDs, are all unimodal with a well-defined maximum; thus, the most voluminous and visually dominant grain size can be determined (Fig. 3.7). In addition, the most voluminous grain size, L_{2D}^{vol}, correlates with the mean grain size, L_{3D}^{mean}, as calculated from the area density of crystals (Fig. 3.12). The most voluminous grain size can, thus, be approximated by this simple approach. This also lends support to the visual definition of the grain size and assures consistency with the instrumental or computational estimates.

3.5.2. Straight log-linear and curved CSDs

Numerical simulations of crystallization help recognize possible trends of the nucleation and growth rates that produce straight CSDs similar to those found in many natural igneous rocks (e.g., Cashman & Marsh, 1988; Wilhelm & Wörner, 1996; Marsh, 1998; Higgins, 2002b; Zieg & Marsh, 2002). The straight nature of the logarithm of the population density *vs*. crystal size relationship is a characteristic feature of simulations employing combination of the exponentially increasing rate of nucleation and the constant rate of growth (*cf*. Marsh, 1998; Hersum & Marsh, 2006). Other combinations of constant, linear, and exponential rates used in this study do not approach the linear behavior of CSDs (Fig. 3.6b), although multiple nucleation and growth rate functions consistent with any given (including straight) CSD can be constructed numerically by the method of Špillar & Dolejš (2013). The combination of exponential nucleation rate and constant growth rate appears to be a reasonable approximation of the crystallization kinetics in natural magmas provided that the nucleation rate is a much stronger function of the driving force of crystallization (e.g., undercooling) than the growth rate.

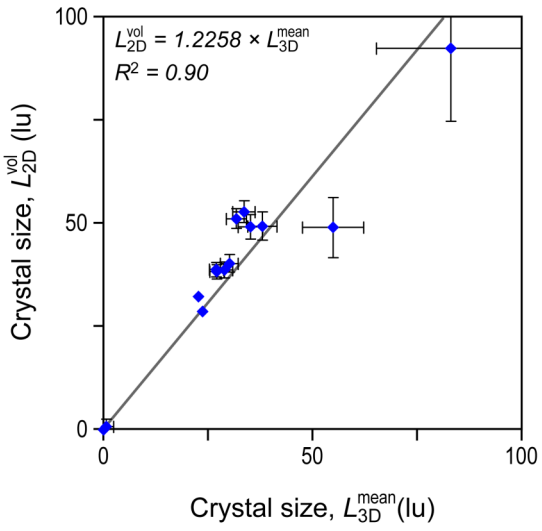

Fig. 3.12. *Correlation between mean three-dimensional crystal size, L_{3D}^{mean}, calculated from the volumetric number density of crystals, and the most voluminous crystal size in two-dimensional section, L_{2D}^{vol}. Error bars represent relative magnitudes of error, calculated as the inverse of a number of grains, and are scaled arbitrarily. Where not shown, error bars are smaller than the symbol size.*

All simulated textures exhibit some discernible curvature of their CSDs. For exponential nucleation rates, this affects the smallest crystal sizes only while the rest of the CSD remains straight, and we designate all such CSDs as straight. In all other cases of nucleation and growth rate functions the downward curvature of CSDs is more pronounced and distributed over the full range of crystal sizes. Curved CSDs that are depleted in small crystals were reported in numerous studies from large intrusive bodies of both felsic and mafic composition and were frequently ascribed to texture coarsening or annealing (Bindeman, 2003; Higgins, 2002a; Boorman et al., 2004; Simakin & Bindeman, 2008). Our simulations show that curved CSDs may result directly from the specific combinations of nucleation and growth rates and do not require post-crystallization modification of the texture.

For Gaussian nucleation and growth rates, the CSD curvature is inversely proportional to the temporal difference between the peak of nucleation and growth (Lasaga, 1998; *cf.* G1G1 *vs*. G2G1; Fig. 3.6b). When the maximum nucleation succeeds the maximum of the growth rate, the crystallization cannot continue and some residual melt always remains.

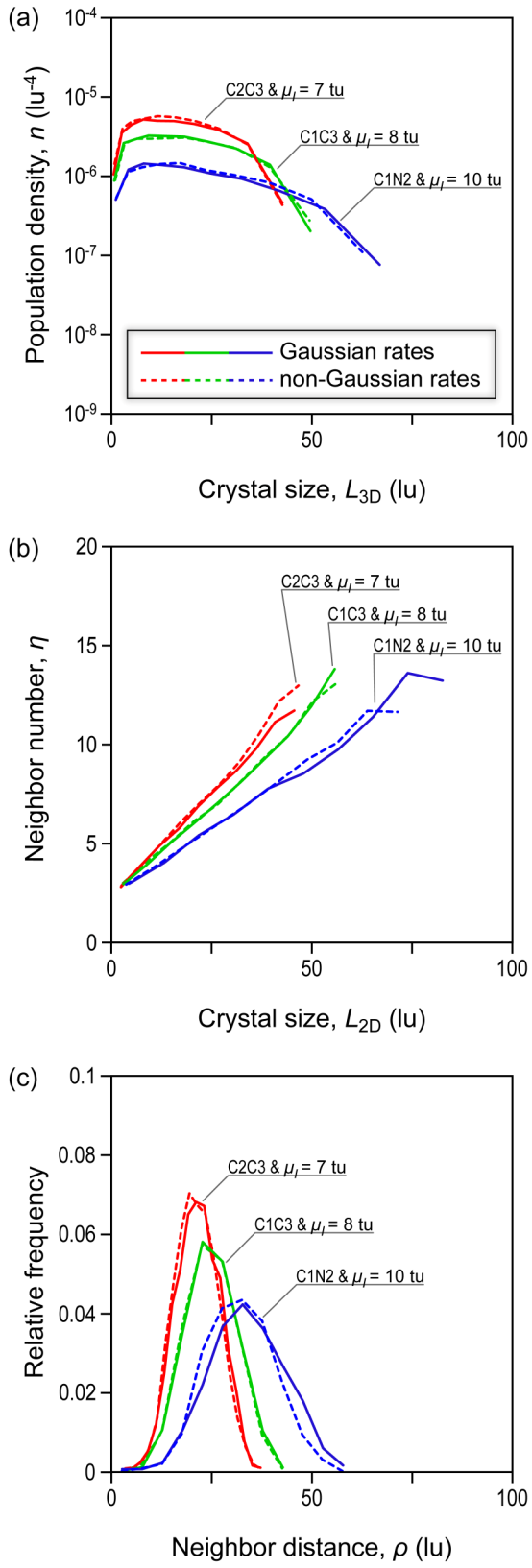

◄ **Fig. 3.13.** *Comparison of pairs of similar textures formed by different combinations of the nucleation and growth rate functions.* **(a)** *distribution of true crystal sizes, L_{3D}, based on the volume data.* **(b)** *dpendence of a neighbor number, η, on apparent crystal size, L_{2D}.* **(c)** *fequency distribution of an average neighbor distance, ρ. In each pair, the Gaussian rates (solid line) are set to obtain a texture that matches the textural parameters of one of the previously simulated texture (dashed line). For the Gaussian nucleation rate, μ_I and σ_I, are the mean value and the standard deviation, respectively, used in the following formula:*

$$I(t) = 5 \times 10^{-4} \cdot \left(2\pi\sigma_I\right)^{-1/2} \cdot \exp\left(-(t-\mu_I)^2/(2\sigma_I^2)\right).$$

Value of the standard deviation is fixed to σ_I = 3 tu, whereas the value of μ_I was adjusted. Symbol tu are arbitrary time units.

3.5.3. Covariance behavior of nucleation and growth rates

Natural and synthetic textures can be conveniently described by scalar quantities. Various functional parameters describing size, shape, contact and spatial relationships of crystals can be employed to gain a more thorough description of a texture but some are inherently interrelated. Several distinct textures in our simulation set (e.g., C1C3 *vs*. L1C3) yield similar CSDs but also approach each other in other quantitative textural parameters (e.g., spatial distribution pattern, contact relationship). To test if distinct combinations of rate functions leading to identical CSDs will also have identical other textural parameters, we performed an additional set of simulations with Gaussian rates of nucleation and growth. Parameters of the Gaussian rates were adjusted stepwise in order to obtain textures, the CSDs of which would be identical to some of the previously simulated non-Gaussian textures. The CSDs and contact parameters of three examples are shown in Fig. 3.13. The close correspondence between the CSDs and the other textural parameters empirically confirms that: (*i*) contrasting histories of nucleation and growth rates can lead to identical textures. Therefore, both the rate functions describing nucleation and growth cannot be simultaneously and uniquely determined from the texture. (*ii*) A CSD is a sufficient function to describe the texture and all other quantitative parameters of the texture can be uniquely determined from the CSD provided that the textures originate by spatially random nucleation and grain size-independent growth only.

On the other hand, textural parameters determined indirectly from the known CSD of a texture of interest can be compared with those actually measured on the texture. If any difference is found, then it must be due to other processes than spatially random nucleation in melt and size-independent growth of crystals. This method, therefore, opens an avenue for identifying textural evidence of other processes than simple nucleation and growth that could have operated during magma crystallization.

3.5.4. Invariant properties of textures and implications for magmatic processes

Textural variations observed in our models result from variations of nucleation and growth rates. These textures must be considered as limiting kinetic cases with no involvement of crystal coarsening or mechanical sorting (e.g., Marsh, 1988, 1998; Higgins, 2011). While such effects can be incorporated into future models of texture evolution, we attempt to identify textural parameters, which are insensitive (invariant) to the nature of the nucleation and growth rate in our simulations, and their variations in natural samples would, thus, point to the action of other processes such as heterogeneous nucleation (Hammer at al., 2010), existence of chemically modified boundary layers (Muncill & Lasaga, 1987, 1988; Acosta-Vigil et. al., 2006), size-dependent growth (Eberl et al., 2002; Kile & Eberl, 2003), mechanical clustering of crystals in a suspension (Schwindinger, 1999), textural coarsening, etc. (e.g., Higgins, 2011).

Several rate-invariant properties are illustrated in Fig. 3.10. The number of neighbors of a crystal, η, depends linearly on the crystal size, L_{2D}, but individual trends have a common intercept, $\eta_I = 2.434 \pm 0.087$ (1σ) (Tab. 3.4). This quantity represents an average number of neighbors of a crystal approaching zero size. For natural textures, η_I varies between 1 and 3, as a very small crystal may form an inclusion in a larger crystal, be located at a boundary between two other crystals or at a triple junction. Deviation of η_I from the theoretical value (~2.4) provides information on other crystallization processes unrelated to nucleation and growth. Heterogeneous nucleation on crystal surfaces increases the number of interstitial grains and the value of η_I is lowered. On the other hand, suppression of nucleation in a chemically modified melt boundary layer has the opposite effect, similar to texture coarsening, which, in an extreme case, leads to equigranular honeycomb-like texture, where each grain has 6 neighbors.

The average neighbor distance, ρ, also linearly depends on the crystal size, L_{2D}, and the slope of this relationship remains nearly constant, $\rho_S = 0.424 \pm 0.029$ (1σ), for all simulated textures (Fig. 3.10b). The slope represents an increment by which the average distance to the contact neighbor increases per unit increase of the crystal size, and this quantity is expected to be altered when other than random nucleation and size-independent growth occurred during

crystallization. We emphasize that values presented here are based on the growth rate that is isotropic in three directions (that is, growth form is a cube) and will be modified when other growth forms such as plates or prisms are considered.

Tab. 3.4. *Fits for the invariants of the simulated textures.*

Nucleation rate curve	Growth rate curve	Fit to $\eta(L_{2D})$		Fit to $\rho(L_{2D})$	
		Slope [lu^{-1}]	Intercept [n.d.]	Slope [n.d.]	Intercept [lu]
C1	C3*	0.179 ± 0.003	2.399 ± 0.053	0.399±0.010	16.142±0.263
C1	E1	0.169	2.334	0.393	17.311
C1	E2	0.158	2.453	0.418	17.644
C1	N1	0.146	2.381	0.399	20.250
C1	N2	0.135	2.406	0.393	21.371
C2	C3	0.218	2.283	0.393	13.644
L1	C3	0.181	2.387	0.406	16.333
L2	C3	0.204	2.401	0.400	14.360
E1	C1**	745.2 ± 31.46	2.526 ± 0.166	0.458 ± 0.013	0.0039 ± 0.0001
E1	C2**	7.476 ± 0.363	2.468 ± 0.181	0.466 ± 0.007	0.385±0.007
E2	C2**	7.363 ± 0.362	2.536 ± 0.154	0.461 ± 0.009	0.386±0.009
E3	C3*	0.160 ± 0.005	2.492 ± 0.087	0.445±0.013	18.490±0.527
E3	C4*	0.060 ± 0.004	2.446 ± 0.179	0.439±0.034	48.038±2.014
E4	C3*	0.294 ± 0.006	2.473 ± 0.088	0.465±0.008	9.587±0.179
E4	C4	0.088	2.664	0.464	31.408
G1	G1	0.233	2.367	0.411	12.216
G2	G1	0.137	2.364	0.401	23.293
Invariants – all textures (± 1σ):			**η_I = 2.434 ± 0.087**	**ρ_S = 0.424 ± 0.029**	

The $\eta(L_{2D})$ is the linear dependence of the neighbor number on the crystal size, whereas $\rho(L_{2D})$ is the linear dependence of average neighbor distance on crystal size. To avoid statistical fluctuations due to the low number of observations, fits are calculated from zero to half of the maximum value of L_{2D} only; at higher values of L_{2D}, observations are sparser and fits suffer from undesired statistical fluctuations. Where indicated, multiple realizations of a single simulation were performed and averaged to obtain statistically more stable results. Symbols lu are arbitrary length units. Units n.d. indicate dimensionless quantity. All errors are 1σ values.

* average of 20 repeated simulations.

** average of 10 repeated simulations.

3.5.5. Spatial distribution of crystals and random textures

Our simulations allow comparison of the spatial arrangement of crystals with textural parameters in case of random distribution. By definition, random distribution of points is characterized by unit value of the clustering index, *R* (e.g., Clark & Evans, 1954; Kretz, 1966). In real textures with finite size of crystals, the value of *R* for random distribution becomes a function of crystallinity. To characterize this effect, random distribution of spheres was introduced as a reference (e.g., Jerram et al., 1996). In contrast to the random sphere model, however, new crystals nucleate during the crystallization in the available melt pools, and their locations are constrained by other crystals already present in the melt. As our simulation algorithm treats homogeneous nucleation as occurring at random locations in the melt, the simulated textures provide a reference for random textures formed during

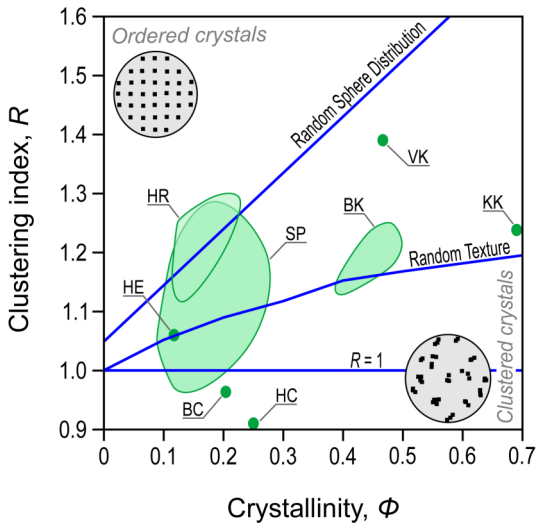

Fig. 3.14. *Degree of ordering vs. clustering of crystals in representative natural textures: BC – Belingwe komatiite, Zimbabwe, olivine in the basal chill zone (Jerram et al., 2003); BK – Belingwe komatiite, Zimbabwe, olivine in the cumulate zone (Jerram et al., 1996); HC – Holyoke flood basalt, Connecticut/Massachusetts, plagioclase in the colonnade zone (Jerram et al., 2003); HE – Holyoke flood basalt, Connecticut/Massachusetts, plagioclase in the entablature zone (Jerram et al., 2003); HR – Halle rhyolite, Germany, quartz, alkali feldspar, and plagioclase phenocrysts (Mock et al., 2003); KK – Kambalda komatiite, Western Australia, olivine in the cumulate zone (Jerram et al., 2003); SP – Shanggusi granite porphyry, China, quartz phenocrysts (Yang, 2012); VK – Vammala komatiite, Finland, olivine in the cumulate zone (Jerram et al., 2003). Random sphere distribution line (RSDL) according to Jerram et al. (1996). The random texture trend is drawn for simulated textures with straight CSDs, and it is believed to separate between clustering and ordering in natural textures.*

continuous nucleation and growth, and for the evolution of the clustering index, *R*, as a function of crystallinity (random texture trend, RTT).

All textures with straight CSDs share a common RTT (Fig. 3.11), whereas RTTs consistent with textures having non-straight CSDs can also be calculated using our simulation algorithm. The RTT obtained in this study differs significantly from the random sphere distribution line used by Jerram et al. (1996) and in subsequent studies (e.g., Ikeda et al., 2002; Jerram et al., 2003; Mock et al., 2003). Textures resulting from random nucleation in a melt would be considered as clustered, according to the classification of Jerram et al. (1996), whereas natural textures considered as clustered should now be regarded as more ordered with respect to the new RTT trend (Fig. 3.14). Any deviations found in natural textures from the theoretically predicted RTT, therefore, indicate that process(es) other than random nucleation and size-independent growth must have influenced magma crystallization. Comparison of natural textures with the predicted RTT may provide better insight into cluster-forming heterogeneous nucleation or aggregation of crystals during the crystal settling, or it may indicate crystal mush compaction in cumulates (e.g., Jerram et al., 1996, 2003).

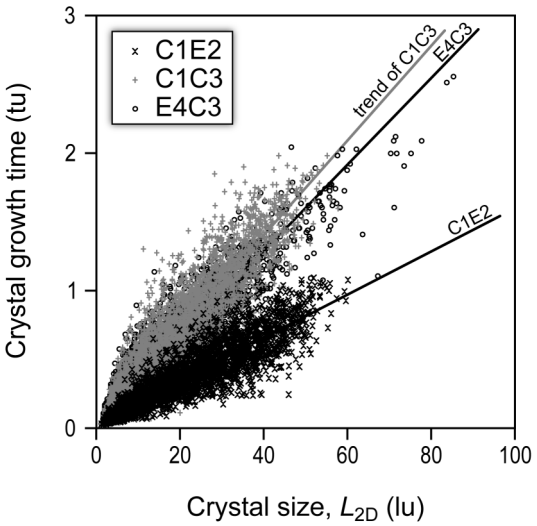

Fig. 3.15. *Crystal size, L_{2D}, vs. crystal growth time for populations of crystals in three representative textures. The crystal growth time is estimated from two-dimensional sections as a time interval from the instant when the crystal enters the sectioning plane to the point when it is completely impinged (stops growing) in that section.*

3.5.6. Crystallinity evolution and crystallization time

We define growth time of a grain as the time span between nucleus formation and the end of crystal growth when all faces of the crystal are impinged by neighboring crystals, or when the growth rate decreases to zero. As a total crystallization time we define the time needed for the whole simulation domain to reach 100 % crystallinity. All crystallization simulations reveal a universal positive correlation between crystal size and crystal growth time (Fig. 3.15). The growth time of the largest crystals (in a two-dimensional section) spans up to about 75 % of the total crystallization time for a magma. In detail, however, individual crystals in the population show significant spread around the linear trend in Fig. 3.15, as the growth times of individual, similarly sized crystals differ by several factors. Similarly sized crystals may, thus, record vastly different time spans and conditions of magma crystallization.

The slope of the linear relationship in the crystal size *vs*. crystal growth time space is inversely related to the *effective* growth rate of the crystals. The effective growth rate (e.g., Lasaga, 1998; Marsh, 1998) accounts for the impingement of crystals and various orientations of the crystal faces with respect to the plane of section. We observe that the effective growth rate mainly depends on the growth rate function, whereas the dependence on the nucleation rate is weak and secondary (Fig. 3.15). However, the variations in the growth rate with time do not alter the linear correlation between the crystal size and its growth time. The effective growth rate is, thus, meaningfully defined even in complex cases where the nucleation and growth rates have varied with time.

The evolution of crystal fraction (crystallinity) with time is illustrated in Fig. 3.16. In all cases, the crystallinity-time evolution follows a sigmoidal trend with a slow onset, rapid progress at intermediate crystal fraction, and a slow approach towards full crystallinity. These trends are in excellent agreement with analytical predictions from the Avrami theory (Avrami, 1939, 1940; Lasaga, 1998; Marsh, 1998), and such behavior results from the universal variation of crystal surface area that is available for grain growth. This area is small during early stages of crystallization, progressively increases with increasing grain size, and decreases

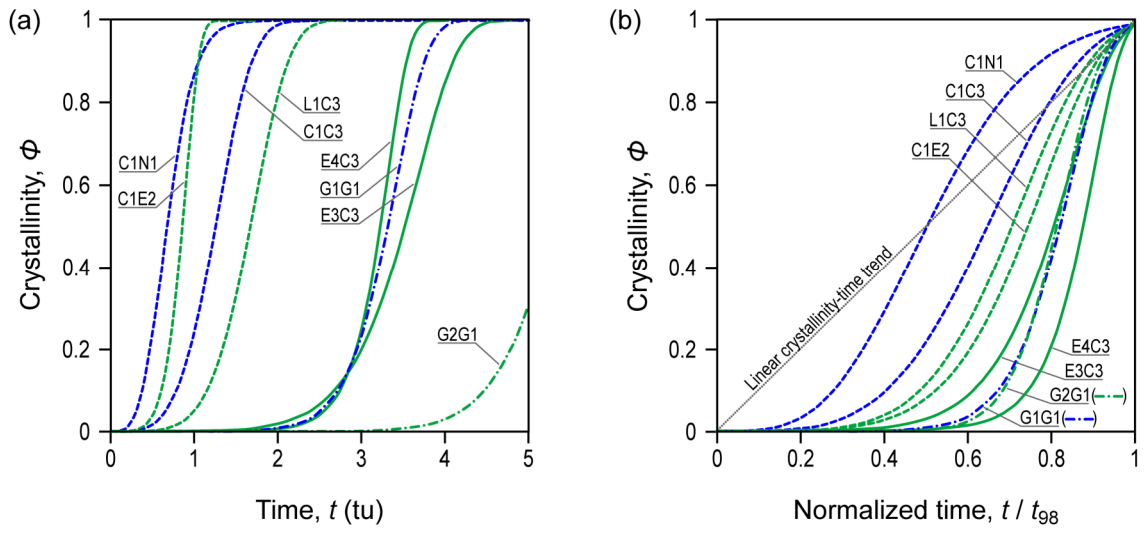

Fig. 3.16. *Crystallinity-time relationships in textural simulations:* **(a)** *original data and* **(b)** *normalized to time interval to reach 98 % crystallinity.*

near the end of crystallization due to impingement of most of the crystals and decreasing size of residual melt pockets.

The total crystallization time is specific for each simulation but it is generally related to the nucleation rate at the liquidus, i.e. onset of crystallization (Fig. 3.16a). Simulations with constant or linearly increasing nucleation rate exhibit the shortest crystallization time lag. Those with exponential or Gaussian nucleation rates, that is, with the slower onset of nucleation at the beginning of crystallization, show greater delays in crystallinity increase. To compare the evolution of crystallinity, we normalized all simulations to a common time scale when they reach 98 % crystallinity (Fig. 3.16b). This level, rather than 100 % crystallinity, was chosen to avoid artifacts or instabilities resulting from asymptotic approach to infinity at full crystallinity. Simulations with constant nucleation rate and decreasing or constant growth rate (C1N1, C1C3) provide normalized time-crystallinity relationships, which are closest to linear. Exponential nucleation (e.g., E3C3, E4C3), on the other hand, leads to crystallinity that is almost negligible during the first half of the crystallization time, but then increases rapidly. Models with exponential nucleation, thus, provide the greatest departure from simple proportionality between the time and crystal fraction. Importantly, only the models

with exponential nucleation rates produce textures with straight CSDs that are known from a wide range of natural volcanic and mafic intrusive rocks (e.g., Cashman & Marsh, 1988; Wilhelm & Wörner, 1996; Marsh, 1998; Zieg & Marsh, 2002). Kinetic models that are closer to the linear time-crystallinity relationship result in concave-down CSDs, which are observed, for instance, in large silicic systems (e.g., Bindeman, 2003; Simakin & Bindeman, 2008).

The magnitude of the departure from the linear time-crystallinity relationship may provide inferences about the degree of disequilibrium during crystallization. If a quasi-linear crystallinity-temperature relationship is assumed, as predicted by melting and cooling experiments (e.g., Marsh, 1981; Annen et al., 2008), and when cooling proceeds at approximately constant rate, the departure of the crystallinity from the quasi-linear trend is directly proportional to the degree of disequilibrium. This observation indicates that samples showing straight CSDs were at greater disequilibrium during crystallization, whereas more equilibrium crystallization occurred in those cases where concave-down CSD patterns are observed.

3.6. Concluding remarks

We developed a new high-resolution kinetic model for the simulation of texture evolution in a three-dimensional magma domain. The model incorporates homogeneous nucleation and crystal growth rates, and it was employed to perform exploratory simulations of crystallization of a single type of solid phase using various combinations of constant, linear, exponential, and Gaussian rate functions for nucleation and growth. The simulated textures were quantified by true three-dimensional CSDs and a variety of apparent spatial, contact, and shape parameters in a two-dimensional section. The resulting textures broadly resemble natural ones and cover a range from equigranular to seriate types with considerable variation of grain size and size distribution. Porphyritic types, however, were not observed in any of the kinetic models and their formation apparently requires a sudden increase of crystal nucleation and/or abrupt decrease in the growth rate. A more likely and common way to

produce porphyritic textures is by episodic annealing or by mixing crystal populations through the processes of crystal recycling/accumulation (e.g., Morgan et al., 2007; Martin et al., 2010; Johnson & Glazner 2010; Mills et al., 2011). In a multiphase system, a porphyritic texture can form if second and additional saturating phases appear after a substantial time lag, when the phenocrysts of the first liquidus phase are allowed to nucleate and sufficiently grow.

Different combinations of the nucleation and growth rate functions can lead to textures with identical CSDs, contact, spatial, and shape parameters. In addition, we have identified conventional and new textural parameters that are either sensitive or invariant to processes of random nucleation and growth. Their simultaneous evaluation on natural igneous rocks and mutual comparison of individual parameters offers a powerful tool for identifying and separating effects of other crystallization processes such as heterogeneous nucleation, formation of melt boundary layers, mechanical interactions of crystals or textural coarsening.

3.7. Acknowledgements

This study was financially supported by the Charles University Research Program P44 and the Czech Science Foundation Nr. 210/12/0986 (to D. D.). We thank Dougal Jerram and Bruce Marsh for their detailed and constructive reviews. Careful editorial handling by Uwe Reimold is greatly appreciated.

3.8. References

ACOSTA-VIGIL A., LONDON D., MORGAN G. B. & DEWERS T. A. (2006): Dissolution of quartz, albite, and orthoclase in H_2O-saturated haplogranitic melt at 800°C and 200 MPa: Diffusive transport properties of granitic melts at crustal anatectic conditions. – *Journal of Petrology* 47, 231–254.

AMENTA R., EWING A., JENSEN A., ROBERTS S., STEVENS K., SUMMA M., WEAVER S. & WERTZ P. (2007): A modeling approach to understanding the role of microstructure development on crystal-size distributions and on recovering crystal-size distributions from this slices. – *American Mineralogist* 92, 1936–1945.

ANNEN C., PICHAVANT M., BACHMANN O. & BURGISSER A. (2008): Conditions for the growth of a long-lived shallow crustal magma chamber below Mount Pelee volcano (Martinique, Lesser Antilles Arc). – *Journal of Geophysical Research* 113, B07209.

ANNEN C. (2009): From plutons to magma chambers: Thermal constraints on the accumulation of eruptible silicic magma in the upper crust. – *Earth and Planetary Science Letters* 284, 409–416.

AVRAMI M. (1939): Kinetics of phase change I. General theory. – *Journal of Chemical Physics* 7, 1103–1112.

AVRAMI M. (1940): Kinetics of phase change II. Transformation-time relation for random distribution of nuclei. – *Journal of Chemical Physics* 8, 211–224.

BACHMANN O. & BERGANTZ G. (2008): The magma reservoirs that feed supereruptions. – *Elements* 4, 17–21.

BADDELEY A. & TURNER R. (2005): Spatstat: An R package for analyzing spatial point patterns. – *Journal of Statistical Software* 12, 1–42.

BEA F. (2010): Crystallization dynamics of granite magma chambers in the absence of regional stress: Multiphysics modeling with natural examples. – *Journal of Petrology* 51, 1541–1569.

BINDEMAN I. N. (2003): Crystal sizes in evolving silicic magma chambers. – *Geology* 31, 367–370.

BOORMAN S., BOUDREAU A. & KRUGER F. J. (2004): The Lower Zone-Critical Zone transition of the Bushveld Complex: A quantitative textural study. – *Journal of Petrology* 45, 1209–1235.

BURKHARD D. J. M. (2002): Kinetics of crystallization: Example of micro-crystallization in basalt lava. – *Contributions to Mineralogy and Petrology* 142, 724–737.

CABANE H., LAPORTE D. & PROVOST A. (2005): An experimental study of Ostwald ripening of olivine and plagioclase in silicate melts: Implications for the growth and size of crystals in magmas. – *Contributions to Mineralogy and Petrology* 150, 37–53.

CASHMAN K. V. (1993): Relationship between plagioclase crystallization and cooling rate in basaltic melts. – *Contributions to Mineralogy and Petrology* 113, 126–142.

CASHMAN K. V. & MARSH B. D. (1988): Crystal size distribution (CSD) in rocks and the kinetics and dynamics of crystallization II: Makaopuhi lava lake. – *Contributions to Mineralogy and Petrology* 99, 292–305.

CLARK P. J. & EVANS F. C. (1954): Distance to nearest neighbour as a measure of spatial relationships in populations. – *Ecology* 35, 445–453.

CROSS W., IDDINGS J. P., PIRSSON L. V. & WASHINGTON H. S. (1906): The texture of igneous rocks. – *Journal of Geology* 14, 692–707.

DEVROYE L. (1986): *Non-uniform random variate generation*. – Springer-Verlag, New York, 843 pp.

DONNELLY K. (1978): Simulations to determine the variance and edge-effect of total nearest neighbor distance. – *In*: HODDER I. (ed): *Simulations Methods in Archeology*, Cambridge University Press, Cambridge, pp. 91–95.

EBERL D. D., KILE D. E. & DRITS V. A. (2002): On geological interpretation of crystal size distributions: Constant *vs*. proportionate growth. – *American Mineralogist* 87, 1235–1241.

ELLIOTT M. T., CHEADLE M. J. & JERRAM D. A. (1997): On the identification of textural equilibrium in rocks using dihedral angle measurements. – *Geology* 25, 355–358.

FOKIN V. M., ZANOTTO E. D., YURITSYN N. S. & SCHMELZER J. W. P. (2006): Homogeneous crystal nucleation in silicate glasses: A 40 years perspective. – *Journal of Non-Crystalline Solids* 352, 2681–2714.

FOKIN V. M., YURITSYN N. S., ZANOTTO E. D., SCHMELZER J. W. P. & CABRAL A. A. (2008): Nucleation time-lag from nucleation and growth experiments in deeply undercooled glass-forming liquids. – *Journal of Non-Crystalline Solids* 354, 3785–3792.

GERYA T. V. & BURG J.-P. (2007): Intrusions of ultramafic magmatic bodies into the continental crust: Numerical simulation. – *Physics of Earth and Planetary Interiors* 160, 124–142.

HAMMER J. E. (2008): Experimental studies of the kinetics and energetics of magma crystallization. – *Reviews in Mineralogy and Geochemistry* 69, 9–59.

HAMMER J. E., SHARP T. G. & WESSEL P. (2010): Heterogeneous nucleation and epitaxial crystal growth of magmatic minerals. – *Geology* 38, 367–370.

HERSUM T., HILPERT M. & MARSH B. (2005): Permeability and melt flow in simulated and natural partially molten basaltic magmas. – *Earth and Planetary Science Letters* 237, 798–814.

HERSUM T. G. & MARSH B. D. (2006): Igneous microstructures from kinetic models of crystallization. – *Journal of Volcanology and Geothermal Research* 154, 34–47.

HIGGINS M. D. (2000): Measurement of crystal size distributions. – *American Mineralogist* 85, 1105–1116.

HIGGINS M. D. (2002a): A crystal size-distribution study of the Kiglapait layered mafic intrusion, Labrador, Canada: Evidence for textural coarsening. – *Contributions to Mineralogy and Petrology* 144, 314–330.

HIGGINS M. D. (2002b): Closure in crystal size distribution (CSD), verification of CSD calculations, and significance of CSD fans. – *American Mineralogist* 87, 171–175.

HIGGINS M. D. (2006): *Quantitative textural measurements in igneous and metamorphic petrology*. – Cambridge University Press, Cambridge, 265 pp.

HIGGINS M. D. (2011): Textural coarsening in igneous rocks. – *International Geology Review* 53, 354–376.

HIRSCH D. M., KETCHAM R. A. & CARLSON W. D. (2000): An evaluation of spatial correlation functions in textural analysis of metamorphic rocks. – *Geological Material Research* 2, 1–41.

HOOVER S. R., CASHMAN K. V. & MANGA M. (2001): The yield strength of subliquidus basalt – experimental results. – Journal *of Volcanology and Geothermal Research* 107, 1–18.

IKEDA S., TORIUMI M., YOSHIDA H. & SHIMIZU I. (2002): Experimental study of the textural development of igneous rocks in the late stage of crystallization: The importance of interfacial energies under non-equilibrium conditions. – *Contributions to Mineralogy and Petrology* 142, 397–415.

JARET S. J., MAYNE R. G. & MCSWEEN H. Y. (2008): Demystifying crystal size distribution (CSD): A comparison of methodologies using eucrite meteorites. – *39th Lunar and Planetary Science Conference*, League City, #1487 (abstract).

JERRAM D. A., CHEADLE M. J., HUNTER R. H. & ELLIOTT M. T. (1996): The spatial distribution of grains and crystals in rocks. – *Contributions to Mineralogy and* Petrology 125, 60–74.

JERRAM D. A. & CHEADLE M. J. (2000): On the cluster analysis of rocks. – *American Mineralogist* 85, 47–67.

JERRAM D. A., CHEADLE M. J. & PHILPOTTS A. R. (2003): Quantifying the building blocks of igneous rocks: Are clustered crystal frameworks the foundation? – *Journal of Petrology* 44, 2033–2051.

JERRAM D. A., MOCK A., DAVIS G. R., FIELD M. & BROWN R. J. (2009): 3D crystal size distributions: A case study on quantifying olivine populations in kimberlites. – *Lithos* 112S, 223–235.

JOHNSON B. R. & GLAZNER A. F. (2010): Formation of K-feldspar megacrysts in granodioritic plutons by thermal cycling and late-stage textural coarsening. – *Contributions to Mineralogy and Petrology* 159, 599–619.

KILE D. E. & EBERL D. D. (2003): On the origin of size-dependent and size-independent crystal growth: Influence of advection and diffusion. – *American Mineralogist* 88, 1514–1521.

KRETZ R. (1966): Grain-size distribution for certain metamorphic minerals in relation to nucleation and growth. – *Journal of Geology* 74, 147–173.

KRETZ R. (1969): On the spatial distribution of crystals in rocks. – *Lithos* 2, 39–66.

KURZYDŁOWSKI K. J. & RALPH B. (1995): *The quantitative description of the microstructure of materials*. – CRC Press, Boca Raton, 418 pp.

LASAGA A. C. (1998): *Kinetic theory in the Earth sciences.* – Princeton University Press, Princeton, 811 pp.

LE MAITRE R. V. (ed.) (2002): *Igneous rocks. A classification and glossary of terms. Recommendations of the International Union of Geological Sciences subcommission on the systematics of igneous rocks* (2nd ed.). – Cambridge Univeresity Press, Cambridge, 236 pp.

MARSH B. D. (1981): On the crystallinity, probability of occurrence, and rheology of lava and magma. – *Contributions to Mineralogy and Petrology* 78, 85–98.

MARSH B. D. (1988): Crystal size distribution (CSD) in rocks and the kinetics and dynamics of crystallization I. Theory. – *Contributions to Mineralogy and Petrology* 99, 277–291.

MARSH B. D. (1998): On the interpretation of crystal size distributions in magmatic systems. – *Journal of Petrology* 39, 553–599.

MARTIN V. M., DAVIDSON J. P., MORGAN D. J. & JERRAM D. A. (2010): Using the Sr isotope composition of feldspars and glass to distinguish magma system components and dynamics. – *Geology* 38, 539–542.

MATSUMOTO M. & NISHIMURA T. (1998): Mersenne twister: a 623-dimensionally equidistributed uniform pseudo-random number generator. – *ACM Transactions on Modeling and Computer Simulation* 8, 3–30.

MEANS W. D. & PARK Y. (1994): New experimental approach to understanding igneous texture. – *Geology* 22, 323–326.

MILLS R. D., RATNER J. J. & GLAZNER A. F. (2011): Experimental evidence for crystal coarsening and fabric development during temperature cycling. – *Geology* 39, 1139–1142.

MOCK A., JERRAM D. A. & BREITKREUZ C. (2003): Using quantitative textural analysis to understand the emplacement of shallow-level rhyolitic laccoliths – A case study from the Halle Volcanic Complex, Germany. – *Journal of Petrology* 44, 833–849.

MOCK A. & JERRAM D. A. (2005): Crystal size distribution (CSD) in three dimensions: Insight from the 3D reconstruction of a highly porphyritic rhyolite. – *Journal of Petrology* 46, 1525–1541.

MORGAN D. J. & JERRAM D. A. (2006): On estimating crystal shape for crystal size distribution analysis. – *Journal of Volcanology and Geothermal Research* 154, 1–7.

MORGAN D. J., JERRAM D. A., CHERTKOFF D. G., DAVIDSON J. P., PEARSON D. G., KRONZ A. & NOWELL G. M. (2007): Combining CSD and isotopic microanalysis: Magma supply and mixing processes at Stromboli Volcano, Aeolian Islands, Italy. – *Earth and Planetary Science Letters* 260, 419–431.

MUNCILL G. E. & LASAGA A. C. (1987): Crystal-growth kinetics of plagioclase in igneous systems: One-atmosphere experiments and applications of a simplified growth model. – *American Mineralogist* 72, 299–311.

MUNCILL G. E. & LASAGA A. C. (1988): Crystal-growth kinetics of plagioclase in igneous system: Isothermal H_2O-saturated experiments and extension of a growth model to complex silicate melts. – *American Mineralogist* 73, 982–992.

NIGGLI P. (1954): *Rocks and mineral deposits*. – Freeman, San Francisco, 559 pp.

R DEVELOPMENT CORE TEAM (2011): *R: A language and environment for statistical computing*. – R Foundation for Statistical Computing, Vienna, Austria. ISBN 3-900051-07-0, URL: http://www.R-project.org/.

RANDOLPH A. D. & LARSON M. A. (1971): *Theory of particulate processes*. – Academic Press, New York, 251 pp.

RUDGE J. F., HOLNESS M. B. & SMITH G. C. (2008): Quantitative textural analysis of packing of elongate crystals. – *Contributions to Mineralogy and Petrology* 156, 413–429.

SCHIAVI F., WALTE N. & KEPPLER H. (2009): First in situ observation of crystallization processes in a basaltic-andesitic melt with the moissanite cell. – *Geology* 37, 963–966.

SCHWINDINGER K. (1999): Particle dynamics and aggregation of crystals in a magma chamber with application to Kilauea Iki olivines. – *Journal of Volcanology and Geothermal Research* 88, 209–238.

SIMAKIN A. G. & BINDEMAN I. N. (2008): Evolution of crystal sizes in the series of dissolution and precipitation events in open magma systems. – *Journal of Volcanology and Geothermal Research* 17, 997–1010.

ŠPILLAR V. & DOLEJŠ D. (2013): Calculation of time-dependent nucleation and growth rates from quantitative textural data: Inversion of crystal size distribution. – *Journal of Petrology* 54, 913–931.

TEUSCHER E. O. (1933): Methodisches zur quantitativen Strukturgliederung körniger Gesteine. – *Tschermaks Mineralogische und Petrologische Mitteilung* 44, 410–421.

VERHOEVEN J. & SCHMALZL J. (2009): A numerical method for investigating crystal settling in convecting magma chambers. – *Geochemistry, Geophysics, Geosystems* 10, 1–21.

WALSH S. D. C. & SAAR M. O. (2008): Numerical models of stiffness and yield stress growth in crystal-melt suspension. – *Earth and Planetary Science Letters* 267, 32–44.

WILHELM S. & WÖRNER G. (1996): Crystal size distribution in Jurassic Ferrar flows and sills (Victoria Land, Antarctica): Evidence for processes of cooling, nucleation, and crystallisation. – *Contributions to Mineralogy and Petrology* 125, 1–15.

WOJNAR L. (1999): *Image analysis: applications in materials engineering*. – CRC Press, Boca Raton, 245 pp.

YANG Z.-F. (2012): Combining quantitative textural and geochemical studies to understand the solidification process of a granite porphyry: Shanggusi, East Qinling, China. – *Journal of Petrology* 53, 1807–1835.

ZIEG M. J. & MARSH B.D. (2002): Crystal size distributions and scaling laws in the quantification of igneous textures. – *Journal of Petrology* 43, 85–101.

Preface to Chapter 4

A number of experimental crystallization studies has proven homogeneous nucleation of crystals from undercooled melt to be difficult. Nucleation is eased by presence of solid surfaces that lower the energy barrier and act as the sites of preferential nucleation. Consequently, spatially constrained heterogeneous nucleation leads to the formation of clusters of crystals. This affects rheology of crystal mushes and enhances gravitational crystal-liquid separation. In this chapter, we extend the three-dimensional model of crystallization by nucleation and growth of crystals (Chapter 3) to include the effect of heterogeneous nucleation. We then calibrate a set of quantitative relationships between the heterogeneous to homogeneous nuclei number ratio and derive textural parameters, such as CSD curvature or clustering index, measurable on natural samples and experimental products.

This chapter was published as **ŠPILLAR, V.** & DOLEJŠ, D. (2015): *Heterogeneous nucleation as the predominant mode of crystallization in natural magmas: numerical model and implication for crystal-melt interaction.* – ***Contributions to Mineralogy and Petrology*** *169, 1–16*. The manuscript was formatted to conform to general layout of this thesis.

Chapter 4.

Heterogeneous nucleation as the predominant mode of crystallization in natural magmas: Numerical model and implications for crystal-melt interaction

4.0. Abstract

Crystallization of natural magmas is inherently a disequilibrium process, which involves nucleation and growth kinetics, melt-crystal mechanical interactions and subsolidus modifications, which are all recorded in the resulting rock texture. We use a new high-resolution three-dimensional numerical model to address the significance and consequences of homogeneous *vs*. heterogeneous crystal nucleation in silicate magmas. With increasing amount of heterogeneous nuclei during crystallization, initially equigranular textures evolve to porphyritic, bimodal and spherulitic types. The corresponding crystal size distributions (CSDs) become concave-up curved, the clustering index progressively decreases, and the grain contact relationships record increased clustering. Concave-up curved CSD previously interpreted as resulting from multistage crystallization, mixing of crystal populations, grain agglomeration, or size-dependent growth are now predicted, consistently with other size, spatial and clustering parameters, to form by heterogeneous crystal nucleation. Correlation relationships between various textural parameters and the fraction of heterogeneous nuclei are calibrated and used on representative volcanic and plutonic rocks, including cumulate rocks, to deduce the fraction of heterogeneous nuclei. The results indicate that ~60 % to ~99 % of all nuclei are heterogeneous. For plutonic and cumulate rocks the estimate of the heterogeneous nuclei fraction based on the clustering index is significantly lower than other estimates. Such

discrepancies, in general, point to the occurrence of other processes and here the results imply that crystal mush compaction and interstitial melt extraction was involved during the magma solidification. Formation of crystals in clusters, implicit for heterogeneous nucleation, implies that greater efficiency of crystal-melt separation is expected in these situations.

Key words:

Heterogeneous nucleation; CSD; crystal cluster; crystallization; quantitative texture measurement.

4.1. Introduction

Magma chambers are complex systems whose internal dynamics and temporal evolution is determined by rheological properties of crystal mush which forms and evolves as crystallization progresses (e.g., Marsh, 1989; Bachmann & Bergantz, 2008; Bea, 2010). Magma crystallization is inherently a non-equilibrium process, and its time-integrated result is recorded by texture of the solidified magmatic product. Textural studies have proven to be useful in providing estimates for the rates of nucleation and growth of crystals as well as the residence time of crystals in natural magmas (e.g., Marsh, 1998; Hersum & Marsh, 2007). These quantitative textural measurements, in combination with theoretical predictions, have revealed that crystal size distributions (CSDs) of various magmatic rocks are well approximated by a linear relationship in the logarithmic population density *vs*. crystal size space (e.g., Cashman & Marsh, 1988; Mock et al., 2003; Higgins & Chandrasekharam, 2007). Deviations from the straight trends are, however, rather common and the concave-up segments of the CSDs were documented in many studies (Armienti et al., 1994; Higgins, 1996, 2002; Higgins & Roberge, 2003; Yang, 2012). This concave-up curvature of the CSDs has been attributed to various processes such as size-dependent crystal growth (Marsh, 1998; Eberl et al., 2002), continuous to sudden changes in intensive variables, which drive the crystallization (e.g., Yang, 2012), agglomeration of crystals in a magma (Burkhart et al.,

1980; Pupiere et al., 2008), and multiple-stage crystallization or mixing of crystal populations from distinct magma batches (Armienti et al., 1994; Higgins, 1996). Remarkably, non-linear CSDs were reported in experimental crystallization studies under closed and steady conditions, where most of the processes postulated above cannot operate (Burkhard, 2002; Zieg & Lofgren, 2006; Pupier et al., 2008; Brugger & Hammer, 2010). Thus, non-linear CSDs may represent an implicit feature of silicate melt crystallization, whose origin may not be yet fully understood.

An independent approach to understanding of the crystallization processes is provided by the analysis of crystal spatial ordering and degree of clustering (e.g., Jerram et al., 1996, 2003). Numerous volcanic and plutonic rocks have a non-random spatial distribution of their crystals and show a tendency towards clustering (e.g., Vance, 1969; Schwindinger, 1999; Ikeda et al., 2002; Jerram et al., 1996; 2003; Hammer et al., 2010). The clustering was interpreted to result from heterogeneous nucleation on preexisting crystal surfaces (e.g., Hammer at al., 2010), adhesion of crystals during mechanical settling in a suspension (Schwindinger, 1999), remobilization of previously accumulated and sintered crystals (e.g., Higgins & Chandrasekharam, 2007), or adjustment of crystal positions and orientations due to the surface energy minimization (Ikeda et al., 2002). Although many of these processes appear to be plausible, no consistent explanation exists for non-linear CSDs and clustered crystal patterns frequently observed in nature. In this work we explore the role of heterogeneous nucleation for the origin of these textural features in detail.

The term heterogeneous nucleation has been used with different meanings in petrological and materials-science literature (e.g., Spry, 1969; Shelley, 1992; Lasaga, 1998; Philpotts & Ague, 2009; Christian, 2002). It refers to the inhomogeneous formation of new nuclei at preferred sites, most commonly on the surface of preexisting solid phases excluding syntaxial growth (heterogeneous nucleation *sensu lato*), or it is restricted to the nucleation on the surface of preexisting but compositionally or structurally different solid phases (heterogeneous nucleation *sensu stricto* or heterophase nucleation; Machlin, 2007).

Here we consider heterogeneous nucleation as a preferential nucleation on melt-crystal interfaces, frequently facilitated by the presence of heterogeneities of any kind such as crystal

surfaces, dislocations, or other defects (e.g., Philpotts & Ague, 2009). This mechanism has long been recognized as a viable, important and more efficient means of nucleation of crystals and bubbles under magmatic conditions (e.g., Fenn, 1977; Lofgren, 1983; Davis & Ihinger, 1998; Mourtada-Bonnefoi, & Laporte 2004; Hammer et al., 2010). In the case of a solid phase nucleating from a melt, the interfacial energy between the nucleus and existing solid phase is expected to be lower that that of the nucleus and a melt because of lesser number of broken bonds between two solid phases. The solid surface therefore provides a site of energetically favorable nucleation, which is statistically preferred. Experimental studies (Lofgren, 1983) demonstrated that a nucleating phase tends to prefer structurally similar substrates. Although we illustrate crystallization of a single solid phase, that is, the nucleating and substrate phases are identical, our results are directly applicable to multiphase systems if nuclei are marked.

Spatial relationship of heterogeneous nuclei to their parent crystals ensures formation of crystal clusters. These clusters have been observed in experimental crystallization studies (e.g., Hammer et al., 2010) and their formation is consistent with clustering of crystals known from natural magmatic textures. In terms of texture evolution, heterogeneous nuclei are younger than their parental crystals, therefore, on average, grow to smaller sizes and may contribute to abundant population of small crystals in textures characterized by concave-up CSDs.

We employ three-dimensional high-resolution numerical simulations of crystal nucleation and growth and demonstrate that *both* concave-up curvature of CSDs and clustering of crystals are consistently produced by extensive occurrence of heterogeneous nucleation in crystallizing magmas. Based on simulated textures robust correlation relationships between quantitative size and spatial parameters of textures and fraction of heterogeneously nucleating crystals were derived. Multiple correlation relationships were then used simultaneously to compare synthetic textures to those found in natural samples and to estimate the fraction of crystals nucleating heterogeneously in a quantitative manner. We show that the combined characterization of size and spatial relationships in crystal population can provide strong quantitative inferences about the mechanisms of crystal nucleation in natural magma chambers.

4.2. Numerical model

4.2.1. Simulation of crystallization textures by homogeneous and heterogeneous nucleation

Texture evolution during melt solidification was modeled using the new high-resolution VoxelTex numerical algorithm (Špillar & Dolejš, 2014), which simulates crystallization by nucleation and growth of crystals in a three-dimensional domain. The algorithm is based on a voxel method of Hersum & Marsh (2006) and it utilizes 70 million discrete volume elements to describe crystal-crystal interfaces while crystal-melt interfaces are tracked using continuous interface tracking method. Due to the memory requirements the three-dimensional domain has 1 : 1 : 1/4 dimensions. The spatial resolution of the model is limited to 1000 × 1000 grid cells in a two dimensional section passing through the center of the simulation domain and parallel to its largest faces. The computational grid was coarsened with increasing distance from the sectioning plane.

Initially, all voxels in the simulation domain are assigned to the melt phase. Crystallization is simulated as a series of discrete time steps of nucleation of new crystals and growth of the preexisting ones. Individual crystals, while unimpinged, are randomly oriented six-sided parallelepipeds, whose faces propagate into the melt. When face of a crystal propagates through the center of a voxel, the voxel is assigned to the crystal and it becomes part of a solid phase. While crystal-melt interfaces are tracked continuously as positions of the crystal faces, the crystal-crystal interface is recorded when two adjacent voxels are assigned to different crystals. This mixed tracking approach allows us to represent a texture discretely but discretization artifacts are minimized.

In the present version, the model simulates kinetic crystallization by homogeneous and heterogeneous nucleation and growth of crystals in static environment. The growth rate is considered constant through space and with respect to crystals size. Fluctuations in the growth rate, which would arise from variable melt composition including possible formation of boundary layers or other heterogeneities, are not considered here. Furthermore, the model is

suited to study kinetic textures (e.g., Higgins, 2011) where subsequent modification due to textural coarsening was not important. Our approach simulates crystallization in a static environment, where relative movement of crystals and melt can be neglected, due to either unfavorably high melt viscosity or much shorter time scales of crystallization compared to those of crystal movement or deformation.

In the model, the crystals nucleate homogeneously on random positions in the melt, or heterogeneously but randomly distributed on the surfaces of other preexisting crystals. For the modeling purpose, possible heterogeneous nucleation taking place on submicroscopic seed particles (e.g., Lofgren, 1983) is considered as a contribution to the homogeneous nucleation since the seeds themselves are randomly distributed in the melt and they are indistinguishable in the model due to resolution limitations. Both types of nuclei are considered to be randomly oriented in space to simulate isotropic textures without any preferred orientation of crystals.

The rates of homogeneous and heterogeneous nucleation and the growth rate are specified as functions of time. To characterize an overall effect of heterogeneous nucleation, the ratio of numbers of heterogeneous to homogeneous nuclei in the simulation domain, N, is evaluated as a function of the progress of solidification. In contrast to homogeneous nucleation, the formation of heterogeneous nuclei is energetically favorable due to presence of other solid surfaces (e.g., Volmer, 1939; Lasaga, 1998). A heterogeneous nucleus shares part of its surface with another solid phase, which lowers the total surface energy of the nucleus, and, therefore, reduces the energy barrier of nucleation. Both nucleation modes thus differ by a factor in the nucleation energy barrier but share common thermodynamic driving force, the Gibbs energy of crystallization (e.g., Lasaga, 1998). This implies that the rates of homogeneous and heterogeneous nucleation are mutually coupled. As the most simple and robust first-order approximation we use linear proportionality relationship between the rates of homogeneous, I, and heterogeneous, H, nucleation (*cf.*, Lofgren, 1983), $H = \xi I$, where ξ is the proportionality constant and both rates I and H are functions of time. The proportionality constant was varied in successive simulations in order to obtain textures with variable N ratios. For $\xi = 0$, nucleation is purely homogeneous whereas with increasing ξ the nucleation becomes progressively heterogeneous and confined to preexisting crystal faces. More general

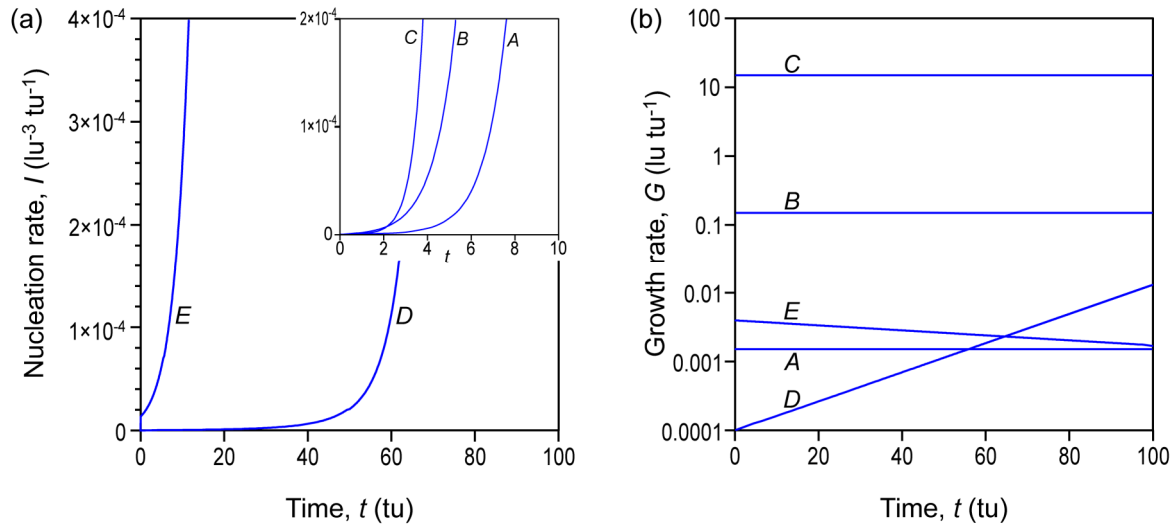

Fig. 4.1. (a) *ncleation rate functions;* **(b)** *growth rate functions used in simulations. Rate functions denoted with same letter are used jointly. All pairs of the rate functions are chosen to produce textures with straight CSDs (Špillar & Dolejš, 2013) in the limiting case of zero heterogeneous nucleation. The rate functions are chosen so that: (i) the slope of the CSD thus the typical grain size of a texture ranges about two orders of magnitude (rates A, B, C); and (ii) to produce a textures with identical CSD via different kinetic paths (rates C, D, E). Rate functions are: exponential nucleation and constant growth (A, B, C), exponentially increasing growth rate and corresponding numerically determined nucleation rate (D), and exponentially decreasing growth rate and corresponding nucleation rate (E). See table Electronic Appendix 4.1. Symbols lu and tu are arbitrary length and time units, respectively.*

power-law relationship between I and H was tested in exploratory manner but it has no qualitative effect on the results.

The rates of nucleation and growth were chosen to obtain textures with straight log-linear CSDs in the limiting case of no heterogeneous nucleation. Several combinations of rate functions (Fig. 4.1; table Electronic Appendix 4.1) producing textures with straight CSDs, including exponential rate of nucleation and constant rate of growth (Marsh, 1998; Špillar & Dolejš 2013) were tested in order to address potential dependence of the resulting textures on the rates of nucleation and growth (Section 4.3.5). For each pair of the nucleation and the growth rate functions, the proportionality constant, ξ, was varied in order to obtain a series of textures with progressively increasing ratio of the heterogeneous to homogeneous nuclei numbers, N. First, the ξ was set to zero and a purely homogeneous nucleation texture with $N = 0$ was produced as a reference case. About ten subsequent simulations used progressively greater positive values of ξ (up to 1-10), leading to N in the order of hundreds, i.e., strong

predominance of the heterogeneous nuclei in the resulting texture. Generally, the N ratio evolves during progressive crystallization in a single simulation run because the crystal surface area available for heterogeneous nucleation increases as the crystallization progresses.

The predicted slopes of the CSDs in the natural logarithm of the population density *vs*. grain size space varied over two orders of magnitude, and this covers substantial part of the variations from natural plutonic to volcanic rocks (e.g., Marsh, 1998; Zieg & Marsh, 2002). In the majority of simulations the growth rate of all crystals was considered to be identical in three perpendicular directions and crystals therefore grew as cubes until impinged. Additional simulations for various anisotropic growth rates (inequant crystal morphologies including prisms and plates) were also performed.

4.2.2. Quantitative description of simulated textures

The three-dimensional simulation volume was sectioned by a two-dimensional plane during and after the solidification, in which apparent CSDs, spatial, and contact parameters of the grain population were evaluated. Using this approach, the simulation results are directly comparable to the measurements in petrographic thin section without introducing artifacts related to stereological transformation.

The sections are raster images, 1000 by 1000 pixels large, due to voxel nature of the simulation algorithm, and they capture hundreds to thousands of individual crystals. Raster sections are post-processed to provide apparent size in a two-dimensional section, L_{2D}, number of neighbors, η, the average neighbor distance, ρ, and the coordinates of the center of mass for all grains in the section (Fig. 4.2, for details, see Špillar & Dolejš, 2014). Only those crystals that are not trimmed by the domain edge are used in further analysis. We estimate the apparent crystal size, L_{2D}, as a diameter of equal-area circle. This definition of crystal size is preferred over more complex methods (e.g., Higgins, 2006) due to its simplicity and robustness to variations in the crystal shape (Špillar & Dolejš, 2014). As (contact) neighbors we consider only those grains that share part of their boundary in the section. Consideration of

textural parameters in a two-dimensional section is preferred over the use of the true three-dimensional data because it is more simple and it enables direct comparison with the data from petrographic thin sections, where stereological corrections would be ambiguous or impossible. All CSDs are constructed using the two-dimensional crystal size, L_{2D}. Ten bins of the crystal size are employed and the bin sizes are exponential (e.g., Higgins, 2000); each bin is 1.2 times wider than the previous one.

The clustering index, R, of the simulated texture (Jerram et al., 1996) is evaluated using the following procedure: each crystal is first represented by its center in a two-dimensional section and the entire texture pattern is thus simplified to a set of points. The nearest neighbor for each crystal center (point) is identified and the nearest neighbor distances are arithmetically averaged over all points (crystals) in the texture. The clustering index, R, is calculated as a ratio of the observed average nearest neighbor distance to its theoretically derived value in a randomly distributed set of points (Jerram et al., 1996). The value of $R = 1$ thus indicates random distribution, whereas lower values point to clustering. The values of $R > 1$ indicate greater than random distances between the points and are attributed to ordered (anticlustered) distribution (e.g., Jerram et al., 1996, 2003). Apart from the clustering index, the spatial distribution pattern of the texture is characterized by the apparent number of the contact neighbors of each crystal and by their center-to-center distances.

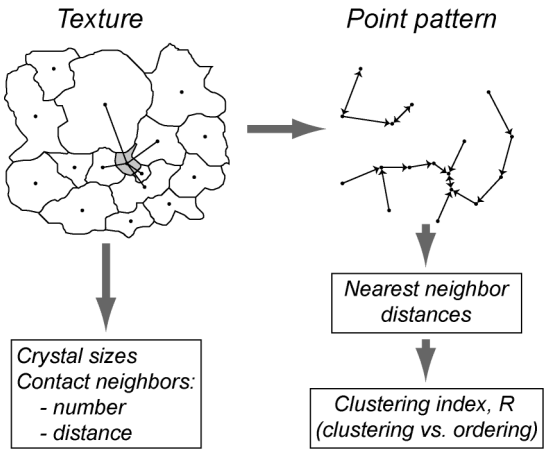

Fig. 4.2. *Contact and spatial parameters measured in a texture and in a corresponding point patters. A random grain with its contact neighbors are highlighted in a texture. Average neighbor distance of a grain is calculated as a mean of the distances to all contact neighbors of the grain. In a point pattern, the nearest neighbor distances used to calculate the clustering index, R, are indicated by arrows. Modified from Špillar & Dolejš (2014).*

Each textural simulation was repeated ten times to constrain confidence intervals of the resulting quantities (table Electronic Appendix 4.2). Because the crystallization is determined by random positions and orientations of the nuclei, repeated runs of a simulation with the same kinetic and other settings can also be regarded as multiple samplings of a single texture. Therefore, all textural parameters from ten repetitive simulations were averaged to

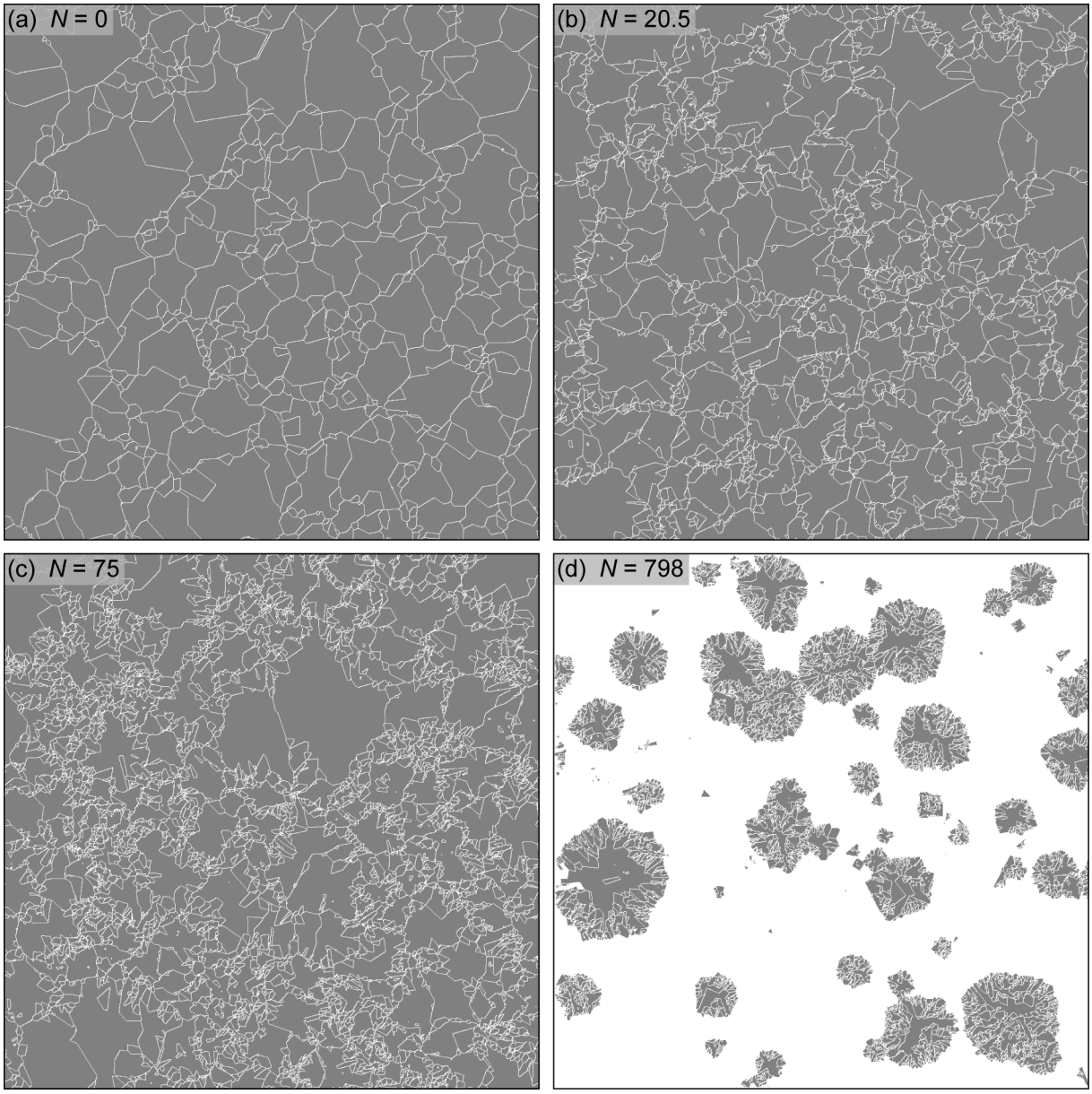

Fig. 4.3. *Representative simulated textures with various ratios of the numbers of heterogeneous to homogeneous nuclei, N.* **(a)** *N = 0, homogeneous nucleation only.* **(b)** *N = 20.45 (95 % of heterogeneous nuclei), serial texture.* **(c)** *N = 75 (98.7 % of heterogeneous nuclei), porphyritic texture.* **(d)** *N = 798 (99.9 % of heterogeneous nuclei), spherulitic texture (intensive heterogeneous nucleation). The % het. nucl. shortcut stands for the percentage of heterogeneous nuclei. Each texture is 1 length unit across. The textures are produced using the nucleation and the growth rate C (Fig. 4.1).*

yield statistically robust and representative results. The strategy of repetitive simulations was used instead of evaluating multiple sections through the simulation domain because the computational grid is inhomogeneous and refined in the vicinity of the sectioning plane (passing through the center of the simulation domain). Based on our modeling results we propose a series of fits that link size and spatial parameters to the ratio of heterogeneous to homogeneous nuclei, *N*. These correlation relationships enable multiple values of *N* to be estimated for a given natural texture using multiple textural parameters and to assess what other processes affected the crystallization.

4.3. Results

4.3.1. General textural observations

Set of 98 simulations (table Electronic Appendix 4.2) with variable CSD slopes, combinations of the nucleation and growth rate functions, growth rate anisotropy, and for various fractions of heterogeneous nuclei were performed. Each simulation was repeated 10 times with identical settings in order to average the results. The simulation set revealed that an increasing fraction of crystals originating as heterogeneous nuclei affects both qualitative texture appearance and its quantitative descriptors, although the system can accommodate surprisingly large number of heterogeneous nuclei before they are recognized visually. Effects of heterogeneous nucleation become discernible at $N \approx 2$ (i.e., when the heterogeneously nucleating crystals are about twice more abundant than their homogeneous counterparts, corresponding to ~65 % heterogeneous nuclei) and are manifested by an increased number of small interstitial crystals surrounding large grains. As *N* increases further, the texture becomes serial ($N \approx 20$; ~95 % heterogeneous nuclei) and eventually porphyritic ($N \approx 75$; ~99 % heterogeneous nuclei), whereby margins of the phenocrysts are intergrown with the matrix (Fig. 4.3; animations Electronic Appendices 4.3 and 4.4; Electronic Appendix 4.5). Radial rims of the wedge-shaped crystals bordering larger grains are common. At *N* on the order of

hundreds (> 99 % of heterogeneous nuclei), the crystallization proceeds by nucleation and growth of heterogeneous nuclei on isolated clusters and a spherulitic texture forms (Fig. 4.3d). Since crystallization inherently starts with the formation of homogeneous nuclei, the N ratio always increases during the crystallization. This is in agreement with progressive increase in the surface area of all homogeneous and heterogeneous crystals, which further accelerates heterogeneous nucleation.

4.3.2. Curvature of crystal size distributions

The resulting textural sequence, as N increases, is quantitatively recorded in the systematic variations of the CSDs (Fig. 4.4a). For homogeneous nucleation only ($N = 0$; 0 % heterogeneous nuclei), the CSD is straight in a log-linear projection with a minor decrease in the population of the smallest crystal sizes. This depletion in very fine crystal fraction results from diminishing of the melt volume available for new nucleation during the final stages of crystallization in a closed system (Marsh, 1998). With increasing N, the CSD progressively curves up due to increasing population of small crystals originating as heterogeneous nuclei while the distribution of larger crystals remains unaffected. In order to characterize the shape of the curved CSDs, we evaluate the slope of its steeper, b_1, and shallower, b_2, segments and use the b_1/b_2 slope ratio as quantitative measure of the CSD curvature. To obtain value of b_1 we use linear fit through population densities in the third, fourth and fifth crystal size bin, because the population densities of the smallest crystal fractions are strongly affected by effects of closed-system crystallization. For the b_2 slope, we fit the population densities in the second to fourth last crystal size bin to eliminate large error on the density of large but very few crystals. This method of evaluating two piecewise slopes is preferred over more robust fits (e.g., sum of two negative exponentials) due to convergence issues arising during fitting of such complex functional forms. Conventional use of the logarithmic scale for the population density ensures that the superposition of the two straight lines produces a gradual curvature. Simulated curved CSDs are thus accurately described by the two values of slope.

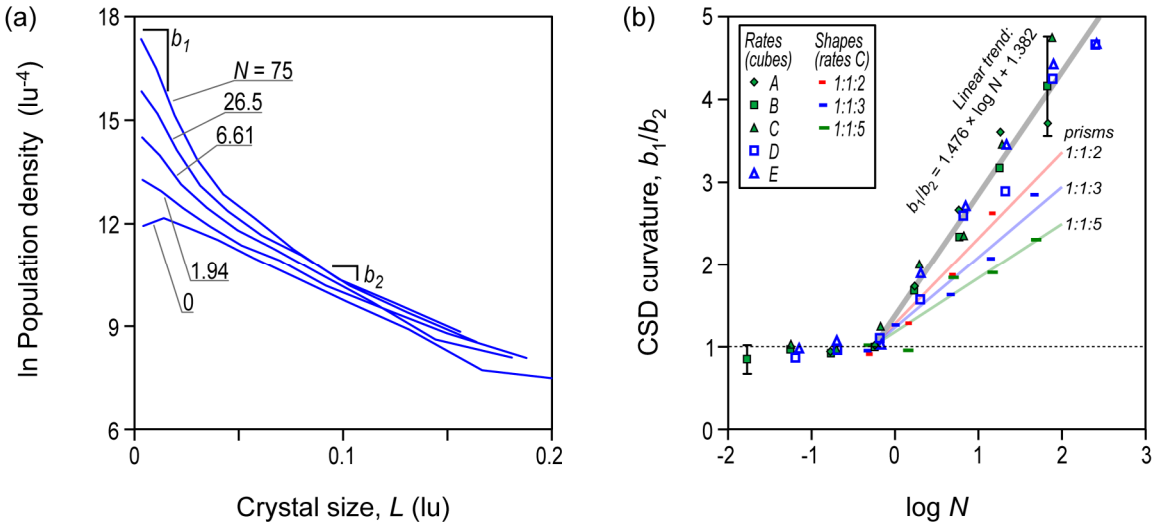

Fig. 4.4. (a) *crystal size distribution of textures with progressively increasing fraction of heterogeneous nuclei, N. Data points are in the middle of the bins and interpolated dotted lines illustrate slopes b_1 and b_2. Nucleation and growth rate functions used in crystallization simulations are rates C (Fig. 4.1). The diameter of equal-area circle is considered as crystal size, L_{2D}, which ensures simple comparison with two-dimensional natural data from the thin-sections.* **(b)** *crvature of the CSDs (b_1 to b_2 slope ratio) as a function of N. Simulations for cubic crystals (with various kinetic rates, A, B, C, D, and E as defined in Fig. 4.1 and Electronic Appendix 4.1) and prismatic crystal shapes (with various elongations and fixed kinetic rate C) are compared. Simulations are at full crystallinity, Φ = 100 %. Other crystallinities provide indistinguishable results. Note that the textures resulting from various kinetic rate functions define common trend of the CSD curvature. Indicated error bars are representative 2σ confidence intervals as determined from 10 repetitive crystallization simulations. The ticks on the vertical axis show measured values of the CSD curvature in natural samples. The % het. nucl. shortcut stands for the percentage of heterogeneous nuclei and lu are arbitrary length units.*

The CSD curvature, as expressed by the b_1/b_2 value, correlates positively with the logarithm of N. The b_1/b_2 ratio is used instead of the slope b_1 itself because the ration is dimensionless and therefore unrelated to the characteristic grain size of the texture. For N below ~1 (< 50 % heterogeneous nuclei), the heterogeneous nuclei are too sparse to cause measurable textural effect and the b_1/b_2 value fluctuates within the range of 0.2 around unity. However, as N increases above ~1, the b_1/b_2 ratio also increases and it yields a common trend that is identical for all simulated textures and is independent of b_2 (Fig. 4.4, Tab. 4.1). The relationship between N and b_1/b_2 is therefore invariant with respect to the rate of homogeneous nucleation and to the growth rate. This simple heuristic relationship also holds true for hemicrystalline textures that did not reach 100 % crystallinity and it may serve for estimating the proportion of heterogeneous nuclei from textural data of natural igneous rocks as discussed further below.

***Tab. 4.1**. Empirical fits for functional relationships between N and texture parameters.*

Texture parameter	Fitted relationship
CSD curvature, b_1/b_2	$\frac{b_1}{b_2} = 1.382 + 1.476 \times \log N$ Calibration range of log *N*: from -0.2 to 2.4.
Clustering index, R	$R = \frac{p_1 x^2 + p_2 x + p_3}{x^2 + q_1 x + q_2}$, where $x = \log N$ Fit parameters and calibration ranges as a function of crystallinity, Φ:

Φ	p_1	p_2	p_3	q_1	q_2	Calibration range (log *N*)	
						from	to
1	1.059	-2.577	3.117	-2.273	3.027	-2	2.4
0.5	1.056	-3.318	4.069	-2.814	3.918	-2	1.9
0.4	1.039	-3.303	4.064	-2.806	4.026	-2	1.7
0.3	1.022	-3.176	3.493	-2.749	3.569	-2	1.6
0.2	0.9809	-2.731	2.866	-2.382	3.042	-2	1.4
0.1	0.9558	-1.922	1.396	-1.778	1.542	-2	1.1

Calibration for all CSD slopes.

Slope of the neighbor number dependence on crystal size, η_S	$\eta_S = p_1 x^3 + p_2 x^2 + p_3 x + p_4$, where $x = \log N$ Fit parameters and calibration ranges as a function of crystallinity, Φ:

Φ	p_1	p_2	p_3	p_4	Calibration range (log *N*)	
					from	to
1	0.0128	0.0790	0.1466	2.0455	-0.8	1.8
0.5	0.0476	0.1616	0.1943	1.5862	-0.8	1.3
0.3	0.0410	0.2105	0.3007	1.3137	-0.9	1.1
0.2	0.0357	0.2353	0.3828	1.1445	-0.6	0.9

Calibration for the slope of shallower part of the CSD, b_2 = -29 lu^{-1}. Before use in a texture with arbitrary CSD slope, $b_2^{arbitrary}$, measured value of the $\eta_S^{arbitrary}$ must be first recalculated to its equivalent value, η_S^{29} useful with present calibration *:

$$\log \eta_S^{29} = \log \eta_S^{arbitrary} + \log \frac{29}{-b_2^{arbitrary}} .$$

Intercept of the average neighbor distance dependence on crystal size, ρ_I

$\rho_I = p_1 x^4 + p_2 x^3 + p_3 x^2 + p_4 x + p_5$, where $x = \log N$

Fit parameters and calibration ranges as a function of crystallinity, Φ:

Φ	p_1	p_2	p_3	p_4	p_5	Calibration range (log N)	
						from	to
1	-0.0020	-0.0188	-0.0559	-0.0627	-1.5345	-0.8	1.8
0.5	0	0	-0.0543	-0.0877	-1.4565	-0.8	1.3
0.3	0	-0.0051	-0.0332	-0.0588	-1.4501	-0.9	1.1
0.2	0	0	-0.0303	-0.0676	-1.4334	-0.6	0.9

Calibration for the slope of shallower part of the CSD, b_2 = -29 lu^{-1}. Before use in a texture with arbitrary CSD slope, $b_2^{arbitrary}$, measured value of the $\rho_I^{arbitrary}$ must be first recalculated to its equivalent value, ρ_I^{29} useful with present calibration *:

$$\log \rho_I^{29} = \log \rho_I^{arbitrary} - \log \frac{29}{-b_2^{arbitrary}}.$$

* Units lu are arbitrary length units. CSD slope is considered using natural log units of the population density.

4.3.3. Contact relationships and spatial distribution patterns

Qualitative inspection of textural variations with changing N suggests that additional contact and spatial parameters of a crystal population in a two-dimensional section vary according to the fraction of heterogeneous nuclei. We will now introduce set of contact parameters which will be subsequently used for interpretation of natural samples. In general, the number of contact neighbors of a crystal, η, and the average center-to-center distance between a crystal and its contact neighbors, ρ, when evaluated over discrete size bins, are linear functions of the crystal size (Fig. 4.5). The slopes of the η dependence on crystal size, η_S, and the intercepts of the ρ dependence on crystal size, ρ_I, vary regularly with the fraction of heterogeneous nuclei. Increasing N implies larger number of surrounding interstitial grains, thus η increases more steeply with crystal size; consequently, η_S is higher (Fig. 4.6a). The value of ρ_I behaves in the opposite way and it decreases as N increases (Fig. 4.6b). Both trends of η_S and ρ_I as a function of N depend on the volume fraction of solid phase

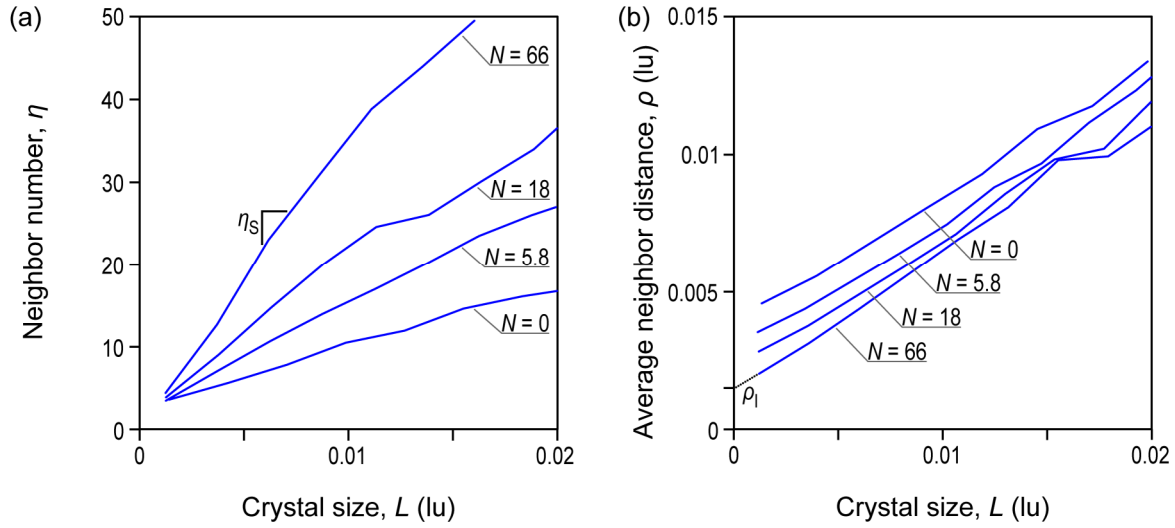

Fig. 4.5. (a) *nighbor number, η, and* **(b)** *average neighbor distance, ρ, as a function of the crystal size, L_{2D}. As the ratio of the heterogeneous to homogeneous nuclei number, N, increases the slope, η_S, also increases and the intercept, ρ_l, reduces. The % het. nucl. shortcut stands for the percentage of heterogeneous nuclei and lu are arbitrary length units. The nucleation and the growth rates used in crystallization simulations are rates B (Fig. 4.1) and all parameters are derived from textures with 100 % crystallinity.*

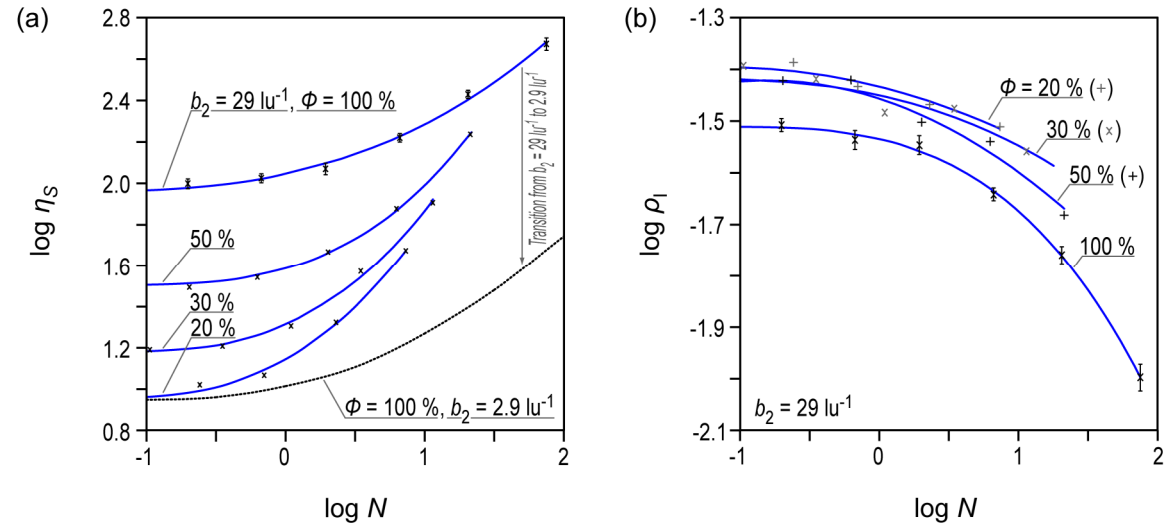

Fig. 4.6. *Contact parameters as functions of the ratio N.* **(a)** *sope of the dependence of neighbor number on crystal size, η_S.* **(b)** *intercept of the dependence of average neighbor distance on crystal size, ρ_l. The curves are functions of the volume fraction of crystals, Φ, and they scale with the slope of a shallower CSD segment, b_2 (see text). The % het. nucl. shortcut stands for the percentage of heterogeneous nuclei. The nucleation and the growth rates used in crystallization simulations for textures with CSD slope b_2 = -29 lu^{-1} are rates C (Fig. 4.1). The symbol lu are arbitrary length units. Error bars are 2σ confidence intervals determined from 10 repetitive crystallization simulations.*

(crystallinity); at lower crystal fractions the trends are steeper (Fig. 4.6, Tab. 4.1). At full crystallinity, η_S and ρ_I differ by ~0.6 orders of magnitude as N increases from 0.1 to 100 (10 to 99 % heterogeneous nuclei).

In contrast to the dimensionless CSD curvature, ρ_I and η_S have units of length and reciprocal length, respectively, which suggests that each value additionally depends on the characteristic length scale of texture. Before η_S and ρ_I can be used to estimate N in an arbitrary texture the values must be first transformed to the length scale of a texture for which the trends of η_S and ρ_I as a function of N are provided by the numerical model. Such simple scaling relationships aid interpretation of natural textures. We consider the characteristic grain size which is inversely proportional to the negative CSD slope, b_2, (e.g., Marsh 1998) as the characteristic length scale of texture. The CSD slope b_2 is used as a texture descriptor independent of the value of N, which is generally unknown prior to the transformation procedure. Based on simulations performed for various slopes b_2, the simple relationships for transforming of ρ_I and η_S between two textures (*cf.* Fig. 4.6a) were derived:

$$\begin{aligned} \log \eta_S^A &= \log \eta_S^B + \log \frac{b_2^A}{b_2^B}, \\ \log \rho_I^A &= \log \rho_I^B - \log \frac{b_2^A}{b_2^B}, \end{aligned} \tag{4.1}$$

where superscripts A and B denote two different textures. Using the above relationships, ρ_I and η_S can be converted from texture with a unique CSD slope to equivalent values for texture with another CSD slope.

Experimental studies demonstrated that heterogeneous nucleation leads to increased clustering of crystals (Hammer et al., 2010). Our simulations demonstrate similar effect of heterogeneous nucleation and show that with increasing fraction of heterogeneous nuclei, N, crystals are progressively more clustered and the clustering index, R decreases (Fig. 4.7, Tab. 4.1). The relationship between N and R is identical for all textures irrespective of their CSD slopes, which is similar to the behavior of CSD curvature. The N vs. R trend, however, depends on the volume fraction of crystals, which is a measurable quantity both in

simulations and in natural samples. Clustering is more pronounced at lower crystallinities and it is reduced as volume fraction of crystals increases. At 100 % crystallinity, the clustering index decreases from approximately 1.08 to 0.85 as N increases from zero to 100 (0 to 99 % heterogeneous nuclei; Fig. 4.7). With the clustering index greater than unity, the textures formed predominantly by homogeneous nucleation ($N < 1$, that is, < 50 % heterogeneous nuclei) are partially ordered. At the constant value of N the clustering index increases with increasing crystallinity. This trend of increasing ordering results from progressive constraining of nuclei into diminishing melt pockets within the expanding crystal framework. However, when N increases, such a trend shifts towards lower values of the clustering index (i.e., more clustered textures) owing to the predominance of heterogeneous nucleation.

At low N values ($N < 1$, i.e., < 50 % heterogeneous nuclei), the ordering increases with increasing crystallinity beyond 50 % crystals in the magma, but subsequently decreases as the full crystallinity is approached (*cf.* $\Phi \leq 50$ % *vs.* $\Phi = 100$ % in Fig. 4.7). Such a decrease of ordering and return towards more random crystal distribution is a consequence of large number of new crystals nucleating randomly in the interstitial melt pockets (see also Špillar & Dolejš, 2014).

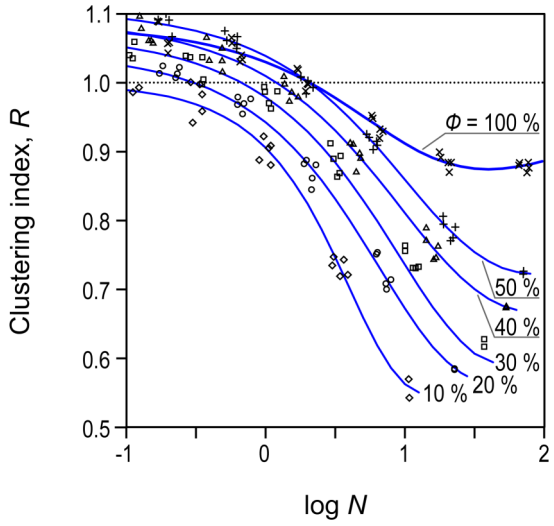

Fig. 4.7. *Clustering index, R, as a function of the ratio N. Individual curves and point symbols are for various volume fractions of crystals, Φ. At any value of Φ, various kinetic rate functions define common trends and are considered jointly. The % het. nucl. shortcut stands for the percentage of heterogeneous nuclei. The ticks on the vertical axes show measured values of the CSD curvature in natural samples.*

4.3.4. Effect of anisotropic crystal growth

The majority of simulations were performed with crystals growing isotropically in three dimensions, that is, the euhedral shape is cubic. Additional simulations for various prismatic, tabular and intermediate crystal geometries reveal that the resulting textural descriptors show greater scatter and are subject to larger uncertainties than in the case of cubic growth. This is due to (*i*) a large number of possible configurations that any inequant crystal can have with respect to the sectioning plane. Therefore, a greater number of crystals is needed to provide statistically representative sample; (*ii*) inequant crystals sectioned near their larger dimension are likely to be more often trimmed by the domain boundary, hence edge effects become significant.

All textural parameters and their relationships to the heterogeneous to homogeneous nuclei number ratio, N, are quantitatively affected by the growth shape of crystals. For increasingly prismatic shapes up to 1:1:5, the CSD curvature is reduced when compared to that for the cubes at any value of N (Fig. 4.4b). The CSD curvature for tabular crystal shapes is also less than that for cubes but the distinction between individual tabular and intermediate tabular-prismatic shapes is much less obvious due to large uncertainties.

The clustering index, R, *vs*. N curves are almost identical for all crystal geometries at low crystallinities. At higher crystallinity, the value of R for prisms and plates is closer to unity than for cubes at identical N and the total range of variations of R is reduced (figures Electronic Appendix 4.6a, b). The η_S values for inequant crystal geometries are slightly greater than for cubes but the difference diminishes as N increases and η_S for cubes eventually becomes greater than for the inequant shapes (figures Electronic Appendix 4.6c, d).

In general, inequant crystal morphologies lead to slight modification of the relationships between N and textural descriptors. Use of the relationships derived for cubic crystal geometries for textures with arbitrary crystal shapes will in most cases only provide the minimum limit for the proportion of heterogeneous nuclei, N. More precise estimates of N for textures with arbitrary crystal morphologies require crystallization simulations performed for the specific crystal shape of interest.

4.3.5. Role of kinetic path of crystallization

Closed system crystallization and the resulting texture are uniquely defined by temporal evolution of the rates of nucleation and growth. Inverse textural interpretation, however, is non-unique and any texture can be reproduced by multiple combinations of both rate functions (Špillar & Dolejš, 2014), e.g., by multiple kinetic paths.

We have tested sensitivity of the simulations to multiple combinations of the nucleation and growth rate functions that all produce textures with identical CSD (Fig. 4.4b). The textures with the same value of heterogeneous to homogeneous nuclei number ratio, N, but employing various pairs of the rate functions yield identical results for all textural descriptors. Therefore, relationships between N and textural descriptors are universal and invariant with respect to nucleation and growth rate function. This enables application of our results and calibrations to estimation of N in natural or synthetic experimental samples, where the nucleation and growth rate functions are unknown.

4.4. Interpretation of natural igneous textures

4.4.1. Methodology

The relationships between textural descriptors and the heterogeneous to homogeneous nuclei number ratio, N, derived from the crystallization simulations (Tab. 4.1) can be employed to estimate the fraction of heterogeneously nucleating crystals in natural igneous rocks. To illustrate the approach and results, we performed complete textural analysis on five samples covering volcanic, plutonic and cumulate rocks (Tab. 4.2, Fig. 4.8). The sample CS-12 is porphyritic trachybasalt with 17 vol. % clinopyroxene phenocrysts dispersed in fine-grained matrix (Ulrych & Pivec, 1997; Ulrych et al., 2002, 2011) and only the phenocryst population was analyzed in this sample. Other samples are holocrystalline granites from the Fichtelgebirge batholith (e.g., Hecht et al., 1997; Siebel et al., 1997, 2010) and dunite

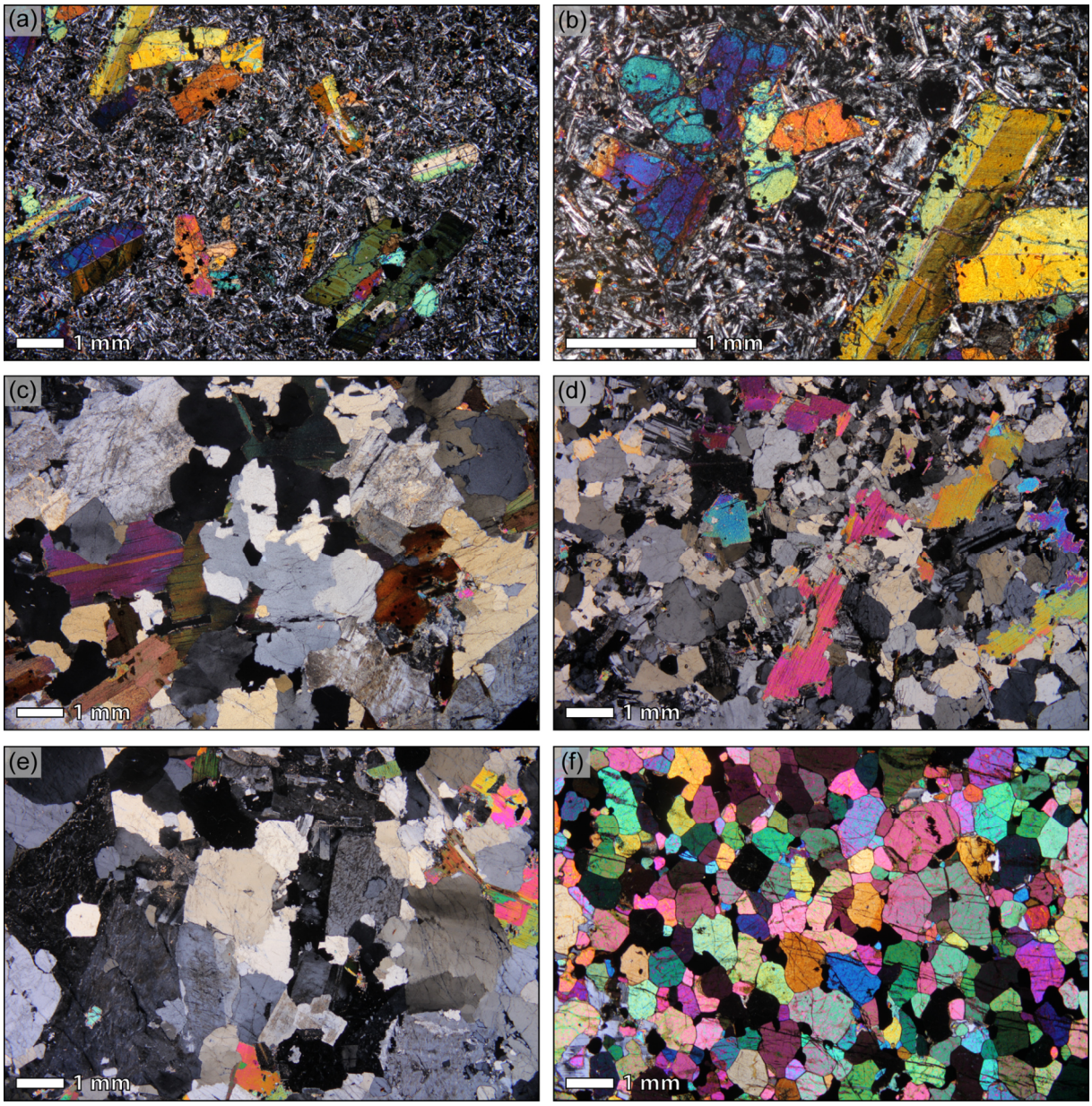

Fig. 4.8. *Photomicrographs of individual rocks samples (crossed polarizers).* **(a)** *porphyritic trachybasalt with clinopyroxene phenocrysts, CS-12.* **(b)** *a cluster of clinopyroxen phenocrysts in the CS-12 sample.* **(c)** *weakly porphyritic coarse-grained granite, FG-25.* **(d)** *equigranular medium-grained granite, FG-51.* **(e)** *weakly porphyritic coarse-grained granite, FG-63.* **(f)** *dunite cumulate, KD-3.*

cumulate from the Kdyně mafic intrusion (Vejnar, 1986; Bues et al., 2002; Dörr et al., 1998, 2002); entire crystal population (100 vol. %) was employed in the analysis. In the polymineralic samples, all mineral phases are considered jointly in the textural analysis. This approach provides valid estimate of N when individual minerals have comparable surface properties relevant for heterogeneous nucleation intensity. By contrast, if kinetic properties of

Tab. 4.2. *Sample description.*

Sample	Description	Crystallinity	Geological unit and location	Age (Ma)
CS-12	Porphyritic trachybasalt with clinopyroxene phenocrysts.	17 %	České středohoří Mts. N 50.6171° E 14.3688°	31-25 [(a)]
FG-25	Weakly porphyritic coarse-grained two-mica granite, G3 variety.	100 %	Fichtelgebirge batholith N 49.9998° E 11.9472°	291[(b)]
FG-51	Equigranular medium-grained two mica granite, G1S variety.	100 %	Fichtelgebirge batholith N 50.1254° E 12.1495°	326[(c)]
FG-63	Weakly porphyritic coarse-grained two-mica granite, G3 variety.	100 %	Fichtelgebirge batholith N 50.1412° E 11.8570°	291[(b)]
KD-3	Dunite cumulate with ilmenite.	100 %	Kdyně basic intrusion N 49.3373° E 13.0752°	524[(d)]

All coordinates are in WGS84 format.

References: [(a)] Ulrych et al. 2002; [(b)] Siebel et al. 2010; [(c)] Hecht et al. 1997; [(d)] Dörr et al. 1998.

Tab 4.3. *Textural parameters and estimates of the fraction of heterogeneous nuclei.*

Parameter \ Sample	CS-12	FG-25	FG-51	FG-63	KD-3
b_2 (mm^{-1})	-1.8	-0.7	-2.5	-1.0	-2.5
b_1/b_2	2.06	2.71	3.88	3.20	2.0
% het. nuclei	**74** (59; 85)	**89** (79; 94)	**98** (95; 99)	**94** (88; 97)	**72** (57; 84)
R	0.811	1.013	1.051	1.038	1.074
% het. nuclei	**77** (72; 80)	**61** (43; 72)	**32** (6; 52)	**44** (19; 61)	**7** (0; 32)
log η_S (mm^{-1})	-0.043	0.613	1.332	0.817	1.0
% het. nuclei	**63** (59; 67)	**88** (86; 90)	**95.7** (94.6; 95.8)	**91.7** (89.2; 92.1)	**57** (48; 65)
log ρ_I (mm)	-0.597	-0.080	-1.138	-0.287	-0.665
% het. nuclei	**~100** [(a)]	**91.7** (90.3; 92.8)	**99.40** (99.36; 99.44)	**94.3** (94.2; 95.6)	**94.2** (93.3; 95.0)

The % het. nuclei is the percentage of heterogeneous nuclei in a texture based on individual textural parameters and it is calculated as $N / (N + 1) \times 100$ %, where N is the ratio of numbers of heterogeneous to homogeneous nuclei. Relationships for calculating of N from the textural parameters are given in Tab. 4.1. The values in brackets represent 2σ confidence intervals and are obtained from the bounds of relationship between the textural parameter *vs*. fraction of heterogeneous nuclei as derived from repetitive crystallization simulations.

Symbols: b_1, b_2 – slopes of the shallower and steeper part of the CSD, respectively; b_1/b_2 – CSD curvature; R – clustering index; η_S – slope of the neighbor number dependence on crystal size; ρ_I – intercept of the average neighbor number dependence on crystal size.

Comment: [(a)] calculation of the fraction of heterogeneous nuclei based on the ρ_I diverges in case of the CS-12 sample; therefore the percentage of heterogeneous nuclei is close to 100.

individual minerals were different, then the resulting N represents an average value for the crystallizing assemblage. In addition, complete textural analysis allows comparison of the approaches based on different textural parameters and identification of any inconsistencies in estimates of heterogeneous nuclei fraction between individual methods.

Standard or large thin sections (13 to 140 cm^2) were prepared and scanned in plane polarized light. Orientations of individual thin sections were chosen at random as our samples do not show any macroscopic fabric or preferred orientation of crystals. One thin section was prepared from each sample and the section size was adapted to adequately represent the rock texture and to include a large number (several hundreds to thousands) of individual crystals. In raster images, crystal outlines were traced using a drawing tablet and commercial image editing software. Multiple images in various orientations with respect to the light polarization plane were used in order to accurately separate individual touching crystals. Custom image analysis program and R language facilities (R Development Core Team 2011) were used to evaluate CSD curvature (b_1/b_2), clustering index (R), slope of the dependence of the number of contact neighbors on crystal size (η_S), and intercept of the dependence of the average contact neighbor distance on crystal size (ρ_I) for each sample. In order to determine the fraction of heterogeneous nuclei in the sample, quantitative relationships between N and textural descriptors were calibrated using our simulation results (Tab. 4.1).

4.4.2. Results and discussion

Trachybasalt, CS-12, yields ~70 % heterogeneous and ~30 % homogeneous nuclei ($N \approx 2.3$) for its population of clinopyroxene phenocrysts. Independent estimates from the CSD curvature, clustering index, and neighbor number are all consistent within their 95 % confidence intervals (Fig. 4.9, Tab. 4.3). The estimate based on the average neighbor distance, however, is significantly greater and it yields nearly 100 % heterogeneous nuclei. All granite samples, FG, irrespective of textural variety, yield comparable estimates of ~90 to 98 % heterogeneous nuclei ($N \approx 10$ to 50) based on the CSD curvature, neighbor number, and

neighbor distances. However, the estimates using clustering index are significantly lower for all granite samples, ~30 to 60 % heterogeneous nuclei ($N \approx 0.4$ to 1.5; Fig. 4.9, Tab. 4.3). Dunite cumulate, KD-3, yields ~60 to 70 % heterogeneous nuclei ($N \approx 1.5$ to 2.3) when using the CSD curvature and neighbor number, whereas the estimates based on the clustering index and the average neighbor distance are significantly different, yielding ~7 and ~95 % heterogeneous nuclei ($N \approx 0.1$ and 20), respectively (Fig. 4.9, Tab. 4.3).

Generally, consistent estimates of the fraction of heterogeneous nuclei provided by independent textural parameters indicate kinetic crystallization in a closed system without additional mechanical crystal-melt interaction or modification by annealing or coarsening. On the other hand, discrepancies between estimates using distinct textural descriptors help identify involvement of other physicochemical or mechanical process(es) during crystallization. Explanation of textural patterns observed in our samples requires at least two such processes: (*i*) process A that increases the clustering index hence lowers the estimate of N based on the clustering index, but has no effect on other textural characteristics; (*ii*) process B that reduces the value of ρ_I, thus increases the estimate of N calculated from the average

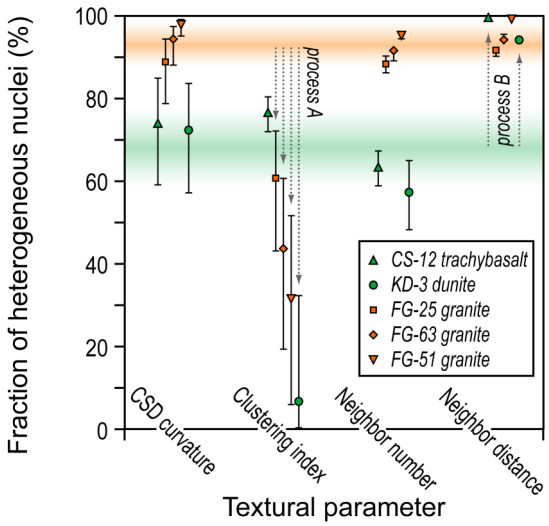

Fig. 4.9. *Estimate of the heterogeneous nuclei fraction in natural samples using four independent textural parameters. All error bars represent 2σ confidence intervals and are obtained from the bounds of the textural parameter vs. heterogeneous nuclei fraction relationships, as derived from repetitive crystallization simulations. Where not shown the error bars are smaller than the symbol size. N is the ratio of heterogeneous to homogeneous nuclei number and the symbol ∞ stands for infinite value of N. See text for the discussion on hypothetical processes A and B.*

neighbor distances. The process A was involved in the crystallization of all granite samples whereas the process B occurred in the sample of trachybasalt, and a combination of both A and B is required in case of the dunite cumulate (Fig. 4.9).

Compaction of the crystal suspension, that is, extraction of interstitial melt, is known to increase the value of the clustering index of a texture (e.g., Jerram et al., 1996). To illustrate, all crystals and crystal aggregates are compressed into a smaller volume during melt extraction. Individual crystals, however, cannot approach each other more closely than is the sum of their respective sizes. Therefore, the crystals during melt extraction event remain more distant, the clustering index increases and the texture is seen as more ordered. As the system acquires smaller volume, the population densities of all crystal sizes increase during compaction, but their relative proportions and therefore the CSD curvature remain unaffected. Due to the increase of crystallinity, extraction of the interstitial melt enhances the incidence of touching crystals and it therefore modifies the contact relationships of the rock texture. Since compaction causes relative increase of crystallinity and population density in the same way as progressive closed-system crystallization, we expect that the melt extraction modifies contact relationships in similar way as progressive crystallization and continuing growth. This assumption is valid in dilute magma suspensions, but it is violated in textures which were compacted to a large extent and compaction fabric started to develop. Our samples, however, show no apparent fabric and the amount of compaction is expected to have been within the limits of a magma mush of randomly oriented crystals. We propose that the clustering index is expected to be the textural descriptor most sensitive to the melt extraction. In view of these considerations, the process A is most likely melt extraction and/or compaction of the crystal suspension. This is consistent with appearance of process A in plutonic samples only and this finding implies that both the granites and the dunite cumulate, as expected, have lost portion of interstitial residual melt.

The process B is characterized by reduction of the ρ_1 value, that is, reduction of the average contact neighbor distances, while keeping other textural descriptors unmodified. A simple plausible way of reducing the average distance to the contact neighbors of any grain but not altering the number of neighbors is to align the orientations of neighboring crystals so

that the distance between their centers is shorter than it would be in the case of random orientation. Oriented attachment of crystals is possible, e.g., as a result of synneusis due to hydrodynamic interactions in turbulent suspension (e.g., Schwindinger, 1999) or when compaction fabric starts to develop. Alternatively, formation of oriented intergrowths was proposed to result from heterogeneous nucleation itself when orientation of heterogeneous nuclei is predetermined by the structure of substrate and nucleus phases (e.g., Hammer et al., 2010). The process B was particularly extensive in samples of trachybasalt and dunite cumulate, where we evaluate a *single mineral* textural pattern. Oriented heterogeneous nucleation may therefore provide an explanation for anomalously high estimate of the heterogeneous nuclei fraction based on the neighbor distances in the CS-12 and KD-3 samples, in contrast to slightly elevated values obtained in all granite samples, which are polymineralic (Fig. 4.9).

Despite the limitations resulting from exploratory application of numerical modeling and complete textural analysis, we propose that combination of heterogeneous nucleation with other processes consistently explains quantitative textural patterns observed in various rock types. The combined use of other, less conventional, textural descriptors can identify and discriminate other kinetic or mechanical processes active during magma crystallization. As demonstrated in this study, clustering index is particularly sensitive to texture modification by melt extraction and/or crystal mush compaction. In addition to predicting consistently high fraction of heterogeneous nuclei in both volcanic and plutonic samples, the independent textural descriptors point to operation of selective mechanisms of heterogeneous nucleation, which are likely to be identified in single-phase textural patterns.

In summary, we suggest that the highest amount of heterogeneous nuclei, ~90 to 98 % ($N \approx 10$ to 50), appears in all granite samples. Significant deviation from this range appears in the estimate based on the clustering index which records superimposed effects of heterogeneous nucleation with other process, preferably the extraction of portion of interstitial melt. About 70 % heterogeneous nuclei ($N \approx 2.3$) are found in case of trachybasalt, where all estimates are consistent apart from the one based on the average neighbor distances. The least certain result, 60 to 70 % of heterogeneous nuclei ($N \approx 1.5$ to 2.3), is obtained in case of

dunite cumulate. In this sample, only two of four independent textural descriptors are consistent and both estimates based on the clustering index and on the average neighbor distances deviate. Since the two deviations are similar to those found in the samples of granites and trachybasalt, we suggest that the superimposition of both processes anticipated in above samples is required in case of dunite cumulate.

4.5. Implication for magma crystallization and crystal-melt interaction

High-resolution numerical simulation of crystallization shows that magmatic textures change systematically with increasing fraction of heterogeneous nuclei. With increasing fraction of heterogeneous nuclei, the number of small crystals in a texture also increases, and the rock gains seriate to porphyritic appearance when the ratio of heterogeneous to homogeneous nuclei number exceeds ~10 (> 90 % heterogeneous nuclei). Multiple textural parameters, including CSD curvature, clustering index, and contact relationships correlate with the ratio of numbers of heterogeneous to homogeneous nuclei, but are insensitive to the nucleation and growth rates of a texture. This heuristic observation allows us to meaningfully determine the fraction of heterogeneous nuclei from natural samples without recourse to the underlying kinetics of crystallization. The curved CSDs enriched in the fine grain fraction frequently observed in volcanic and plutonic rocks (e.g., Armienti et al., 1994; Higgins, 1996, 2002; Higgins & Roberge, 2003; Yang, 2012) were interpreted by discontinuous crystallization or magma mixing, but are now self-consistently explained by heterogeneous crystal nucleation. This finding, when supported by other quantitative textural indicators, implies widespread occurrence of heterogeneous nucleation in nature.

Predominantly heterogeneous mode of nucleation is consistent with lower energy barrier associated with the formation of heterogeneous rather than homogeneous nuclei (e.g., Lasaga, 1998). Extensive to almost exclusive role of heterogeneous nucleation in crystallizing magmas was reported by experimental studies (e.g., Lofgren, 1983). Under high

undercooling, crystals nucleate and grow as spherulitic clusters (Swanson & Fenn, 1986; MacLellan & Trembath, 1991; Baker & Freda, 2001), not dissimilar to those predicted by our numerical models (Fig. 4.3d), or nucleation starts heterogeneously on the walls of experimental container (Fenn, 1977; Swanson, 1977). In addition to heterogeneous nucleation on solid substrates, boundaries of gas bubbles were also reported to act as a substrate for heterogeneous nucleation of crystals (Davis & Ihinger, 1998).

Complete textural analysis and application of new calibration relationships to representative igneous rocks indicates >90 % nuclei ($N > 10$) formed in a heterogeneous manner during polyphase crystallization of granitic magmas, but only ~60 to 70 % heterogeneous nuclei ($N \approx 1.5$ to 2.3) in monomineralic mafic or ultramafic suspensions. Each is a multiple estimate using CSD curvature, clustering index, and contact relationships independently, and any discrepancies point to additional effects of other physico-chemical or mechanical processes. In the specific examples discussed here, plutonic samples including dunite cumulate provide additional independent evidence for interstitial melt extraction, whereas low-fraction volcanic suspension records *oriented* heterogeneous nucleation. If widespread, heterogeneous nucleation is expected to lead to substantial clustering of mineral phases and greater efficiency of crystal settling and residual melt extraction in diverse magmatic systems (e.g., Schwindinger, 1999; Hammer et al., 2010). We argue that complete textural analysis not only demonstrates significant role of heterogeneous nucleation in general, but is capable of unraveling other processes such as crystal movement, mush compaction and melt extraction, or oriented heterogeneous nucleation and growth during magma solidification.

4.6. Acknowledgements

This study was financially supported by the Charles University Research Program P44 and the Czech Science Foundation Project Nr. 210/12/0986. We thank Hana Ditterová for providing us with the quantitative textural data for the sample CS-12. We greatly appreciate

detailed and constructive reviews by George Bergantz, Sarah Gelman, Julia Hammer, Jillian Schleicher and an anonymous reviewer and editorial handling by Mark Ghiorso.

4.7. References

ARMIENTI P., PARESCHI M. T., INNOCENTI F. & POMPILIO M. (1994): Effect of magma storage and ascent on the kinetics of crystal growth. – *Contributions to Mineralogy and Petrology* 115, 402–414.

BACHMANN O. & BERGANTZ G. (2008): The magma reservoirs that feed supereruptions. – *Elements* 4, 17–21.

BAKER D. R. & FREDA C. (2001): Eutectic crystallization in the undercooled Orthoclase-Quartz-H_2O system: experiments and simulations. – *European Journal of Mineralogy* 13, 453–466.

BEA F. (2010): Crystallization dynamics of granite magma chambers in the absence of regional stress: Multiphysics modeling with natural examples. – *Journal of Petrology* 51, 1541–1569.

BRUGGER C. R. & HAMMER J. E. (2010): Crystal size distribution analysis of plagioclase in experimentally decompressed hydrous rhyodacite magma. – *Earth and Planetary Science Letters* 300, 246–254.

BUES C., DÖRR W., FIALA J., VEJNAR Z. & ZULAUF G. (2002): Emplacement depths and radiometric ages of Paleozoic plutons of the Neukirchen-Kdyně massif: differential uplift and exhumation of Cadomian basement due to Carboniferous orogenic collapse (Bohemian Massif). – *Tectonophysics* 352, 225–243.

BURKHARD D. J. M. (2002): Kinetics of crystallization: Example of micro-crystallization in basalt lava. – *Contributions to Mineralogy and Petrology* 142, 724–737.

BURKHART L. E., HOYT R. C. & OOLMAN T. (1980): Control of particle size distribution and agglomeration in continuous precipitations. *In*: KUCZYNSKI G. C. (ed): *Sintering Processes*. – Plenum, New York, pp 23–38.

CASHMAN K. V. & MARSH B. D. (1988): Crystal size distribution (CSD) in rocks and the kinetics and dynamics of crystallization II: Makaopuhi lava lake. – *Contributions to Mineralogy and* Petrology 99, 292–305.

CHRISTIAN J. W. (2002): *The theory of transformations in metals and alloys* (3rd edition). – Elsevier, Oxford, 1113 pp.

DAVIS M. J. & IHINGER P. D. (1998): Heterogeneous crystal nucleation on bubbles in silicate melt. – *American Mineralogist* 83, 1008–1015.

DÖRR W., FIALA J., VEJNAR Z. & ZULAUF G. (1998): U-Pb zircon ages and structural development of metagranitoids of the Teplá Crystalline complex: evidence for pervasive Cambrian plutonism within the Bohemian massif (Czech Republic). – *Geologische Rundschau* 87, 135–149.

DÖRR W., ZULAUF G., FIALA J., FRANKE W. & VEJNAR Z. (2002): Neoproterozoic to Early Cambrian history of an active plate margin in the Teplá-Barrandian unit–a correlation of U-Pb isotopic-dilution-TIMS ages (Bohemia, Czech Republic). – *Tectonophysics* 352, 65–85.

EBERL D. D., KILE D. E. & DRIFTS V. A. (2002): On geological interpretations of crystal size distributions: Constant *vs*. proportionate growth. – *American Mineralogist* 87, 1235–1241.

FENN P. M. (1977): The nucleation and growth of alkali feldspars from hydrous melts. – *Canadian Mineralogist* 15, 135–161.

HAMMER J. E., SHARP T. G. & WESSEL P. (2010): Heterogeneous nucleation and epitaxial growth of magmatic minerals. – *Geology* 38, 367–370.

HECHT L., VIGNERESSE J. L. & MORTEANI G. (1997): Constraints on the origin of zonation of the granite complexes in the Fichtelgebirge (Germany and Czech Republic): Evidence from a gravity and geochemical study. – *Geologische Rundschau* 86, S93-S109.

HERSUM T. G. & MARSH B. D. (2006): Igneous microstructures from kinetic models of crystallization. – *Journal of Volcanology and Geothermal* Research 154, 34–47.

HERSUM T. G. & MARSH B. D. (2007): Igneous textures: On the kinetics behind the words. – *Elements* 3, 247–252.

HIGGINS M. D. (1996): Magma dynamics beneath Kameni volcano, Thera, Greece, as revealed by crystal size and shape measurements. – *Journal of Volcanology and Geothermal Research* 70, 37–48.

HIGGINS M. D. (2000): Measurement of crystal size distributions. – *American Mineralogist* 85, 1105–1116.

HIGGINS M. D. (2002): A crystal size-distribution study of the Kiglapait layered mafic intrusion, Labrador, Canada: Evidence for textural coarsening. – *Contributions to Mineralogy and Petrology* 144, 314–330.

HIGGINS M. D. (2006): *Quantitative textural measurements in igneous and metamorphic petrology*. – Cambridge University Press, Cambridge, 265 pp.

HIGGINS M. D. (2011): Textural coarsening in igneous rocks. – *International Geology Reviev* 53, 354–376.

HIGGINS M. D. & CHANDRASEKHARAM D. (2007): Nature of sub-volcanic magma chambers, Deccan Province, India: Evidence from quantitative textural analysis of plagioclase megacrysts in the Giant Plagioclase Basalts. – *Journal of Petrology* 48, 885–900.

HIGGINS M. D. & ROBERGE J. (2003): Crystal size distribution of plagioclase and amphibole from Soufrière Hills Volcano, Montserrat: Evidence for dynamic crystallization-textural coarsening cycles. – *Journal of Petrology* 44, 1401–1411.

IKEDA S., TORIUMI M., YOSHIDA H. & SHIMIZU I. (2002): Experimental study of the textural development of igneous rocks in the late stage of crystallization: The importance of interfacial energies under non-equilibrium conditions. – *Contributions to Mineralogy and Petrology* 142, 397–415.

JERRAM D. A., CHEADLE M. J., HUNTER R. H. & ELLIOTT M. T. (1996): The spatial distribution of grains and crystals in rocks. – *Contributions to Mineralogy and Petrology* 125, 60–74.

JERRAM D. A., CHEADLE M. J. & PHILPOTTS A. R. (2003): Quantifying the building blocks of igneous rocks: Are clustered crystal frameworks the foundation? – *Journal of Petrology* 44, 2033–2051.

LASAGA A. C. (1998): *Kinetic theory in the Earth sciences*. – Princeton University Press, Princeton, 811 pp.

LOFGREN G. E. (1983): Effect of heterogeneous nucleation on basaltic textures: A dynamic crystallization study. – *Journal of Petrology* 24, 229–255.

MACHLIN E. S. (2007): *An introduction to aspects of thermodynamics and kinetics relevant to materials science* (3rd edition). – Elsevier, Oxford, 461 pp.

MACLELLAN H. E. & TREMBATH L. T. (1991): The role of quartz crystallization in the development and preservation of igneous texture in granitic rocks: Experimental evidence at 1 kbar. – *American Mineralogist* 76, 1291–1305.

MARSH B. D. (1989): Magma chambers. – *Annual Review of Earth and Planetary Sciences* 17, 439–474.

MARSH B. D. (1998): On the interpretation of crystal size distributions in magmatic systems. – *Journal of Petrology* 39, 553–599.

MOCK A., JERRAM D. A. & BREITKREUZ C. (2003): Using quantitative textural analysis to understand the emplacement of shallow-level rhyolitic laccoliths – A case study from the Halle Volcanic Complex, Germany. – *Journal of Petrology* 44, 833–849.

MOURTADA-BONNEFOI C. C. & LAPORTE D. (2004): Kinetics of bubble nucleation in a rhyolitic melt: An experimental study of the effect of ascent rate. – *Earth and Planetary Science Letters* 218, 521–537.

PHILPOTTS A. & AGUE J. (2009): *Principles of igneous and metamorphic petrology* (2nd edition). – Cambridge University Press, Cambridge, 684 pp.

PUPIER E., DUCHENE S. & TOPLIS M. J. (2008): Experimental quantification of plagioclase crystal size distribution during cooling of a basaltic liquid. – *Contributions to Mineralogy and Petrology* 155, 555–570.

R DEVELOPMENT CORE TEAM (2011): *R: A language and environment for statistical computing*. – R Foundation for Statistical Computing, Vienna, Austria. ISBN 3-900051-07-0, URL: http://www.R-project.org/.

SCHWINDINGER K. (1999): Particle dynamics and aggregation of crystals in a magma chamber with application to Kilauea Iki olivines. – *Journal of Volcanology and Geothermal Research* 88, 209–238.

SHELLEY D. (1992): *Igneous and metamorphic rocks under the microscope.* – Chapman & Hall, London, 445 pp.

SIEBEL W., TRZEBSKI R., STETTNER G., HECHT L., CASTEN U., HÖHNDORF A. & MÜLLER P. (1997): Granitoid magmatism of the NEW Bohemian massif revealed: gravity data, composition, age relations and phase concept. – *Geologische Rundschau* 86, S45–S63.

SIEBEL W., SHANG C. K. & PRESSER V. (2010): Permo-Carboniferous magmatism in the Fichtelgebirge: dating the youngest intrusive pulse by U-Pb, $^{207}Pb/^{206}Pb$ and $^{40}Ar/^{39}Ar$ geochronology. – *Zeitschrift für geologische Wissenschaften* 38, 85–98.

ŠPILLAR V. & DOLEJŠ D. (2013): Calculation of time-dependent nucleation and growth rates from quantitative textural data: Inversion of crystal size distribution. – *Journal of Petrology* 54, 913–931.

ŠPILLAR V. & DOLEJŠ D. (2014): Kinetic model of nucleation and growth in silicate melts: Implications for igneous textures and their quantitative description. – *Geochimica et Cosmochimica Acta* 131, 164–183.

SPRY A. (1969): *Metamorphic textures.* – Pergamon Press, Oxford, 350 pp.

SWANSON S. E. (1977): Relation of nucleation and crystal-growth rate to the development of granitic textures. – *American Mineralogist* 62, 966–978.

SWANSON S. E. & FENN P. M. (1986): Quartz crystallization in igneous rocks. – *American Mineralogist* 71, 331–342.

ULRYCH J. & PIVEC E. (1997): Age-related contrasting alkaline volcanic series in North Bohemia. – *Chemie der Erde* 57, 311–336.

ULRYCH J., SVOBODOVÁ J. & BALOGH K. (2002): The source of Cenozoic volcanism in the České středohoří Mts., Bohemian Massif. – *Neues Jahrbuch für Mineralogie Abhandlungen* 177, 133–162.

ULRYCH J., DOSTAL J., ADAMOVIČ J., JELÍNEK E., ŠPAČEK P., HEGNER E. & BALOGH K. (2011): Recurrent Cenozoic volcanic activity in the Bohemian Massif (Czech Republic). – *Lithos* 123, 133–144.

VANCE J. A. (1969): On synneusis. – Contributions to Mineralogy and Petrology 24, 7–29.

VEJNAR Z. (1986): The Kdyně massif, South-West Bohemia – a tectonically modified basic layered intrusion. – *Sborník Geologických Věd*, *Geologie* 41, 9–67.

VOLMER M. (1939): *Kinetik der Phasenbildung*. – Theodor Steinkopff Verlag, Dresden, 220 pp.

YANG Z.-F. (2012): Combining quantitative textural and geochemical studies to understand the solidification process of a granite porphyry: Shanggusi, East Qinling, China. – *Journal of Petrology* 53, 1807–1835.

ZIEG M. J. & LOFGREN G. E. (2006): An experimental investigation of texture evolution during continuous cooling. – *Journal of Volcanology and Geothermal Research* 154, 74–88.

ZIEG M. J. & MARSH B. D. (2002): Crystal size distribution and scaling laws in the quantification of igneous textures. – *Journal of Petrology* 43, 85–101.

Preface to Chapter 5

Spatial distribution of crystals in a magma records not only the kinetic crystallization process, but, in addition, depends on the mechanical interactions. We noticed that phenocrysts in magmatic rocks frequently are non-randomly distributed and such textural feature may serve as simple indicator of mechanical interactions between crystals and melt. In this chapter, we introduce the methods of computational statistical mechanics and develop a new Monte Carlo model of texture evolution during accumulation of crystals, or alternatively, extraction of interstitial melt, from the crystal suspension. The model allows us to quantitatively assess the extent of crystal accumulation in magmatic rocks based on textural record.

This chapter was published as **ŠPILLAR, V**. & DOLEJŠ, D. (2015): *Melt extraction from crystal mushes: numerical model for texture evolution and calibration of crystallinity-ordering relationships*. – ***Lithos*** *239, 19–32*. The manuscript was formatted to conform to general layout of this thesis.

Chapter 5.

Melt extraction from crystal mushes: Numerical model of texture evolution and calibration of crystallinity-ordering relationships

5.0. Abstract

Mechanical crystal-melt interactions in magmatic systems by separation or accumulation of crystals or by extraction of interstitial melt are expected to modify the spatial distribution of crystals observed as phenocrysts in igneous rocks. Textural analysis of porphyritic products can thus provide a quantitative means of interpreting the magnitude of crystal accumulation or melt loss and reconstructing the initial crystal percentage, at which the process occurred. We present a new three-dimension numerical model that evaluates the effects of crystal accumulation (or interstitial melt removal) on the spatial distribution of crystals. Both processes lead to increasing apparent crystallinity but also to increasing spatial ordering expressed by the clustering index (R). The trend of progressive crystal packing deviates from a random texture trend, produced by static crystal nucleation and growth, and it is universal for any texture with straight log-linear crystal size distribution. For sparse crystal suspensions (5 vol. % crystals, R = 1.03), up to 97 % melt can be extracted, corresponding to a new crystallinity of 65 vol. % and R = 1.32, when the rheological threshold of crystal interlocking is reached. For initially crystal-rich suspensions the compaction path is shorter, this is because the initial crystal population is more aggregated and it reaches the limit of interlocking sooner. Crystal suspensions with ~35 vol. % crystals cannot be compacted without mechanical failure. These results illustrate that the onset of the rheological threshold

of magma immobility strongly depends on the spatial configuration of crystals in the mush: the primary rigid percolation threshold (~35 vol. % crystals) corresponds to touching or interlocking crystal framework produced by *in-situ* closed-system crystallization, whereas the secondary rigid percolation threshold (~35 to ~75 vol. % crystals) can be reached by compaction, which is particularly spatially efficient when acting on sparse crystal suspensions. Illustrative quantitative evaluation of the crystallinity-clustering relationships to representative porphyritic granites from a single intrusive unit of the Krkonoše-Jizera pluton (central Europe) reveals a single crystal accumulation path starting at low initial crystallinity (5–7 vol. % K-feldspar phenocrysts), with 24–84 % melt extracted leading to the observed crystallinity of 9–26 vol. %. By contrast, a camptonite dyke from the České středohoří volcanic province has experienced the onset of crystal accumulation later (18 vol. % amphibole crystals) and lost 23 % interstitial melt only. The combination of modal and clustering analysis offers a sensitive tool for identifying differentiation processes in natural magma chambers, and here it illustrates examples of mechanically-dominated open-system *vs*. *in-situ* nearly closed-system crystallization from two contrasting magmatic settings.

Key words:

Magma crystallization; melt extraction; crystal accumulation; texture quantification; crystal size distribution.

5.1. Introduction

Magma differentiation by fractionation of crystals from their parental liquids is a process fundamental to igneous differentiation and it has been thoroughly geochemically documented (e.g., Collins et al., 2006; Deering et al., 2011; Gelman et al., 2014). The separation of melt and crystals can occur in response to gravitational forces by mineral settling or floating, by melt motion, or by mechanical melt extraction from crystal suspension due to other mechanical forces. The record of such processes often remains ambiguous, both texturally and chemically. Geochemical evidence is provided by the departure from the

known or reconstructed liquid line of descent, but becomes progressively inapplicable in multiply saturated eutectic assemblages. In contrast, the textural record of crystal or melt accumulation or loss should be interpretable because the pattern of spatial organization of crystals in magma is distinctly affected by mechanical interaction compared to *in-situ* nucleation and growth.

Recent advances in understanding silicate melt crystallization using *in-situ* observations (e.g., Means & Park, 1994; Schiavi et al., 2009, 2010) and by three-dimensional numerical models (e.g., Hersum & Marsh, 2006; Špillar & Dolejš, 2014) made it possible to study kinetic textures (e.g., Higgins, 2011) during arbitrary instants of their formation. In comparison to numerical predictions (e.g., Špillar & Dolejš, 2014), natural porphyritic textures, for example those observed in granites or rhyolites (e.g., Mock et al., 2003), show markedly lower frequency of touching crystal aggregates and have much less clustered appearance of the whole texture. The fraction of polycrystalline clusters generally increases with rising crystallinity – the lower apparent abundance of crystal aggregates can be achieved if the crystallization was interrupted at lower crystallinity by rapid loss of interstitial melt, which produced greater apparent crystal fraction. Qualitative differences of textures crystallized *in-situ* and those discussed here provides a possibility to identify the melt extraction/crystal accumulation process using quantitative textural measurements.

We present a new model of texture evolution during an event of melt extraction or crystal accumulation from the crystal mush, building on our high-resolution numerical VoxelTex algorithm (Špillar & Dolejš, 2014). The model uses a three-dimensional melt domain, with crystallization driven by preset functions of crystal nucleation and growth followed by compaction of the crystal assembly. We show and calibrate correlation relationships between crystal fraction and spatial distribution patterns of crystals, and by comparing the natural and simulated numerical spatial distribution patterns we quantitatively assess the crystallinity at the onset of crystal accumulation or compaction event and the amount of melt extracted. The applications indicate that the combination of crystal accumulation modeling and clustering analysis is capable of detecting mechanical melt-crystal interactions in fossil magma chambers.

5.2. Model of crystal accumulation and melt extraction

Our model simulates textural evolution of a crystal mush during discrete steps of crystal accumulation or extraction of interstitial melt from the system of interest (Figs. 5.1 and 5.2). The model starts with a preparation of the initial assembly of crystals by simulating static *in-situ* crystallization until the desired level of crystallinity is reached (e.g., by VoxelTex numerical method; Špillar & Dolejš, 2014). Nucleation and growth of crystals is then terminated and the population of crystals and crystal aggregates is subjected to the subsequent steps of crystal accumulation. This is equivalent to the extraction of interstitial melt or compaction of crystal mush in a control volume – crystal accumulation and melt extraction are thus two views of a single process of packing of all crystals and crystal aggregates into the smaller volume while some crystal-free melt is effectively extracted from the system (Fig. 5.1). In this study the terms crystal accumulation, melt extraction, and crystal mush compaction are therefore used interchangeably as they refer to a single conceptual phenomenon from the view point of melt and crystal mass balance as their net result. During compaction, crystals are not allowed to further grow or to nucleate (Fig. 5.2).

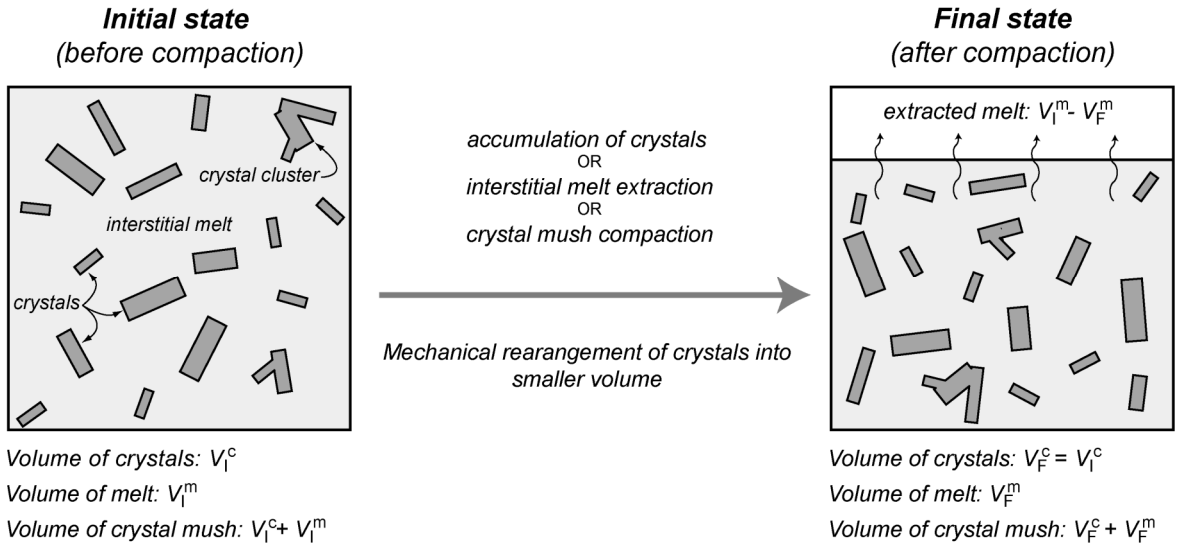

Fig. 5.1. *Nomenclature and symbols for a general crystal-melt interaction event (crystal accumulation, melt extraction, or crystal mush compaction). During the process, crystals and crystal aggregates rearrange into the smaller volume of crystal mush while some melt is left crystal-free and removed. Note that the crystals before and after the event remain identical but are only spatially rearranged.*

After each packing step and increment of crystallinity, the three-dimensional simulation domain is sectioned by a plane on which the spatial distribution pattern of crystals is analyzed. Two-dimensional analysis is used in order to provide data directly comparable to those obtained by studies of thin-sections or natural outcrop patterns without the need for stereological conversions.

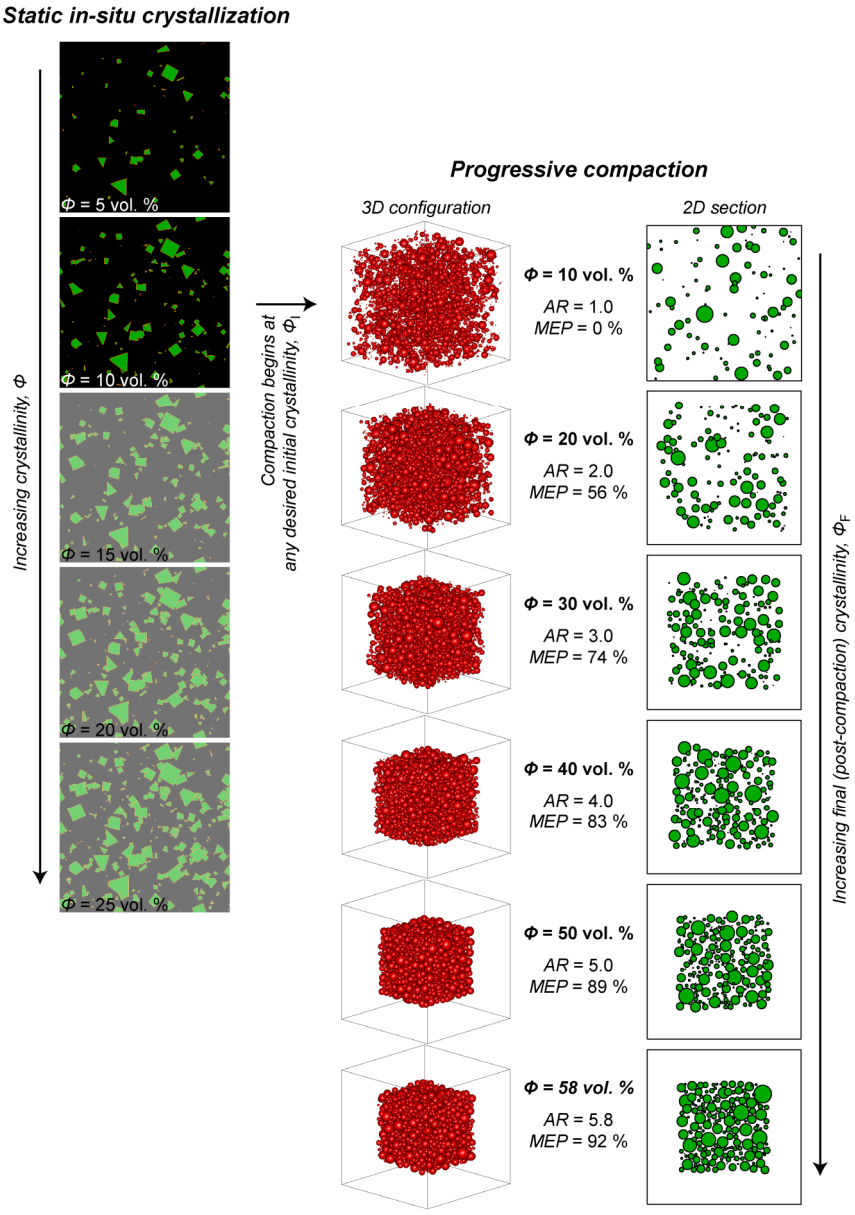

Fig. 5.2. *Textural evolution during the static in-situ crystallization followed by the mush compaction-melt extraction event. During the stage of in-situ crystallization, the system reaches a predefined initial crystallinity, Φ_I (10 % in this case). Sizes and configurations of crystals in crystal aggregates are then transferred as input parameters to the numerical compaction procedure which continues in discrete steps until the close packing is reached. All calculation steps are fully three-dimensional. The AR and MEP stands for the accumulation ratio and the melt extraction percentage, respectively.*

Instead of a forward first-principles simulation of the dynamics of accumulating suspension, which would include complex crystal-melt and crystal-crystal interactions, we apply a simple Monte Carlo approach inspired by the methods used in computational statistical mechanics (e.g., Frenkel & Smit, 2002). During the simulated accumulation process the position and orientation of any crystal or crystal cluster is chosen randomly and it is constrained by positions and boundaries of other crystals, as it would be in the case of physical accumulation of crystals from magmatic suspension. The random positioning of crystals into the compacted assembly does not simulate any specific fluid-mechanical process within the suspension. By contrast, the method explores the configurational space of the system by repetitive statistical simulations and it thus provides configuration-averaged properties of the compacted assembly. In nature, dynamic flow, magma convection, or chaotic crystal-crystal interactions during crystal settling tend to randomize the positions and orientations of individual crystals and therefore approach the result of our averaged simulations. The present stochastic approach provides direct connection between the initial and compacted configuration of the crystal assembly but it remains general and unaffected by the assumptions regarding physics of the accumulation process. The method thus allows calculation of statistical properties of the compaction textures while it is effectively process-independent.

5.2.1. Initial crystal assembly

The initial population or assembly of crystals, which will undergo the accumulation or extraction process, may consist of isolated crystals and crystal aggregates (touching crystals that share at least one common boundary). For simplicity, individual crystals in the assembly are regarded as spheres of equivalent volume rather than shapes with complex geometries. This procedure substantially simplifies the algorithm, improves computational performance, while maintaining the physical accuracy of the model (for an analogous treatment of the effect of anisotropic crystal shape see Section 5.2.2.2). We discuss two types of initial assemblies:

(*i*) an assembly of isolated spheres for the purpose of illustrating the compaction algorithm, and (*ii*) an assembly of isolated spheres and their aggregates that mimics synthetic or natural crystallization texture.

The assembly of isolated spheres, with no aggregates present, is fully characterized by the volume of the simulation domain and by sizes and distribution of individual spheres (crystals). In practice, such assembly is created by generating a certain number of spheres in the simulation volume so that their sizes fulfill any desired crystal size distribution (CSD).

The assemblies of phenocrysts in natural porphyritic rocks are more complex and include both isolated crystals and crystal aggregates. We generate initial assemblies of such objects, that mimic the configuration of natural crystallization textures, with the VoxelTex numerical code (Špillar & Dolejš, 2014; Fig. 5.2). This model simulates static *in-situ* crystallization by nucleation and growth in three dimensions. The crystallization simulation employs arbitrary rates of nucleation and growth as a function of time. We have proven that any CSD and all other textural parameters of interest can be produced by an arbitrary number of combinations of the nucleation and growth rate functions (Špillar & Dolejš, 2013). Therefore, the initial crystal assembly can be created using an arbitrary pair of the rate functions that is consistent with any desired resulting CSD. Such a pair of rate functions can be obtained by choosing one function arbitrarily (either the nucleation rate or the growth rate) and calculating the other by the CSD inversion method (Špillar & Dolejš, 2013). The crystallization model is then terminated at the desired stage of crystallinity (crystal fraction), and the crystal sizes and their spatial configurations (distances and directions) are transferred to the compaction procedure. For simplicity, we assume that individual crystals grow as isometric cubes in the crystallization simulation, but crystal shape can be arbitrarily modified in the VoxelTex model. To enhance statistical validity of the initial crystallization simulation, particularly when a small number of large clusters is involved, the compaction calculations are repeated for $N_{\text{rep-init}}$ (typically $N_{\text{rep-init}} = 10$) variations of the initial assembly. Multiple ($N_{\text{rep-init}}$) crystallization simulations are performed using identical rate functions and each initial assembly is subjected to the compaction procedure.

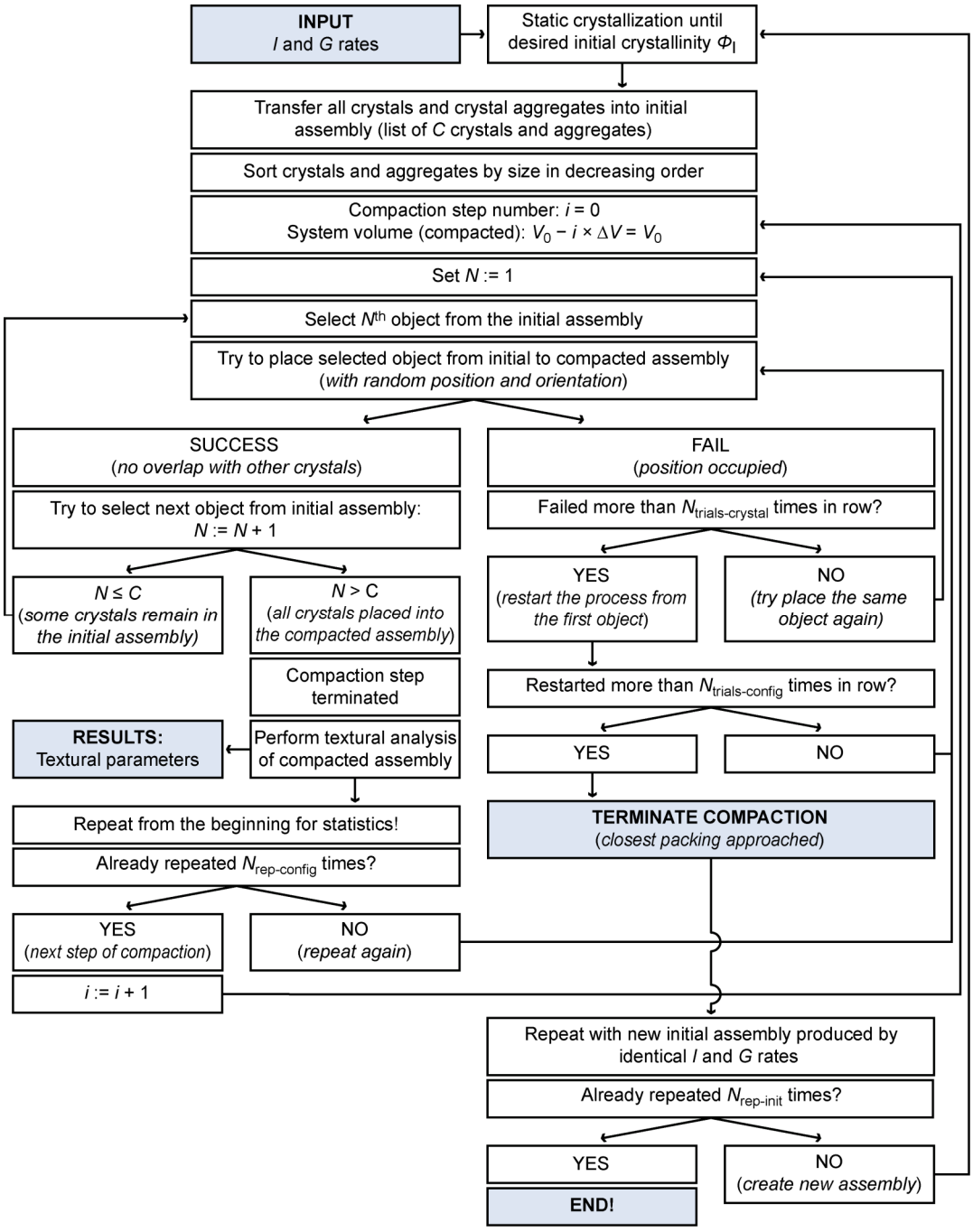

Fig. 5.3. *Flowchart of the numerical procedure of crystal packing.*

Tab. 5.1. *Variables used in the packing procedure.*

Symbol	Description	Typical value
$N_{rep\text{-}init}$	number of variations of the initial assembly	10
$N_{rep\text{-}config}$	number of repetitions of the packing procedure for each initial assembly	100
$N_{trials\text{-}crystal}$	maximum number of attempts to place the crystal (crystal cluster) into the compacting assembly	100000
$N_{trials\text{-}config}$	maximum number of attempts to configure the compacted assembly	5

5.2.2. Compaction of the crystal assembly

5.2.2.1. Geometry of crystal packing

During crystal mush compaction, all crystals, which initially occupy a cubic box of volume V_0, must be packed into a smaller volume, $V_1 = V_0 - \Delta V$, where ΔV is the volume of the extracted melt (Figs. 5.1 and 5.3). Packing consists of sequential transfer of each crystal or a crystal aggregate into the smaller box by assigning it some random position and orientation. The position is determined by three independent and uniformly distributed random numbers and the orientation is obtained by applying random rotation in three dimensions (Kirk, 1992). A Mersenne-Twister random number generator (Matsumoto & Nishimura, 1998) is used to provide uniformly distributed random numbers of high quality. Only the positions and orientations of newly added crystals or crystal aggregates, which do not overlap with other crystals already present in the box, are accepted, otherwise the random generation of position and orientation is repeated. In order to decide when two crystals overlap we regard crystals as equivalent-volume spheres instead of treating complex crystal shapes (see further below). If no suitable position and orientation for the addition of a crystal is found after a preset maximum number of trials, $N_{\text{trials-crystal}}$ (Tab. 5.1), the entire crystal assembly is discarded and the packing procedure starts with all crystals anew. Once all crystals (spheres) are fitted in the smaller volume, the compaction step is successfully terminated, and the assembly is stored and subjected to textural analysis.

During the packing procedure, the crystals and crystal aggregates are added into the smaller box in the order of decreasing size (volume), that is, starting with the largest crystal or crystal aggregate. This approach yields two benefits: (*i*) as larger crystals are placed into the domain earlier the compacted configurations are created more easily with lesser number of failed attempts; (*ii*) the edge effect due to preferential occurrence of larger crystals closer to the domain boundary is minimized. To prove that the addition of crystals in size order does not affect regular sampling of the configuration space, consider two crystal sizes only – small and large crystals. During the packing procedure, let us add the crystals into the domain in a *reversed* order, that is, starting from the small ones and proceeding toward the larger ones.

After all crystals from the small-size group were placed into the domain, only configurations where voids left are still large enough to accommodate the incoming group of larger crystals. All other configurations fail by definition because the large crystals do not fit the available pore space. In other words, only such configurations lead to successful completion where the small crystals have been placed at the locations as if the large crystals were already present in the system. The set of all attainable configurations is therefore not affected by the order in which the crystals are placed into the domain and we can insert large crystals first without introducing any artifacts.

In order to predict textural evolution during progressive compaction, the crystal accumulation procedure is repeated with the same initial crystal assembly from the simulation volume V_0, but packed into a successively smaller volume $V_i = V_0 - i \cdot \Delta V$. The volume change, ΔV, determines the step of the compaction at which the textural data are acquired. At each step we decrement the volume of the system by ~3 %, which corresponds to a reduction of the linear dimension of the simulation box by 1 %. With the increasing number of steps, i, the packing procedure becomes less feasible due to the random search for a suitable spatial configuration. If no acceptable crystal assembly is found after $N_{\text{trials-config}}$ restarts, that is, after $N_{\text{trials-crystal}}$ has been reached $N_{\text{trials-config}}$ times, the search procedure is terminated. In practice, this corresponds to the densely packed configuration which has approached the geometrical limit of the closest possible packing. The approach to the limit of closest packing is, however, asymptotic with the number of trials and the limit itself is never fully reached.

For each volume V_i, the packing procedure is performed $N_{\text{rep-config}}$ times (typically $N_{\text{rep-config}}$ = 100). This ensures that the entire configuration space of the system is sampled regularly and that statistically robust results are obtained in case that the simulation domain contained only a limited number of crystals. From multiple realizations, the textural data (e.g., the clustering index; see below) are averaged in order to yield statistically robust results. Available computational resources set upper bounds for the $N_{\text{trials-crystal}}$ and $N_{\text{trials-config}}$ values at a trade-off such that for the low numbers of trials the algorithm fails to find closely packed configurations with a high amount of crystal accumulation. In our calculations, we use $N_{\text{trials-crystal}}$ = 100 000 and $N_{\text{trials-config}}$ = 5 as a reasonable combination of limits that enables to reach

a high degree of compaction while keeping tolerable computational requirements. Using significantly higher number of trials leads to a only minor increase in the degree of compaction.

The numerical crystal accumulation process is biased by the edge effect. During random packing procedure, the crystals are sequentially added into the simulation domain such that they do not overlap with other crystals and that their centers are present within the domain. As the amount of crystals inside of the domain increases it becomes progressively more difficult to find a suitable position for any new crystal. Positions close to the domain boundary are, therefore, favored as the region outside of the domain imposes no constraints on overlapping parts of the crystals and as no crystals enter the domain from outside. Generally, the magnitude of the edge effect increases with increasing crystallinity. The edge effect can be fully treated by using periodic boundary conditions in the crystal packing procedure. The periodicity would, however, add undesired complexity to otherwise computationally extensive calculations. Therefore, we use two different approaches to reduce the edge effect: (*i*) during the packing procedure, we place large crystals, whose positions are most constrained, into the simulation domain first (see above); (*ii*) to remove any other inherent heterogeneities near the domain boundaries, we only process the crystals which are more distant from the walls than 10 % of the linear dimension of the simulation box.

5.2.2.2. Effect of crystal shape

During the crystal packing procedure, the shape of individual crystals has been neglected and all crystals were approximated by equal-volume spheres. During compaction of the real crystal assembly, however, both the sizes and shapes of individual crystals are essential as they determine spatial configuration when impingement occurs. Since the full treatment of the packing of crystals with real shapes would be both computationally and algorithmically difficult, we derive a method to approximate the crystals by spheres having equivalent geometric behavior. The sizes of the equivalent spheres are determined in such a way that they conserve the collision properties of the assembly rather than the volume of

individual crystals. As a result, the collision-equivalent spheres approximate the compaction behavior of real crystal assemblies while the computational performance and physical accuracy remains feasible.

Let us assume that real crystals are rectangular parallelepipeds with dimensions a, b, and c. We define the diameter of a collision-equivalent sphere, L_{CE}, as twice the average distance from the center to the surface of the parallelepiped. The average distance to the surface is expressed in terms of the integrals over the surface S of the parallelepiped as follows:

$$L_{\mathrm{CE}} = 2\frac{\oint_S |\boldsymbol{r} - \boldsymbol{r}_{\mathrm{C}}| \,\mathrm{d}S}{\oint_S \mathrm{d}S}, \tag{5.1}$$

where $\boldsymbol{r}$ is a radius vector of a point on the surface, $\boldsymbol{r}_{\mathrm{C}}$ is a radius vector of the center of the parallelepiped, and the symbol |.| denotes Euclidean distance. For various prismatic and platy crystals the L_{CE} sizes and the sizes of equal-volume spheres, L_{EV}, are summarized in Tab. 5.2. Note that for the cubic crystal shape both these sizes are almost equal; L_{CE} = 1.28 and L_{VE} = 1.24 for a unit cube.

For arbitrary crystal shape, both L_{CE} and L_{VE} sizes are related by a factor C,

$$L_{\mathrm{CE}} = C \cdot L_{\mathrm{VE}}, \tag{5.2}$$

which is generally greater than unity (Tab. 5.2). That is, the collision-equivalent spheres are larger than equal-volume spheres, and the total volume of collision-equivalent spheres in the system is thus greater than the true volume of crystals. This approach defines apparent collision-equivalent crystallinity, Φ_{CE}, which is greater than the true crystallinity, Φ. Since the volume of a sphere scales with the 3$^{\mathrm{rd}}$ power of its linear dimension both crystallinities are related by cube of the factor C:

$$\Phi_{\mathrm{CE}} = C^3 \cdot \Phi\,. \tag{5.3}$$

Tab. 5.2. *L_{CE} and L_{VE} sizes for various crystal morphologies.*

a	*b*	*c*	L_{CE}	L_{VE}	*C*
1	1	1	1.2808	1.2407	1.0323
1	1	2	1.7038	1.5632	1.0899
1	1	3	2.1402	1.7894	1.1960
1	1	4	2.5920	1.9695	1.3161
1	1	5	3.0549	2.1216	1.4399
1	2	2	2.1143	1.9695	1.0735
1	2	3	2.5284	2.2545	1.1215
1	2	4	2.9573	2.4814	1.1918
1	2	5	3.3993	2.6730	1.2717
1	3	3	2.9193	2.5808	1.1312
1	3	4	3.3255	2.8405	1.1707
1	3	5	3.7466	3.0598	1.2244
1	4	4	3.7100	3.1264	1.1867
1	4	5	4.1109	3.3678	1.2207
1	5	5	4.4929	3.6278	1.2384

Symbols: *a*, *b*, *c* – crystal shape coefficients, as edge-lengths of a rectangular parallelepiped; L_{CE} – collision-equivalent crystal size; L_{VE} – crystal size as a diameter of equal-volume sphere; *C* – the ratio of L_{CE} to L_{VE}. Note that crystal shape coefficients are normalized to *a* = 1 and that *b* and *c* coefficients are interchangeable due to shape symmetry.

The difference between the true and virtual crystallinity remains small for isometric crystal shapes (e.g, 10 % for 1:1:1 cube). With increasing anisotropy the difference of both crystallinities also increases (e.g., ~300 % for 1:1:5 prisms) and it highlights progressively the more difficult compaction process of crystal mushes consisting of highly anisotropic crystals.

In this work, we study compaction behavior of textures consisting of cubic crystals and neglect the effects of anisotropic crystal shape. For crystals of low anisotropy, our results can be approximately adapted using proper collision-equivalent crystallinity instead of its true value. However, a better approximation is obtained by redefining the initial crystal assembly using collision-equivalent sizes appropriate for a given crystal shape and performing the

compaction simulations using the modified initial assembly. With the increasing crystal-shape anisotropy the crystallization textures progressively deviate from that of cubic crystals and the geometry of crystal aggregates becomes more complex. A rigorous solution for anisotropic crystal shapes thus requires starting with a crystallization simulation and performing the VoxelTex modeling (Section 5.2.1) with the crystal shape of interest. The resulting texture is then converted to the initial assembly using the collision-equivalent crystal size and the assembly is used as an input in the compaction calculations.

5.2.2.3. Progress variables of the compaction process

At any stage, the crystal mush consists of solid crystals and interstitial melt (Fig. 5.1). Let us denote the *initial* and *final* volume of crystals before and after the crystal accumulation event as $V_{\mathrm{I}}^{\mathrm{c}}$ and $V_{\mathrm{F}}^{\mathrm{c}}$, respectively, and the *initial* and *final* volume of melt before and after the accumulation event as $V_{\mathrm{I}}^{\mathrm{m}}$ and $V_{\mathrm{F}}^{\mathrm{m}}$, respectively. The crystallinity, i.e., the volume fraction of crystals, before and after the accumulation, that is, *initial* and *final* crystallinity, is thus defined as:

$$\Phi_{\mathrm{I}} = \frac{V_{\mathrm{I}}^{\mathrm{c}}}{V_{\mathrm{I}}^{\mathrm{c}} + V_{\mathrm{I}}^{\mathrm{m}}}, \quad \Phi_{\mathrm{F}} = \frac{V_{\mathrm{F}}^{\mathrm{c}}}{V_{\mathrm{F}}^{\mathrm{c}} + V_{\mathrm{F}}^{\mathrm{m}}}. \tag{5.4}$$

While the volume of crystals remains unaffected by the crystal accumulation event, $V_{\mathrm{I}}^{\mathrm{c}} = V_{\mathrm{F}}^{\mathrm{c}}$, some melt escapes, thus $V_{\mathrm{I}}^{\mathrm{m}} > V_{\mathrm{F}}^{\mathrm{m}}$, and the crystallinity increases from its initial to the final value (Fig. 5.1).

The value of crystallinity, Φ, is monitored during the crystal accumulation process. The unbiased value of crystallinity is obtained by simply dividing the total volume of all spheres (crystals) by the domain volume. The true volume of spheres within the domain is lower since some parts of the spheres are allowed to overlap outside of the domain boundaries. This overlapping volume is, however, compensated for by the theoretical volume of spheres that would overlap into the domain if the texture was not truncated by the domain boundary.

To characterize the amount of net crystal accumulation that the system has experienced we define the *accumulation ratio*, *AR*, as the ratio of final and initial crystallinities (Fig. 5.4):

$$AR = \frac{\Phi_F}{\Phi_I}. \tag{5.5}$$

Note that during compaction the *AR* is always greater or equal to unity, since the crystallinity cannot, by definition, decrease during a period of crystal accumulation. To characterize the same process as the melt extraction event we define the *melt extraction percentage*, *MEP*, as the percentage of melt volume extracted from the crystal mush:

$$MEP = \frac{V_I^m - V_F^m}{V_I^m} \cdot 100\ \%. \tag{5.6}$$

Substituting from Eqn. (5.4) and noting that $V_I^c = V_F^c$, the *MEP* is readily expressed in terms of the initial and final crystallinities:

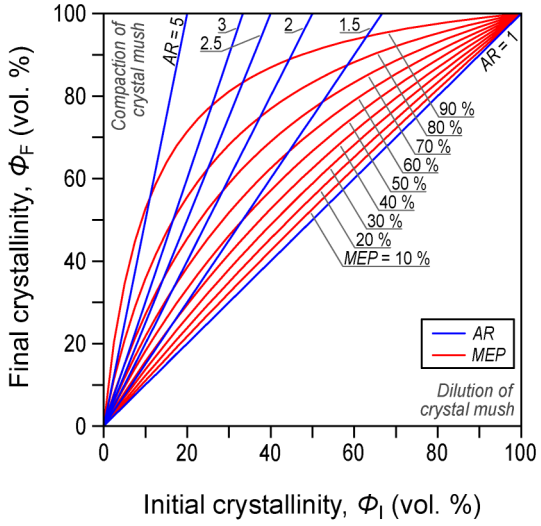

Fig. 5.4. *Isolines of the progress variables – accumulation ratio (AR) and melt extraction percentage (MEP) – during the crystal compaction process. The crystal packing starts from initial crystallinity, Φ_I, reached by in-situ crystallization. During the compaction (melt extraction) procedure the crystallinity further increases AR-times to its final value, Φ_F, while MEP fraction of the interstitial melt is extracted. Note that MEP is a function of both AR and one of the crystallinities. Processes, whereby crystal mush is depleted by crystal removal (e.g., settling) or addition of crystal-free melt, will appear in the lower-right half-space of the diagram.*

$$MEP = \left[1 - \frac{\Phi_I \left(1 - \Phi_F\right)}{\Phi_F \left(1 - \Phi_I\right)} \right] \cdot 100\ \%. \tag{5.7}$$

Both quantities *AR* and *MEP* are interrelated and characterize the progress of the crystal accumulation process (Fig. 5.4).

5.2.3. Quantitative description of the compacted texture

The model operates with fully three-dimensional configurations, but we employ a two-dimensional description of crystal clustering in order to facilitate direct comparison with spatial distributions of phenocrysts in natural rocks, which are determined from thin sections, polished surfaces or outcrop patterns (e.g., Jerram et al., 1996, 2004; Mock et al., 2003; Higgins, 2006;). After each simulation run, the resulting crystal configuration was sectioned by an *x*-*y* plane through the center of the simulation box and all crystals intersected by the plane were represented by their centers of mass with respect to their cross-section outline (e.g., Jerram et al., 1996; Higgins, 2006). A set of crystal centers provides a point pattern, which is analyzed by the two-dimensional spatial distribution analysis (e.g., Baddeley, 2008; Rudge et al., 2008). We use the clustering index, *R*, to quantitatively characterize the clustering/ordering relationship of crystals (Clark & Evans, 1954; Kretz 1966, 1969; Jerram et al., 1996, 2003). This index is defined as a ratio of the average nearest neighbor distance observed in a specific point pattern, R_A, to the average nearest neighbor distance in a randomly distributed set of points, R_E:

$$R = \frac{R_A}{R_E}. \tag{5.8}$$

The value of R_E depends on the number of points, *N*, and the area of the point pattern, *A*, as follows (e.g., Kretz, 1966):

$$R_E = \frac{1}{2} \cdot \sqrt{\frac{A}{N}} \tag{5.9}$$

By definition, in Eqn. (5.8), the value of R = 1 indicates a random distribution of points, whereas lower or greater values indicate clustered or ordered (i.e., anti-clustered) distributions, respectively (e.g., Kretz, 1966; Jerram et al., 1996). The clustering index calculated for the point pattern studied on a finite area is biased by the edge effect, because points (crystal centers) located close to the section boundary may lack some of their neighbors that would lie outside of the evaluated area. As a result, R is generally overestimated and we use the empirical correction method of Donnelly (1978) to correct for the edge effect and obtain unbiased value of the clustering index.

5.3. Results

During the mechanical crystal accumulation (melt extraction) crystals cannot approach each other closer than the sum of their respective sizes. Crystal centers are therefore more distant than they would be if the crystals were point objects and the accumulation process thus induces ordering (i.e., anti-clustering) in the spatial distribution pattern of crystal centers. Since individual crystals have nonzero sizes at the time of the crystal accumulation event, the melt-extraction texture is expected to differ from that of crystallinity increase by sustained nucleation and growth. We characterize the textural pattern resulting from crystal accumulation for (*i*) the assembly of isolated spheres characterized by a size distribution of the spheres, and (*ii*) the assembly of isolated and clustered spheres that mimics natural igneous textures.

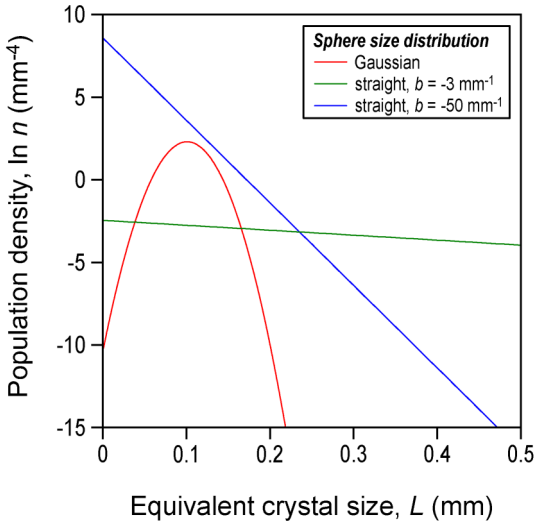

Fig. 5.5. *Three distinct sphere size distributions, SSDs, used as input for the compaction simulations of unclustered textures (i.e., isolated, untouching spheres). We consider sphere diameter as the equivalent crystal size, L. Straight SSDs have the slopes b = -3 and -50 mm^{-1}, and 2000 and 3000 individual spheres, respectively. The Gaussian SSD has a mean sphere size of 0.1 mm, with one standard deviation of 0.02 mm (3000 individual spheres).*

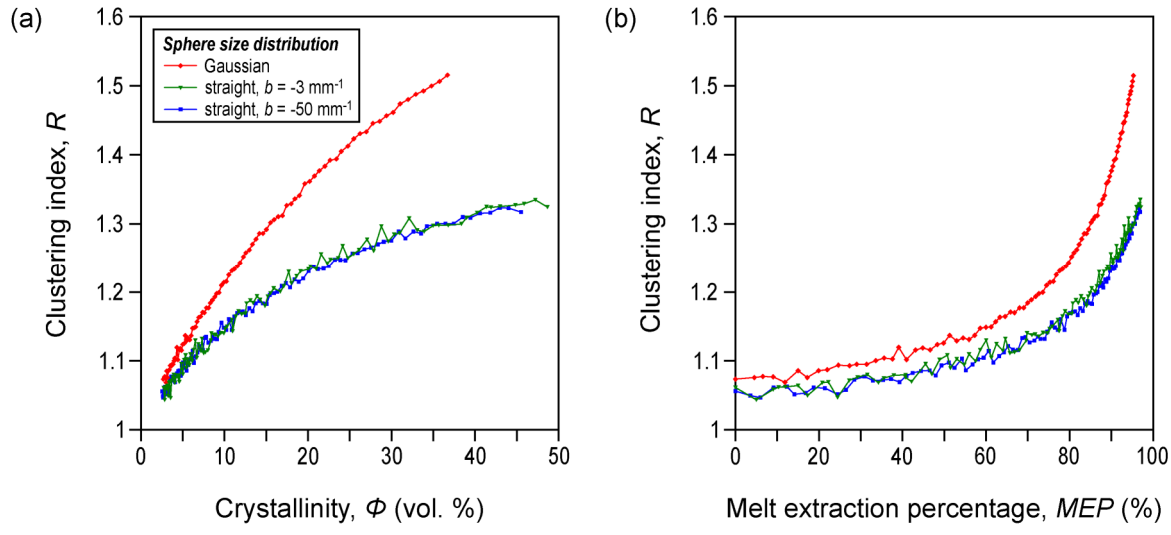

Fig. 5.6. *Progressive compaction of the assemblies of isolated spheres, defined in Fig. 5.5. For each compaction step, the calculations are repeated 200 times ($N_{rep\text{-}init}$ = 200). The initial crystallinities are 2.7, 2.5, and 2.6 vol. %, for the assemblies with straight SSDs and slopes b = -3 and -50 mm^{-1}, and for the assembly with Gaussian SSD, respectively. The clustering index, R, always increases as a function of* **(a)** *crystallinity, Φ, or* **(b)** *the melt extraction percentage, MEP. Note that the evolution of the clustering index with the progressive compaction is invariant for both straight SSDs, hence universally applicable.*

5.3.1. Compaction of unclustered textures

We have performed the simulations of crystal accumulation with three assemblies of untouching spheres characterized by three different size distributions. Two initial assemblies with straight three-dimensional sphere size distributions (SSD) were generated to approximate the textures of natural rocks, which often have straight CSDs in plots of the natural logarithm of the population density *vs*. crystal size (e.g., Marsh, 1998; Higgins, 2006; Philpotts & Ague, 2009). The SSD slopes chosen, b = -3 mm^{-1} (case 1) and -50 mm^{-1} (case 2), correspond to the most abundant (by volume) grain size of 0.06 and 1 mm, respectively, and are comparable to volcanic or plutonic textures (Fig. 5.5). In these textures small crystals are exponentially more abundant than the large ones. For comparison, the third initial assembly was generated with a Gaussian SSD having the mean sphere size of 0.1 mm and the standard deviation of the sphere size of 0.02 mm (Fig. 5.5). Prior to the compaction event, all assemblies have a crystallinity ~3 vol. % and they consist of two to three thousand individual spheres (see Fig. 5.5 for details).

In all three cases, compaction leads to progressive ordering of the spatial distribution pattern of the spheres. For the limit of zero crystallinity the extrapolated clustering index approaches unity which corresponds to a perfectly random distribution of points (Fig. 5.6). As compaction progresses and crystallinity increases the clustering index monotonously increases and the sphere assembly is described as more ordered. Exact R–crystallinity relationships are, however, different for the assemblies with Gaussian and straight sphere size distributions. For the Gaussian SSD the clustering index increases rapidly and it reaches R = 1.5 at 35 vol. % of spheres (crystals), which corresponds to the extraction of 95 % of the initial amount of interstitial melt. In the two other cases with straight SSDs the clustering index increases steeply but only reaches R = 1.3 at 35 vol. % of spheres (crystals).

The textures with straight SSDs therefore evolve to a less ordered state than those with Gaussian SSDs because abundant small spheres in simulations with straight SSDs can more easily fit into the interstitial spaces between the large spheres and the positions of most spheres are thus less constrained. By contrast, in the run with Gaussian SSDs the average-

sized spheres are the most abundant. The space filling becomes less random when spheres of similar size predominate, hence the positions of individual spheres are more constrained by the others producing a higher degree of ordering. As a general observation, good initial size sorting produces more ordered textures (higher R) upon compaction.

Independently of the large difference in slope b (by a factor of 15 between cases 1 and 2), both assemblies with initially straight SSD follow a common path in the R–Φ space during progressive compaction (Fig. 5.6). We thus infer that the evolution of the clustering index during compaction is identical for all textures with straight sphere (crystal) size distribution and with the same initial crystallinity, Φ_0. This is expected because straight textures are generally self-similar and related to one another by simple length scaling.

5.3.2. Compaction of clustered textures

Initial assemblies that include crystal aggregates were produced by *in-situ* kinetically driven crystallization during simultaneous nucleation and growth of crystals using the VoxelTex simulation algorithm (Špillar & Dolejš, 2014). The resulting crystal suspensions consist of both isolated crystals and touching crystals forming polycrystalline aggregates. We simulated two textures with straight CSDs having slope b = -332 and -3.28 mm^{-1}, corresponding to the most abundant (by volume) grain size of 0.01 and 1 mm, respectively, and approximating volcanic and plutonic rocks (Fig. 5.7). As crystallinity increases during the crystallization progress, the clustering index first increases but after reaching a maximum value of ~1.18 at 80 vol. % crystals it drops slightly to 1.14 at 100 vol. % crystals (Fig. 5.8, Fig. 11 in Špillar & Dolejš, 2014). This trend, denoted as the random texture trend, RTT, is unique for all textures resulting from static crystallization by nucleation and growth and having straight log-linear CSDs (Špillar & Dolejš, 2014). Since the clustering index is greater than unity at all stages of crystallization, it formally points to ordering of the spatial distribution pattern of crystal centers. The apparent ordering is simply an implicit result of behavior of crystals, which nucleated later during the crystallization and are unavoidably

restricted to the remaining void space of melt and could not nucleate randomly in space where other crystals are already present.

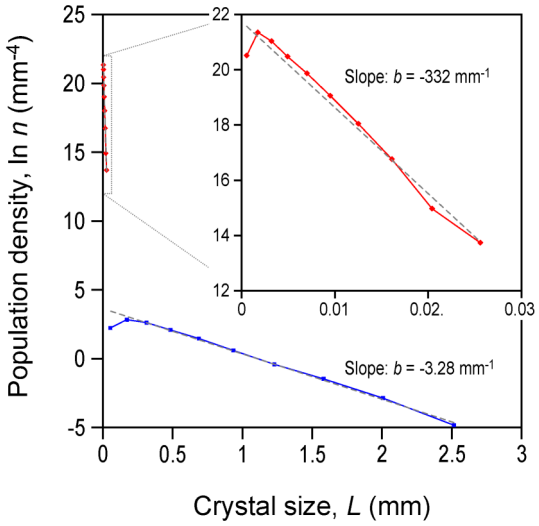

Fig. 5.7. *The CSDs of the crystal mushes including crystal aggregates used as in input for the compaction calculations. The crystal mushes were produced by static in-situ crystallization with the constant growth rate and the nucleation rate exponentially increasing in time (e.g., Marsh, 1998; Špillar & Dolejš, 2014). The rate functions used in the crystallization simulations are G = 0.0015 and 0.15 mm s^{-1}, respectively, and I = 1 × 10^{-7} e^{t} and 1 × 10^{-6} e^{t} mm^{-3} s^{-1}, respectively, where G is the growth rate, I is the nucleation rate, and t is time. The resulting CSDs are straight with the slopes b = -332 and -3.28 mm^{-1}, respectively (the smallest crystal fraction was omitted from the slope regression).*

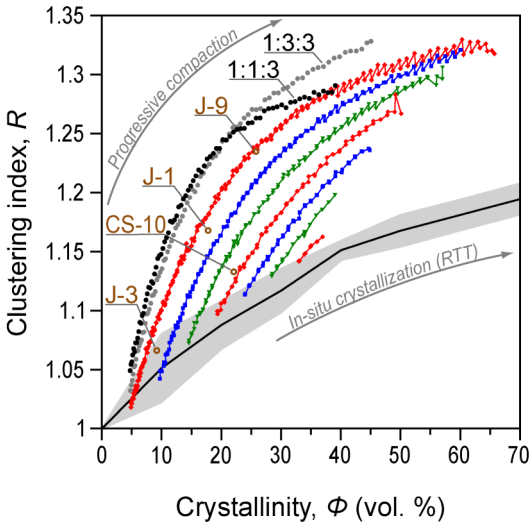

Fig. 5.8. *Evolutionary paths during the crystal compaction starting at various initial crystallinities. The trends are combined for both CSD input assemblies from Fig. 5.7. The trends 1:1:3 and 1:3:3 are for needles and plates, respectively, whereas other data are for cubic crystal morphologies. Grey area represents the confidence interval of the random texture trend, RTT. Open circles represent the data for natural samples (see Section 5.5).*

Each texture was captured at seven steps, at 5 vol. % crystallinity increments, as crystallization progressed up to 35 vol. % crystals. Above the ~35 vol. % crystallinity the crystal mush formed by nucleation and growth is highly interlocked and essentially forms a rigid framework, which is difficult to further compact without a mechanical failure. When compaction was applied to each of the incremental textures, the clustering index departs from the RTT towards higher values as crystallinity increases (Fig. 5.8). Compaction induces additional ordering of crystals that is distinct from the intrinsic ordering trend due to crystal nucleation and growth. At the highest crystallinity, when close packing is reached and no further compaction is mechanically possible, the clustering index reaches the highest value, which corresponds to the *most ordered* state. Individual values of crystallinity and clustering index at the highest possible compaction depend on the initial crystallinity at which compaction began (Fig. 5.8). In general, sparse suspensions can be compacted to much higher crystallinities (higher *AR* and *MEP* values) and reach higher values of the clustering index (Fig. 5.8). By contrast, a suspension with initially higher crystallinity can undergo moderate compaction only and the increase in the clustering index is more limited. For example, the crystal mush with 5 vol. % crystals can be compacted up to 65 vol. % crystals (R = 1.32) at close packing, which corresponds to the extraction of ~97 % interstitial melt. This high value is not surprising considering that (*i*) the amount of the melt extracted relates to initially very high melt fraction, and (*ii*) certain crystal geometries (e.g., cubes) allow complete space filling, that is, reaching to the theoretical limit of the 100 % melt extraction. On the other hand a mush with initially 25 vol. % crystals begins to already mechanically lock at 45 vol. % crystals when R = 1.24 (Fig. 5.8). This behavior is a general feature of inherently clustered textures resulting from nucleation and growth. At low crystallinity, crystals are nearly all isolated and can be reconfigured easily when compacted. At higher crystallinities many of the crystals are present in aggregates with complex geometries, which are difficult to reconfigure into smaller volume.

Despite the difference by two orders of magnitude in the CSD slope b in both simulations, both textures behave identically in the R–Φ space during compaction (Fig. 5.8). This finding further reinforces universality observed during the compaction of isolated

spheres. We infer that all textures with straight CSDs behave identically as they only differ by length scaling. Compaction trajectories in the R–Φ space are thus invariant for all textures with straight log-linear CSDs and Fig. 5.9 shows a universal calibration of isolines of initial crystallinity, Φ_0, and of melt extraction percentage, *MEP*, as a function of R and Φ for interpretation of natural samples (see Tab. 5.3 for calibration details).

Additional simulations performed for non-cubic crystal morphologies (1:1:3 columns and 1:3:3 plates) show compaction trajectories that are qualitatively similar to those for cubes. With the increasing shape anisotropy, however, the trends are shifted towards the higher values of R (Fig. 5.8) This implies that the texture with the same phenocryst fraction and degree of clustering will be produced by less melt extraction or from mushes with initially higher crystallinities than predicted for rocks with isotropic crystals.

Tab. 5.3. *Polynomial fits for the initial crystallinity, Φ_I, and for the melt extraction percentage, MEP.*

Fit for the melt extraction percentage, *MEP*.

$$MEP = a_1\Phi^3 + a_2\Phi^2R + a_3\Phi^2 + a_4\Phi R^2 + a_5\Phi R + a_6\Phi + a_7R^3 + a_8R^2 + a_9R + a_{10}$$

a_1 = 404.3832	a_5 = 5401.7028	a_9 = 29992.9242
a_2 = -3939.3505	a_6 = -5415.6043	a_{10} = -12559.2192
a_3 = 4877.1032	a_7 = 6212.9121	
a_4 = -1015.9597	a_8 = -23624.5656	

Fit for the initial crystallinity, Φ_I.

$$\Phi_I = b_1\Phi^3 + b_2\Phi^2R + b_3\Phi^2 + b_4\Phi R^2 + b_5\Phi R + b_6\Phi + b_7R^3 + b_8R^2 + b_9R + b_{10}$$

b_1 = -10.4019	b_5 = 121.7443	b_9 = 86.4774
b_2 = 39.2773	b_6 = -57.2857	b_{10} = -28.1001
b_3 = -36.9961	b_7 = 29.6135	
b_4 = -63.0533	b_8 = -87.9978	

Fits were calculated using the Polyfitn toolbox in MATLAB® software.

Symbols: Φ – crystallinity (volume fraction, i.e., $\Phi \in \langle 0;1 \rangle$); Φ_I – initial crystallinity (volume fraction) prior to the crystal accumulation / melt extraction event; R – clustering index; *MEP* – melt extraction percentage (%); $a_1 \ldots a_{10}$, $b_1 \ldots b_{10}$ – fit coefficients.

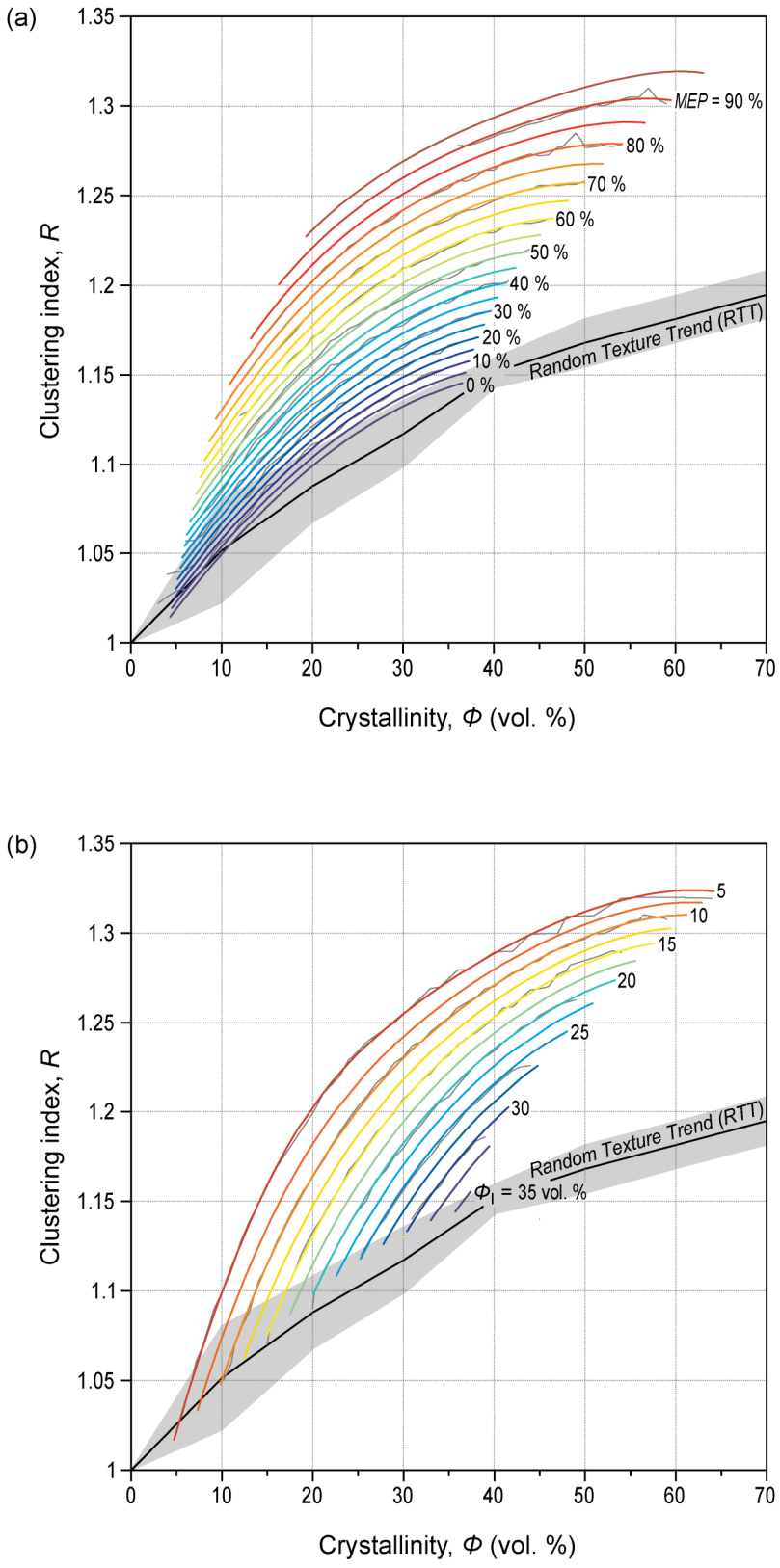

Fig. 5.9. *Isolines of the melt extraction percentage, MEP* **(a)**, *and the initial crystallinity, Φ_I* **(b)** *in the clustering index, R, vs. crystallinity, Φ, space. The isolines are derived from an empirical polynomial fit (Tab. 5.3) of the simulated data (Fig. 5.8). Linearly interpolated isolines of the original data are shown as thin grey lines. These two plots may be used to retrieve the melt extraction percentage and the initial crystallinity (prior to the compaction event) from the crystallinity and the clustering index measured on natural samples.*

5.4. Implications for rheology of crystal mushes

The results of the compaction simulations can provide additional inferences about rheology of dense crystal mushes. The upper limit of compaction above which further rearrangement of crystals and crystal aggregates into smaller volume requires an excessive number of trials, is therefore statistically improbable and may be regarded as a proxy for the rigid percolation threshold or rheologically critical solid fraction (Marsh, 1981; Vigneresse et al., 1996; Petford, 2003). Above the critical solid fraction the crystals form a touching framework that is capable of bearing a load and magma mush starts to develop a yield strength (e.g., Vigneresse & Tikoff, 1999; Saar et al., 2001). In our simulations, the upper limit of compaction is variable; it corresponds to ~65 vol. % apparent crystallinity for initial crystallinity of 5 vol. %, whereas textures initially with ~35 vol. % crystals are essentially uncompacting (Fig. 5.8). The suspensions produced by *in-situ* (static) nucleation and growth of cubes are thus able to compact until the crystallinity of ~35 vol. % is reached; above this crystallinity level the texture is mechanically locked.

We term the rheological locking reached by *in-situ* crystallization at ~35 vol. % crystals as a *primary rigid percolation threshold*, PRPT. This value is higher than 22 vol. %, the rigid percolation threshold determined by numerical percolation studies (Saar et al., 2001), and higher than 25 vol. %, the volume percentage at which plagioclase chain network forms in basalts (Philpotts et al., 1998), but it remains considerably lower than the traditionally assumed value of ~55 vol. % (e.g., Marsh, 1981, 1989; Vigneresse & Tikoff, 1999). Our value of the PRPT crystallinity compares rather well to the experimental results of Arbaret et al. (2007), which are, however, relevant for more complex than isometric crystal geometries.

The *in-situ* crystallization textures, which undergo compaction from low initial crystallinities (lower than PRPT), are predicted to exceed the PRPT until the crystal mush becomes locked and uncompactable. We term this rheological threshold reached by progressive compaction (as opposed to *in-situ* nucleation and growth) as a *secondary rigid percolation threshold*, *SRPT*. This is the limit of the close packing when mechanical reconfigurations of the suspension become essentially impossible and the suspension

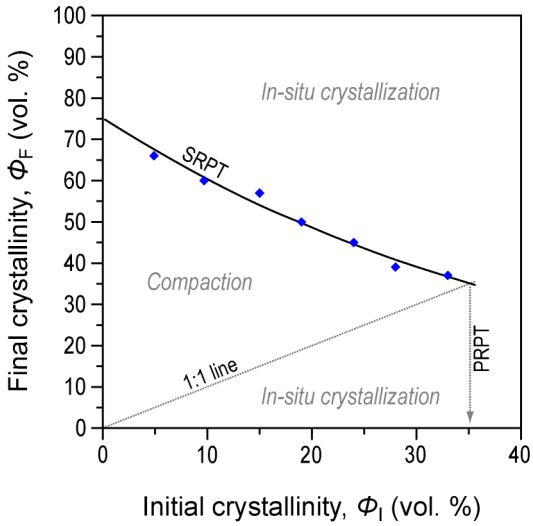

Fig. 5.10. *Crystallinity, at which the secondary rigid percolation threshold, SRPT, has been reached during packing as a function of the initial crystallinity, Φ_I. Texture crystallized in-situ to crystal content greater than the primary rigid percolation threshold, PRPT, is completely touching (interlocked) and cannot be compacted without mechanical failure. Above the SRPT, the solidification can only continue by static (in-situ) crystallization. The calculated values of crystallinity at SRPT, Φ_{SRPT}, are interpolated by the function: $\Phi_{SRPT} = 75.01 \times \exp(-0.02173 \times \Phi_I)$.*

approaches the rheological threshold of mechanical immobility (Fig. 5.10). For our simulations with the most dilute initial suspension (5 vol. % crystals), the SRPT has been reached at the crystalinity of ~65 vol. %, thus exceeding the conventional rheological threshold crystallinity value of ~55 vol. % (e.g., Marsh, 1981, 1989; Vigneresse & Tikoff, 1999). For elongate or platy crystal morphologies, the extent of permissible compaction is reduced, and with the increasing crystal anisotropy the rheological locking occurs at progressively lower crystallinities. The most dilute suspensions (5 vol. % crystals initially) reach the SRPT at ~39 and ~45 vol. % for the 1:1:3 columnar and 1:3:3 platy crystals, respectively.

The SRPT crystallinity is path-dependent. Its lower limit is equal to the PRPT (~35 vol. %) and its upper limit corresponds to ~75 vol. % (compaction of a hypothetical infinitely dilute suspension of cubic crystals). In nature, the SRPT will be reached at a specific crystallinity which reflects mutual significance of *in-situ* nucleation and growth *vs*. mechanical rearrangement. Natural occurrence of lavas with crystallinity greater than the

PRPT of ~35 vol. % (e.g., Marsh, 1981; Bachmann & Bergantz, 2004; Huber et al., 2010) suggests that their crystallinities were not achieved by closed-system crystallization but have been enhanced by mechanical interactions or remobilization of crystal-enriched mushes.

5.5. Application to natural igneous rocks

5.5.1. Sample selection and processing

Systematic ordering of crystal centers, expressed by increasing value of the clustering index in a texture undergoing progressive crystal accumulation or melt extraction provides the opportunity to detect these processes directly by textural analysis. We illustrate the approach on four samples of porphyritic rocks (Tab. 5.4). Three samples (J-1, J-3 and J-9) are porphyritic biotite granites (Jizera type) from the Krkonoše-Jizera plutonic complex (Bohemian Massif, Czech Republic; Žák & Klomínský, 2007; Žák et al., 2013; Kusiak et al., 2014). The sampled intrusive unit has a coarse-grained matrix and is variably porphyritic, with up to 10 cm large K-feldspar megacrysts. In our sample set, the amount of megacrysts ranges from 9 to 26 vol. % (Tab. 5.5, Fig. 5.11). The sample J-3 shows more irregular distribution of the phenocrysts and a weak planar magmatic fabric. Since our method uses the distances of the nearest neighbors, it remains insensitive to the orientation of crystals in the

Tab. 5.4. *List of samples.*

Sample	Description	Location	Area (cm^2)	Crystal number
CS-10	Camptonite	N 50.71211° E 14.19283°	33.2	761
J-1	Porphyritic granite	N 50.86013° E 15.19027°	4727	324
J-3	Porphyritic granite	N 50.85868° E 15.19279°	7440	297
J-9	Porphyritic granite	N 50.84079° E 15.18353°	2455	296

Geographic coordinates are given in the WGS 84 format.

space. The fourth sample (CS-10) is an alkali lamprophyre (camptonite) from a ~1 m-thick dyke in the České středohoří volcanic province (Czech Republic; Jelínek et al., 1989; Ulrych & Balogh, 2000; Skála et al. 2014). The CS-10 is characterized by a very fine grained matrix hosting 22 vol. % amphibole phenocrysts with most abundant grain size of ~1.7 mm (Figs. 5.12 and 5.13).

Due to the large size of phenocrysts in the granite samples, textural analysis of the Jizera granites was performed on the outcrop scale. All phenocrysts in a rectangular area, 0.25–0.75 m^2 large, of a flat and fresh outcrop surface were traced on a transparent foil and scanned. About 300 phenocrysts were recorded at each site, which is sufficient for a statistically robust estimate of the clustering index (Jerram et al., 1996). The resulting bitmap images were processed using commercial image-editing software (Fig. 5.12). For the camptonite sample (CS-10), the bitmap image of phenocryst population was obtained by scanning the polished rock slab (55 × 60 mm) and tracing the scanned image on a computer drawing tablet. All raster images were processed by our custom image analysis program to provide sizes of all crystals and two-dimensional coordinates of their centers (Fig. 5.12). The R language facilities (R Development Core Team, 2011) were used to calculate the area (volume) fraction of phenocrysts (crystallinity), the clustering index, and the apparent two-dimensional crystal size distribution. The correction procedure of Donnelly (1978) was used to correct the clustering index for the edge effect (see Section 5.2.3).

Tab. 5.5. *Results of textural measurements.*

Sample	Φ (vol. %)	R	Φ_0 (vol. %)	*MEP* (%)
CS-10	22.1	1.133	17.9	23
J-1	17.8	1.168	6.7	67
J-3	9.2	1.066	5.2	24
J-9	25.9	1.235	7.1	84

Symbols: Φ – actual crystallinity (i.e., volume percentage of phenocrysts); Φ_0 – initial crystallinity prior to crystal accumulation / melt extraction event; R – clustering index; *MEP* – melt extraction percentage.

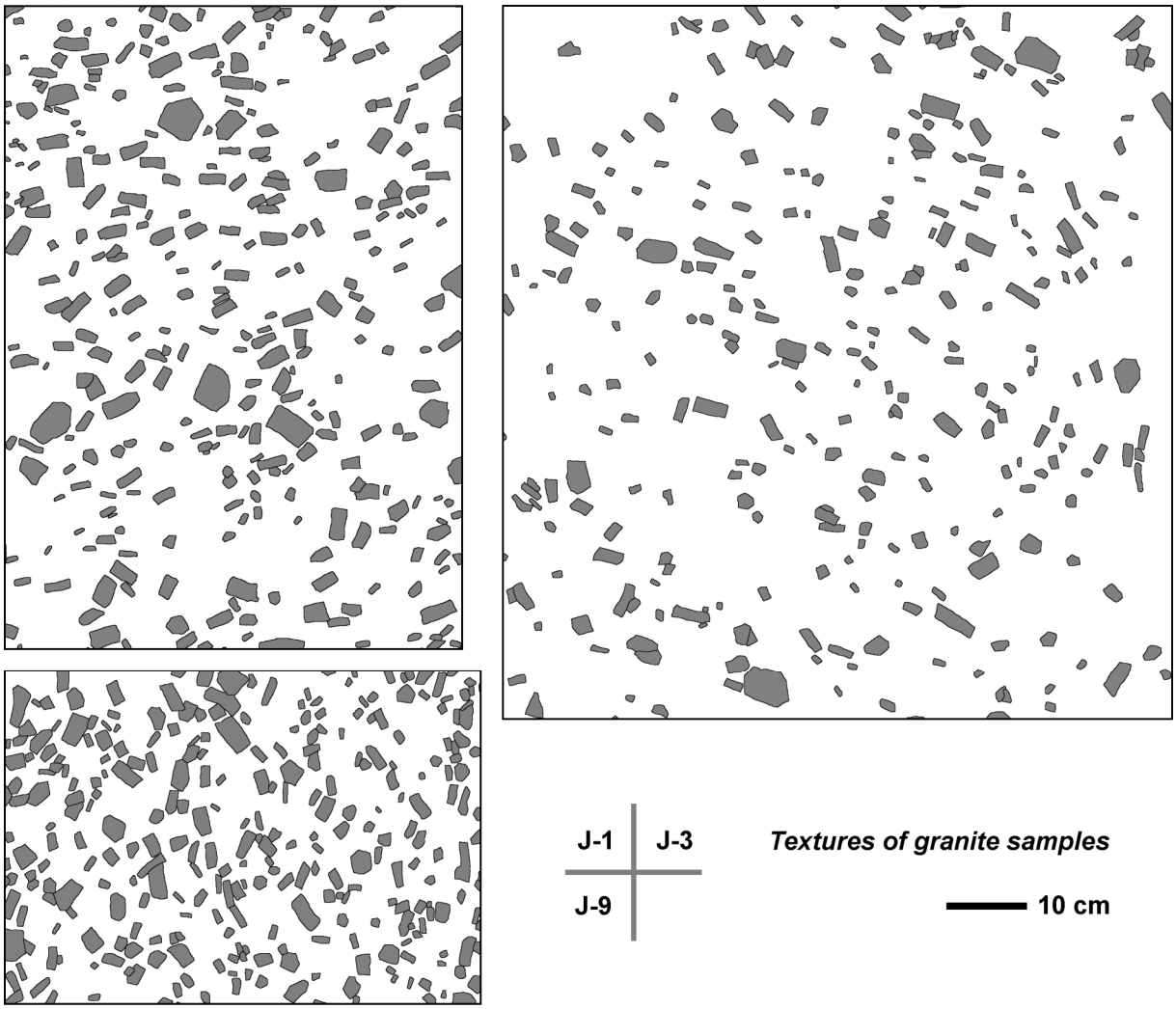

Fig. 5.11. *Digitized textures of the K-feldspar phenocrysts in the granite samples.*

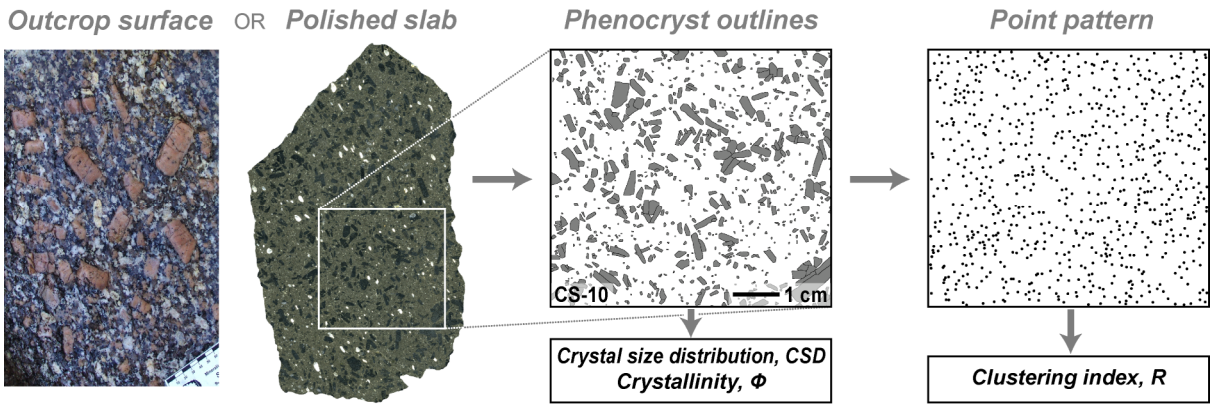

Fig. 5.12. *Process scheme for interpretation of the natural samples. Phenocryst outlines are drawn manually on the outcrop surface or polished rock slabs. Digitized crystal pattern provides crystallinity (volume fraction of phenocrysts) and the intersection areas of crystals are used to calculate the CSDs. Geometrical centers of all crystals from the digitized image form a point pattern which is used to calculate the clustering index, R.*

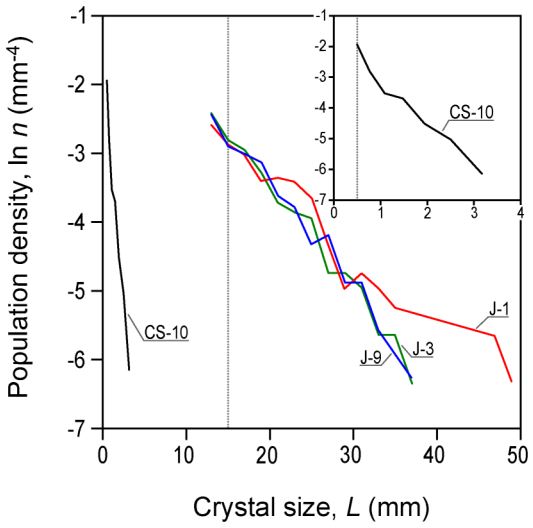

Fig. 5.13. *The CSDs of the granite and camptonite samples. The thin vertical lines illustrate the lower resolution limit of the digitizing procedure.*

5.5.2. Results and discussion of the samples

Phenocryst populations of all samples have straight log-linear CSDs (Fig. 5.13). Therefore, they can be directly processed using our model calibration (Fig. 5.9, Tab. 5.3). The sample of the camptonite dyke (CS-10) slightly deviates from the random texture trend. The amphibole phenocryst population (22 vol. %) is only weakly ordered (R = 1.13), which corresponds to extraction of 23 % of interstitial melt, that occurred at the initial crystallinity of 18 vol. %. The phenocryst populations of the porphyritic granites (samples J-1, J-3 and J-9) show much greater departures from the random distribution trend and, in addition, a monotonous increase in the clustering index with the phenocryst fraction defining a common compaction path, which indicates that the samples are derived from a common suspension (5–7 vol. %) by various degree of crystal accumulation. The amount of melt extracted from the crystal suspension ranged from 24 to 84 % of the initial melt volume (Tab. 5.5, Fig. 5.9), producing the present-day *apparent* crystallinities from 9 to 26 vol. %. Despite the generally high viscosity of granitic melts (e.g., Scaillet et al., 1998), the cooling regime in this plutonic complex does not appear to have imposed any constraint on the efficacy of the crystal accumulation or melt extraction.

In our granite samples, the crystal accumulation event is expected to have started at crystallinities of ~5 vol. %, which is substantially lower than the crystallinities usually invoked in the models of melt extraction from generally static crystal mushes, e.g., production of rhyolitic melts from granitic mushes near 40–50 vol. % crystallized (Bachmann & Bergantz, 2004). In our case study, the suspensions prior to and during the compaction are interpreted to be very to moderately dilute, with effective viscosity compared to the pure melt greater by only up to a factor of ~2.5 (Barnea & Mizrahi, 1973; Picard et al., 2013). Assuming a representative viscosity of 10^6 Pa s for hydrous granitic melts (e.g., Scaillet et al., 1998; Petford, 2003), and the crystal and melt density difference of 200 kg m^{-3}, a 2 cm-large crystal will gravitationally travel from the roof to the base of a 1 km-thick magma chamber on the order of thousands of years, and directly comparable results will be obtained by considering the rate of advance of the local solidification front (Mangan & Marsh, 1992). Such a crystal travel time is much shorter that the expected crystallization time of such a magma chamber imposed by simple cooling models. Compared to the geochemical estimates of the melt extraction from static crystal mushes (e.g., up to ~50 % for the Searchlight pluton, Nevada; Gelman et al., 2014), our range of melt extraction extends to slightly higher values and were most likely facilitated by the onset of compaction at very low crystallinities.

5.5.3. Discussion of the method

The method devised in this paper allows quantitative estimation of the extent of mechanical separation of crystals and interstitial melt using the divergence of phenocryst spatial distribution patterns from a random arrangement. Processes altering the spatial pattern of crystals other than crystal accumulation (by settling or floating) are, for example, heterogeneous nucleation on preexisting crystal faces, which induces clustering of crystals. Extensive heterogeneous nucleation reduces the value of the clustering index and leads to underestimation of the amount of extracted melt (*MEP*). Textural coarsening invoked in many studies to explain the origin of large phenocrysts, especially in granitic rocks (e.g., Johnson &

Glazner, 2010; Higgins, 2011), is also expected to quantitatively increase ordering of the spatial distribution pattern of phenocrysts.

Heterogeneous nucleation has profound effects on the CSD of a texture, manifested by its concave-up curvature (Špillar & Dolejš, 2014). Similarly, textural coarsening is associated with systematic changes of the CSD. During progressive coarsening small crystals are dissolved and their constituents are transferred to larger grains. The CSD becomes concave-down, with depletion in small crystals (e.g., Cashman & Ferry, 1988; Waters & Boudreau 1996; Higgins, 1998, 2002, 2006, 2011). Since we have evaluated CSDs of all our samples (Fig. 5.13) we infer that neither heterogeneous nucleation nor textural coarsening substantially altered the spatial distribution of the studied phenocryst populations. In general, the significance of other superimposed processes should be verified by using complementary textural descriptors (e.g., Špillar & Dolejš, 2014) and, in the future, more sophisticated spatial distribution parameters (e.g., radial distribution functions; Rudge et al., 2008) should be calibrated and used to further quantify the respective roles of nucleation kinetics, crystal accumulation, and textural coarsening.

5.6. General implications

Numerical simulations of textures of mechanically compacted (accumulated) crystal mushes show that the spatial distribution pattern of crystals systematically evolves from a random to ordered distribution as the amount of melt extracted or crystals accumulated increases. The spatial ordering results from the inherent inability of the crystals to overlap with each other. Crystal suspensions that have initially non-uniform crystal size distributions achieve the higher level of compaction (crystal packing), but then lower degree of ordering when compared to magmas with size-sorted crystals. Evolutionary trends of the clustering index as a function of increasing crystallinity only depend on the initial crystallinity and on the crystal size distribution (CSD) of the texture, and are otherwise universal. The extent of mechanically permissible compaction strongly depends on the initial crystallinity (phenocryst

fraction) and on the nature of the crystal size distribution. For straight log-linear CSDs, which most commonly occur in natural igneous rocks, sparse suspensions (~5 vol. % crystals) can be compacted up to the crystallinities of ~65 vol. % (secondary rigid percolation threshold) when mutual crystal-to-crystal interactions hinder further compaction and a rigid crystal framework forms. This corresponds to a rheological threshold where the magma gains yield strength and loses its ability to flow or erupt (e.g., Marsh, 1981; Vigneresse & Tikoff, 1999; Saar et al., 2001). By contrast, dense suspension with initial crystallinity of ~35 vol. % produced by *in-situ* crystal nucleation and growth in a closed system has a rather complex spatial configuration of the crystals with substantial proportion of touching crystal aggregates (primary rigid percolation threshold). In this case only a negligible compaction is possible without brittle fracturing or ductile deformation of the crystal framework. Therefore, no unique crystallinity level exists at which the rheological threshold is reached because it depends, among other factors, on previous crystallization *vs*. compaction history of the crystal mush. Crystallinities greater than 35–40 vol. % of some erupted lavas (e.g., Marsh, 1981; Bachmann & Bergantz, 2004; Huber et al., 2010) suggest that these could be remobilized crystal accumulations.

Our new method was tested on a representative sample set of porphyritic granites and porphyritic lamprophyre camptonite whose phenocryst textures, when characterized by the clustering index, show moderately ordered spatial distributions. Absence of significant concave-up curvature of CSDs of the studied samples suggests that neither the textural coarsening nor heterogeneous nucleation were the dominant processes during their crystallization and therefore the spatial distribution can be interpreted by the crystal accumulation/melt extraction model. For the granitic plutonites, the compaction started early at very low crystallinities (5-7 vol. % K-feldspar megacrysts) but moderate to high amounts of the melt (24-84 vol. %) was extracted. By contrast, the crystal accumulation in a camptonite dyke was late and minor (increase from 18 to 22 vol. % amphibole phenocrysts). These two contrasting observations may imply a direct relationship to dominantly thermal *vs*. mechanical processes in determining the final crystal content of natural magmas. The results of this study suggest two end-members of magmatic crystallization, which may act to variable

extent: (*i*) *in-situ* or closed-system crystallization, whereby the touching crystal framework forms statically, reaches the limit of no compaction early and with a large fraction of interstitial melt remaining, and (*ii*) open-system crystallization by mechanical crystal addition or melt removal. The significance of both processes depends on thermomechanical conditions in a magma chamber or setting: (*i*) sites dominated by rapid cooling and mechanical stagnation such as pluton margins will form an interlocking crystal framework early and in a chemically closed system. Mechanical interactions, for instance, residual melt extraction, are expected to be associated with substantial mechanical failure (e.g., submagmatic fracturing; Bouchez et al. 1992); (*ii*) locations of dominantly mechanical interactions such as pluton interiors or feeding channels, which modify the crystal fraction more efficiently than production by nucleation and growth. Samples from these units are predicted to return low or variable initial crystalinities, but high degrees of spatial ordering.

In summary, we show that, complementary to geochemical studies, the quantitative analysis of spatial distribution of crystals in magmatic rocks can reveal a detailed record of crystal accumulation or melt extraction from magmatic suspensions.

5.7. Acknowledgements

This study was financially supported by the Charles University Research Program P44 and the Czech Science Foundation Project Nr. 210/12/0986. Constructive reviews of Bruce Marsh and an anonymous reviewer are greatly appreciated. We thank Stephen Collett for grammar suggestions.

5.8. References

ARBARET L., BYSTRICKY M. & CHAMPALLIER R. (2007): Microstructures and rheology of hydrous synthetic magmatic suspensions deformed in torsion at high pressure. – *Journal of Geophysical Research* 112, B10208.

BACHMANN O. & BERGANTZ G. W. (2004): On the origin of crystal-poor rhyolites: Extracted from batholithic crystal mushes. – *Journal of Petrology 45*, 1565–1582.

BADDELEY A. (2008): *Analyzing spatial point patterns in R. Workshop notes.* – CSIRO online technical publication, http://www.csiro.au/resources/pf16h.html.

BARNEA E. & MIZRAHI J. (1973): A generalized approach to the fluid dynamics of particulate systems. Part I. General correlation for fluidization and sedimentation in solid multiparticulate systems. – *Chemical Engineering Journal* 5, 171–189.

BOUCHEZ J. L., DELAS C., GLEIZES G. & NÉDÉLEC A. (1992): Submagmatic microfractures in granites. – *Geology* 20, 35–38.

CASHMAN K. V. & FERRY J. M. (1988): Crystal size distribution (CSD) in rocks and the kinetics and dynamics of crystallization III. Metamorphic crystallization. – *Contributions to Mineralogy and Petrology* 99, 410–415.

CLARK P. J. & EVANS F. C. (1954): Distance to nearest neighbour as a measure of spatial relationships in populations. – *Ecology* 35, 445–453.

COLLINS W. J., WIEBE R. A., HEALY B. & RICHARDS S. W. (2006): Replenishment, crystal accumulation and floor aggradation in the megacrystic Kameruka Suite, Australia. – *Journal of Petrology* 47, 2073–2104.

DEERING C. D., COLE J. W. & VOGEL T. A. (2011): Extraction of crystal-poor rhyolite from a hornblende-bearing intermediate mush: a case study of the caldera-forming Matahina eruption, Okataina volcanic complex. – *Contributions to Mineralogy and Petrology* 161, 129–151.

DONNELLY K. (1978): Simulations to determine the variance and edge-effect of total nearest neighbor distance. – *In*: HODDER I. (ed): *Simulations Methods in Archeology*, Cambridge University Press, Cambridge, pp. 91–95.

FRENKEL D. & SMIT B. (2002): *Understanding molecular simulations: From algorithms to applications* (2nd ed). – Academic Press, New York, 664 pp.

GELMAN S. E., DEERING C. D., BACHMANN O., HUBER C. & GUTIÉRREZ F. J. (2014): Identifying the crystal graveyards remaining after large silicic eruptions. – *Earth and Planetary Science Letters* 403, 299–306.

HERSUM T. G. & MARSH B. D. (2006): Igneous microstructures from kinetic models of crystallization. – *Journal of Volcanology and Geothermal Research* 154, 34–47.

HIGGINS M. D. (1998): Origin of anorthosite by textural coarsening: Quantitative measurements of a natural sequence of textural development. – *Journal of Petrology* 39, 1307–1323.

HIGGINS M. D. (2002): A crystal size-distribution study of the Kiglapait layered mafic intrusion, Labrador, Canada: evidence for textural coarsening. – *Contributions to Mineralogy and Petrology* 144, 314–330.

HIGGINS M. D. (2006): *Quantitative textural measurements in igneous and metamorphic petrology*. – Cambridge University Press, Cambridge, 265 pp.

HIGGINS M. D. & CHANDRASEKHARAM D. (2007): Nature of sub-volcanic magma chambers, Deccan Province, India: Evidence from quantitative textural analysis of plagioclase megacrysts in the Giant Plagioclase Basalts. – *Journal of Petrology* 48, 885–900.

HIGGINS M. D. (2011): Textural coarsening in igneous rocks. – *International Geology Review* 53, 354–376.

HUBER C., BACHMANN O. & DUFEK J. (2010): The limitations of melting on the reactivation of silicic mushes. – *Journal of Volcanology and Geothermal Research* 195, 97–105.

JELÍNEK E., SOUČEK J., TVRDÝ J. & ULRYCH J. (1989): Geochemistry and petrology of alkaline dyke rocks of the Roztoky volcanic centre, České Středohoří Mountains, ČSSR. – *Chemie der Erde* 49, 201–217.

JERRAM D. A., CHEADLE M. J., HUNTER R. H. & ELLIOTT M. T. (1996): The spatial distribution of grains and crystals in rocks. – *Contributions to Mineralogy and Petrology* 125, 60–74.

JERRAM D. A., CHEADLE M. J. & PHILPOTTS A. R. (2003): Quantifying the building blocks of igneous rocks: Are clustered crystal frameworks the foundation? – *Journal of Petrology* 44, 2033–2051.

JOHNSON B. R. & GLAZNER A. F. (2010): Formation of K-feldspar megacrysts in granodioritic plutons by thermal cycling and late-stage textural coarsening. – *Contributions to Mineralogy and Petrology* 159, 599–619.

KIRK D. (1992): *Graphics Gems III*. – Academic Press, London, 631 pp.

KRETZ R. (1966): Grain-size distribution for certain metamorphic minerals in relation to nucleation and growth. – *Journal of Geology* 74, 147–173.

KRETZ R. (1969): On the spatial distribution of crystals in rocks. – *Lithos* 2, 39–66.

KUSIAK M. A., WILLIAMS I. S., DUNKLEY D. J., KONEČNY P., SLABY E. & HERVÉ M. (2014): Monazite to the rescue: U-Th-Pb dating of the intrusive history of the composite Karkonosze pluton, Bohemian Massif. – *Chemical Geology* 364, 76–92.

MANGAN M. & MARSH B. D. (1992): Solidification front fractionation in phenocryst-free sheet-like magma bodies. – *Journal of Geology 100*, 605–620.

MARSH B. D. (1981): On the crystallinity, probability of occurrence, and rheology of lava and magma. – *Contributions to Mineralogy and Petrology* 78, 85–98.

MARSH B. D. (1998): On the interpretation of crystal size distributions in magmatic systems. – *Journal of Petrology* 39, 553–599.

MATSUMOTO M. & NISHIMURA T. (1998): Mersenne twister: a 623-dimensionally equidistributed uniform pseudo-random number generator. – *ACM Transactions on Modeling and Computer Simulation* 8, 3–30.

MEANS W. D. & PARK Y. (1994): New experimental approach to understanding igneous texture. – *Geology* 22, 323–326.

MOCK A., JERRAM D. A. & BREITKREUZ C. (2003): Using quantitative textural analysis to understand the emplacement of shallow-level rhyolitic laccoliths – a case study from the Halle Volcanic Complex, Germany. – *Journal of Petrology* 44, 833–849.

PETFORD N. (2003): Rheology of granitic magmas during ascent and emplacement. – *Annual Review of Earth and Planetary Sciences* 31, 399–427.

PHILPOTTS A. R., SHI J. & BRUSTMAN C. (1998): Role of plagioclase crystal chains in the differentiation of partly crystallized basaltic magma. – *Nature* 395, 343–346.

PHILPOTTS A. R. & AGUE J. (2009): *Principles of igneous and metamorphic petrology* (2nd ed). – Cambridge University Press, Cambridge, 667 pp.

PICARD D., ARBARET L. PICHAVANT M., CHAMPALLIER R. & LAUEAU P. (2013): The rheological transition in plagioclase-bearing magmas. – *Journal of Geophysical Research* 118, 1363–1377.

RUDGE J. F., HOLNESS M. B. & SMITH G. C. (2008): Quantitative textural analysis of packing of elongate crystals. – *Contributions to Mineralogy and Petrology* 156, 413–429.

R DEVELOPMENT CORE TEAM (2011): *R: A language and environment for statistical computing*. – R Foundation for Statistical Computing, Vienna, Austria. ISBN 3-900051-07-0, URL: http://www.R-project.org.

SAAR M. O., MANGA M., CASHMAN K. V. & FREMOUW S. (2001): Numerical models of the onset of yield strength in crystal-melt suspensions. – *Earth and Planetary Letters* 187, 367–379.

SCAILLET B., HOLTZ F. & PICHAVANT M. (1998): Phase equilibrium constraints on the viscosity of silicic magmas 1. Volcanic-plutonic comparison. – *Journal of Geophysical Research* 120, 45–53.

SCHIAVI F., WALTE N. & KEPPLER H. (2009): First in situ observation of crystallization processes in a basaltic-andesitic melt with the moissanite cell. – *Geology* 37, 963–966.

SCHIAVI F., WALTE N., KONSCHAK A. & KEPPLER H. (2010): A moissanite cell apparatus for optical in situ ibservation of crystallizing melts at high temperature. – *American Mineralogist* 95, 1069–1079.

SKÁLA R., ULRYCH J., ACKERMAN L., JELÍNEK E., DOSTÁL J., HEGNER E. & ŘANDA Z. (2014): Tertiary alkaline Roztoky Intrusive Complex, České středohoří Mts., Czech Republic: petrogenetic characteristics. – *International Journal of Earth Sciences* 103, 1233–1262.

ŠPILLAR V. & DOLEJŠ D. (2013): Calculation of time-dependent nucleation and growth rates from quantitative textural data: Inversion of crystal size distribution. – *Journal of Petrology* 54, 913–931.

ŠPILLAR V. & DOLEJŠ D. (2014): Kinetic model of nucleation and growth in silicate melts: Implications for igneous textures and their quantitative description. – *Geochimica et Cosmochimica Acta* 131, 164–183.

ULRYCH J. & BALOGH K. (2000): Roztoky Intrusive Centre in the České středohoří Mts.: Differentiation, emplacement, distribution, orientation and the age of dyke series. – *Geologica Carpathica* 51, 383–397.

VIGNERESSE J. L., BARBEY P. & CUNEY M. (1996): Rheological transitions during partial melting and crystallization with application to felsic magma segregation and transfer. – *Journal of Petrology* 37, 1579–1600.

VIGNERESSE J. L. & TIKOFF B. (1999): Strain partitioning during partial melting and crystallizing felsic magmas. – *Tectonophysics* 312, 117–132.

WATERS C. & BOUDREAU A. E. (1996): A reevaluation of crystal size distribution in chromite cumulates. – *American Mineralogist* 81, 1452–1459.

ŽÁK J. & KLOMÍNSKÝ J. (2007): Magmatic structures in the Krkonoše-Jizera Plutonic Complex: evidence for localized multiphase flow and small-scale thermal-mechanical instabilities in a granitic magma chamber. – *Journal of Volcanology and Geothermal Research* 164, 254–267.

ŽÁK J., VERNER K., SLÁMA J., KACHLÍK V. & CHLUPÁČOVÁ M. (2013): Multistage magma emplacement and progressive strain accumulation in the Krkonoše-Jizera plutonic complex, Bohemian Massif. – *Tectonics* 32, 1493–1512.

Preface to Chapter 6

Practical application of the crystal accumulation modeling (Chapter 5) is illustrated in an exploratory study of the K-feldspar phenocryst textures in the porphyritic granite of the Krkonoše-Jizera pluton (Bohemian massif). In this chapter, we employ a detailed, outcrop-scale texture quantification in order to study textural variations over more than 550 m high vertical section of the porphyritic granite. Textural relationships allowed us to study the mode and rate of emplacement of granitic pluton and the mechanism of its internal differentiation. Results suggest that the intrusive unit was emplaced as a single magmatic pulse which underwent subsequent differentiation by combination of crystal settling and capture within the solidification fronts.

This chapter is a submission being prepared to the ***Journal of Petrology*** as **ŠPILLAR, V**. & DOLEJŠ, D.: *Internal dynamics of granitic magma chambers revealed by quantitative analysis of K-feldspar size and spatial distribution pattern: A case study from the Krkonoše-Jizera pluton, Bohemian massif.* The manuscript was formatted to conform to general layout of this thesis.

Chapter 6.

Internal dynamics of granitic magma chambers revealed by quantitative analysis of K-feldspar size and spatial distribution pattern: A case study from the Krkonoše-Jizera Pluton, Bohemian Massif

6.0. Abstract

Granitic batholiths are ubiquitous features of the Earth's continental crust. However, the mode and rate of their emplacement as well as mechanisms of their internal differentiation remain poorly understood. In this study we employ quantitative textural analysis of the K-feldspar and plagioclase phenocryst textures in the porphyritic Jizera granite (Krkonoše-Jizera plutonic complex, Bohemian Massif, Central Europe), to constrain the size of magma batches and mechanism of their differentiation. Compared to the numerical model of texture evolution during melt extraction, the studied textures indicate that variable part of the interstitial melt was extracted, thus the crystals variably accumulated at the mush stage of the magma crystallization. In total, ~20 % of melt was extracted and transported to shallower crustal levels but the efficacy of the melt extraction varies systematically with vertical position within the magma body. In detail, the melt extraction is greatest near the floor and roof of the magma chamber and almost negligible in the center. While intensive melt extraction (crystal accumulation) near the chamber floor is consistent with gravitational settling of crystals, intensive accumulation near the roof requires a differentiation mechanism unrelated to the sense of gravity. We suggest that convection of magmatic suspension through part of the

solidification front leads to the filtering of crystals in the rigid crystal framework of the front and is consistent with large crystal accumulation near the chamber boundaries. Regular variations of textural and melt extraction parameters suggest that more than 550 m thick granitic body was emplaced as a single batch of magma that underwent subsequent mechanical differentiation. Thermal constraints imply the flux of magma in the order of 0.1 km^3 $year^{-1}$ which is comparable to the magmatic fluxes reported from active volcanic arcs.

Key words:

Granite; crystal accumulation; melt extraction; K-feldspar phenocryst; texture quantification; numerical modeling.

6.1. Introduction

Magma chambers are complex system where multitude of mechanical and physico-chemical processes can operate on variable length and time scales. Compared to the mafic systems, the internal processes in granitic magma chambers remain far less understood and shrouded in controversies. Specifically, the mode of existence of granitic magma chambers itself remains unclear as it can range from incremental assembly of small magma bathes to the magmatic "big tank" (e.g., Glazner et al., 2004; Marsh, 2006; Lipman, 2007; Annen, 2009; de Saint Blanquat et al., 2011). The size of individual batches, however, is decisive for the internal dynamics of magma chamber as well as for its possible eruptive behavior or volcano-plutonic connection (e.g., Bachmann et al., 2007). Additionally, the role of sub-solidus processes and textural modification in granitic rocks remains questionable (e.g., Johnson & Glazner, 2010) and it poses potentially significant difficulty in the interpretation of granitic structures (e.g., Vernon, 1986; Paterson et al., 2005; Vernon & Collins, 2011). While geochemistry has long been bringing important insight to the understanding of magmatic systems it can hardly decipher the nature of more structurally and texturally related processes indicated above. In spit of that, the textural record remains largely unexploited source of

information about kinetics and mechanics of granitic magma crystallization (Mock et al., 2003; Farina et al., 2011; Yang, 2012).

In this paper, we examine a textural record of the K-feldspar and plagioclase phenocrysts in porphyritic Jizera granite of the Krkonoše-Jizera plutonic complex, Bohemian Massif (e.g., Žák & Klomínský, 2007; Słaby & Martin, 2008; Žák et al., 2009, 2013; Kusiak et al., 2014). Based on the textural digitization on the outcrop scale we evaluate a crystal size distribution, CSD, and a spatial distribution pattern of phenocrysts in the porphyritic granite. Systematic variations of textural parameters with altitude allowed us to constrain the mode and rate of magma emplacement. Interpretation of measured textural descriptors with the numerical model of texture evolution during crystal mush compaction (Špillar & Dolejš, 2015) provides an insight into the mechanism of internal differentiation of granitic magma chambers. The results suggest that mechanical magma differentiation process based on the interplay of the solidification front growth and convection through the permeable crystal network is involved in the crystallization of granitic magma chambers.

6.2. Geological setting

6.2.1. Regional setting

The Carboniferous Krkonoše-Jizera plutonic complex (KJPC; also variably referred to as Krkonoše-Jizera pluton or Karkonosze pluton) is a product of the late Variscan magmatic activity in the Saxothuringian zone of the Bohemian Massif, Central Europe (e.g., Žák et al., 2013). The pluton has E-W elongated "double-lobed" shape (Fig. 6.1) with its longest dimension ~70 km long and it covers an area of ~1000 km^2 in a map view. It intrudes Neoproterozoic to Paleozoic complexes dominated by various units of phyllites, mica shists and orthogneisses which underwent variscan blueshist-facies metamorphism with subsequent greenshist facies overprint (e.g., Mazur et al., 2006; Žáčková et al., 2010; Faryad & Kachlík, 2013; Žák et al., 2013).

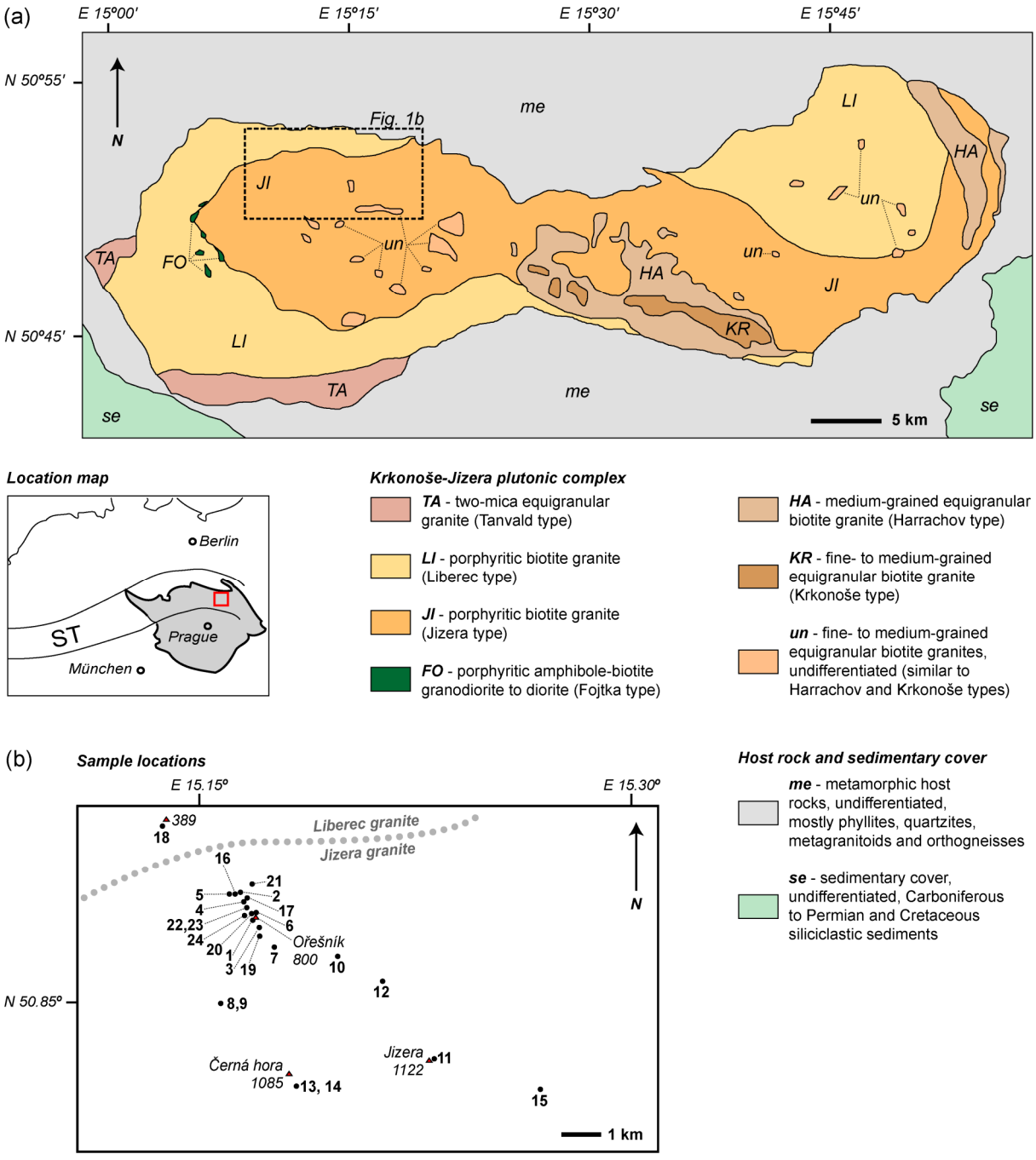

Fig. 6.1. *Geology of the Krkonoše-Jizera plutonic complex and sample locations.* **(a)** *simplified geological map of the Krkonoše-Jizera plutonic complex, Bohemian Massif, Central Europe. Bohemian Massif highlighted in gray in the location map, ST is the Saxothuringian Zone of the Bohemian Massif. Modified after Žák et al. (2013).* **(b)** *location of sampling points.*

The contact with surrounding units is sharp, discordant and it dips steeply to moderately outwards. Thermal effects of granite intrusion on the host lithologies are documented by up to 2.5 km wide zone of contact metamorphism in which regionally

metamorphosed host rocks were transformed to hornfels and spotted shists. Contact metamorphic mineral assemblages suggest that the granites were emplaced to moderate depth of no more than ~7 – 10 km (e.g., Ilnicki, 2011).

As suggested by gravimetric measurements (Sedlák et al., 2007), the pluton has tongue-like shape in three dimensions and it extends to the depth of ~8 km below the present-day surface. In eastern lobe of the complex pronounced negative gravity anomaly suggests even greater vertical extend of granitic material and is interpreted as a feeding or root zone of the pluton (Sedlák et al., 2007; Žák et al., 2013).

6.2.2. Internal structure

Krkonoše-Jizera plutonic complex is dominated by several intrusive units of porphyritic to equigranular biotite to two-mica granites to granodiorites (Fig. 6.1; Cloos, 1925; Klomínský, 1969; Žák & Klomínský, 2007; Słaby & Martin, 2008; Žák et al., 2009, 2013; Kusiak et al., 2014). On the western and south western margin, the KJPC is rimmed by two bodies of medium-grained equigranular two-mica granite (Tanvald granite), which represents probably the oldest intrusive event of the complex. Emplacement of the Tanvald granite was followed by at least two injections of two types of porphyritic biotite granites (Liberec and Jizera granite; Fig. 6.2) which constitue main part of the plutonic complex. While the radiometric dating remains rather inconclusive (317.3 ± 2.1 Ma *vs*. 319.5 ± 2.3 Ma for Tanvald and Liberec granites, respectively; Žák et al., 2013), the outcrop situation suggests that the intrusion of porphyritic Liberec granite followed that of equigranular Tanvald type (Klomínský et al., 2006; Žák et al., 2006).

Liberec granite is medium to coarse-grained weakly porphyritic biotite granite with K-feldspar phenocrysts typically ~3 cm large. In a broad gradational zone the Liberec granite transitions to "stratigraphically" higher positioned medium-grained strongly porphyritic biotite Jizera granite with larger and more elongate K-feldspar phenocrysts, typically ~5 – 10 cm long. Gradational contact of both porphyritic types suggests that their emplacement was

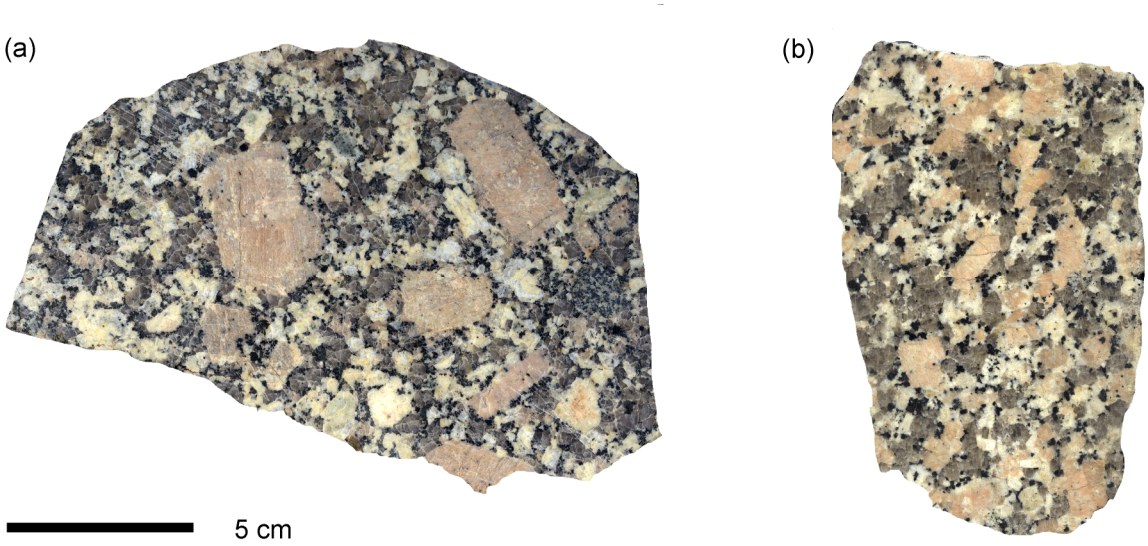

Fig. 6.2. *Representative textures of the porphyritic granites on a polished rock slabs.* **(a)** *Jizera granite;* **(b)** *Liberec granite*.

roughly coeval which is also supported by the radiometric ages of the Jizera granite, 320.1 ± 3.0 Ma and 319.3 ± 3.7 Ma, respectively (Žák et al., 2013). Apart from K-feldspar, plagioclase phenocrysts are occasional in Jizera granite, but are rarer in Liberec granite. In both facies, however, plagioclase occasionally forms thin rims of K-feldspar phenocrysts (rapakivi feldspar). Internal transitional zone between both porphyritic types is locally accompanied by blocks or smaller bodies of porphyritic quartz diorite to granodiorite (Fojtka granodiorite).

In the central and highest part of the KJPC the medium-grained equigranular biotite granite (Harrachov granite) overlaid by the fine to medium-grained equigranular biotite granite (Krkonoše granite) crops out. Equigranular biotite granites are younger than the porphyritic types (315.0 ± 2.7 Ma for Harrachov granite) and similar fine-grained rocks also appear as smaller subhorizontal sheet-like intrusions in the porphyritic granites (Žák et al., 2013). Within the porphyritic granites, the fine-grained bodies are more common in highest elevations.

Since Cloos (1925), the porphyritic granites of the Krkonoše-Jizera plutonic complex are a classical area of granite structural geology (e.g., Žák & Klomínský, 2007; Žák et al., 2009, 2013). Recent study focused on anisotropy of magnetic susceptibility and macroscopic

phenocryst fabric (Žák et al., 2013) suggests that internal structure of the Liberec granite records primary margin-parallel magmatic fabric related to magma emplacement. In the Jizera granite, the K-feldspar magmatic fabrics are more complex and are inferred to reflect superposition of multiple regional stress field orientations. In both cases, the fabric formation occurred at magmatic stage without pervasive solid-state overprint (Žák et al., 2013).

In otherwise homogeneous porphyritic granites local inhomogeneities such as schlieren channels, ladder dikes, or local K-feldspar accumulations are scattered. These structures are interpreted as a result of localized flow, crystal settling, or local melt migration during the mush stage of magma crystallization (Žák & Klomínský, 2007). Both porphyritic granites are also rich in decimeter-scale microgranular enclaves of more mafic composition (e.g., Słaby & Martin, 2008; Słaby et al., 2008). These enclaves macroscopically resemble fragments of the Fojtka granodiorite from the transitional zone of the Liberec and Jizera granites which suggests that they might originate from similar magmas.

6.3. Quantitative textural analysis

Magmatic textures provide an integrated record of both kinetic and mechanical processes active during magma crystallization. In order to decipher such processes in granitic magma chamber, we analyzed K-feldspar and plagioclase phenocryst textures in the porphyritic Jizera granit of the Krkonoše-Jizera plutonic complex.

6.3.1. Field textural analysis and sampling strategy

To provide statistically robust and representative data sets the textures were studied on the outcrop scale. On each sampling point, a part of the outcrop surface was covered with transparent foils on which individual phenocrysts were outlined. Where it was possible,

Tab 6.1. *List of studied samples.*

Sample details								Mafic enclaves			Phenocryst mode and clustering index			Phenocryst CSD		
Sample	**Facies**	**North**	**East**	**Alt.**	***W***	***H***	N_{all}	***v***	***f***	***Φ***	***plg***	***R***	N_{lim}	***S***	***I***	R^2
J-1	J	50.86013	15.19027	785	580	815	324	0	0	17.75		1.17	263	-0.17	-11.39	0.93
J-2	J	50.86606	15.18473	565	1249	1180	1258	0.47	3.4	18.60		1.20	1036	-0.16	-11.40	0.97
J-3	J	50.85868	15.19279	805	835	891	297	0	0	9.19		1.06	261	-0.15	-12.51	0.99
J-4	J	50.86406	15.18621	620	593	831	445	0.82	4.1	17.76		1.15	311	-0.15	-11.78	0.99
J-5	J	50.86528	15.18063	525	830	590	294	2.97	4.1	18.38		1.16	231	-0.13	-12.16	0.97
J-6	J	50.86196	15.19127	705	888	830	531	0.06	2.7	14.41	14.02	1.12	412	-0.14	-12.06	0.95
J-7	J	50.85468	15.19901	875	889	831	314	0	0	10.72		1.11	280	-0.13	-12.73	0.96
J-8	J	50.84056	15.18315	1063	888	833	473	0	0	12.32	23.63	1.10	349	-0.14	-12.32	0.99
J-9	J	50.84073	15.18340	1065	593	414	296	0	0	25.85	48.93	1.23	241	-0.15	-10.98	0.97
J-10	J	50.85452	15.22148	950	890	832	337	0.60	2.7	10.56	26.65	1.13	287	-0.12	-13.04	0.95
J-11	J	50.83425	15.26009	1105	891	831	180	0.02	1.4	3.20	31.22	1.01	140	-0.27	-11.93	0.96
J-12	J	50.85031	15.23825	1055	885	834	262	0.07	1.4	7.43		1.05	222	-0.19	-12.04	0.95
J-13	J	50.82445	15.21271	1070	891	834	198	0	0	4.79	18.13	1.05	161	-0.18	-12.69	0.95
J-14	J	50.82447	15.21296	1065	891	843	184	0	0	2.63		0.97	105	-0.26	-12.48	0.95
J-15	J	50.83053	15.29852	1020	892	829	109	0	0	3.13		1.00	94	-0.36	-10.26	0.93

J-16	J	50.86556	15.18334	560	836	890	646	0.23	2.7	21.62	1.22	503	-0.11	-12.17	0.91
J-17	J	50.8649	15.18708	590	891	834	514	0.51	5.4	15.76	1.17	416	-0.15	-11.67	0.95
J-18	L	50.87858	15.15507	375	835	594	516	0	0	15.32	1.10	357	-0.27	-9.30	0.98
J-19	J	50.85692	15.19329	830	829	887	373	0	0	12.56	1.10	293	-0.09	-13.41	0.92
J-20	J	50.86172	15.18936	725	831	894	459	0	0	15.04	1.14	379	-0.13	-12.15	0.98
J-21	J	50.86843	15.18823	485	828	892	543	0	0	16.22	1.18	416	-0.14	-11.97	0.97
J-22	J	50.86332	15.18747	650	831	888	540	0.90	9.5	18.35	1.18	433	-0.13	-12.14	0.99
J-23	J	50.86332	15.18747	650	832	293	180	0	0	24.75	1.16	149	-0.11	-12.26	0.95
J-24	J	50.86109	15.18782	735	831	888	559	0	0	14.20	1.12	414	-0.14	-12.01	0.99

Symbols and abbreviations: Facies – intrusive facies of the porphyritic granite (J – Jizera granite; L – Liberec granite); North and East – sample location in the WGS84 coordinate system; Alt. – altitude of the sampling point (m a. s. l.); W, H – width and height of the analyzed outcrop surface (mm); N_{all} – number of all phenocrysts in the studied are; v – volume percentage of mafic enclaves (vol. %) measured on the studied area of the outcrop surface; f – frequency of mafic enclaves (no. m^{-2}) on the studied area of the outcrop surface; Φ - mode of phenocrysts (vol. %); *plg* – volume percentage of plagioclase in phenocrysts. Missing values indicate that plagioclase and K-feldspar were not distinguished. R – clustering index of phenocrysts; N_{lim} – number of phenocrysts larger than the lower cut-off size, 12.5 mm; S – CSD slope (mm^{-1}); I – CSD intercept (population densities are considered as a natural logarithm of mm^{-4}).

occasional phenocrysts of plagioclase were discriminated from those of K-feldspar. Only the outcrops with flat, clean, and non-weathered surface were chosen for analysis. On each sampling point, the studied area was rectangular, 0.25 – 1.5 m^2 large, and it contained several hundreds to more than a thousand of individual phenocrysts (Tab. 6.1). The foils were subsequently scanned on an ordinary flat scanner and cleaned using commercial image editing software to obtain raster image maps of the textures. Scanning was performed in a resolution of 100 DPI which ensured that even the small phenocrysts were tens of pixels across and raster effects were thus minimized. This approach in texture digitization was chosen as the ability to resolve individual phenocrysts on the outcrop surface is far superior compared to outlining the phenocrysts on, for example, digital photographs of the outcrops.

On a total of 24 sampling points the textures were measured (Tab. 6.1, Fig. 6.1). The sampling points were chosen to set up an approximate profile from the northern margin of the Jizera granite body to south to its central part. Along the profile, elevation of sampling points increases by 620 m, from 485 m a. s. l. (J-21) to 1105 m a. s. l. (J-11). In the northern part of the profile the sampling density is high and elevation increases rapidly along the profile, whereas in the southern part, above ~900 m a. s. l., the profile is more leveled and sampling localities are widely scattered due to limited outcrop situation.

Field textural analysis is relevant for the population of larger phenocrysts, more than ~1 cm across (see Section 6.3.2.1). Therefore, the analysis of textures performed on the outcrops was supplemented by a textural measurements on a rock-slabs cut from the J-2 sample. The rock slabs were scanned and their textures treated in an analogous manner to the outcrop textures. After merging of the two data sets, this approach allows considerable extension of the length scale on which the crystal size distribution, CSD, is determined.

6.3.2. Data processing

Raster texture maps were processed by our custom image analysis program to provide sizes of all crystals and two-dimensional coordinates of their centers (Špillar & Dolejš, 2014).

The R language environment (R Development Core Team, 2011) was used to calculate the area (volume) fraction of phenocrysts (crystallinity), the clustering index, and the apparent two-dimensional crystal size distribution.

6.3.2.1. Crystal size distributions, CSDs

Crystal size distribution, CSD, is traditional and convenient mean of describing grain-size variations in rocks (e.g., Cashman & Marsh, 1988; Marsh, 1998, 2007; Higgins, 2006). CSD is defined as a probability density function that relates crystal size to frequency of its occurrence. In this work, CSDs were calculated based on a two-dimensional crystal sizes as which a diameter of equal-area circle was considered. This definition of crystal size is preferred over more complex methods (e.g., Higgins 2006) due to its simplicity and robustness to variations in the crystal shape (Špillar & Dolejš 2014). During the CSD calculation, only such crystals whose outline was not intersected by the study area boundaries were considered. Since only shapes and relative differences of CSDs were considered in this study we did not attempt to use any 2D-to-3D correction when dealing with CSDs (e.g., Higgins, 2000) and our analysis remained restricted to two-dimensional data sets.

In one sample (J-2) the range of crystal sizes over which the CSD was determined was extended to smaller sizes by supplementing the data acquired from transparencies by textural analysis of polished rock slabs, where smaller grains could successfully be outlined. A total of six slabs were cut from the porphyritic granite from J-2 location. The slabs were scanned, K-feldspar phenocrysts outlined in a commercial image editing software, and resulting raster images processed in a same way as those from transparencies. Each slab was approximately 2 dm^2 in size and on all the slabs a total of 149 K-feldspar phenocrysts were outlined. Superposition of CSDs from transparencies and rock slabs (Fig. 6.3a) suggests that transparency-derived CSDs are valid down to the crystal size of ~10 – 15 mm. Below this size limit the CSDs from transparencies become artificially concave-down as only fraction of small grains can be resolved on the outcrop surface. Therefore, we use mid of the size interval suggested, 12.5 mm, as a lower cut-of size for CSDs derived from transparencies. Due to

apparent uniformity of all studied CSDs the "overlap" approach was employed in one sample only and we suggest that the results can be reasonably extrapolated to other samples.

6.3.2.2. Clustering index, R

Apart from crystal sizes, the spatial distribution of crystals provides important means of quantitatively characterizing and interpreting a rock texture (e.g., Jerram, 1996, 2003; Rudge et al., 2008). Specifically, we employ the clustering index, *R* (Clark and Evans, 1954; Kretz 1966, 1969; Jerram et al., 1996, 2003), to characterize the spatial distribution of phenocrysts in porphyritic granite. The clustering index is defined as a ratio of the average nearest neighbor distance observed in a texture, R_A, to the average nearest neighbor distance in a randomly distributed set of points, R_E:

$$R = \frac{R_A}{R_E}. \tag{6.1}$$

We consider distance of crystal centers as a distance of crystals. The value of R_E depends on the number of points, *N*, and the area over which the points are distributes, *A*, as follows (e.g., Kretz, 1966):

$$R_E = \frac{1}{2} \cdot \sqrt{\frac{A}{N}}. \tag{6.2}$$

As follows from the Eqn. (1), the value of $R = 1$ indicates random distribution of points, whereas lower or greater values indicate clustered or ordered (i.e., anti-clustered) distributions, respectively (e.g., Kretz, 1966; Jerram et al., 1996).

During texture digitization some of the smallest phenocrysts could not be resolved on the outcrop surface and the population of small crystals is thus incomplete (see Section 6.3.2.1). Therefore, only crystals above the cut-off size of 12.5 mm were used in the clustering index calculation as above this size the population of crystals is supposed to be

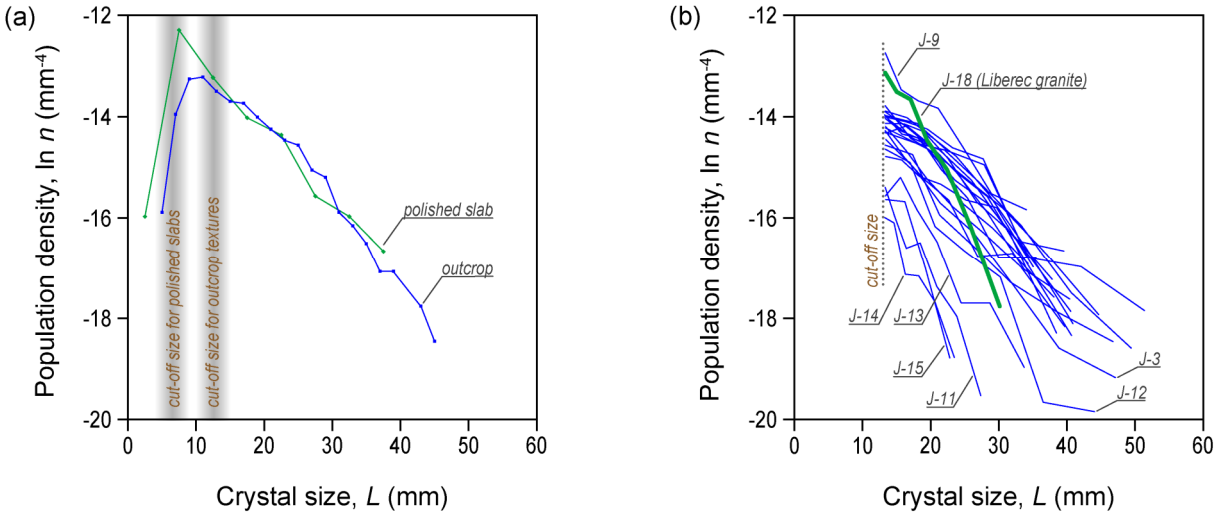

Fig. 6.3. *Phenocryst crystal size distributions of the porphyritic granites.* **(a)** *superposition of the CSDs derived from the outcrops and from the polished rock slabs (J-2 sample);* **(b)** *outcrop-derived CSDs of all samples.*

complete. Textural measurements were performed on a finite area and the area boundaries introduce a bias in calculation of the clustering index. Crystals close to the boundaries lack some of their neighbors which would be located outside of the studied area and the value of the clustering index is thus generally overestimated. To obtain unbiased value of the clustering index the empirical correction procedure of Donnelly (1978) was employed.

6.3.2.3. Estimate of three-dimensional crystal shape

Modeling of melt extraction from crystal mush (see later) requires the knowledge of true crystal shape in three dimensions. Three-dimensional shape of K-feldspar megacrysts was estimated using the CSDslice method of Morgan & Jerram (2006). The method compares measured ratios of the longest to shortest dimensions of 2D crystal sections to the database of the ratios determined computationally for a wide array of crystal shapes and returns the best fitting shapes.

We performed the shape determination for the sample J-2, where largest number of individual crystal outlines was captured. The best fitting shape is prismatic with axial ratio of

1:1.8:2.3 and with the goodness of fit, R^2 = 0.87. Second and following best fitting shapes closely match the best one which proves the robustness of determination. Since no qualitative variations of the phenocryst shape are observed we use the above determined value as a representative estimate for the whole Jizera granite.

6.3.3. Results of textural measurements

Quantitative textural analysis was performed in homogeneous porphyritic granite, away from local inhomogeneities such as mafic schlierens or K-feldspar accumulation. These structures are scattered across the pluton (Žák & Klomínský, 2007; Žák et al., 2013). In the study area (Fig. 6.1) the inhomogeneities are rare excepting in highest altitudes (~1000 m a.s.l.), where subhorizontal schlierens and schlieren channels are quite common. Similarly, small, apparently sheet-like bodies of fine-grained equigranular granite are common in higher altitudes. On the other hand, the mafic enclaves are qualitatively more frequent in lower parts of the studied domain and rarer in higher elevations. While not statistically robust, the data on mafic enclave frequency and volume percentage of enclaves within the rock derived from our transparencies suggest similar trend (Fig. 6.4, Tab 6.1).

6.3.3.1. Modal abundance of phenocrysts

Modal abundance of phenocrysts ranges from ~3 vol. % to ~26 vol. % (Fig. 6.5a, Tab. 6.1) and it varies regularly with altitude, therefore, with "stratigraphic" position within the ancient magma chamber. In lower part of the profile (~550 m a.s.l.) the amount of phenorysts ranges between ~15 and ~22 vol. % with an exceptional value of 25 vol. % (sample J-23) and it decreases to ~10 vol. % at around 950 m a.s.l (sample J-10). This trend continues further up and at the upper most part of the profile (~1100 m a.s.l.) the phenocryst content is around 3 – 5 vol. %. In the uppermost part, however, the values are more scattered with couple of outliers (12 and 26 vol. % in samples J-8 and J-9, respectively). The phenocryst

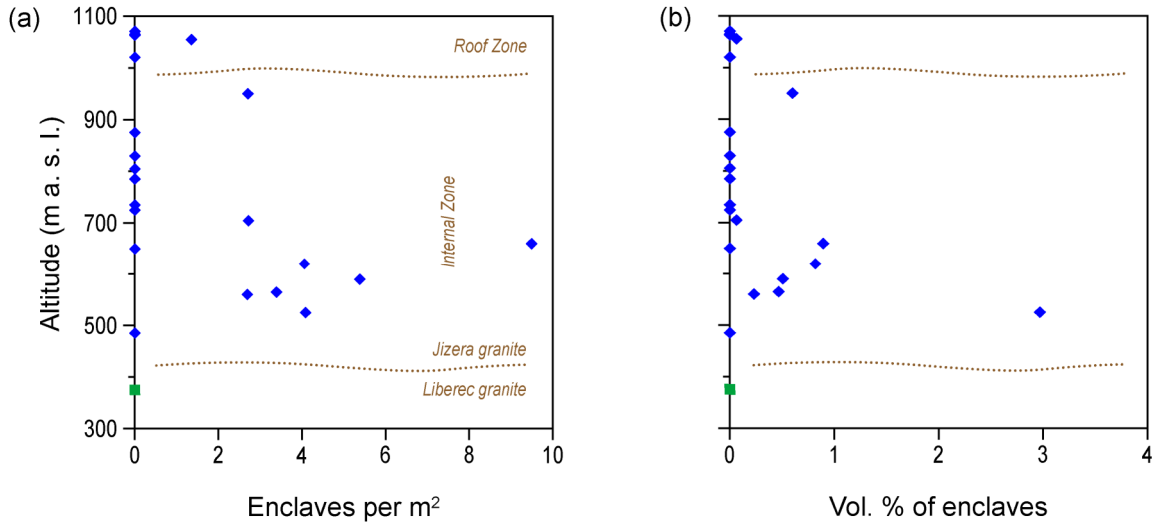

Fig. 6.4. *Occurrence of mafic enclaves as a function of altitude.* **(a)** *number of mafic enclaves per square meter of outcrop surface;* **(b)** *volume percent (area percent) of mafic enclaves on the outcrop surface. See text for a definition of zones.*

content thus steadily decreases with altitude through more than 600 m of vertical elevation difference. Detailed look at the lower most part of the profile may suggest slight reversal of this trend, which is, however, mainly due to 16 vol % of phenocrysts in the J-8 sample. Below ~400 to ~450 m a.s.l. the Jizera granite transitions to less porphyritic and texturally different Liberec granite (sample J-18 at 375 m a.s.l.).

In 7 samples where it could be determined the relative volumetric amount of plagioclase in phenocrysts ranges from 14 % to 31 % with exceptional value of 49 % (Tab. 6.1). While the highest fraction of plagioclase is found in one of the uppermost samples, J-9, we do not otherwise observe any systematic trend between altitude and plagioclase content in phenocrysts.

6.3.3.2. Clustering index

Within the sample set the values of the clustering index, *R*, range from 0.97 to 1.22 (Tab. 6.1) and it strongly and positively correlates with the mode of phenocrysts (Fig. 6.6b). Majority of the studied textures are ordered as they plot above the random texture trend (Špillar & Dolejš, 2014) in the clustering index *vs*. phenocryst mode diagram (Fig. 6.6b). The phenocryst-richest samples are those with highest values of the clustering index, therefore

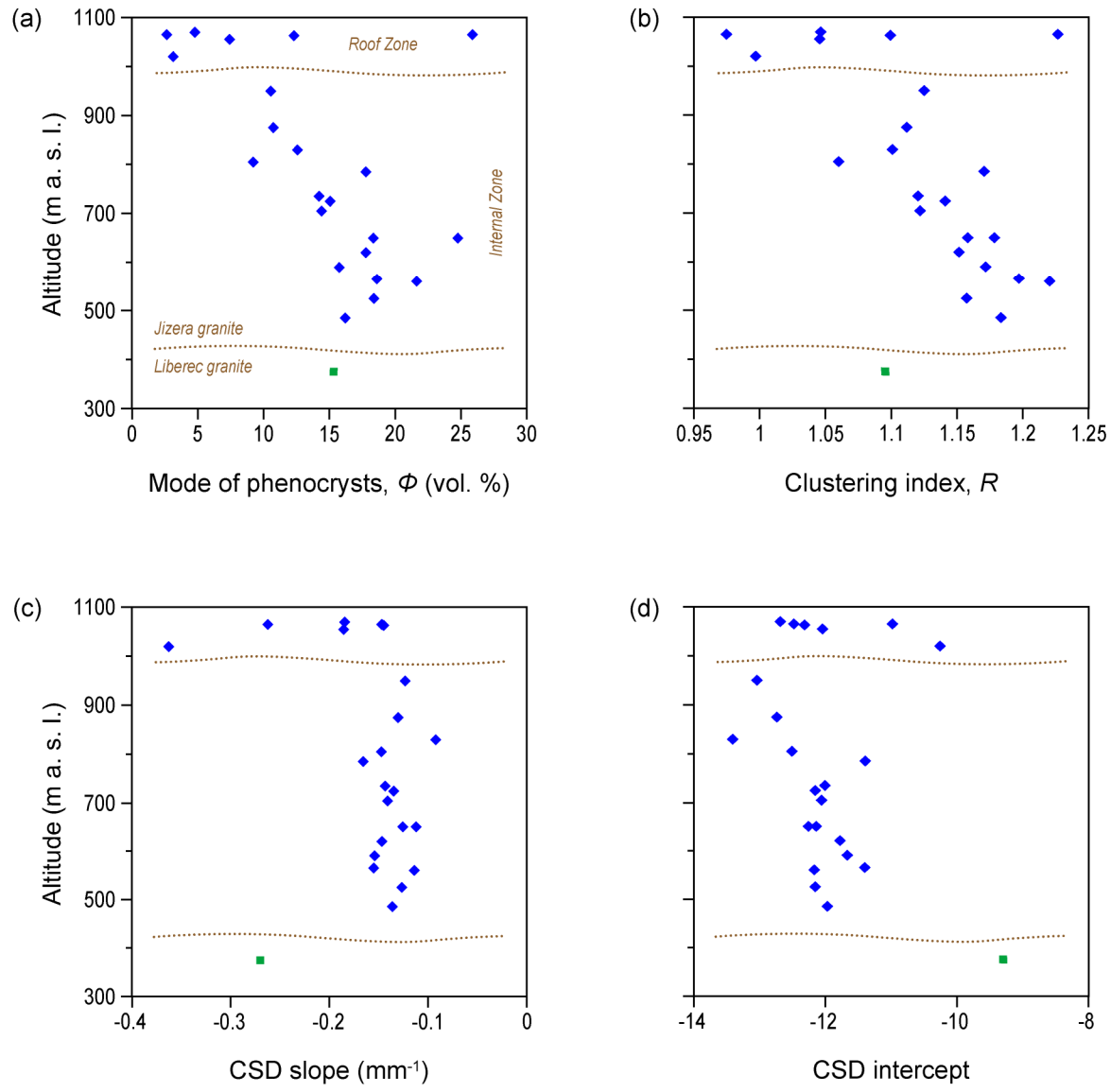

Fig. 6.5. *Textural data as a function of altitude.* **(a)** *modal content of phenocrysts;* **(b)** *clustering index of phenocrysts;* **(c)** *slope of the phenocryst CSD;* **(d)** *intercept of the phenocryst CSD. See text for the definition of zones.*

with most *ordered* textures. Only the most phenocryst-poor samples plot close to the random texture trend and spatial distribution of their phenocrysts is thus random or weakly order/weakly clustered.

In the Jizera granite, the clustering index varies systematically with altitude (Fig. 6.5b). Textures in the lowermost part, around 500 m a.s.l., are most ordered with highest values of the clustering index, $R \approx 1.2$. As altitude increases the clustering index decreases to ~1.1 in the central part of the studied profile (~800 m a.s.l.) with possible slight reversal in the

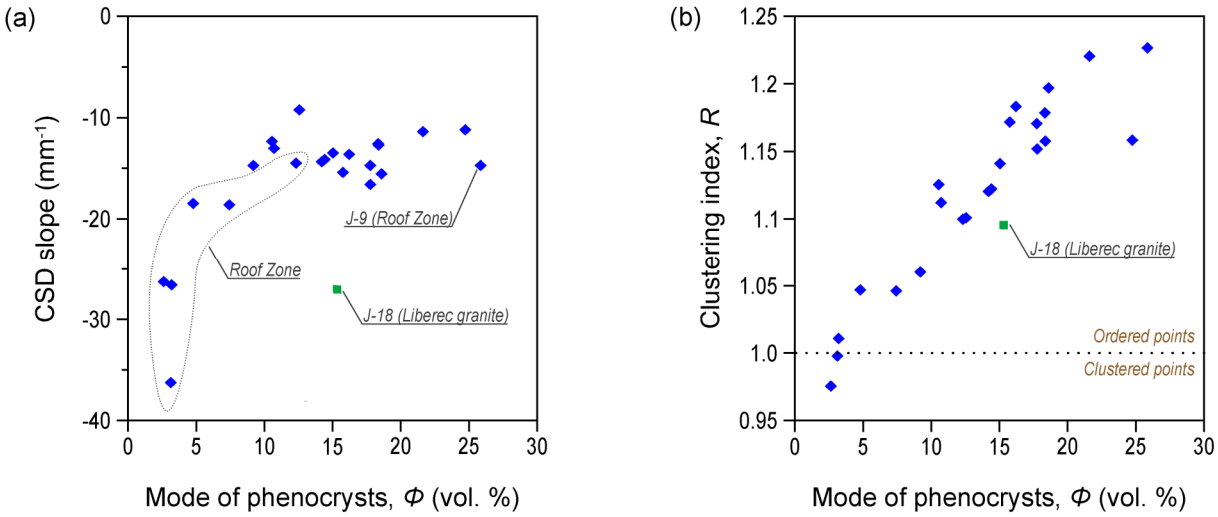

Fig. 6.6. *Textural parameters as a function of mode of phenocrysts.* **(a)** *correlation of the mode of phenocrysts with the CSD slope. Note that the slope is almost independent of the mode outside of the Roof Zone.* **(b)** *clustering index of phenocrysts as a function of phenocryst mode.*

upper half (sample J-10 with R = 1.13). In the uppermost part, above ~1000 m a.s.l., the values of the clustering index are more scattered between 0.97 and 1.23 (Fig. 6.5b). In the underlying unit of Liberec granite, the phenocryst texture is less ordered with R = 1.10 (sample J-18).

6.3.3.3. Crystal size distributions

To the first order, CSDs of phenocrysts are straight in conventional size *vs*. natural log of population density space (Fig. 6.3b). When plotted together, the CSDs of Jizera granite samples form a wide fan as they pivot around a common intercept and their slope varies. The slope and intercept values from linear regression of CSDs are summarized in Tab. 6.1. Across the studied profile the values of the intercept are quite homogeneous with variations restricted to the interval between -9.3 and -13 (Fig. 6.5d). The CSD slope ranges between -0.09 and -0.17 mm^{-1} everywhere excepting in the uppermost part of the profile, where CSDs are steeper and the slope reaches up to -0.36 mm^{-1} (Fig. 6.5c). In the case of J-9 sample, the CSD lies little above the fan of all other CSDs of Jizera granite. It is parallel to the CSD of neighboring J-8 sample, but it is shifted towards higher intercept value (-12.3 *vs*. -10.0) to accommodate

considerably higher modal content of phenocrysts (25.9 *vs*. 12.3 vol. % in J-9 and J-8, respectively).

The CSD slope correlates with the modal content of phenocrysts (Fig. 6.6a). The phenocryst poor samples from the uppermost part of the studied profile are these with steepest CSDs, therefore, with smallest phenocryst size. As values of the CSD intercepts are much more homogeneous and restricted in variations, similar relationship does not exist between the phenocryst content and CSD intercept.

Stratigraphically lower-most sample, J-18, belongs to the less porphyritic Liberec granite. Compared to the Jizera granite, Liberec facies has smaller phenocrysts and it is quantitatively reflected in steeper slope of its CSD (Fig. 6.3b). Contrasting intercept and slope values of this CSD thus break the trends defined by the Jizera granite samples (Figs. 6.5, 6.6a) and in the vertical profiles it clearly marks lower margin of the Jizera granite extent.

In detail, some of the Jizera granite CSDs are not perfectly straight but show slight concave-down curvature with deficient population of small grains (e.g., J-1, J-2, J-5, J-21, Fig. 6.3b). Generally, the concave-down curvature of a CSD can be either an inherent feature of a texture resulting from specific crystallization process (e.g., textural coarsening; Higgins, 2011) or methodological artifact when some of the small grains are missed during acquisition of textural data. To distinguish between the two we performed additional texture digitization from polished rock slabs to better characterize the population of small crystals in the J-2 sample, the sample with largest dataset under study (Section 6.3.2.1). The superimposition of CSDs from the outcrop and the rock slabs suggests that true CSD continues linearly to the smaller grain sizes (Fig. 6.3a). We thus infer that observed week curvature of some CSDs is an artifact of imperfect texture digitization from rough outcrop surface rather than a result of the crystallization process. In the concave-down CSDs the deviation from linearity is rather limited and not strong enough to significantly distort related parameters such as CSD slope and intercept derived from linear regression.

6.4. Modeling of melt extraction

6.4.1. Origin of ordered textures by melt extraction

Our measurements of K-feldspar and plagioclase phenocryst textures in porphyritic Jizera granite reveal that the spatial distributions of phenocrysts are variably ordered (or anti-clustered) when compared to textures resulting from *in-situ* nucleation and growth of crystals. Ordered textures can result from either mechanical accumulation of crystals or textural coarsening due to surface energy minimization (see later).

During mechanical accumulation of crystals from magmatic suspension the crystals can be compacted to fit into smaller volume of melt while some melt is left crystal free or with reduced amount of crystals and is virtually extracted from the system. In this process, the individual crystals – or already existing crystal aggregates – are geometrically reconfigured to approach closer to each other than they used to be in a pre-accumulation stage. However, once two crystals touch each other they cannot further approach. As a result, the crystal centers are generally more distant in the compacted crystal mush then they would be in *in-situ* crystallized mush of the same crystal content. Such textures are classified as ordered or anti-clustered and the extent of crystal accumulation (or alternatively of melt extraction) is expected to be proportional to the degree of ordering of a texture, therefore to the clustering index (Špillar & Dolejš, 2015).

Alternatively to crystal accumulation, ordered textures can also result from textural coarsening due to surface energy minimization. In this process the material is transferred by diffusion from smaller grains to the larger ones. Since material transfer is faster between more closely separated grains the textural coarsening ultimately leads to a texture consisting of evenly distributed equal-sized crystals. Apart from increasing ordering of the spatial distribution pattern, the textural coarsening also affects CSD and it promotes its concave-down shape as the population of small grains is progressively consumed.

The CSDs of phenocrysts in studied granites are straight and do not show any significant deficit in the small-grain population. Therefore, we suggest that the observed

ordered spatial distribution patterns are likely a result of mechanical accumulation of crystals and extraction of interstitial melt rather than of textural coarsening. In subsequent sections we will apply the model of texture evolution during the melt extraction event (Špillar & Dolejš, 2015) in order to estimate the quantitative role of this process in solidification of porphyritic granites.

6.4.2. Statistical model of mechanical melt extraction

6.4.2.1. Principles of melt extraction modeling

After adaptation to the real crystal shape of K-feldspar phenocrysts, 1:1.8:2.3, (Section 6.3.2.3) the model of Špillar & Dolejš (2015) was used to study textural effects of crystal accumulation or melt extraction in porphyritic granite. While details of the calculation procedure can be found in the original study we provide only a brief summary here. The crystal accumulation/melt extraction model operates in two steps: (*i*) crystallization; (*ii*) crystal accumulation. In the first step, *in-situ* kinetic crystallization by nucleation and growth of crystals from melt is simulated until the system reaches a desired pre-compaction crystallinity, Φ_I. The VoxelTex model is used to accomplish this step and the rates of crystal nucleation and growth are prescribed to generate a texture with straight CSD (Špillar & Dolejš, 2014), as observed in our samples.

In the crystal accumulation step the virtual crystal mush generated by *in-situ* crystallization is packed into smaller post-compaction volume which leads to greater post-compaction crystallinity, Φ_F. Instead of complex fluid-dynamic simulation of crystal mush compaction we apply simple Monte Carlo approach (e.g., Frenkel and Smit, 2002). We construct the compacted crystal mush progressively by sequentially and randomly adding individual crystals and crystal aggregates from the *in-situ* crystallized mush into the voids remaining within the compacted mush (Špillar & Dolejš, 2015). After all crystals are relocated to the compacted system the crystal mush is sectioned by a plane and a clustering index, R, of crystal centers is evaluated on this two-dimensional section. The compaction step

is repeated many times (typically, 100 times) to obtain statistically robust averaged results for the clustering index.

The post-compaction volume, thus the post-compaction crystallinity, is arbitrarily chosen value smaller than the initial volume of the crystal mush. In case that the post-compaction volume is chosen to small then some crystals will remain for which no large enough voids can be found. In such case the mechanical limit of compaction was exceeded (Špillar & Dolejš, 2015). For all volumes (crystallinities) in the range between initial and limiting value the compacted crystal mush can be constructed and the clustering index calculated. The method thus allows studying evolution of the clustering index with progressive compaction from initial to limiting crystallinity.

Our Monte Carlo approach does not simulate any specific fluid-dynamic process within the magmatic suspension. In stead, by repetitive random simulations, the method explores the configurational space and provides configuration-averaged properties of the compacted mush. In natural magmas, dynamic processes such as magma flow, convection, or chaotic crystal-crystal interactions tends to randomize crystal positions and orientations and therefore approach their textural signatures to those derived by Monte Carlo simulations. Such method thus remains general and unbiased by the assumptions regarding physics of specific process of crystal accumulation (Špillar & Dolejš, 2015).

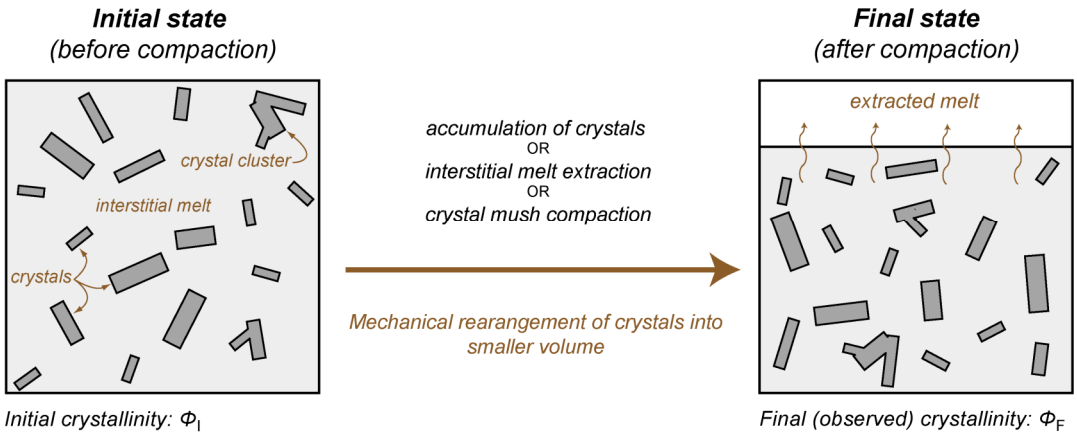

Fig. 6.7. *Crystal accumulation scheme. During the compaction, part of the interstitial melt is extracted, crystallinity increases from the intial, Φ_I, to final, Φ_F, and the crystals and crystal clusters are rearranged to fit into a smaller volume. Final crystallinity corresponds to the observed value, for example to the observed mode of phenocrysts, Φ. Modified after Špillar & Dolejš (2015).*

When analyzing outcrop textures of porphyritic granites the lower cut-off size was established below which not all of the crystals could had been resolved on the outcrop surface (Section 6.3.2.1). The clustering index derived from the outcrop data is thus relevant only for the crystal population from which all the crystals below the cut-off size were eliminated. To yield comparable values of the clustering index also from the simulated compaction textures the crystals whose size in a two-dimensional section was below the cut-off size were omitted from the clustering index calculation.

6.4.2.2. Calibration of melt extraction vs. *ordering relationship*

Let us assume some control volume, V_I, of magma with initial mode of crystals, Φ_I. During the crystal accumulation event the crystals from the volume V_I are packed into the smaller volume, V_F, with final crystallinity, Φ_F. The difference between the two volumes, V_I - V_F, is the volume of crystal-free melt; therefore the volume of melt which is effectively extracted from the system (Fig. 6.7). To characterize the extent of the crystal accumulation we define the accumulation ratio, AR, as a ratio of final and initial crystallinities:

$$AR = \frac{\Phi_F}{\Phi_I}. \tag{6.3}$$

By definition, the AR is always grater than unity after crystal accumulation event. Opposite case, $AR < 1$, implies that the crystal mush was "diluted" by some melt incoming from the outside. Same crystal accumulation process can be characterized as a melt migration event with some fraction of interstitial melt being extracted from the system. Using the initial and final crystallinities the percentage of extracted melt, MEP, can be expressed as (Špillar & Dolejš, 2015):

$$MEP = \left[1 - \frac{\Phi_I\left(1-\Phi_F\right)}{\Phi_F\left(1-\Phi_I\right)}\right] \cdot 100\ \%. \tag{6.4}$$

For any initial crystallinity, Φ_I, the melt extraction (crystal accumulation) model (Section 6.4.2.1) allows to calculate the evolution of the clustering index, R, as a function of final crystallinity, Φ_F. Since the accumulation ratio, AR, and the melt extraction percentage, MEP, are functions of exclusively Φ_I and Φ_F, both AR and MEP can be related to R. We performed 8 sets of crystal accumulation simulations for the initial crystallinities varying from 2.5 to 20 vol. % with 2.5 vol % step. Within each set, the final crystallinity was varied from the initial value up to the mechanical limit with 0.1 to 1 vol. % step and for each pair of the Φ_I and Φ_F the R, MEP, and AR were evaluated. Fig. 6.8 shows a calibration of isolines of the initial crystallinity, Φ_I, and of the melt extraction percentage, MEP, as a function of the final (observable) crystallinity, Φ_F, and of the clustering index, R (see Tab. 6.2 for calibration details). These calibrations are analogous to that of Špillar & Dolejš (2015) but here we use real crystal shape of the K-feldspar phenocrysts in the Jizera granite, 1:1.8:2.3, instead of isotropic cubes which quantitatively affects the calibrations. The calibrations (Fig. 6.8 and Tab. 6.2) will be used further to interpret melt extraction (crystal accumulation) efficacy in granitic crystal mushes.

6.4.3. Melt extraction and crystal accumulation in Jizera granite

Quantitative relationship between the melt extraction and the clustering index allowed us to calculate the amount of melt extraction, the accumulation ratio, and the initial (pre-extraction) mode of phenocrysts in the porphyritic Jizera granite. A total of 18 statistically representative samples with more than 200 phenocrysts larger than the lower cut-off size (Section 6.3.2.1) were used in these calculations. Calculated values are summarized in Tab. 6.3. All derived parameters, initial phencryst mode, accumulation ratio, and melt extraction show complex variations as a function of altitude (Fig. 6.9).

Initial mode of phenocrysts present in a magmatic suspension prior to the melt extraction or crystal accumulation event, Φ_I, is most commonly between 10 – 15 vol. %. In

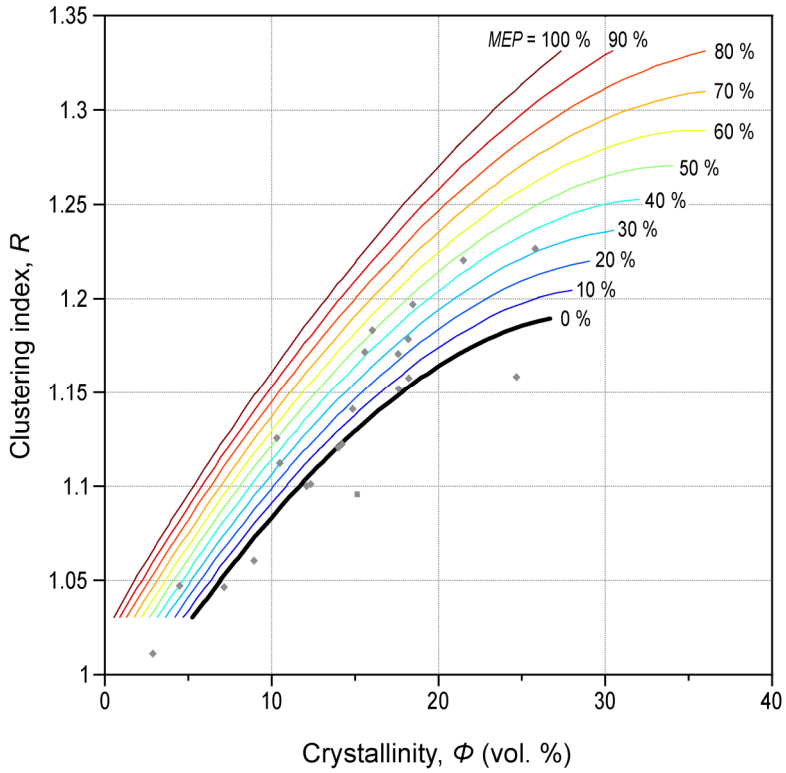

Fig. 6.8. *Isolines of the melt extraction percentage, MEP, as a function of the final (observed) mode of crystals (phenocrysts), Φ, and of the clustering index, R. Isolines are based on the polynomial fit (Tab. 6.2) to the simulation results are shown on such part of the R-Φ space only where the fit was calibrated. Gray points are measured data from the porphyritic granites.*

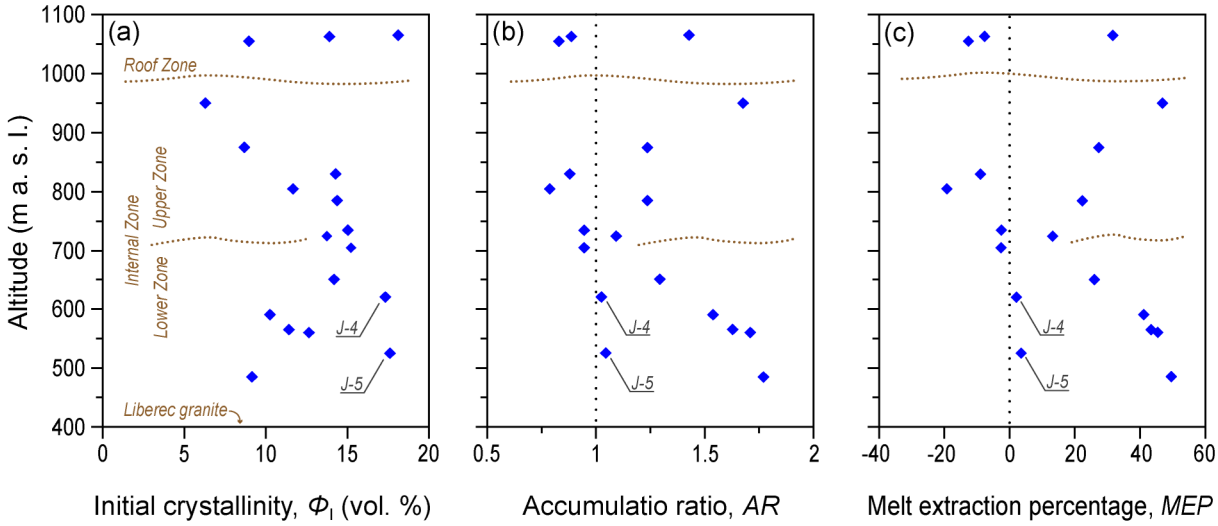

Fig. 6.9. *Calculated melt extraction / crystal accumulation parameters as a function of the altitude.* **(a)** *initial mode of phenocrysts, Φ_I, prior to the compaction event;* **(b)** *crystal accumulation ratio, AR;* **(c)** *melt extraction percentage, MEP. See text for definition of the zones.*

Tab. 6.2. *Polynomial fits for the initial crystallinity, Φ_I, and for the melt extraction percentage, MEP, as a function of the final (observed) crystallinity, Φ, and clustering index, R.*

Fit for the melt extraction percentage, *MEP*.

$$MEP = a_1\Phi^3 + a_2\Phi^2 R + a_3\Phi^2 + a_4\Phi R^2 + a_5\Phi R + a_6\Phi + a_7 R^3 + a_8 R^2 + a_9 R + a_{10}$$

a_1 =	-1849.8936	a_5 =	-38992.7066	a_9 =	-24292.0336
a_2 =	-13258.1454	a_6 =	19117.7147	a_{10} =	7386.4140
a_3 =	21042.5881	a_7 =	-8076.5004		
a_4 =	17476.7117	a_8 =	25046.7214		

Fit for the initial crystallinity, Φ_I.

$$\Phi_I = b_1\Phi^3 + b_2\Phi^2 R + b_3\Phi^2 + b_4\Phi R^2 + b_5\Phi R + b_6\Phi + b_7 R^3 + b_8 R^2 + b_9 R + b_{10}$$

b_1 =	-17.2889	b_5 =	87.9559	b_9 =	51.8640
b_2 =	50.0862	b_6 =	-41.4062	b_{10} =	-18.0457
b_3 =	-54.0045	b_7 =	15.1082		
b_4 =	-43.5479	b_8 =	-48.9967		

Fits were calculated using the Polyfitn toolbox in MATLAB® software.

Symbols: Φ – crystallinity (volume fraction, i.e., $\Phi \in \langle 0;1 \rangle$); Φ_I – initial crystallinity (volume fraction) prior to the crystal accumulation / melt extraction event; R – clustering index; *MEP* – melt extraction percentage (%); $a_1 \ldots a_{10}$, $b_1 \ldots b_{10}$ – fit coefficients.

detail, it forms a D-shaped profile as a function of altitude (Fig. 6.9a). The Φ_I first increasesfrom ~9 to ~15 vol. % from the lowermost to the central part of the intrusive unit and it then decreases back to ~6 vol. % in the upper part. In the uppermost locations, around 1050 m a. s. l., the regular trend terminates and Φ_I varies between 9 and 18 vol. % at constant altitude. In the lower part of the profile, two samples, J-4 and J-5, lie out of the D-shaped curve with higher initial phenocryst mode of ~17 vol. % which approaches the values typical for the central part of the intrusive unit.

The crystal accumulation ratio, *AR*, is defined as a ratio of actual and initial modes of phenocrysts (Eqn. 6.3) and its physical meaning is similar to that of the melt extraction percentage, *MEP*. The *AR* ranges from ~0.8 (slight dilution of the crystal suspension by

Tab. 6.3. *Melt extraction (crystal accumulation) parameter of Jizera granite samples.*

Sample	Altitude	N_{lim}	Φ	Φ_I	*AR*	*MEP*
J-21	485	416	16.22	9.17	1.77	49.6
J-5	525	231	18.38	17.60	1.04	3.6
J-16	560	503	21.62	12.65	1.71	45.4
J-2	565	1036	18.60	11.42	1.63	43.3
J-17	590	416	15.76	10.24	1.54	41.1
J-4	620	311	17.76	17.34	1.02	2.1
J-22	650	433	18.35	14.17	1.29	26.0
J-6	705	412	14.41	15.23	0.95	-2.7
J-20	725	379	15.04	13.75	1.09	13.1
J-24	735	414	14.20	15.03	0.94	-2.5
J-1	785	263	17.75	14.36	1.24	22.3
J-3	805	261	9.19	11.66	0.79	-19.3
J-19	830	293	12.56	14.27	0.88	-8.9
J-7	875	280	10.72	8.67	1.24	27.3
J-10	950	287	10.56	6.30	1.68	46.9
J-12	1055	222	7.43	8.95	0.83	-12.7
J-8	1063	349	12.32	13.90	0.89	-7.7
J-9	1065	241	25.85	18.11	1.43	31.6

Symbols: N_{lim} – number of crystal larger than the lower cut-off size, 12.5 mm; Φ – measured modal volume of phenocrysts (vol. %); Φ_I – calculated initial modal volume of phenocrysts prior to the crystal accumulation / melt extraction event (vol. %); *AR* – accumulation ratio; *MEP* – melt extraction percentage (%).

The samples with N_{lim} lower than 200 were discarded from the calculation procedure as statistically poorly constrained and are not included.

crystal-free melt) to ~1.8 (phenocryst mode almost doubled by crystal accumulation or melt extraction). Corresponding range of *MEP* is from -20 (20 % of melt *added*) to 50 (half of the interstitial melt *removed*). Both *AR* and *MEP* vary in the way which is opposite to the

variations of Φ_I and they define a C-shaped profiles as a function of altitude (Figs. 6.9b, c). From the *AR* = ~1.8 and *MEP* = ~50 % in the lower part of the intrusive unit both values decrease to ~1 and ~0 %, respectively, in the center and they increase again to ~1.7 and ~47 % in the upper part. The crystal accumulation (melt extraction) was thus most intensive in the marginal parts of the magma chamber whereas it was virtually inefficient in the center.

The outliers J-4 and J-5 which were away from the trend of the initial phenocryst mode, Φ_I, are also away from the *AR* and *MEP* trends as they show only little to no crystal accumulation and melt extraction. Similarly as in the case of initial phenocryst mode, also the regular trends of the *AR* and *MEP* terminate in the uppermost part of the intrusive unit. The *AR* there varies between ~0.8 and ~1.4 and corresponding *MEP* from ~-13 % to ~32 % at approximately constant altitude.

6.5. Discussion

6.5.1. Mode and rate of emplacement of granitic plutons

6.5.1.1. Single vs. *multiple magma batches?*

In the last decades, there has been a considerable debate about the mode and rate of emplacement and existence of granitic magma chambers (e.g., Glazner et al., 2004; Coleman et al., 2004). In general, two end-member scenarios are possible: (*i*) a step-wise emplacement of a large number of smaller pulses with significant cooling and crystallization between arrival of subsequent magma batches; (*ii*) a "big tank" model, in which large volume of magma is emplaced either at once or as multiple batches, but is allowed to communicate internally as single magma body (e.g., Glazner et al., 2004; Marsh, 2006; Lipman, 2007; Annen, 2009; de Saint Blanquat et al., 2011). While emplacement by successive magmatic pulses is evident in some magma bodies (e.g., Paterson et al., 2008) in other cases large volumes of magma present at a single occasion are required. Clear evidence for the "big tank" magma chambers of felsic compositions comes from large ignimbrite deposits, commonly

exceeding hundreds to thousands cubic kilometers in volume (e.g., Bachmann et al., 2007; Lipman, 2007; Huber et al., 2012). Alternative evidence for large volumes of magma present in the crust me be drawn from observations of continuous geochemical, modal, or textural variation across significant distances within the solidified magma body. To produce continuous internal zoning the magma chamber or its zoned part must have been present in a liquid or mushy state as only in such state some process of internal differentiation in which individual parts of the chamber communicate may be effective.

Based on the observed modal and textural variations we define a Roof Zone and an Internal Zone within the Jizera granite of the Krkonoše-Jizera plutonic complex and we suggest that the Internal Zone provides an example of internally differentiated continuously zoned magma chamber. Through the Internal Zone, the mode of phenocrysts and the clustering index decrease systematically as altitude increases from ~450 to ~1000 m a. s. l. while the CSD slope and intercept remain almost constant (Figs. 6.5c, d). Above ~1000 m a. s. l., the range of modal and textural variations is wider. Also, the textures are more heterogeneous on the outcrop scale with more abundant local inhomogeneities such as mafic schlierens, schlieren channels, local phenocryst accumulations, and sheets of fine-grained equigranular granite (Section 6.2.2). We suggest that heterogeneous textural record in this zone indicates close proximity of the roof or boundary of the magmatic pulse. In the boundary zone, sharp thermal, viscosity, and velocity gradients are expected to exist and to enhance the formation of various localized magmatic structures (Žák & Klomínský, 2007) while rapid crystallization is essential for preserving the heterogeneities. Moreover, sharp viscosity gradients may facilitate later emplacement of the fine-grained sheets into this zone. The granites of the fine-grained sheets resemble the Krkonoše and Harrachov facies of the Krkonoše-Jizera pluton (Žák et al., 2013). We thus infer that the occurrence of isolated sheets of this composition may suggest close proximity of the stratigraphically higher positioned bodies of the Krkonoše and Harrachov granite, which overlay the pulse of Jizera granite itself.

Stratigraphically below the Roof Zone the Internal Zone of the Jizera granite is located in which textural and modal parameters vary smoothly over more than 550 m of vertically. We suggest that such continuous variations are only possible if the whole body of that

thickness was allowed to coexist in a liquid or mushy state so that its individual parts could communicate to form smooth zoning. It is considered highly unlikely that such trends in the mode and clustering of phenocrysts could result from multiple magma injections occurring each after significant solidification of the previous ones. Moreover, CSDs are rather homogeneous across the Internal Zone (Fig. 6.5c, d) with no signs of internal contacts and cooling rate variations affecting the CSD slope (e.g., Cashman, 1993; Zieg & Marsh, 2002).

6.5.1.2. Emplacement rate and magma fluxes

In current erosion level the Jizera granite, including minor areas where it is supposedly overlain by the Krkonoše and Harrachov granites, crops out on the area of approximately 10×60 km. Considering a thickness of the magma batch of more than 550 m, the volume is estimated to more than 330 km^3 of granitic magma, which compares well to the erupted volumes of silicic ignimbrites and volumes of felsic batholithes published elsewhere (e.g., de Silva & Gosnold, 2007; Lipman, 2007; Lipman & Bachmann, 2015). Final parts of this batch must had been emplaced before its majority solidified in order to develop internal zoning. Simple order of magnitude estimate of duration of such process is provided by a characteristic cooling time, $t = L^2/\kappa$, where L is a half-thickness of the magma body and κ is a thermal diffusivity of a country rock (e.g., Marsh, 1989). For crustal thermal diffusivity of 10^{-6} m^2s^{-1}, the characteristic cooling time of 2.4×10^3 years leads to the influx rate of magma of at least 0.14 km^3 $year^{-1}$. The rate of magma influx in the order of 0.1 km^3 $year^{-1}$ compares well to the most productive magmatic systems (e.g., Annen, 2009; de Saint Blanquat et al., 2011). Similar rates are reported from the Aleutian Island Arc (Jicha et al., 2006) or from Elba Island laccoliths (Rocchi et al., 2002). Compared to the published construction rates of granitic batholiths or to the extrusion rates of silicic ignimbrites (e.g., de Silva & Gosnold, 2007; Lipman, 2007), the suggested rate of magma influx is up to several orders of magnitude higher. The published estimates, however, are time-averaged fluxes relevant for the long-term construction of large magmatic suits rather than for the individual magmatic pulses. These long-term rates are expected to vary in time to much higher instantaneous injection rates

compatible with our estimate (e.g., de Saint Blanquat et al., 2011; Lipman & Bachmann, 2015).

6.5.2. Internal dynamics and differentiation of granitic magma chambers

6.5.2.1. The Roof Zone: Evidence for local melt and crystal migration

In the Roof Zone, two neighboring and closely separated samples, J-8 and J-9, differ strongly by their phenocryst crystallinity (12 *vs*. 26 vol. %) and their clustering index (1.10 *vs*. 1.23) (Tab. 6.1). These differences propagate into the different melt extraction and accumulation rations of both samples (-8 *vs*. 32 % melt extracted; Tab. 6.3). While more phenocryst-poor sample, J-8, indicates limited amount of melt infiltration and crystal suspension dilution, the phenocryst-rich sample, J-9, underwent significant amount of melt extraction and crystal accumulation. The CSDs of both samples are almost parallel (Fig. 6.4b). While consistent CSD slopes suggest similar cooling rates (e.g., Zieg & Marsh, 2002), the variation in the CSD intercept is due to a large difference in the phenocryst content. The intercept difference therefore follows from the volume-balance constraints (Higgins, 2002a) and reflects a fact that larger number of grains is needed to accommodate greater mode, while relative numbers of crystals in individual size bins, thus the CSD slope, remain constant.

As suggested by Higgins (2002b) in the study of Kiglapait mafic intrusion, similarly related parallel CSDs can result from the melt migration and crystal accumulation due to gravitational settling. Variations of the calculated melt extraction percentage and differences in the CSD intercepts can thus be consistently explained as a result of *in-situ* crystal accumulation and local melt migration. Difference in the initial crystallinity (Tab. 6.3) suggests that limited advance of crystallization must have occurred between the two samples were derived from originally common magma. The observations of textural and melt extraction variations on the outcrop scale support the hypothesis of mobile phenocrysts capable of movement and accumulation (e.g., Vernon, 1986; Paterson et al., 2005; Vernon &

Collins, 2011) rather than their origin by late-stage coarsening in subsolidus (e.g., Johnson & Glazner, 2010).

6.5.2.2. The Internal Zone: Role of crystal settling in the lower part

Variations of the phenocryst content as well as of the melt extraction percentage with altitude (Tab. 6.3, Figs. 6.5a, 6.9) suggest that mechanical movement and accumulation of crystals was not restricted locally but it was active on the magma chamber scale. The melt extraction percentage and the accumulation ratio vary as a function of elevation in a C-shaped profile. Significant crystal accumulation occurred in the top and bottom parts of the magma chamber while it is essentially absent in the center. Such trend is comparable to the compositional profiles reported from the mafic intrusions, where olivine content or mg-number often decreases towards the center (e.g., Wager & Brown, 1968; Naslund, 1984; Galerne, 2009).

Based on the stratigraphy of the Internal Zone we subdivide it into the Upper and Lower Zones (e.g., Fig. 6.9). While Lower Zone is generally normally zoned with crystal accumulation increasing to the bottom, the zoning of the Upper Zone is reversed. We suggest following hypotheses for the crystallization of the Lower Zone. On its base, phenocrysts are most accumulated because accumulation is easiest from originally sparse magmatic suspension characterized by low initial crystal content (Fig. 6.9a). As lower solidification front (e.g., Marsh, 1989, 1995) advances into the magma chamber, fed partially by arrival of crystals from the chamber interior, the suspension crystallinity gradually increases. In turn, the suspension becomes more viscous and accumulation less effective. Textural record of the Lower Zone thus reflects solidification front advance coupled with progressively hindered crystal settling due to increasing crystallinity. This hypothesis is supported by calculated initial phenocryst crystallinity (Fig. 6.9a) which also increases towards the center of the Internal Zone.

In detail, two samples in the Lower Zone (J-4 and J-5) deviate from the trend described above. In these samples, the initial phenocryst content is high with negligible

crystal accumulation (Figs. 6.9b, c, Tab. 6.3) and it corresponds to reduced values of the clustering index (Tab. 6.1). We suggest that local melt migration/infiltration effects (e.g., Žák & Klomínský, 2007) may cause observed textural signatures, but spatially more thorough sampling would be necessary to provide detailed explanation. Specifically, expulsion and reinjection of interstitial liquid from compacting lower solidification front (e.g., Shirley, 1987; Meurer & Boudreau, 1998; Boudreau & Philpotts, 2002) may locally alter textural signatures. Alternatively, the outliers may represent pathways through which more crystallized crystal mush entered the lower solidification front, either from the chamber interior or from the magma source regions as the Internal Zone was infilling gradually.

6.5.2.3. The Internal Zone: Crystal filtering in the upper solidification front

In the Upper Zone, the amount of crystal accumulation increases towards the inferred roof of the magma chamber (Fig. 6.9b, c). Such reversed trend is incompatible with the effect of crystal settling and is similar to the trends known from mafic intrusion, where olivine mode or mg-number often increases towards the chamber boundaries (e.g., Wager & Brown, 1968; Naslund, 1984; Galerne, 2009). Similarly, reversed trend resembles the upper part of the S-shaped compositional profiles reported from some mafic sills (e.g., Gunn, 1966; Marsh, 1989; Boudreau & Philpotts, 2002; Latypov, 2003). The interpretation of reversed profiles in mafic intrusions and sills remains controversial and individual authors suggest its origin *via* different mechanisms, including convective fractionation (e.g, Rice, 1981; Wyborn et al., 2001) or *in-situ* crystallization with Soret diffusion in a boundary layer (e.g., Latypov, 2003). While these models are able to explain modal and geochemical features they do not provide adequate explanations for variations of textural parameters as reported in this study. Here we suggested that textural and modal variations observed in the Upper Zone of the Jizera granite can be consistently explained by mechanical fractionation during magma convection by filtering of phenocrysts in the solidification front.

Solidification front is a mushy zone through which a volume fraction of interstitial liquid gradually decreases towards a solidified rock (e.g., Marsh, 1989, 1995). Within the

solidification front the crystal content exceeds the solid percolation threshold (e.g., Vigneresse et al., 1996; Petford, 2003) and the crystal suspension or mush which is able to flow transitions to rigid crystal framework. Through most of this zone the melt is organized to form interconnected channels and is able to flow through the crystal framework (e.g., Marsh, 2002; Bea 2010). At the boundary between mobile mush and the rigid framework the interstitial melt is subjected to the sheer stresses generated by flow in the mobile zone (Fig. 6.10b). The interstitial melt is thus mechanically coupled to the suspension zone. If the suspension zone convects due to, e.g., thermal convection, the flow is transmitted into the crystal framework and the solidification front is partially penetrated by the convection cells (Fig. 6.10b). As suspension moves through the porous framework of the solidification front, part of the crystal cargo (e.g., Davidson et al., 2007) suspended in magma is mechanically filtered out and remains accumulated within the solidification front. Magma convection thus provides generic mechanism to accumulate phenocrysts – contrary to gravity – in the upper solidification front (Fig. 6.10). We note that this mechanism is not restricted to the upper front but it is expected to operate equally in the lower solidification front, where the efficacy of crystal accumulation is further enhanced by crystal settling.

The efficacy of the filtering process increases with increasing content of crystals suspended in magma but decreases as the flow velocity diminishes. The flow velocity scales with a Rayleigh number which is proportional to the third power of the magma chamber thickness (e.g., Marsh, 1989). Due to the third power, the role of the chamber thickness dominates and filtering efficacy thus the crystal accumulation is expected to decline as upper and lower solidification fronts approach. This corresponds well to the textural record of the Internal Zone, where crystal accumulation ratio (melt extraction percentage) decreases towards the center while the initial phenocryst content varies in the opposite way (Fig. 6.9, Tab. 6.3).

The Internal Zone was hypothetically emplaced as a pulse of magma with initially ~6 vol. % of phenocrysts (Figs. 6.9a, 6.10) and it started to solidify at upper and lower solidification fronts. At initially low phenocryst content and large thickness of the suspension zone the crystal accumulation by both settling and filtering was effective leading to high

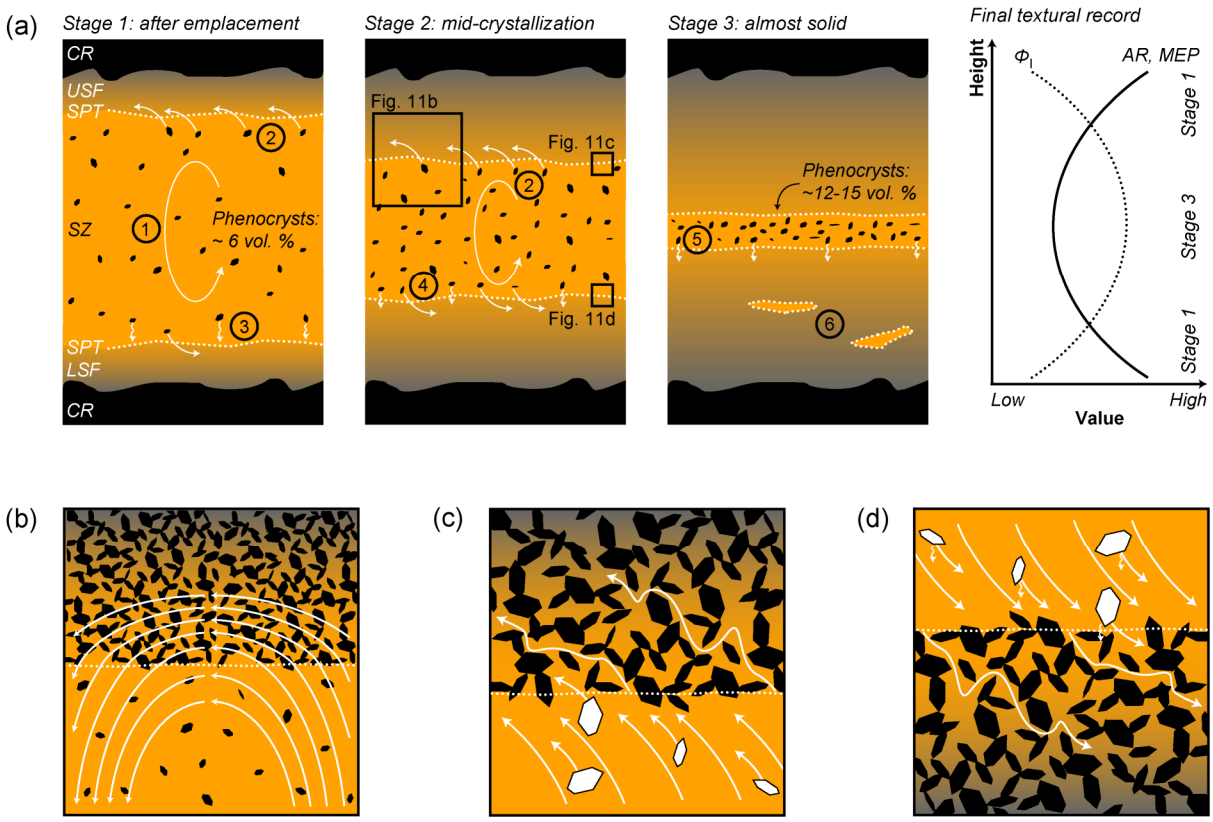

Fig. 6.10. *Conceptual model of the porphyritic granite crystallization.* **(a)** *after the emplacement (Stage 2) into the country rock (CR), the upper and lower solidification fronts (USF, LSF) start to propagate into the magma chamber interior and the suspension zone (SZ) shrinks. The suspension zone and rigid parts of the solidification fronts are separated by the solid percolation threshold (SPT). Initially, the magma contains rapidly convects (1). Convection currents partially penetrate into the solidification fronts where phenocrysts get stuck (2). In the LSF the accumulation of phenocrysts is contributed by Stoke's settling (3). After significant crystallization (Stage 2) the effective viscosity of the SZ increases and crystal settling becomes progressively hindered (4). As the SZ shrinks the convection ceases and crystal settling becomes ineffective (5) due to high effective viscosity of the suspension, but local movement (6) is possible, e.g., due to compaction of the solidification front.* **(b)** *at the suspension zone boundary (sold percolation threshold) the tangential forces generated by the convective currents in the suspension propagate into the solidification front and flow of the interstitial melt is induced.* **(c)** *in the upper solidification front, the convecting suspension invades the interconnected crystal framework and filtering of suspended phenocrysts occurs.* **(d)** *in the lower solidification front, the accumulation effect of the crystal filtering is enhanced by the gravitational crystal settling.*

accumulation ratios and melt extraction percentages at both floor and roof (Figs. 6.9b, c). On the floor, both accumulation mechanisms operated jointly thus the observed final mode of phenocrysts is higher than near the roof, where crystals are accumulated effectively by filtering but the suspension was sparse. As cooling continued and solidification fronts were

advancing into the magma chamber, the suspension zone became denser and thinner, and both accumulation mechanisms less effective. Finally, the suspension zone contained ~12 – 15 vol. % of phenocrysts and it was essentially undifferentiating (melt extraction percentage close to zero) when the solidification fronts joined in the center of the magma chamber.

For the filtering hypothesis to be valid, the convective currents must be able to carry the filtered particles to the upper part of the magma chamber against the gravity. Therefore, the velocity of the convective currents must exceed the settling velocity of individual crystals. Based on the equations of Marsh (1989) the convective velocity of magma can be estimated. With relevant parameters (Tab. 6.4), we obtain the convective velocity in the order of 0.1 m s^{-1}, which exceeds the Stokes settling velocity of 6 cm crystal by four orders of magnitude. The convective velocity is thus by far sufficient to bring the crystals to the upper solidification front and to reduce the overall crystal settling rate which would otherwise lead to complete crystal-liquid separation in the order of months. Larger particles, however, settle with faster velocities which may more approach the convective velocity, especially as the thickness of the mobile suspension zone thus the convective velocity decreases with progressive cooling.

Tab. 6.4. *Parameters for the convective and settling velocity calculations.*

Parameter	Value
Magma chamber half-thickness	270 m
Initial magma temperature	750 °C
Host rock temperature	200 °C
Magma viscosity	10^4 Pa s
Magma density	2300 kg m^{-3}
Thermal diffusivity (magma and host rock)	10^{-6} m^2 s^{-1}
Crystal – melt density difference	200 kg m^{-3}
Thermal expansivity	3.3×10^{-5} K^{-1}

Magma chamber half-thickness is considered as a half of the inferred minimal thickness of the pulse of the Jizera granite. Material properties are typical values and their expected variations do not change results nor the interpretations significantly.

The effect of particle size is consistent with our observation that most of the mafic enclaves are concentrated in the Lower Zone and only scarce exceptions of small enclaves are present in the uppermost part of the Upper Zone (Fig. 6.4). The enclave distribution thus provides independent evidence of mechanical, flow and gravity driven, nature of the Internal Zone differentiation process, which represents large-scale analogy of the crystal accumulation and melt migration processes reported from the Roof Zone.

6.5.3. Implications for magma fluxes and volcano-plutonic connection

The melt extraction percentage, *MEP*, was found to be positive and systematically zoned across the most of the Jizera granite (Tab. 6.3, Fig. 6.9c). Regardless of the exact nature of the differentiation process leading to the observed internal zoning the *MEP*, and the initial crystallinity, Φ_I, can be summed over the height of the magma chamber. We apply this approach to the Internal Zone of the Jizera granite, which arguably represents a single pulse of magmatic activity. Simple mass-balance calculations of the phenocryst and melt volume lead

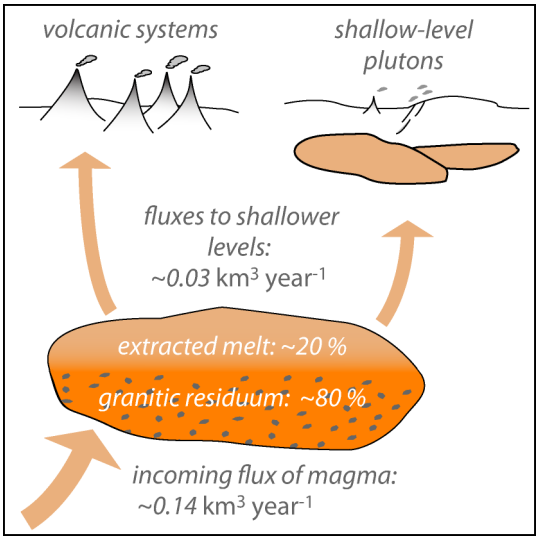

Fig. 6.11. *Magma fluxes estimated based on the melt extraction / crystal accumulation modeling and cooling time-scales.*

to the overall initial mode of phenocrysts ~13 vol. %, while overall final (observed) mode of phenocrysts approaches ~17 vol. %. The phenocrysts are thus accumulated ~1.3 times which is equivalent to the extraction of ~20 % of interstitial melt from the whole Internal Zone.

From the 0.14 km^3 $year^{-1}$ of intruding magma (Section 6.5.1.2), approximately 80 % thus solidified within the Internal Zone of the Jizera granite while remaining ~20 % continued to the overlaying crustal levels. Differentiating pulse of the Jizera granite is thus expected to release ~0.03 km^3 $year^{-1}$ of slightly more evolved magma to feed shallower-level plutons or surface volcanism (Fig. 6.11). While still high, this later magmatic flux is more compatible with published effusive rates (e.g., de Silva & Gosnold, 2007; Lipman, 2007; de Saint Blanquat et al., 2011) and it still represents instantaneous flux rate, not the long-term average. Assuming that all of the extracted liquid erupted as a product of surface volcanism, the above considerations lead to the extrusive-to-intrusive ratio of 1:4. This corresponds well to the extrusive-to-intrusive ratios determined by Lipman & Bachmann (2015) for silicic volcanism of the Southern Rocky Mountains volcanic field and it is in close agreement with the general ratio of 1:5 suggested by White et al. (2006). In reality, at least part of the extracted melt could solidified in plutonic environment and could potentially contributed to petrogenesis of shallower-level granites. Stratigraphically higher positioned and more differentiated, nearly eutectic (Słaby & Martin, 2008) Krkonoše and Harrachov equigranular granites or fine-grained sheets associated with the Roof Zone of the Jizera granite could represent candidates for such melts.

6.6. Concluding remarks

Quantitative parameters of phenocryst textures in apparently homogenous porphyritic granite show regular variations with altitude. Monotonously increasing phenocryst mode and decreasing clustering index with increasing altitude indicate that more than 550 m thick batch of magma had been emplaced as a single pulse that underwent subsequent internal

differentiation. Numerical modeling of texture evolution during melt extraction or crystal accumulation suggests that the porphyritic granite represents a partial cumulate which was variably enriched in phenocryst content. During the crystal accumulation, ~20 % of interstitial melt was removed from the system to form shallower plutons or to feed surface volcanism.

The amount of melt extracted from the crystal mush or the extent of crystal accumulation is not constant but it is largest close to the floor and roof while the textures are devoid of any measurable crystal accumulation effects in the central part of the chamber. Such crystal accumulation pattern is analogous to the compositional profiles known from some mafic intrusions and sills and it cannot be explained by gravitational settling of crystals alone. Here we suggest that in a large thus convecting magma chambers the convective currents penetrate partially the rigid crystal framework of the solidification fronts. The crystal framework then acts as a sieve and mechanically filters large crystals out from the suspension leading to the crystal accumulation near chamber boundaries. As upper and lower solidification fronts approach each other the thickness of the convecting zone decreases and the convecting suspension becomes denser. Both factors reduce the vigor of convection and crystal accumulation (melt extraction) from the crystal mush becomes less effective.

In general, this contribution illustrates that quantitative textural methods are capable of deciphering the cryptic zoning in otherwise homogeneous magmatic bodies and can provide constraints to the size and emplacement timescale of magma batches. In conjunction with numerical models of textural evolution the mechanical or physico-chemical processes responsible for the formation of internal chamber-scale zoning can be elucidated. We suggest that integration of textural and geochemical methods can prove as a fruitful field for future progress of our understanding of magma chamber dynamics.

6.7. Acknowledgements

This study was financially supported by the Charles University Research Program P44, the Czech Science Foundation Project Nr. 210/12/0986 (to David Dolejš) and Nr. 13-06958S (to Shah Wali Faryad).

6.8. References

ANNEN C. (2009): From plutons to magma chambers: Thermal constraints on the accumulation of eruptible silicic magma in the upper crust. – *Earth and Planetary Science Letters* 284, 409–416.

BACHMANN O., MILLER C. F. & DE SILVA S. L. (2007): The volcanic-plutonic connection as a stage for understanding crustal magmatism. – *Journal of Volcanology and Geothermal Research* 167, 1–23.

BEA F. (2010): Crystallization dynamics of granite magma chambers in the absence of regional stress: Multiphysics modeling with natural examples. – *Journal of Petrology* 51, 1541–1569.

BOUDREAU A. & PHILPOTTS A. R. (2002): Quantitative modeling of compaction in the Holyoke flood basalt flow, Hatford Basin, Connecticut. – *Contributions to Mineralogy and Petrology* 144, 176–184.

CASHMAN K. V. & FERRY J. M. (1988): Crystal size distribution (CSD) in rocks and the kinetics and dynamics of crystallization III. Metamorphic crystallization. – *Contributions to Mineralogy and Petrology* 99, 410–415.

CASHMAN K. V. (1993): Relationship between plagioclase crystallization and cooling rate in basaltic melts. – *Contributions to Mineralogy and Petrology* 113, 126–142.

CLARK P. J. & EVANS F. C. (1954): Distance to nearest neighbour as a measure of spatial relationships in populations. – *Ecology* 35, 445–453.

CLOOS H. (1925): *Einführung in die tektonische Behandlung magmatischer Erscheinungen (Granittektonik). 1. Das Riesengebirge in Schlesien*. – Borntraeger, Berlin, 194 pp.

COLEMAN D. S., GRAY W. & GLAZNER A. F. (2004): Rethinking the emplacement and evolution of zoned plutons: Geochronologic evidence for incremental assembly of the Tuolumne Intrusive Suite, California. – *Geology* 32, 433–436.

DAVIDSON J. P., MORGAN D. J., CHARLIER B. L. A., HARLOU R. & HORA J. M. (2007): Microsampling and isotopic analysis of igneous rocks: Implications for the study of magmatic systems. – *Annual Review of Earth and Planetary Sciences* 35, 273–311.

DE SAINT BLANQUAT M., HORSMAN E., HABERT G., MORGAN S., VANDERHAEGHE O., LAW R. & TIKOFF B. (2011): Multiscale magmatic cyclicity, duration of pluton construction, and paradoxical relationship between tectonism and plutonism in continental arcs. – *Tectonophysics* 500, 20–33.

DE SILVA S. L. & GOSNOLD W. D. (2007): Episodic construction of batholiths: Insight from the spatiotemporal development of an ignimbrite flare-up. – *Journal of Volcanology and Geothermal Research* 167, 320–335.

DONNELLY K. (1978): Simulations to determine the variance and edge-effect of total nearest neighbor distance. – *In*: HODDER I. (ed): *Simulations Methods in Archeology*, Cambridge University Press, Cambridge, pp. 91–95.

FARINA F., DINI A., INNOCENTI F., ROCCHI S. & WESTERMAN D. S. (2011): Rapid incremental assembly of the Monte Capanne pluton (Elba Island, Tuscany) by downward stacking of magma sheets. – *Geological Society of America Bulletin* 122, 1463–1479.

FARYAD S. W. & KACHLÍK V. (2013): New evidence of blueschist facies rocks and their geotectonic implication for Variscan suture(s) in the Bohemian Massif. – *Journal of Metamorphic Geology* 31, 63–82.

FRENKEL D. & SMIT B. (2002): *Understanding molecular simulations: From algorithms to applications* (2nd ed). – Academic Press, New York, 664 pp.

GALERNE C. (2009): *Emplacement mechanism and magmatic differentiation induced by magma flow in sill intrusions in sedimentary basins*. – Ph.D. dissertation, University of Oslo, 178 pp.

GLAZNER A. F., BARTLEY J. M., COLEMAN D. S., GRAY W. & TAYLOR R. Z. (2004): Are plutons assembled over millions of years by amalgamation from small magma chambers? – *GSA Today* 14, 4–11.

GUNN B. M. (1966): Modal and element variation in Antarctica tholeiites. – *Geochimica et Cosmochimica Acta* 30, 881–920.

HIGGINS M. D. (2000): Measurement of crystal size distributions. – *American Mineralogist* 85, 1105–1116.

HIGGINS M. D. (2002a): Closure in crystal size distributions (CSD), verification of CSD calculations, and the significance of CSD fans. – *American Mineralogist* 87, 171–175.

HIGGINS M. D. (2002b): A crystal size-distribution study of the Kiglapait layered mafic intrusion, Labrador, Canada: Evidence for textural coarsening. – *Contributions to Mineralogy and Petrology* 144, 314–330.

HIGGINS M. D. (2006): *Quantitative textural measurements in igneous and metamorphic petrology*. – Cambridge University Press, Cambridge, 265 pp.

HIGGINS M. D. (2011): Textural coarsening in igneous rocks. – *International Geology Review* 53, 354–376.

HUBER C., BACHMANN O. & DUFEK J. (2012): Crystal-poor versus crystal-rich ignimbrites: A competition between stirring and reactivation. – *Geology* 40, 115–118.

ILNICKI S. (2011): Variscan prograde P-T evolution and contact metamorphism in metabasites from the Sowia Dolina, Karkonosze–Izera massif, SW Poland. – *Mineralogical Magazine* 75, 185–212.

JERRAM D. A., CHEADLE M. J., HUNTER R. H. & ELLIOTT M. T. (1996): The spatial distribution of grains and crystals in rocks. – *Contributions to Mineralogy and Petrology* 125, 60–74.

JERRAM D. A., CHEADLE M. J. & PHILPOTTS A. R. (2003): Quantifying the building blocks of igneous rocks: Are clustered crystal frameworks the foundation? – *Journal of Petrology* 44, 2033–2051.

JICHA B. R., SCHOLL D. W., SINGER B. S., YOGODZINSKY G. M. & KAY S. M. (2006): Revised age of Aleutian Island Arc formation implies high rate of magma production. – *Geology* 34, 661–664.

JOHNSON B. R. & GLAZNER A. F. (2010): Formation of K-feldspar megacrysts in granodioritic plutons by thermal cycling and late-stage textural coarsening. – *Contributions to Mineralogy and Petrology* 159, 599–619.

KLOMÍNSKÝ J. (1969): The Krkonoše–Jizera granitoid massif. – Journal of Geological Sciences 15, 1–134.

KLOMÍNSKÝ J., SCHOVÁNEK P., JARCHOVSKÝ P., SULOVSKÝ P. & TOUŽIMSKÝ M. (2006): Contact of the Tanvald and Liberec granites near Jablonec nad Nisou, Geoscience Research Reports for 2006, 24–29.

KRETZ R., (1966): Grain-size distribution for certain metamorphic minerals in relation to nucleation and growth. – *Journal of Geology* 74, 147–173.

KRETZ R. (1969): On the spatial distribution of crystals in rocks. – *Lithos* 2, 39–66.

KUSIAK M. A., WILLIAMS I. S., DUNKLEY D. J., KONEČNY P., SLABY E. & HERVÉ M. (2014): Monazite to the rescue: U-Th-Pb dating of the intrusive history of the composite Karkonosze pluton, Bohemian Massif. – *Chemical Geology* 364, 76–92.

LATYPOV R. (2003): The origin of basic-ultrabasic sills with S-, D-, and I-shaped compositional profiles by in-situ crystallization of a single input of phenocryst poor parental magma. – *Journal of Petrology* 44, 1619–1656.

LIPMAN P. W. (2007): Incremental assembly and prolonged consolidation of Cordilleran magma chambers: Evidence from the Southern Rocky Mountains volcanic field. – *Geosphere* 3, 42–70.

LIPMAN P. W. & BACHMANN O. (2015): Ignimbrites to batholiths: Integrating perspectives from geological, geophysical, and geochronological data. – *Geosphere* 11, 705–743.

MARSH B. D. (1989): Magma chambers. – *Annual Review of Earth and Planetary Sciences* 17, 439–474.

MARSH B. D. (1995): Solidification fronts and magmatic evolution. – *Mineralogical Magazine* 60, 5-40.

MARSH B. D. (1998): On the interpretation of crystal size distributions in magmatic systems. – *Journal of Petrology* 39, 553–599.

MARSH B. D. (2002): On bimodal differentiation by solidification front instability in basaltic magmas part 1: Basic mechanics. – *Geochimica et Cosmochimica Acta* 66, 2211–2229.

MARSH B. D. (2006): Dynamics of magma chambers. – *Elements* 2, 287–292.

MARSH B. D. (2007): Crystallization of silicate magmas deciphered using crystal size distributions. – *Journal of American Ceramic Society* 90, 746–757.

MAZUR S., ALEKSANDROWSKI P., KRYZA R. & OBERC-DZIEDZIC T. (2006): The Variscan Orogen in Poland. – *Geological Quarterly* 50, 89–118.

MEURER W. P. & BOUDREAU A. E. (1998): Compaction of igneous cumulates Part I: Geochemical consequences for cumulates and liquid fractionation trends. – *Journal of Geology* 106, 281–292.

MOCK A., JERRAM D. A. & BREITKREUZ C. (2003): Using quantitative textural analysis to understand the emplacement of a shallow-level rhyolitic laccoliths – a case study from the Halle volcanic complex, Germany. – *Journal of Petrology* 44, 833–849.

MORGAN D. J. & JERRAM D. A. (2006): On estimating crystal shape for crystal size distribution analysis. – *Journal of Volcanology and Geothermal Research* 154, 1–7.

NASLUND H. R. (1984): Petrology of the Upper Border Series of the Skaergaard Intrusion. – *Journal of Petrology* 25, 185–212.

PATERSON S. R., VERNON R. H. AND ŽÁK J. (2005): Mechanical instabilities and physical accumulation of K-feldspar megacrysts in granitic magma, Tuolumne Batholith, California, USA. – *Journal of Virtual Explorer* 18, paper 1.

PATERSON S. R., ŽÁK J. & JANOUŠEK V. (2008): Growth of complex sheeted zones during recycling of older magmatic units into younger: Sawmill Canyon area, Tuolumne batholith, Sierra Nevada, California. – *Journal of Volcanology and Geothermal Research* 177, 457–484.

PETFORD N. (2003): Rheology of granitic magmas during ascent and emplacement. – *Annual Review of Earth and Planetary Sciences* 31, 399–427.

R DEVELOPMENT CORE TEAM (2011): *R: A language and environment for statistical computing*. – R Foundation for Statistical Computing, Vienna, Austria. ISBN 3-900051-07-0, URL http://www.R-project.org/.

RICE A. (1981): Convective fractionation – A mechanism to provide cryptic zoning (macrosegregation), layering, crescumulates, banded tuffs and explosive volcanism in igneous processes. – *Journal of Geophysical Research* 86, 405–417.

ROCCHI S., WESTERMAN D. S., DINI A., INNOCENTI F. & TONARINI S. (2002): Two-stage growth of laccoliths at Elba Island, Italy. – *Geology* 30, 983–986.

RUDGE J. F., HOLNESS M. B. & SMITH G. C. (2008): Quantitative textural analysis of packing of elongate crystals. – *Contributions to Mineralogy and Petrology* 156, 413–429.

SEDLÁK J., GNOJEK I., ZABADAL S., FARBISZ J., CWOJDZINSKI S. & SCHEIBE R. (2007): Geological interpretation of a gravity low in the central part of the Lugian Unit (Czech Republic, Germany and Poland). – *Journal of Geosciences* 52, 181–197.

SHIRLEY D. N. (1987): Differentiation and compaction in the Palisade Sill, New Jersey. – *Journal of Petrology* 28, 835–865.

SŁABY E. & MARTIN H. (2008): Mafic and felsic magma interaction in granites: The Hercynian Karkonosze pluton (Sudetes, Bohemian Massif). – *Journal of Petrology* 49, 353–391.

SŁABY E., GÖTZE J., WÖRNER G., SIMON K., WRZALIK R. & SMIGIELSKI M. (2008): K-feldspar phenocrysts in microgranular magmatic enclaves: A cathodoluminescence and geochemical study of crystal growth as a marker of magma mingling dynamics. – *Lithos* 105, 85–97.

ŠPILLAR V. & DOLEJŠ D. (2014): Kinetic model of nucleation and growth in silicate melts: implications for igneous textures and their quantitative description. – *Geochimica et Cosmochimica Acta* 131, 164–183.

ŠPILLAR V. & DOLEJŠ D. (2015): Melt extraction from crystal mushes: Numerical model of texture evolution and calibration of crystallinity-ordering relationships. – *Lithos* 239, 19–32.

VERNON R. H. (1986): K-feldspar megacrysts in granites: Phenocrysts, not porphyroblasts. – *Earth-Science Reviews* 23, 1–63.

VERNON R. H. & COLLINS W. J. (2011): Structural criteria for identifying granitic cumulates. – *Journal of Geology* 119, 127–142.

VIGNERESSE J. L., BARBEY P. & CUNEY M. (1996): Rheological transitions during partial melting and crystallization with application to felsic magma segregation and transfer. – *Journal of Petrology* 37, 1579–1600.

WAGER L. R. & BROWN G. M. (1968): *Layered igneous rocks*. – WH Freeman, San Francisco, 588 pp.

WHITE S. M., CRISP J. A. & SPERA F. A. (2006): Long-term volumetric eruption rates and magma budgets. – *Geochemistry, Geophysics, Geosystems* 7, 1–20.

WYBORN D., CHAPPELL B. W. & JAMES M. (2001): Example of convective fractionation in high-temperature granites from the Lachlan Fold Belt. – *Australian Journal of Earth Sciences* 48, 531–541.

YANG Z.-F. (2012): Combining quantitative textural and geochemical studies to understand the solidification processes of a granite porphyry: Shanggusi, East Qinling, China. – *Journal of Petrology* 53, 1807–1835.

ŽÁČKOVÁ E., KONOPÁSEK J., JEŘÁBEK P., FINGER F. & KOŠLER J. (2010): Early Carboniferous blueschist facies metamorphism in metapelites of the West Sudetes (Northern Saxothuringian Domain, Bohemian Massif). – *Journal of Metamorphic Geology* 28, 361–379.

ŽÁK J. & KLOMÍNSKÝ J. (2007): Magmatic structures in the Krkonoše–Jizera Plutonic Complex, Bohemian Massif: Evidence for localized multiphase flow and small-scale thermal–mechanical instabilities in a granitic magma chamber. – *Journal of Volcanology and Geothermal Research* 164, 254–267.

ŽÁK J., VYHNÁLEK B. & KABELE P. (2006): Is there a relationship between magmatic fabrics and brittle fractures in plutons? A view based on structural analysis, anisotropy of magnetic susceptibility and thermo-mechanical modelling of the Tanvald pluton (Bohemian Massif). – *Physics of Earth and Planetary Interiors* 157, 286–310.

ŽÁK J., VERNER K., KLOMÍNSKÝ J. & CHLUPÁČOVÁ (2009): "Granite tectonics" revisited: Insights from comparison of K-feldspar shape-fabric, anisotropy of magnetic susceptibility (AMS), and brittle fractures in the Jizera granite, Bohemian Massif. – *International Journal of Earth Sciences* 98, 949–967.

ŽÁK J., VERNER K., SLÁMA J., KACHLÍK V. & CHLUPÁČOVÁ M. (2013): Multistage magma emplacement and progressive strain accumulation in the shallow-level Krkonoše-Jizera plutonic complex, Bohemian Massif. – *Tectonics* 32, 1493–1512.

ZIEG M. J. & MARSH B. D. (2002): Crystal size distributions and scaling laws in the quantification of igneous textures. – *Journal of Petrology* 43, 85–101.

7. Summary

This thesis focuses on utilization of the methods of quantitative textural analysis in studies of magmatic crystallization and internal dynamics of magma chambers. Since active magmatic systems are generally inaccessible to direct observation we propose and develop numerical models of texture evolution to understand crystallization processes based on textural attributes of solidified rocks.

In order to understand the rates of crystal nucleation and growth in natural magmas and their dependence on environmental parameters we derive a new method for retrieval of these kinetic parameters from the crystal size distribution (CSD) of interest (Chapter 2). A single CSD trend can be produced by various combinations of the nucleation and the growth rate functions, which, however, lead to different crystallinity-time relationships. In an inverse approach, the CSD of interest in combination with appropriate crystallinity function, constrained by experimental phase equilibria or thermodynamic models, can be used to unambiguously determine the self-consistent nucleation and growth rates as a function of time. For quasi-linear crystallinity-time functions, the growth rate is predicted to be high during initial and final stages of crystallization, but it remains much lower at intermediate crystallinities. Consequently, the initial and final stages of crystallization are expected to record the highest departures from equilibrium. Magnitudes of the rates of nucleation and growth are proportional to the CSD slope. For conditions broadly similar to cooling lava lakes such as in Hawaii we have obtained growth rates of about 10^{-11} cm s^{-1}, in agreement with natural observations.

As the CSD itself does not define unique crystallization history of a rock, we have developed new high-resolution kinetic model for the simulation of texture evolution in a three-dimensional magma domain (Chapter 3). The principal objective is to develop and evaluate additional size, spatial, and contact parameters of magmatic textures and their

response to variations of the kinetic rate functions. The high-resolution crystallization model incorporates homogeneous nucleation and growth of crystals. The resulting textures broadly resemble natural ones and cover a range from equigranular to seriate types with considerable variation in the grain size and its distribution. Different combinations of the nucleation and growth rates can produce textures with identical CSDs, contact, spatial, and shape parameters. Inverse extraction of the kinetic rates from the textural information thus remains ambiguous even in the case that textural parameters other than the CSDs are employed. In addition, new parameters were identified that remain invariant for all textures resulting from homogeneous nucleation and crystal growth and whose values do not depend on the respective rates. Evaluation of the invariant parameters in natural igneous textures offers a powerful tool for identifying and separating the effects of other crystallization processes such as of heterogeneous nucleation, formation of melt boundary layers, mechanical interactions of crystals, or textural coarsening.

Igneous textures produced by heterogeneous nucleation (Chapter 4) evolve systematically from seriate to porphyritic varieties as the fraction of heterogeneous nuclei increases. Multiple textural parameters including CSD curvature, clustering index, and contact relationships correlate with the ratio of numbers of heterogeneous to homogeneous nuclei, but are insensitive to the nucleation and the growth rates during the crystallization. In turn, the relationships between the textural parameters and a fraction of heterogeneous nuclei can be calibrated and the fraction of heterogeneous nuclei can be determined in natural samples. The concave-up curved CSDs enriched in fine grain fractions, which are common in volcanic and plutonic rocks and are otherwise interpreted by discontinuous crystallization or magma mixing, are likely to result from continuous closed-system crystallization by heterogeneous nucleation. Complete textural analysis of several representative igneous rocks indicates that more than 90 % nuclei formed in a heterogeneous manner during polyphase crystallization of granitic magmas, but only ~60 to 70 % heterogeneous nuclei are formed in monomineralic mafic or ultramafic suspensions.

So far, only closed system crystallization by nucleation and growth was considered. To address the effects of open system processes we developed a numerical model of texture

evolution during crystal accumulation or interstitial melt extraction from crystal suspension. Instead of direct simulation of crystal movement we have employed a statistical Monte Carlo approach in which the crystal suspension is compacted by randomly placing crystals into compacted structure. The numerical compaction procedure is repeated many times to obtain averaged textural evolution. Monte Carlo simulations of textures of mechanically compacted (accumulated) crystal mushes show that the spatial distribution pattern of crystals evolves from a random to ordered distribution as the amount of melt extracted or crystals accumulated increases (Chapter 5). During the progress of crystal accumulation (interstitial melt extraction) the clustering index of crystal centers increases which quantify progressively more ordered textures. The evolutionary trend of the clustering index as a function of the crystal accumulation progress is unique and it depends on the initial crystallinity and CSD of a texture only. In turn, complementary to geochemical studies, the quantitative analysis of spatial distribution of crystals in magmatic rocks can reveal a detailed record of crystal accumulation or melt extraction from magmatic suspensions.

The compaction path and the crystallinity at which the rheological threshold (crystal interlocking) occurs depend on the previous crystallization history. Sparse suspensions (~5 vol. % crystals) can be compacted up to the crystallinities of ~65 vol. % when mutual crystal-to-crystal interactions hinder further compaction and a rigid crystal framework forms (secondary rigid percolation threshold). This corresponds to a rheological threshold where the magma gains yield strength and loses its ability to flow or erupt. By contrast, dense suspension with initial crystallinity of ~35 vol. % produced by *in-situ* crystal nucleation and growth in a closed system has a rather complex spatial configuration of the crystals with substantial proportion of touching crystal aggregates (*primary rigid percolation threshold*). In this case only a negligible compaction is possible without brittle fracturing or ductile deformation of the crystal framework. Crystallinities greater than 35–40 vol. % of some erupted lavas therefore suggest that these products could be remobilized partial crystal accumulations.

The new quantitative model of crystal accumulation was employed to interpret the textures of K-feldspar phenocryst in the porphyritic Jizera granite of the Krkonoše-Jizera

pluton, northern Bohemian Massif. Here, the content of phenocrysts and the clustering index continuously decrease in more than 550 m high vertical section of the porphyritic granite and suggest that the granite was emplaced as a single magma batch with no textural discontinuity. Using simple thermal considerations we derive a magma emplacement rate in the order of 0.14 km^3 $year^{-1}$, which is comparable to the rates of magma production in active volcanic arcs. Progressive ordering of spatial distribution pattern of K-feldspar phenocrysts suggests that the porphyritic granite represents a partial cumulate which was variably enriched in phenocrysts or depleted in melt content, respectively. The amount of melt extracted from the crystal mush is not uniform in the pluton section but it is largest near the floor and roof while no detectable crystal accumulation effects were found in the central part. In total, ~20 % of interstitial melt was removed from the magma batch and apparently transported to shallower crustal levels. Gravity-driven crystal accumulation processes, which are unidirectional, are unable to render such symmetrical accumulation profile. By contrast, the symmetrical accumulation profile provides evidence for mechanical filtering and capture of phenocrysts as the convecting suspension percolates through the porous crystal framework of both solidification fronts.

In summary, this thesis successively develops new quantitative methods of textural analysis in igneous systems. It illustrates their utility in forward predictive models of magma solidification as well as in inverse interpretations of specific kinetic and mechanical processes that may occur but were not yet unambiguously demonstrated in natural magma chambers.